A High-Efficiency, Low-Noise Platform for Microwave-to-Optical Quantum Transduction

Thesis by
Sameer Sonar

In Partial Fulfillment of the Requirements for the
Degree of
Doctor of Philosophy

CALIFORNIA INSTITUTE OF TECHNOLOGY
Pasadena, California

2026
Defended June 18, 2025

Sameer Sonar
ORCID: 0000-0002-1082-9360

ACKNOWLEDGEMENTS

It has been a long journey through graduate school, filled with both challenges and rewarding moments. I could not have made it to the end without the support of the following people.

First and foremost, I would like to thank my advisor, Oskar Painter, for welcoming me into his group and giving me the opportunity to work on such exciting and impactful projects. Your deep scientific insights and methodical approach to research have been instrumental in shaping both this work and my growth as a researcher. You taught me to think rigorously and systematically and helped me identify important problems to pursue. Your personal attention and guidance early in my PhD were invaluable.

I am deeply grateful to my work partner and friend, Utku Hatipoglu. Your unwavering persistence has been central to the success of many of the projects in this thesis. To David Lake and Piero Chiappina, I feel fortunate to have had the chance to work with such a fantastic team during my final two years. I also want to thank Srujan Meesala for mentoring both me and Utku and for teaching us the art of cryogenic optical measurements. To Jared Ren, thank you for guiding me early on with optomechanical simulations and nanofabrication techniques and for staying in touch throughout my journey. I would like to thank Prof. Vahala, Prof. Mirhosseini, Prof. Marandi, and Prof. Faraon for serving on my thesis defense and/or candidacy committee.

To Gihwan Kim and Andreas Butler, it has been a privilege to share this journey with you over the past six years. To Lucia De Rose, thank you for bringing boundless energy into the group. I also want to acknowledge Mo Chen, Steven Wood, Eunjong Kim, Sherry Zhang, Alp Sipahigil, Mohammad Mirhosseini, Vinicius Ferreira, Jash Banker, and Roger Luo. To the new grad students, Bastien Bakker, Ricky Parada, John Parker, Olivia Pitcl, and Matthew Davidson, thank you for bringing fresh energy and enthusiasm to the group.

I am grateful to the current and former QPG staff: Barry Baker, the labs would be much messier without you; Matthew McCoy, Brendon Larrowe, Christopher Freestone, Trevor Nash, Harry Liu, and Kamal Yadav, thank you for keeping the Watson labs and Steele cleanrooms running smoothly.

To the KNI staff: Guy DeRose, the late Bert Mendoza, Nathan Lee, Alex Wertheim, Tiffany Kimoto, and all others, thank you for keeping KNI operating so efficiently. It has been a privilege to have access to such a well-maintained and advanced nanofabrication facility.

I am also grateful to Angie Riley, Christy Jenstad, and Jennifer Blankenship for all the support you provide to the group and the department. The mood always lightens after a conversation with Christy.

To my friends in graduate school: Himanshu Chaudhary, thank you for being a constant companion, whether for lunch, the gym, or grocery runs. To Dhruv Desai, Kaustav Kashyap Das, Pranav Kulkarni, Harsha Reddy Narravula, Karteek Dhara, Hirsh Kamakari, Scott Habermehl, Mert Yuksel, Taylan Kargin, Prachi Thureja, and Niyati Desai thank you for your friendship and support. I'm also thankful to Naitik Bhise, Saumya Shivam, and Shounak Bhogale, Saurabh Madur for staying in touch beyond undergrad.

Finally, I want to thank my parents, family, and Shri for your unwavering belief in me. I would not be here without your love and support.

ABSTRACT

Quantum computing platforms based on superconducting qubits have achieved remarkable progress in recent years, with significant advancements in quantum error correction, coherence times, and gate fidelities. However, the path to large-scale, fault-tolerant quantum computing faces a critical scaling bottleneck: the physical limits of single-chip architectures. Integrating millions of qubits on a single superconducting chip presents formidable engineering challenges, including increased thermal load, crosstalk, and complex wiring within the dilution refrigerator.

A promising approach to overcome these limitations is to interconnect multiple smaller superconducting quantum processors via a quantum network, allowing for distributed quantum computation. In this context, telecom-wavelength optical photons (around 1550 nm or 200 THz) are particularly attractive for transmitting quantum information across long distances due to their low propagation loss in optical fiber and negligible thermal occupation at room temperature. However, superconducting qubits typically operate at microwave frequencies (around 5-10 GHz), leading to a fundamental mismatch in operating frequencies that prevents direct coupling between these two domains.

This five-orders-of-magnitude frequency mismatch poses a major challenge for coherent quantum transduction, requiring a highly efficient, low-noise interface to faithfully convert quantum states between microwave and optical photons. A leading approach for transduction involves piezo-optomechanical platforms, where an intermediary acoustic resonator facilitates the conversion between microwave photons and microwave acoustic phonons, which are then converted to optical photons. However, existing designs often suffer from poor conversion efficiency and added noise due to geometric constraints and substrate heating, limiting their scalability for real-world quantum networks. In the first part of this thesis, I will introduce an optimized two-dimensional optomechanical crystal platform with a side-coupled optical waveguide. This geometry significantly improves the noise-efficiency metric for optical photon-acoustic phonon conversion. I will then discuss the integration of piezo-acoustic circuits into these two-dimensional crystals to realize a full microwave-to-optical transducer. I will cover the underlying design principles, fabrication processes, and preliminary measurement results, highlighting the potential of this platform for enabling future quantum communication and distributed quantum computing.

Another critical challenge in quantum networking is the frequency mismatch that arises when attempting to interfere photons emitted by different quantum nodes. This mismatch is primarily caused by variations in fabrication processes. In the second part of this thesis, I will present a novel post-fabrication tuning technique for piezo-optomechanical transducers, based on atomic force microscope (AFM) nano-oxidation. By applying a voltage bias to the AFM tip, we can selectively oxidize the surface of the dielectric device, introducing a controlled, localized change in refractive index and mechanical properties. This allows for precise tuning of both optical and acoustic resonance frequencies. I will demonstrate the effectiveness of this technique through experimental results at both room and cryogenic temperatures, highlighting its potential for scaling quantum networks.

PUBLISHED CONTENT AND CONTRIBUTIONS

1. S. Sonar*, U. Hatipoglu*, S. Meesala, D. P. Lake, H. Ren, and O. Painter. *High-efficiency low-noise optomechanical crystal photon-phonon transducers*. Optica, 12(1): 99–104, 2025.

   DOI: https://doi.org/10.1364/OPTICA.538557
   S.S. contributed to: conception of the project, device modeling, nanofabrication, experimental measurements, theoretical modeling, and manuscript writing.

2. U. Hatipoglu*, S. Sonar*, D. P. Lake, S. Meesala, and O. Painter. *In situ tuning of optomechanical crystals with nano-oxidation*. Optica, 11(3): 371–375, 2024.

   DOI: https://doi.org/10.1364/OPTICA.516479
   S.S. contributed to: conception of the project, nanofabrication, experimental measurements, and manuscript writing.

TABLE OF CONTENTS

LIST OF ILLUSTRATIONS

Number *Page*

LIST OF TABLES

Chapter 1

INTRODUCTION

1.1 Background

Since the invention of the transistor, computers have completely transformed the world. They have reshaped nearly every part of modern life, from communication to scientific research. Today, microprocessors pack billions of transistors into tiny chips, powering everything from smartphones to advanced AI systems. Classical computing, built on simple binary logic, has become incredibly fast and efficient. But the real magic is not just in processing information, it is in how we move it around.

Thanks to a mix of electronics and fiber optics, data can travel across the globe almost instantly. The internet, one of history's most important inventions, connects people, devices, and entire industries, making real-time communication and cloud computing possible.

The key to all this progress? Powerful little devices like transistors and optical transceivers. For years, we kept making them smaller and faster, but now we are hitting a limit. At the tiniest scales, weird quantum effects start causing problems, making it harder to improve traditional computers. That is why scientists are now exploring entirely new ways to compute, like quantum computing, that might take us even further.

Quantum Computation: From Concept to Reality

The idea of using quantum mechanics for computation was first seriously proposed by Richard Feynman in the early 1980s [1]. He pointed out that classical computers struggle to efficiently simulate quantum systems because quantum mechanics inherently involves superposition and entanglement, which require exponentially growing computational resources when mapped onto classical architectures. He suggested that a computer built on quantum principles could naturally and efficiently simulate quantum systems, offering an advantage in many computational tasks.

This idea led to the formalization of quantum computation, where information is processed using qubits, quantum analogs of classical bits, that can exist in superpositions of states. In the 1990s, researchers discovered that quantum computers

could do more than just simulate quantum mechanics: they could outperform classical computers on certain problems. Algorithms like Shor's algorithm for integer factorization [2, 3] and Grover's algorithm for search [4] demonstrated that quantum computers could offer exponential or quadratic speedups for specific computational tasks. These breakthroughs sparked significant interest in building practical quantum computers, leading to experimental efforts in implementing qubits using superconducting circuits, trapped ions, and other quantum platforms.

Quantum computing has rapidly progressed, with major players achieving significant milestones. Google unveiled the Willow processor (105 qubits), demonstrating exponential error reduction and a quantum advantage in random circuit sampling [5]. IBM continues scaling up, with its Condor processor (1121 qubits) and a roadmap toward a fully error-corrected system by 2029 [6]. Amazon has unveiled its error correction Ocelot chip [7], while Xanadu and PsiQuantum reported major quantum computing breakthroughs [8, 9, 10]. China's USTC achieved quantum supremacy with Jiuzhang [11] and Zuchongzhi [12] quantum computers.

The Need for Quantum Interconnects

Classical computers and communication networks are highly interconnected, forming the backbone of modern distributed computing. Data centers around the world exchange vast amounts of information in real time, enabling efficient processing, storage, and retrieval of information across large distances. Similarly, if quantum computing is to become a practical technology, quantum information must be transferred reliably between quantum processors. Unlike classical bits, however, qubits cannot simply be copied due to the no-cloning theorem [13], meaning traditional methods of communication do not work. Instead, quantum information must be transferred coherently, preserving the delicate quantum states that encode computational data.

To achieve this, researchers have explored the concept of quantum networking [14], where multiple quantum processors are linked together through quantum channels. This opens up the possibility of distributed quantum computing, where multiple quantum processors collaborate to solve problems more efficiently than a single device.

Many practical quantum applications are expected to require quantum processors with millions of physical qubits. Superconducting qubits, a leading hardware platform, must operate at cryogenic temperatures near 10 millikelvin. This imposes

strict thermal and spatial constraints, making it impossible to house all the physical qubits within a single cryogenic system like modern dilution refrigerators. A promising workaround is to interconnect multiple smaller quantum processors, each operating in its own cryostat into a unified quantum network.

Microwave-to-optical Transducers

While superconducting qubits are among the most promising candidates for building scalable quantum processors, they inherently operate at microwave frequencies (typically 5-10 GHz), where they interact with microwave photons for quantum state manipulation and readout. However, transmitting quantum information over long distances is best achieved using optical photons (around 200 THz, or telecom wavelengths), which experience significantly lower loss in fiber-based networks.

This five-orders-of-magnitude difference in frequency presents a major challenge because there is no natural coupling between superconducting circuits and optical photons. To bridge this gap, the community has focused on developing engineered devices known as microwave-optical transducers, which can coherently convert quantum states between the microwave and optical domains.

An ideal microwave-optical transducer should satisfy the following key requirements:

- High Efficiency: To minimize information loss and increase entanglement generation rates.
- Low Added Noise: To preserve the fragile quantum coherence of the converted states.
- Bidirectional Operation: To support both upconversion (microwave to optical) and downconversion (optical to microwave), allowing for flexible network architectures.
- Scalability: To enable integration with large-scale quantum networks.

Several physical platforms have been explored for quantum transduction, including electro-optomechanical systems, nonlinear crystals, and atomic ensembles. Among these, piezo-optomechanical systems have emerged as a promising candidate which is the subject of this thesis. This dissertation focuses on a developing a piezo-optomechanical transducer based on side-coupled two-dimensional optomechanical crystals (2D-OMC).

In the following chapters, we will discuss the design, fabrication, and preliminary results that set the foundation for high-efficiency, low-noise microwave-to-optical conversion. The work presented here aims to bridge the gap between superconducting quantum processors and optical quantum networks, enabling the next generation of distributed quantum computing. It is a challenging problem, but one that could unlock the full potential of quantum technologies in the years to come.

In the second part of this thesis, we address a critical challenge in quantum networking: the frequency mismatch that arises when attempting to interfere photons emitted by different quantum nodes. This mismatch is often introduced during the fabrication of piezo-optomechanical devices, where slight variations can lead to significant spectral detuning. we will present a novel post-fabrication tuning technique for piezo-optomechanical transducers, based on Atomic Force Microscope (AFM) nano-oxidation. By applying a voltage bias to the AFM tip, we can selectively oxidize the surface of the dielectric device, allowing for precise tuning of both optical and acoustic resonance frequencies. The experimental results presented in this work demonstrate the effectiveness of this tuning strategy for achieving spectral alignment across quantum nodes at cryogenic temperatures, providing a scalable path toward practical quantum networks.

1.2 Thesis organization

This dissertation is divided into two parts.

Part I: High-Efficiency Low-Noise Platform for Piezo-Optomechanical Transducers

Part I focuses on the development of high-efficiency, low-noise piezo-optomechanical transducers based on two-dimensional optomechanical crystals (OMCs).

- **Chapter 2:** Fundamentals of optomechanics, piezo-mechanics, and microwave-to-optical transducers. Using coupled mode theory, we derive the optical, microwave, and acoustic equations of motion that will be used throughout the thesis.
- **Chapter 3:** Design principles of optomechanical crystals, with a focus on side-coupled 2D OMCs. This chapter covers their band structure, mode confinement properties, as well as fabrication techniques and optimization strategies.

- **Chapter 4:** Cryogenic measurements of side-coupled OMCs, demonstration of high-efficiency, low-noise phonon-photon transducers along with an analysis of the dominant sources of thermal noise.
- **Chapter 5:** Possible origins of the optical-absorption induced hot bath that adds thermal population to the acoustic resonator.
- **Chapter 6:** Design principles of a microwave-to-optical transducer based on 2D OMCs.
- **Chapter 7:** Fabrication techniques developed for these transducers, including process optimization and material considerations. Measurement setup, along with preliminary room-temperature and cryogenic measurements of the fabricated devices.

Part II: AFM Nano-Oxidation for Spectral Tuning

Part II explores the use of atomic force microscope (AFM) nano-oxidation for spectral tuning of dielectric devices.

- **Chapter 8:** Room-temperature tuning of optomechanical devices, including a three-OMC tuning experiment to align optical and acoustic resonance frequencies.
- **Chapter 9:** Work on selective room-temperature pre-alignment of the optical modes in OMCs to enable precise wavelength matching at millikelvin temperatures.
- **Chapter 10:** Future directions, including ongoing efforts toward creating a Bell state shared between superconducting qubits, mediated by optical photons.

Part I

High-Efficiency Low-Noise Platform for Piezo-Optomechanical Transducers

Chapter 2

FUNDAMENTALS OF OPTOMECHANICS AND PIEZO-MECHANICS

2.1 Optomechanical systems

At its heart, optomechanics explores the interplay between light and mechanical motion, driven by radiation pressure and phase modulation. When light bounces off a moving surface, the transfer of momentum can push the object, causing it to shift position. At the same time, the object's motion alters the light's phase and frequency. This two-way interaction is the foundation for advanced measurement methods and real-world technologies, from detecting gravitational waves to enabling quantum information transfer.

In the early 20th century, experiments demonstrated that light exerts a force on microscopic particles [15], an effect that later became the basis for laser cooling and optical tweezers, techniques that allow precise control of atoms and biological molecules. On the opposite end of the scale, optomechanics is key to experiments like LIGO, where lasers detect the faintest mirror movements caused by gravitational waves, measuring shifts smaller than a trillionth of an atom's width.

From a technological perspective, optomechanics enables practical applications such as acousto-optic modulators (AOMs), which use mechanical vibrations to alter the frequency and propagation of light. More recently, nanomechanical resonators coupled to optical cavities have become a leading platform for studying quantum effects in macroscopic systems [16]. These devices allow us to observe quantum phenomena in mechanical systems and explore novel methods of information processing.

A typical cavity optomechanical system, as shown schematically in Fig. 2.1a, consists of an optical cavity coupled to a mechanically compliant mirror or resonator with mass m. In such systems, the optical field inside the cavity exerts radiation pressure forces on the mechanical element, whereas the resonator's motion, in turn, shifts the optical cavity frequency. The Hamiltonian describing this system as a function of resonator's position x is given by:

$$\hat{H} = \hbar\omega_a(x)\hat{a}^\dagger\hat{a} + \hbar\omega_b\hat{b}^\dagger\hat{b}, \tag{2.1}$$

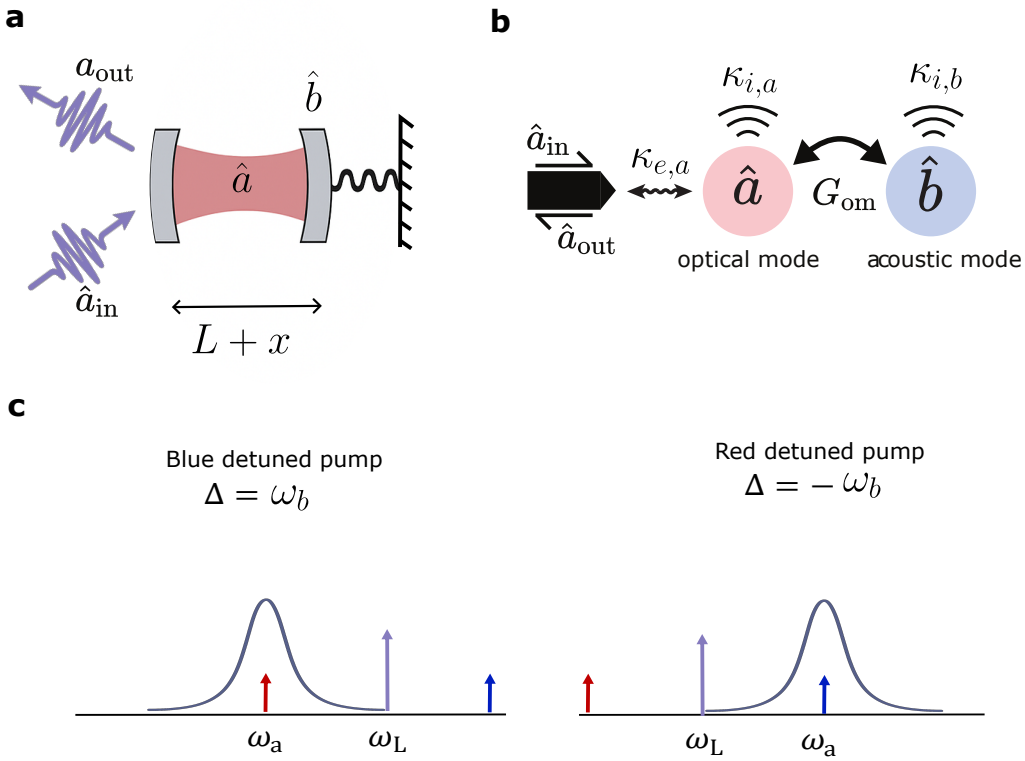

Figure 2.1: **Representation of cavity optomechanics. a,** An optical cavity mode $\hat{a}$ with equilibrium length L is coupled to a movable mirror supporting a mechanical mode $\hat{b}$. Displacements of the mirror by an amount x modulates the cavity length, enabling optomechanical coupling. **b,** Modal diagram of the system. The optical mode $\hat{a}$ is coupled to an external waveguide with external decay rate $\kappa_{e,a}$ and intrinsic loss rate $\kappa_{i,a}$. The acoustic mode $\hat{b}$ couples to the optical mode at a rate G_{om}, and has an intrinsic damping rate $\kappa_{i,b}$.**c,** Typical spectral picture of the optomechanical system with pump laser, ω_L, blue detuned (left) and red detuned (right) with respect to the optical cavity, ω_a. The acoustic scattered sidebands of the pump are represented by red and blue arrows.

where ω_a is the optical resonance frequency, ω_b is the mechanical resonance frequency, and $\hat{a}$, $\hat{b}$ ($\hat{a}^\dagger$, $\hat{b}^\dagger$) are the annihilation (creation) operators for the optical and mechanical modes, respectively.

The optical resonance frequency is sensitive to displacement of the mirror and can be expressed as:

$$\omega_a(x) = \frac{2\pi c}{(L+x)}, \tag{2.2}$$

where c is the speed of light, L is the equilibrium cavity length, and x is the small perturbative displacement of the mirror. For small displacements, $x \ll L$, the frequency can be expanded to first order as:

$$\omega_a(x) \approx \omega_a \left(1 - \frac{x}{L}\right), \tag{2.3}$$

with $\omega_a = 2\pi c/L$ being the optical frequency at equilibrium ($x = 0$).

The mirror's position operator can be expressed in terms of the mechanical mode operators as:

$$\hat{x} = x_{\text{zpf}}(\hat{b} + \hat{b}^\dagger), \tag{2.4}$$

where $x_{\text{zpf}} = \sqrt{\frac{\hbar}{2m\omega_b}}$ is the zero-point fluctuation amplitude of the mechanical motion. Incorporating this into the Hamiltonian, we obtain the total Hamiltonian including the first order interaction term $\hat{H}_{\text{int}}$:

$$\hat{H} = \hbar\omega_a \hat{a}^\dagger \hat{a} + \hbar\omega_b \hat{b}^\dagger \hat{b} \underbrace{-\hbar g_{\text{OM}} \hat{a}^\dagger \hat{a}(\hat{b}^\dagger + \hat{b})}_{\hat{H}_{\text{int}}} \tag{2.5}$$

where the single-photon optomechanical coupling rate is defined as:

$$g_{\text{OM}} = \frac{\omega_a x_{\text{zpf}}}{L}. \tag{2.6}$$

This coupling parameter quantifies the interaction strength between individual photons and phonons in the system. The Hamiltonian reveals that the interaction of the mechanical oscillator with the radiation field is fundamentally a nonlinear process, involving three operators (three wave mixing). To achieve large optomechanical coupling, systems typically require high optical confinement (small cavity lengths, L) and low mechanical mass (m) and high mechanical frequency (ω_b).

An alternative and intuitive way to understand the interaction between the mechanical resonator and the optical field is through the concept of radiation force. Since the mechanical oscillator can be effectively described as a spring-mass system, it is often more straightforward to analyze the coupling by considering the cavity field as exerting a force upon the mechanical oscillator. The radiation force operator, derived from the interaction Hamiltonian, is given by:

$$\hat{F}_{\text{rad}} = -\frac{d\hat{H}_{\text{int}}}{d\hat{x}} = \frac{\hbar g_{\text{OM}}}{x_{\text{zpf}}} \hat{a}^\dagger \hat{a}. \tag{2.7}$$

2.2 Linearied optomechanical equations of motion

The optomechanical systems that typically exist have the condition $\omega_b \ll \omega_a$. It is convenient to go into the rotating frame of the a laser drive ω_L by defining $\Delta = \omega_L - \omega_a$. Additionally, we further simplify the Hamiltonian by linearizing it. For this, we split the cavity field into average coherent amplitude $\bar{\alpha}$ and a fluctuating term, $\hat{a} \rightarrow \bar{\alpha} + \hat{a}$. The total Hamiltonian is then given by

$$\hat{H} \approx \hbar\Delta\hat{a}^\dagger\hat{a} + \hbar\omega_b\hat{b}^\dagger\hat{b} - \hbar g_{\mathrm{OM}}\bar{\alpha}(\hat{a}^\dagger + \hat{a})(\hat{b}^\dagger + \hat{b}), \tag{2.8}$$

where we have ignored terms involving $|\alpha|^2$ which represent a constant energy shift. We can further ignore terms involving $\hat{a}^\dagger\hat{a}$ in equation 2.8 since they are small compared to linear terms leading to the total Hamiltonian:

$$\hat{H} \approx \hbar\Delta\hat{a}^\dagger\hat{a} + \hbar\omega_b\hat{b}^\dagger\hat{b} \underbrace{-\hbar G_{\mathrm{OM}}(\hat{a}^\dagger\hat{b}^\dagger + \hat{a}\hat{b})}_{\hat{H}_{\mathrm{tms}}} \underbrace{-\hbar G_{\mathrm{OM}}(\hat{a}^\dagger\hat{b} + \hat{a}\hat{b}^\dagger)}_{\hat{H}_{\mathrm{bs}}}, \tag{2.9}$$

where $G_{\mathrm{OM}} = g_{\mathrm{OM}}\bar{\alpha} = g_{\mathrm{OM}}\sqrt{n_a}$ is the pump enhanced optomechanical coupling rate with n_a being the average number of photons in the optical cavity. $\hat{H}_{\mathrm{tms}}$ and $\hat{H}_{\mathrm{bs}}$ are called the two-mode-squeezing and beam-splitter Hamiltonian, respectively. For a laser drive at ω_L, these two processes correspond to scattering into Stokes and anti-Stokes sidebands.

To compute the optomechanical scattering rate, we now include dissipation and derive the equations of motion using the Hamiltonian in Equation 2.9. The linear optomechanical system has two detunings (Δ) of interest, $\Delta = -\omega_b$ and $\Delta = +\omega_b$. We assume the laser is red-detuned to the mechanical frequency, i.e., $\Delta = -\omega_b$. This is schematically shown in Figure 2.1d where the upper sideband (blue) of the laser is resonant with the optical cavity. Under this condition, the two-mode squeezing term $\hat{H}_{\mathrm{tms}}$ (red sideband) is rapidly rotating and can be neglected under the rotating wave approximation.

To account for energy loss and fluctuations due to coupling to external baths, we use the quantum Langevin formalism. This approach modifies the Heisenberg equations of motion by including damping terms along with corresponding quantum noise operators.

$$\dot{\hat{O}} = \frac{i}{\hbar}[\hat{H}, \hat{O}] - \frac{\Gamma}{2}\hat{O} + \sqrt{\Gamma}\,\hat{O}_{\mathrm{in}}(t), \tag{2.10}$$

where Γ is the energy decay rate of the mode, and $\hat{O}_{\text{in}}(t)$ is the corresponding quantum input operator of the drive or the noise introduced by the environment.

The optical mode decays at rate κ_a due to both intrinsic loss and coupling to external waveguides $\kappa_a = \kappa_{a,i} + \kappa_{a,e}$, while the mechanical (or acoustic) mode damps at rate $\kappa_{i,b}$ due to coupling to its thermal environment as shown in Figure 2.1b. Throughout this thesis, the terms mechanical and acoustic are used interchangeably to refer to the vibrational mode.

Assuming weak coupling regime $\kappa_a \gg G_{\text{OM}}$, the quantum Langevin equations in the frequency domain are:

$$-i\omega\hat{a}(\omega) = \left(i\Delta - \frac{\kappa_a}{2}\right)\hat{a}(\omega) - iG_{\text{OM}}\hat{b}(\omega) + \sqrt{\kappa_{a,e}}\hat{a}_{\text{in}}(\omega) \tag{2.11}$$

$$-i\omega\hat{b}(\omega) = \left(-i\omega_b - \frac{\kappa_{i,b}}{2}\right)\hat{b}(\omega) - iG_{\text{OM}}\hat{a}(\omega) + \sqrt{\kappa_{i,b}}\hat{b}_{\text{in}}(\omega). \tag{2.12}$$

Ignoring the input terms $\hat{a}_{\text{in}}$ and $\hat{b}_{\text{in}}$ and setting $\omega = \omega_b = -\Delta$ this gives:

$$\frac{\kappa_a}{2}\hat{a} + iG_{\text{OM}}\hat{b} = 0 \tag{2.13}$$

$$\frac{\kappa_{i,b}}{2}\hat{b} + iG_{\text{OM}}\hat{a} = 0. \tag{2.14}$$

According to input-output theory, the optical output field $\hat{a}_{\text{out}}$ is related to the input and intracavity fields by:

$$\hat{a}_{\text{out}} = \hat{a}_{\text{in}} - \sqrt{\kappa_{a,e}}\,\hat{a}.$$

In the case where there is no external input (i.e., $\hat{a}_{\text{in}} = 0$), this simplifies to:

$$\hat{a}_{\text{out}} = -\sqrt{\kappa_{a,e}}\,\hat{a} \tag{2.15}$$

$$= -\frac{-2iG_{\text{OM}}\sqrt{\kappa_{a,e}}}{\kappa_a}\hat{b} \tag{2.16}$$

$$= -i\sqrt{\eta_a}\sqrt{\gamma_{\text{OM}}}\hat{b}, \tag{2.17}$$

where, $\eta_a = \kappa_{a,e}/\kappa_a$ is the external optical coupling efficiency to the waveguide, and the optomechanical scattering rate is given by

$$\gamma_{\text{OM}} = \frac{4G_{\text{OM}}^2}{\kappa_a} = \frac{4g_{\text{OM}}^2 n_a}{\kappa_a}. \tag{2.18}$$

This rate corresponds to the scattering of phonons into optical photons via the beam-splitter interaction and is the basis for sideband cooling and quantum transduction. The total damping rate of the acoustic mode, includes both the intrinsic mechanical damping rate, $\kappa_{i,b}$, and the optomechanically induced damping (or scattering) rate, γ_{OM}.

The optomechanical conversion efficiency, η_{OM}, is defined as the fraction of phonons that are successfully converted to optical photons, which is given by the ratio:

$$\eta_{\mathrm{OM}} = \frac{\gamma_{\mathrm{OM}}}{\gamma_{\mathrm{OM}} + \kappa_{i,b}}. \tag{2.19}$$

2.3 Calibration of photon and phonon occupancy

The intracavity photon number n_c can be derived from the steady-state solution of the optical field under coherent drive. The Heisenberg-Langevin equation for the cavity field $\hat{a}$ is given by:

$$\dot{\hat{a}} = \left(i\Delta - \frac{\kappa_a}{2}\right)\hat{a} + \sqrt{\kappa_{e,a}}\,\alpha_{\mathrm{in}}. \tag{2.20}$$

Here, $\Delta = \omega_L - \omega_a$ is the laser detuning from cavity resonance, κ_a is the total cavity linewidth, and α_{in} is the coherent drive amplitude related to the input power by $|\alpha_{\mathrm{in}}|^2 = P_{\mathrm{in}}/\hbar\omega_L$.

In steady state, we set $\dot{\hat{a}} = 0$ and solve for the mean field amplitude:

$$\bar{\alpha} = \langle\hat{a}\rangle = \frac{\sqrt{\kappa_{e,a}}\,\alpha_{\mathrm{in}}}{\kappa_a/2 - i\Delta}. \tag{2.21}$$

The intracavity photon number is then:

$$n_a = |\bar{\alpha}|^2 = \frac{\kappa_{e,a} P_{\mathrm{in}}/\hbar\omega_L}{\Delta^2 + (\kappa_a/2)^2}. \tag{2.22}$$

This expression is used to determine n_a in experiments based on known input power, cavity parameters, and laser detuning.

Thermal Occupation and Sideband Asymmetry

The mean phonon number in a mechanical mode, or thermal occupancy n_{th}, is determined by the Bose-Einstein distribution:

$$n_{\text{th}} = \frac{1}{\exp\left(\frac{\hbar\omega_b}{k_B T}\right) - 1}, \tag{2.23}$$

where k_B is the Boltzmann constant, T is the temperature of the system. At relatively high temperatures ($k_B T \gg \hbar\omega_b$), this expression simplifies to

$$n_{\text{th}} \approx \frac{k_B T}{\hbar\omega_b}. \tag{2.24}$$

In quantum mechanics, the transition rate between an initial state $|i\rangle$ and a final state $|f\rangle$ induced by a weak perturbation is given by Fermi's golden rule:

$$\Gamma_{i\to f} = \frac{2\pi}{\hbar} \left|\langle f|\hat{H}_{\text{int}}|i\rangle\right|^2 \rho_f, \tag{2.25}$$

where $\hat{H}_{\text{int}}$ is the interaction Hamiltonian, and ρ_f is the density of final states. In the context of optomechanics, this interaction is given by the beam-splitter Hamiltonian for a red-detuned drive, which enables phonon annihilation and photon creation, or the two-mode squeezing Hamiltonian for a blue-detuned drive, which enables phonon creation and photon annihilation.

Applying Fermi's golden rule to the optomechanical interaction $\hat{H}_{\text{int}} \sim \hat{b} + \hat{b}^\dagger$, we obtain the phonon annihilation rate as follows:

$$\Gamma_{n\to n-1} \propto \left|\langle n-1|\hat{H}_{\text{int}}|n\rangle\right|^2 \propto n, \tag{2.26}$$

where the rate is proportional to the phonon occupation n because the probability of removing a phonon scales with the number of available phonons. This type of interaction is activated when $\Delta = -\omega_b$ in the sideband resolved regime and leads to effective "cooling" of the acoustic resonator known as *sideband cooling*.

On the other hand, the phonon creation rate is given by

$$\Gamma_{n\to n+1} \propto \left|\langle n|\hat{H}_{\text{int}}|n+1\rangle\right|^2 \propto n+1, \tag{2.27}$$

where the additional +1 accounts for spontaneous creation of phonons, a purely quantum effect with no classical counterpart. This type of interaction is activated when $\Delta = \omega_b$ in the sideband resolved regime and is used for initialization of the acoustic resonator into first excited state.

The ratio of these scattering rates provides a direct measurement of the phonon occupation:

$$\frac{\Gamma(\Delta = \omega_b)}{\Gamma(\Delta = -\omega_b)} = \frac{n_{\text{th}} + 1}{n_{\text{th}}} = 1 + \frac{1}{n_{\text{th}}}, \tag{2.28}$$

which can be rearranged to give the phonon occupation:

$$n_{\text{th}} = \frac{1}{\left(\frac{\Gamma(\Delta=\omega_b)}{\Gamma(\Delta=-\omega_b)}\right) - 1}. \tag{2.29}$$

This method enables thermometry down to the single-phonon level and is widely used in quantum optomechanics experiments to assess thermal and coherent phonon populations.

2.4 Piezoelectricity

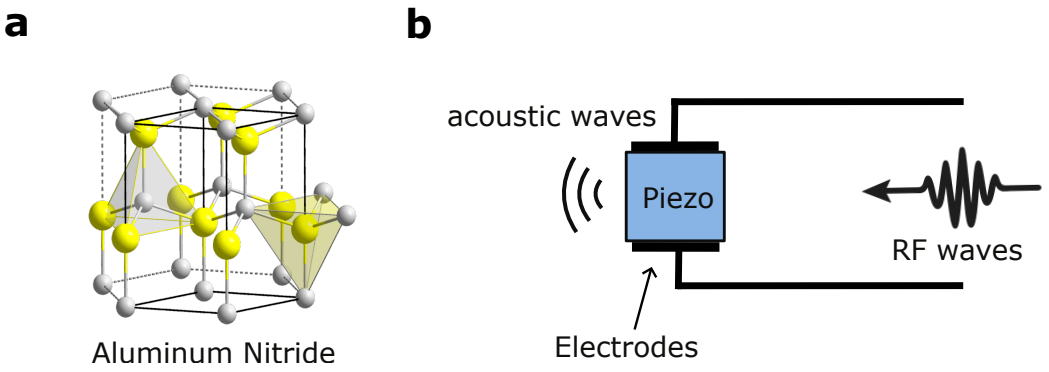

Figure 2.2: **Microwave-acoustic interaction a,** Wurtzite crystal structure of aluminum nitride (AlN), illustrating its non-centrosymmetric unit cell, which is essential for piezoelectricity (source: Wikipedia). **b,** Schematic of a piezoelectric element sandwiched between two electrodes, demonstrating its ability to convert RF waves into acoustic waves and vice versa.

Piezoelectricity is a fundamental property of certain crystalline materials that enables the direct coupling between mechanical and electrical domains. This coupling arises from the intrinsic asymmetry of the crystal structure, which lacks a center of inversion, creating a direct relationship between mechanical strain and electric polarization. Figure 2.2a shows the aluminum nitride Wurtzite crystal structure showing lack of inversion symmetry. This effect was first discovered by Jacques and Pierre Curie in 1880 [17], who observed that certain crystals, such as quartz and Rochelle salt, generate an electric charge when subjected to mechanical stress.

Today, materials like aluminum nitride (AlN), lithium niobate (LN), and Barium Titanate (BTO) are widely used for their strong piezoelectric responses, making them essential for a range of applications, including sensors and actuators.

At the microscopic level, piezoelectricity is described by a linear coupling between the mechanical deformation of a material and the resulting electric field. This relationship can be captured through the strain-charge form of the constitutive equations, which link the mechanical stress tensor T_{jk}, the strain tensor S_{ij}, the electric field E_k, and the electric displacement field D_i. These equations are given as:

$$S_{ij} = s^E_{ijkl} T_{kl} + d_{kij} E_k, \tag{2.30}$$

$$D_i = \epsilon^T_{ij} E_j + d_{ijk} T_{jk}, \tag{2.31}$$

where:

- s^E_{ijkl} is the elastic compliance tensor under a constant electric field,
- ϵ^T_{ij} is the permittivity tensor under constant stress,
- d_{ijk} is the piezoelectric tensor, which quantifies the strength of the coupling.

The piezoelectric tensor d_{ijk} captures the unique coupling between the electrical and mechanical domains. Its components depend on the crystal symmetry and orientation. For materials like AlN, which have a hexagonal wurtzite structure, this tensor is typically sparse, reflecting the specific symmetry constraints of the crystal lattice. The form of the piezoelectric tensor for AlN is:

$$d_{ijk} = \begin{pmatrix} 0 & 0 & 0 & 0 & d_{15} & 0 \\ 0 & 0 & 0 & d_{15} & 0 & 0 \\ d_{31} & d_{31} & d_{33} & 0 & 0 & 0 \end{pmatrix}, \tag{2.32}$$

where the non-zero components d_{15}, d_{31}, and d_{33} represent the primary piezoelectric coefficients for the material. For AlN, the bulk value are $d_{15} = -3.84$ [pC/N], $d_{31} = -1.92$ [pC/N], and $d_{33} = 4.96$ [pC/N]. The strength of these coefficients varies significantly between different materials, reflecting differences in atomic bonding, crystal orientation, and material composition. To achieve optimal coupling between

RF and acoustic modes, the piezo-electrode sandwich geometry (see Figure 2.2b) can be numerically optimized by carefully selecting the appropriate piezoelectric coefficients and electrode configuration.

2.5 Microwave-optical transduction

The optomechanical and piezo elements can be integrated together with a microwave resonator to transducer signals from microwave photons to optical photons. A modal diagram for such a system is shown in Figure 2.3a, where the acoustic mode is simultaneously coupled to both microwave and optical modes. The microwave mode $\hat{c}$ is a LC resonator that is externally coupled to a feedline at a rate $\kappa_{e,c}$ and has an intrinsic damping rate $\kappa_{i,c}$. The coupling Hamiltonian between microwave resonator and acoustic photons is given by

$$\hat{H}_{\text{int}} = g_{\text{pe}} \left(\hat{b}^\dagger \hat{c} + \hat{b} \hat{c}^\dagger \right) \tag{2.33}$$

where the piezoelectric coupling g_{pe} can be derived from the perturbation theory:

$$g_{\text{pe}} = \frac{\omega_b}{4\sqrt{2U_b U_{\text{c}}}} \int_{\text{piezo}} \mathbf{D}_b \cdot \mathbf{E}_{\text{c}} \, dV. \tag{2.34}$$

The integral in equation above is evaluated over the entire piezo slab. Here, $\mathbf{D}_b$ represents the electric displacement field induced by mechanical motion within the piezoelectric region, while $\mathbf{E}_{\text{c}}$ corresponds to the single-photon electric field generated by the loaded microwave resonator across the electrodes. These fields are normalized to their respective zero-point energies, $\hbar\omega_b/2$, which gives rise to the prefactor preceding the integral. The terms U_b and U_{c} denote the total acoustic energy stored in the piezo region and the total electrostatic energy of the microwave circuit. Figure 2.3b shows the lumped-element representation of the microwave-optical transducer circuit, where the acoustic mode is a hybrid between the piezo and a movable mirror.

Similar to the pure optomechanical circuit, the transducer can be operated in two distinct modes depending on whether the drive laser is red- or blue-detuned with respect to the optical cavity resonance frequency ω_a.

Direct frequency conversion

In this mode of operation, the drive laser is red-detuned by the mechanical frequency, i.e., $\Delta = -\omega_b$, which activates a beam-splitter type interaction between the optical

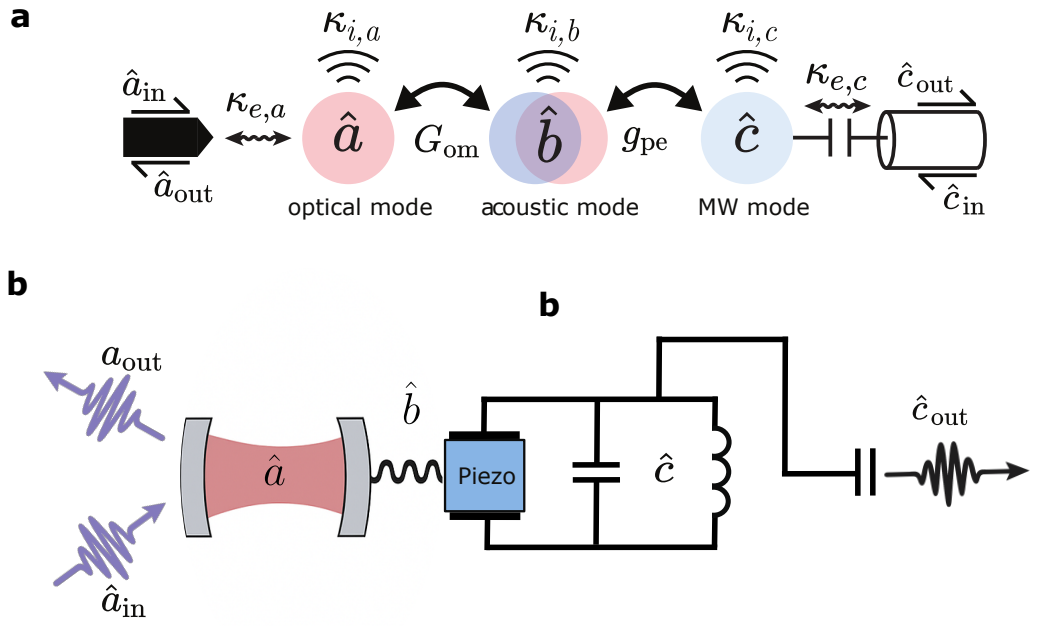

Figure 2.3: **Representation of an acoustic mediated microwave-optical transducer. a,** Modal diagram of the system. The optical mode $\hat{a}$ is coupled to an external waveguide with external decay rate $\kappa_{e,a}$ and intrinsic loss rate $\kappa_{i,a}$. The acoustic mode $\hat{b}$ couples to the optical and microwave mode modes at a rate G_{om} and g_{pe}, and has an intrinsic damping rate $\kappa_{i,b}$. The microwave mode $\hat{c}$ is coupled to a transmission line with external decay rate $\kappa_{e,c}$ and intrinsic loss rate $\kappa_{i,c}$. **b,** Lumped-element representation of the transducer. The optical mode is represented by the optical cavity, the acoustic mode by a mechanical resonator, and the microwave mode by a lumped-element circuit, illustrating the hybrid nature of the system. The transducer operates by mediating energy transfer between microwave and optical signals via the piezoelectric coupling of the acoustic mode.

and mechanical modes. Since the microwave mode also couples to the mechanical mode via a beam-splitter interaction, this configuration enables coherent and reversible transfer of excitations between the microwave and optical domains. As a result, the transducer facilitates direct frequency conversion between microwave and optical photons.

Entanglement generation

In this mode of operation, the drive laser is blue-detuned by the mechanical frequency, i.e., $\Delta = \omega_b$, which activates a two-mode squeezing type interaction between the optical and mechanical modes. This interaction enables the creation of correlated photon-phonon pairs. When the mechanical mode is coupled to a microwave resonator, the process leads to the generation of entangled microwave and optical

photons, which is useful for quantum communication and remote entanglement protocols such as the DLCZ scheme [18].

We now derive an expression for the microwave-optical conversion efficiency. For simplicity, we assume the weak coupling regime $g_{pe} \ll \kappa_c$ and $G_{OM} \ll \kappa_a$. Similar to the optomechanical case, we can write the quantum Langevin equations in the frequency domain as follows:

$$-i\omega\hat{a}(\omega) = \left(i\Delta - \frac{\kappa_a}{2}\right)\hat{a}(\omega) - iG_{\mathrm{OM}}\hat{b}(\omega) + \sqrt{\kappa_{a,e}}\hat{a}_{\mathrm{in}}(\omega) \tag{2.35}$$

$$-i\omega\hat{b}(\omega) = \left(-i\omega_b - \frac{\kappa_{i,b}}{2}\right)\hat{b}(\omega) - iG_{\mathrm{OM}}\hat{a}(\omega) - ig_{\mathrm{pe}}\hat{c} + \sqrt{\kappa_{i,b}}\hat{b}_{\mathrm{in}}(\omega) \tag{2.36}$$

$$-i\omega\hat{c}(\omega) = \left(-i\omega_c - \frac{\kappa_c}{2}\right)\hat{c}(\omega) - ig_{\mathrm{pe}}\hat{b} + \sqrt{\kappa_{i,c}}\hat{c}_{\mathrm{in}}(\omega). \tag{2.37}$$

We assume that the transducer is operated with microwave input $\hat{c}_{\mathrm{in}}$ and all frequencies are resonant, $\omega = \omega_b = \omega_c = -\Delta$, which gives us the following set of equations:

$$\left(\frac{\kappa_a}{2}\right)\hat{a} = -iG_{\mathrm{OM}}\hat{b} \tag{2.38}$$

$$\left(\frac{\kappa_{i,b}}{2}\right)\hat{b} = -iG_{\mathrm{OM}}\hat{a} - ig_{\mathrm{pe}}\hat{c} \tag{2.39}$$

$$\left(\frac{\kappa_c}{2}\right)\hat{c} = -ig_{\mathrm{pe}}\hat{b} + \sqrt{\kappa_{i,c}}\hat{c}_{\mathrm{in}}. \tag{2.40}$$

Rearranging above equations, we obtain

$$\hat{a}\left(\frac{4G_{\mathrm{OM}}^2}{\kappa_a} + \frac{4g_{\mathrm{pe}}^2}{\kappa_c} + \kappa_{i,b}\right) = -2\frac{2G_{\mathrm{OM}}}{\kappa_a}\frac{2g_{\mathrm{pe}}}{\sqrt{\kappa_c}}\sqrt{\frac{\kappa_{i,c}}{\kappa_c}}\hat{c}_{\mathrm{in}}. \tag{2.41}$$

The output optical field $\hat{a}_{\mathrm{out}}$ is given by the input-output theory as $\hat{a}_{\mathrm{out}} = -\sqrt{\kappa_{a,e}}\hat{a}$. The microwave-optical transduction efficiency is then given by

$$\eta_{c\to a} = \left|\frac{\hat{a}_{\mathrm{out}}}{\hat{c}_{\mathrm{in}}}\right|^2 = \kappa_{e,a}\left|\frac{\hat{a}}{\hat{c}_{\mathrm{in}}}\right|^2. \tag{2.42}$$

Inserting Equation 7.7 into Equation 2.42, we obtain

$$\eta_{c\to a} = \eta_a\eta_c\frac{4\gamma_{\mathrm{OM}}\gamma_{\mathrm{pe}}}{(\kappa_{i,b} + \gamma_{\mathrm{OM}} + \gamma_{\mathrm{pe}})^2}, \tag{2.43}$$

where similar to optomechanical scattering rate, we have defined microwave-acoustic scattering rate $\gamma_{\mathrm{pe}} = 4g_{\mathrm{PE}}^2/\kappa_c$ for $\kappa_c \gg g_{\mathrm{PE}}$. $\eta_a = \kappa_{e,a}/\kappa_a$ and $\eta_c = \kappa_{e,c}/\kappa_c$ are the external coupling efficiencies of optical and microwave modes. The transduction efficiency is maximized for the case $\gamma_{\mathrm{pe}} = \gamma_{\mathrm{OM}}$ which is the impedance matching condition.

Chapter 3

OPTOMECHANICAL CRYSTALS

Among various optomechanical designs, optomechanical crystals (OMCs) have emerged as a particularly attractive platform for quantum information processing, quantum transduction, and for probing the fundamental material limits of dissipation. OMCs are nanostructures engineered to simultaneously confine light and mechanical vibrations within dielectric cavities at sub-wavelength scales [19]. These structures can achieve significant single-photon optomechanical coupling strengths, typically on the order of $g_{\mathrm{OM}}/2\pi \approx 1\,\mathrm{MHz}$ [20], enabling interaction between gigahertz-frequency mechanical resonances and optical photons at telecom wavelengths.

3.1 Photonic crystals

Photonic crystals are materials with a spatially periodic dielectric function, such that

$$\varepsilon(\mathbf{r}) = \varepsilon(\mathbf{r} + \mathbf{R}), \tag{3.1}$$

where $\mathbf{R}$ denotes a lattice translation vector. This periodic modulation in refractive index leads to Bragg scattering, which can inhibit the propagation of electromagnetic waves within specific frequency ranges—forming what is known as a *photonic bandgap*.

Starting from Maxwell's equations, the wave equation for the magnetic field in such periodic media can be written as

$$\nabla \times \left[\frac{1}{\varepsilon(\mathbf{r})}\nabla \times \mathbf{H}(\mathbf{r})\right] = \left(\frac{\omega}{c}\right)^2 \mathbf{H}(\mathbf{r}), \tag{3.2}$$

where ω is the optical frequency and c is the speed of light. The solutions to this equation take the form of Bloch waves,

$$\mathbf{H}(\mathbf{r}) = \mathbf{H}_0 e^{i\mathbf{k}\cdot\mathbf{r}} u_{\mathbf{k}}(\mathbf{r}), \tag{3.3}$$

with $\mathbf{k}$ being the wavevector and $u_{\mathbf{k}}(\mathbf{r})$ a function that shares the periodicity of the lattice.

By solving this eigenvalue problem for all $\mathbf{k}$ in the Brillouin zone, one obtains the photonic band structure, which defines the allowed and forbidden frequency ranges

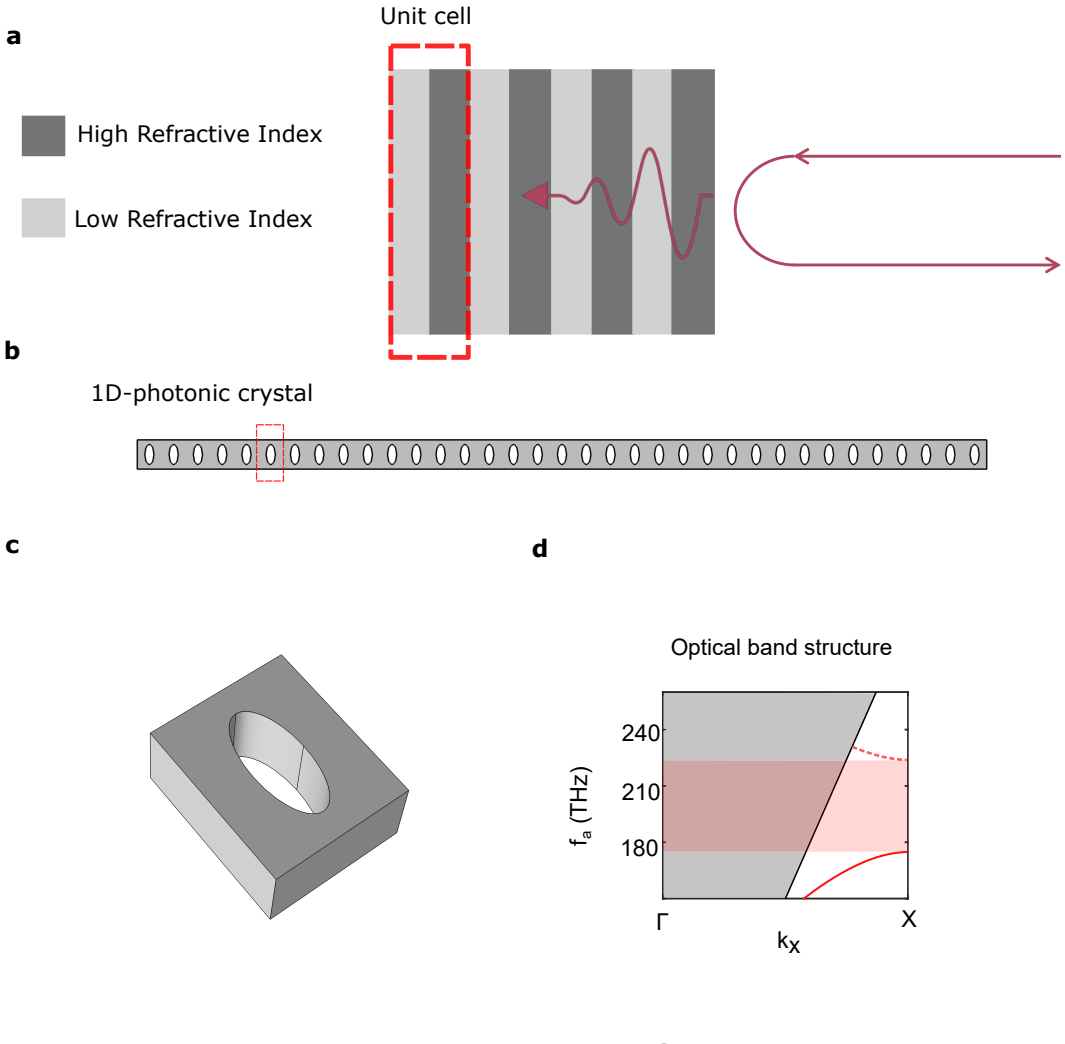

Figure 3.1: **Photonic crystals. a,** A photonic crystal consists of periodic regions of high and low refractive index, which create destructive interference that reflects incident electromagnetic waves. **b,** A one-dimensional photonic crystal structure composed of a periodic array of elliptical elements. **c,** Perspective view of a single unit cell from the 1D photonic crystal shown in panel b. **d,** The optical band structure, with the red shaded region indicating the frequency range where wave propagation through the crystal is forbidden (the photonic bandgap). The slanted line denotes the edge of the light cone, while the grey shaded region lies inside the light cone. The solid and dashed red curves represent the optical modes that define the edges of the bandgap.

for wave propagation. This concept is illustrated in Fig. 3.1a, where periodic modulation of the refractive index leads to Bragg reflection of incident electromagnetic waves, preventing their transmission through the structure and resulting in a photonic bandgap, a frequency range in which light propagation is forbidden due to

destructive interference.

Figure 3.1b shows a practical implementation of a 1D photonic crystal using a periodic array of elliptical air holes in a dielectric waveguide. In such structures, light is confined in the transverse directions by total internal reflection and guided along the longitudinal axis, while the photonic bandgap restricts propagation within the periodic region.

Fig. 3.1c presents a perspective view of the unit cell from panel b, showing the geometry of a single elliptical hole in a dielectric block. Fig. 3.1d shows the computed optical band structure. The shaded red region marks the photonic bandgap, while the solid and dashed red lines indicate the optical modes that define its boundaries. The grey area represents the light cone, and the slanted line denotes its edge. Optical modes lying above this cone are not well-confined and tend to leak into free space.

3.2 Phononic crystals

Periodic structuring of dielectric materials can also be employed to control the propagation of mechanical (acoustic) waves. Much like photonic crystals inhibit light propagation within certain frequency ranges via Bragg interference, phononic crystals exhibit *phononic bandgaps*—frequency bands where elastic waves cannot propagate through the medium. These bandgaps arise from periodic modulation of the material's elastic properties or mass density.

The distinct physical properties of optical and acoustic waves lead to very different frequency scales, even when the structures confining them are of similar physical dimensions. The frequency of a wave in a periodic medium is determined by the dispersion relation:

$$f = \frac{v}{\lambda}, \tag{3.4}$$

where f is the frequency, v is the phase velocity of the wave, and λ is its wavelength in the medium.

For optical waves at telecom wavelengths, the wavelength in vacuum is $\lambda_a \sim 1.5\,\mu$m, and the phase velocity in a dielectric material with refractive index n is $v_{\text{opt}} = c/n \sim 2 \times 10^8$ m/s (for $n \sim 1.5$). Using the vacuum wavelength to calculate the corresponding frequency:

$$f_{\text{a}} \approx \frac{c}{\lambda_a} = \frac{3 \times 10^8\,\text{m/s}}{1.5 \times 10^{-6}\,\text{m}} \approx 200\,\text{THz}. \tag{3.5}$$

In contrast, acoustic waves in the same material (say Silicon) typically travel at $v_b \sim 5 \times 10^3$ m/s. Using a similar wavelength scale ($\lambda_b \sim 1\ \mu$m), the corresponding acoustic frequency is:

$$f_b \approx \frac{5 \times 10^3\ \text{m/s}}{1 \times 10^{-6}\ \text{m}} = 5\,\text{GHz}. \tag{3.6}$$

This large difference in wave velocities allows for photonic and phononic bandgaps to coexist in structures with similar feature sizes, enabling simultaneous control over both light and sound in engineered materials.

3.3 Optomechanical crystal cavities

Optomechanical crystal (OMC) cavities are engineered nanostructures that simultaneously confine optical and mechanical modes by leveraging the bandgap properties of periodic photonic and phononic crystals. These structures act as mirrors for both light and sound, creating cavities with co-localized photon and phonon modes.

The confinement is achieved by introducing a local defect into a perfect periodic crystal, such as modifying the unit cell spacing or shape. This defect breaks the crystal's translational symmetry, creating a region where both optical and mechanical modes can resonate within the bandgaps. The surrounding crystal acts as a mirror, suppressing wave propagation at the target frequencies and trapping energy in the defect, similar to a Fabry-Pérot resonator.

Figure 3.2a illustrates this concept in a 1D photonic crystal cavity, where a few central periods have altered refractive index, allowing an optical mode to localize in the center. Similarly, Fig. 3.2b and shows the simulated optical and mechanical modes of a 1D OMC. These modes are typically co-localized in the same defect region and overlap significantly, which is essential for achieving strong optomechanical interaction.

To ensure that the optical and acoustic modes are both well-confined and experience minimal scattering losses, the defect must be designed with care. Tapered transitions between the defect and mirror regions help reduce radiation loss, especially for optical modes. Optical losses can also be quantified in terms of optical quality factor which is the ratio of optical frequency ω_a and the decay rate κ_a

$$Q_{\text{opt}} = \frac{\omega_a}{\kappa_a}. \tag{3.7}$$

In one-dimensional OMCs, optimized device designs have demonstrated optical quality factors as high as 1.2×10^6 [20].

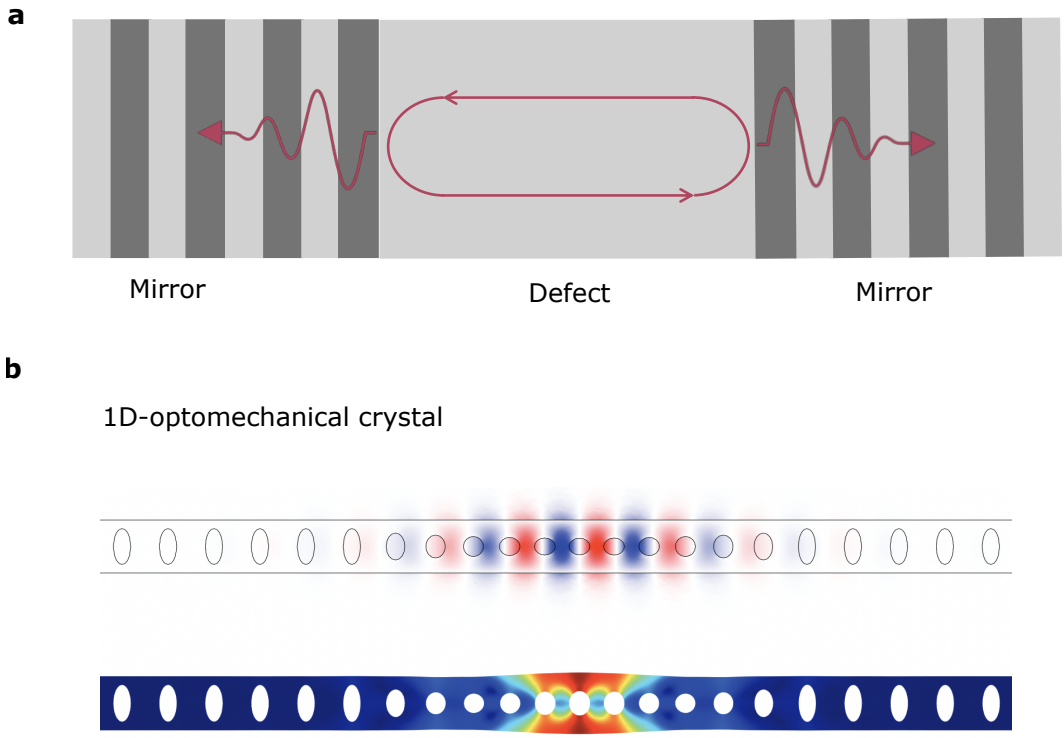

Figure 3.2: **Optomechanical crystals. a,** Illustration of the concept of optomechanical crystal cavity with localized optical and acoustic defect surrounded by the 'mirror' region that reflects optical and acoustic waves. **b,** FEM-simulated mode profile of the fundamental optical resonance (E_y component of the electric field), with red (blue) indicating positive (negative) field amplitude. The corresponding acoustic displacement profile is shown at the bottom, where the magnitude of the displacement is represented by color (large displacement in red, zero displacement in blue).

3.4 Optomechanical coupling

Following Equation 2.6, optomechanical coupling in optomechanical crystals can be derived using a perturbative approach:

$$g_{\mathrm{OM}} = \frac{d\omega_a}{d\alpha} x_{\mathrm{zpf}}, \tag{3.8}$$

where α is a generalized coordinate representing the amplitude of the mechanical mode, and x_{zpf} is the zero-point fluctuation associated with the mechanical oscillator (as defined in the previous chapter).

To compute the shift $d\omega_a/d\alpha$, we apply first-order electromagnetic perturbation theory. The total shift is typically decomposed into two parts: the moving boundary (MB) and the photoelastic (PE) contributions:

$$\frac{d\omega_a}{d\alpha} = \left(\frac{d\omega_a}{d\alpha}\right)_{\text{MB}} + \left(\frac{d\omega_a}{d\alpha}\right)_{\text{PE}}. \tag{3.9}$$

The MB term arises from the physical motion of dielectric boundaries caused by mechanical deformation, which perturbs the optical mode by changing the boundary conditions. The PE term originates from strain-induced changes in the refractive index within the material (via the photoelastic effect), leading to a shift in the optical mode frequency due to the modified dielectric environment.

Moving Boundary Contribution:

$$\left(\frac{d\omega_a}{d\alpha}\right)_{\text{MB}} = -\frac{\omega_a}{2}\frac{\int \left(\Delta\varepsilon|\mathbf{E}_{\parallel}|^2 - \Delta\varepsilon^{-1}|\mathbf{D}_{\perp}|^2\right)\mathbf{q}\cdot\hat{n}\,dA}{\int_V \varepsilon|\mathbf{E}|^2 dV}. \tag{3.10}$$

Here, $\mathbf{q}(\mathbf{r})$ is the normalized mechanical mode shape, $\hat{n}$ is the outward-pointing unit normal vector, and $\Delta\varepsilon = \varepsilon_{\text{diel}} - \varepsilon_{\text{vac}}$ is the dielectric contrast across the boundary The integration is performed over all surfaces of the geometry.

Photoelastic Contribution:

$$\left(\frac{d\omega_a}{d\alpha}\right)_{\text{PE}} = -\frac{\omega_a}{2}\frac{\int_V \varepsilon^2 E_i^* E_j p_{ijkl} S_{kl}\,dV}{\int_V \varepsilon|\mathbf{E}|^2 dV}, \tag{3.11}$$

where p_{ijkl} is the rank-4 photoelastic tensor and $S_{kl} = \frac{1}{2}\left(\partial_k q_l + \partial_l q_k\right)$ is the linearized strain tensor derived from the displacement field $\mathbf{q}(\mathbf{r})$. The integration is performed over the dielectric volume of the geometry.

With the knowledge of material properties such as permittivity ε, density ρ, and the photoelastic tensor p_{ijkl}, we can numerically evaluate g_{OM} for arbitrary device geometries and material systems using simulated optical and mechanical eigenmodes [21, 22]. In one-dimensional OMCs, optimized device designs have demonstrated vacuum optomechanical coupling rates as high as $g_{\text{OM}}/2\pi \sim 1.1$ MHz [20].

3.5 Two-dimensional optomechanical crystals

Having introduced principles of optomechanical crystals and optomechanical couplings, we will go through the process of designing two dimensional optomechanical

crystal (2D-OMC) cavity and the optical coupling waveguide. 2D OMCs provide significant advantages over their one-dimensional counterparts, including improved lateral optical confinement, higher achievable optical quality factors [23], and enhanced thermal conductance to the substrate for better heat dissipation which we will explore in detail in the following chapter.

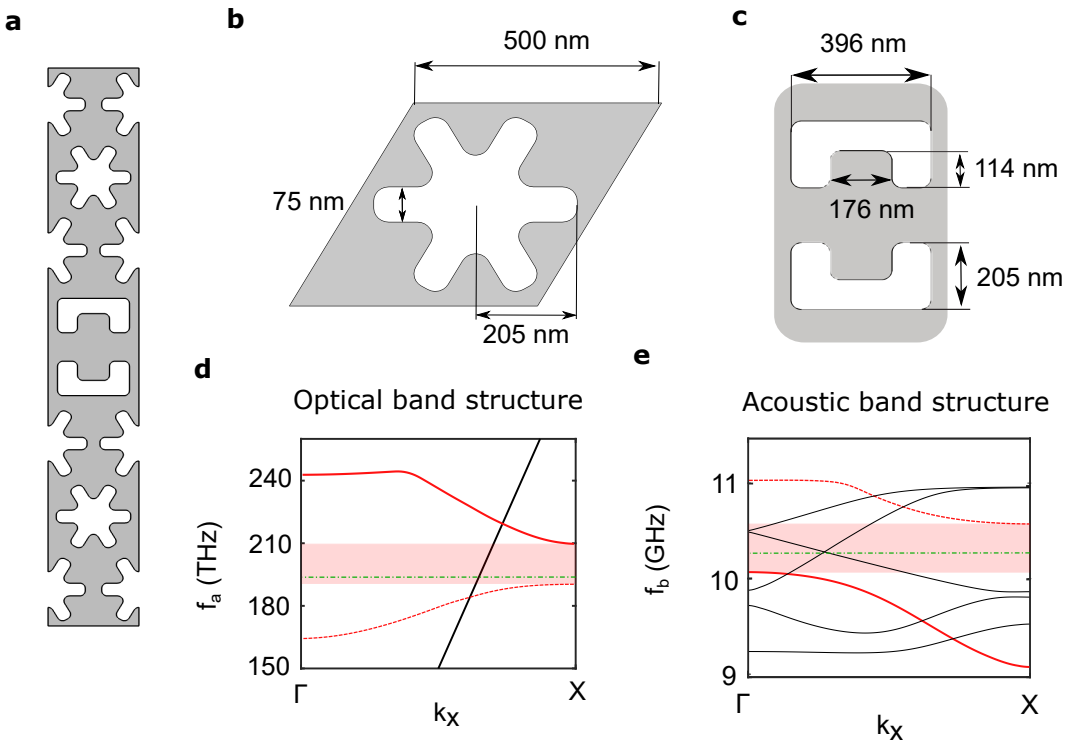

Figure 3.3: **2D OMC unitcell and band structure.** **a,** Unit cell of a 2D optomechanical crystal (OMC) design in a 220 nm thick silicon device layer. **b, c,** Dimensions of the snowflake and fishbone unit cells, respectively. **d, e,** Optical and acoustic band structures of the unit cell in (a). Only even-symmetry ($\sigma_z = +1$) optical modes are shown. The solid red curves highlight the target bands of interest, while dashed red curves represent other guided modes that define the photonic and phononic bandgaps. Green dash-dotted lines indicate the localized optical and acoustic cavity modes. The black curves in (e) correspond to modes of different symmetry.

To design a 2D OMC, we begin with a snowflake crystal based on a hexagonal lattice, which supports simultaneous photonic and phononic bandgaps in the near-infrared and gigahertz frequency ranges, respectively [24]. A line-defect is created by replacing one row of snowflakes with a specially engineered "fishbone" unit cell, forming a waveguide capable of confining both optical and acoustic modes. The schematic of the resulting waveguide geometry is shown in Fig. 3.3a, with detailed

dimensions of the snowflake and fishbone unit cells illustrated in Figs. 3.3b and 3.3c, respectively.

Due to fabrication constraints from state-of-the-art lithography and etching processes, these geometries exhibit finite radii of curvature, which are accounted for in numerical simulations. Measurements indicate typical radii in the range of 30–40 nm for both snowflake and fishbone features.

The optical band structure is shown in Fig. 3.3d, highlighting a photonic bandgap that spans from 190 to 210 THz. The plot includes only optical bands with even vertical mirror symmetry, i.e., $\sigma_z = +1$. In an ideal crystal, modes with different symmetries do not couple. However, fabrication-induced disorder can break these symmetry constraints, leading to mode mixing and degradation of the optical quality factor. The slanted black line represents the light cone. The solid red line corresponds to the optical mode of interest, which defines the upper edge of the optical bandgap. The green dash-dotted line in the band structure indicates the target frequency for an optical cavity mode.

Note that the mode defining the lower edge of the bandgap is mainly localized in the dielectric and is referred to as the *dielectric-mode*, while the mode defining the upper edge is primarily localized in the air slots and is termed the *air-mode* [25]. For 1D-OMCs, the mode of interest is typically the dielectric-mode, where the dominant contribution to the optomechanical coupling arises from the photoelastic effect. In contrast, if the mode of interest is the air-mode, the moving boundary contribution can dominate the optomechanical coupling. This offers greater design flexibility for optimizing the coupling. However, a key drawback of air-modes is their sensitivity to surface roughness, which can limit the achievable optical quality factors. The highest quality 2D-OMC cavities, which aim to maximize optical Q-factors, typically rely on the dielectric-mode as the mode of interest [23].

Figure 3.3e shows the acoustic band structure. The solid red curve highlights the acoustic mode of interest, while the dotted red curve indicates other guided acoustic modes that define the bandgap. Black curves represent modes of different symmetry. The green dash-dotted line marks the frequency of a target acoustic resonance.

It is important to design the acoustic mode of interest with strong dispersion (i.e., a large group velocity), as this reduces its sensitivity to fabrication-induced disorder. In contrast, the first 2D-OMC geometry [26], based on snowflake structures, employed a defect waveguide that exhibited flat dispersion for the relevant acoustic

mode and shows acoustic mode-splitting in the spectroscopy. Such signatures of multi-mode splitting are also observed in more recent work at high optical powers [27]. This limitation was carefully addressed in the previous work from our group [28].

The final step in the 2D OMC cavity design involves introducing a taper to the waveguide in Figure 3.3a along the x-axis, the propagation direction of both optical and acoustic modes. This is achieved by gradually modifying the geometric parameters of the fishbone unitcell, (h_i, w_i, h_o, w_o), such that the modulation increases approximately quadratically with distance from the center of the cavity (Fig. 3.4a,b). This spatial variation induces a corresponding quadratic shift in the frequencies of the waveguide modes along the propagation axis. For optical and acosutic waveguide modes of interest at the edge of the bandgap, this frequency modulation leads to mode localization, thereby forming a confined cavity mode within the respective bandgaps.

Figure 3.4c (top) shows the y-component of the Electric field for the localized optical cavity. The optical energy of the cavity is mainly localized in the air slots with >80% contribution while the rest is in silicon. We obtain simulated optical quality factor $Q_a > 10 \times 10^6$. Figure 3.4d shows the total displacement profile of the localized acoustic resonator with the excitation decaying quickly outside the defect region.

3.6 Design optimization of 2D OMC cavity

In 1D-OMCs, the dominant contribution to the optomechanical coupling rate comes from the photoelastic effect, whereas the contribution from the moving boundary is either negative or very small. Figure 3.5(a) illustrates the various boundaries within a 1D-OMC that contribute to the optomechanical coupling. The inner boundaries of the ellipses exhibit a phase opposite to that of the outer boundaries. The simulated 1D-OMC geometry has a total $g_{\mathrm{OM}}/2\pi$ = 967 kHz, out of which 920 kHz is the contribution due to photoelastic coupling, $g_{\mathrm{OM,PE}}/2\pi$. The moving boundary contribution from the inner boundaries (adjacent to ellipses) and the outer boundaries (outer edges), $g_{\mathrm{OM,MB\text{-}in}}/2\pi$ and $g_{\mathrm{OM,MB\text{-}out}}/2\pi$ are -341 kHz and 388 kHz, respectively, leading to net 47 kHz moving boundary contribution.

For 2D-OMC, all the moving boundaries are designed to be in-phase, resulting in a net positive contribution to the optomechanical coupling, as depicted in Figure 3.5(b). Furthermore, the moving boundary contribution can be significantly enhanced by reducing the gap size $h_o - h_i$. Figure 3.5(c) shows $g_{\mathrm{OM,PE}}/2\pi$, $g_{\mathrm{OM,MB}}/2\pi$

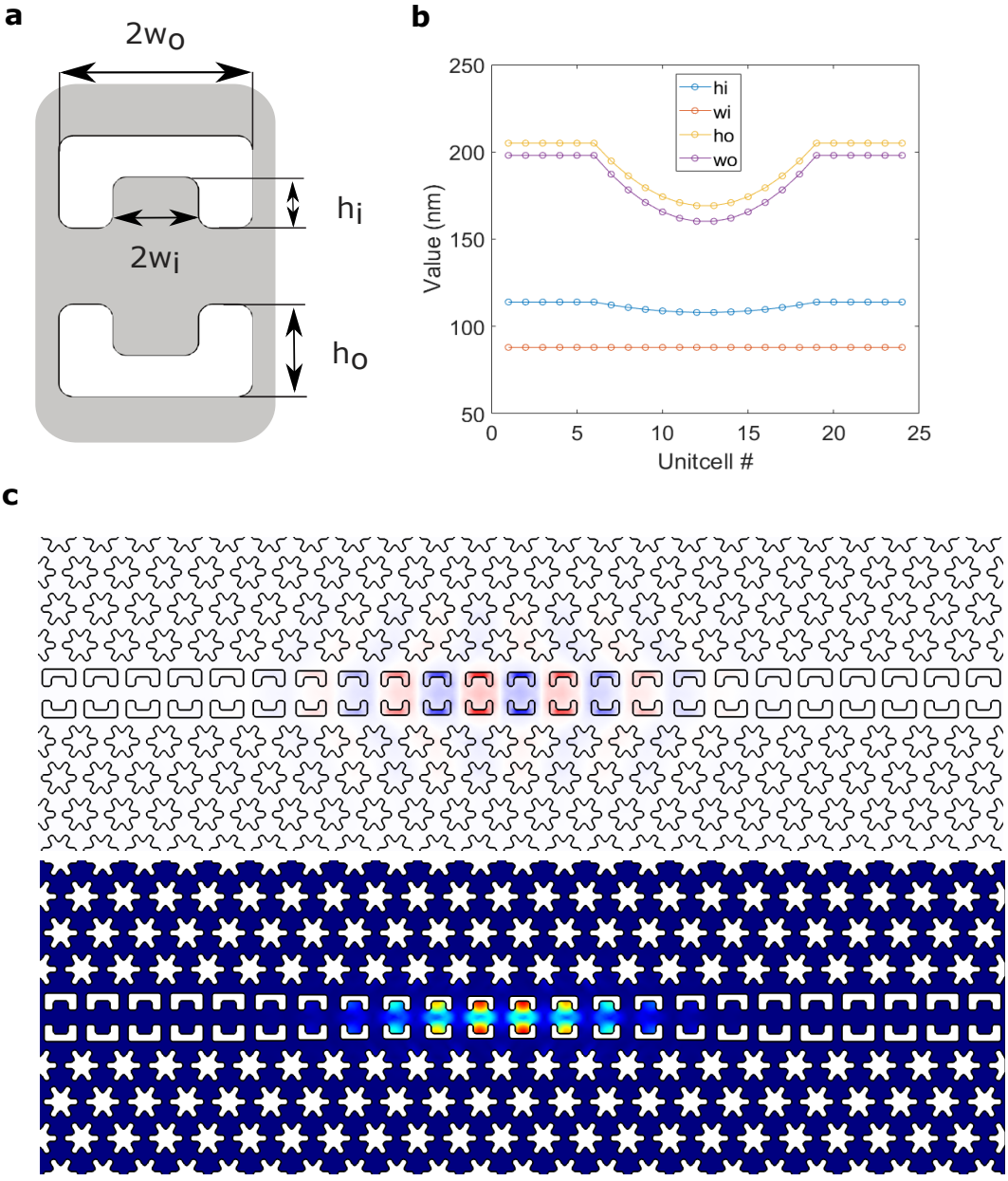

Figure 3.4: **2D OMC geometry. a, b,** Variation of fishbone unitcell parameters (h_i, w_i, h_o, w_o) from left to right to create a localized optical and acoustic cavity. **c,** (top) FEM-simulated mode profile of the fundamental optical resonance (E_y component of the electric field) at $\omega_a/2\pi = 194$ THz, with red (blue) indicating positive (negative) field amplitude. The corresponding acoustic displacement profile for the fundamental acoustic resonance at $\omega_b/2\pi = 10.3$ GHz is shown at the bottom, where the magnitude of the displacement is represented by color (large displacement in red, zero displacement in blue).

and total optomechanical coupling $g_{\mathrm{OM}}/2\pi$ as a function of $h_o - h_i$. For comparison, the $g_{\mathrm{OM}}/2\pi$ for 1D-OMC is in the range 900 kHz - 1.1 MHz. For each value of

$h_o - h_i$, we run Nelder-Mead Simplex algorithm [28] to optimize the coupling rate. For gap size of 20 nm, $g_{\mathrm{OM}}/2\pi$ of 2.45 MHz have been obtained numerically. Experimentally, gap sizes as small as 30 nm have been realized in thin film SOI [29] using standard nano-fabrication techniques. Additionally, self assembly techniques have been used to realize gap sizes as small as 2 nm in a bow-tie cavity architecture [30]. However, we note that with smaller gaps, the optical Q factors become sensitive to surface roughness as more electric field intensity is concentrated in smaller gaps [31], which ultimately limits the optomechanical scattering rate γ_{OM}. In our design, we limit the minimum gap size to > 70 nm which leads to theoretical $g_{\mathrm{OM}}/2\pi \approx 1.2$ MHz.

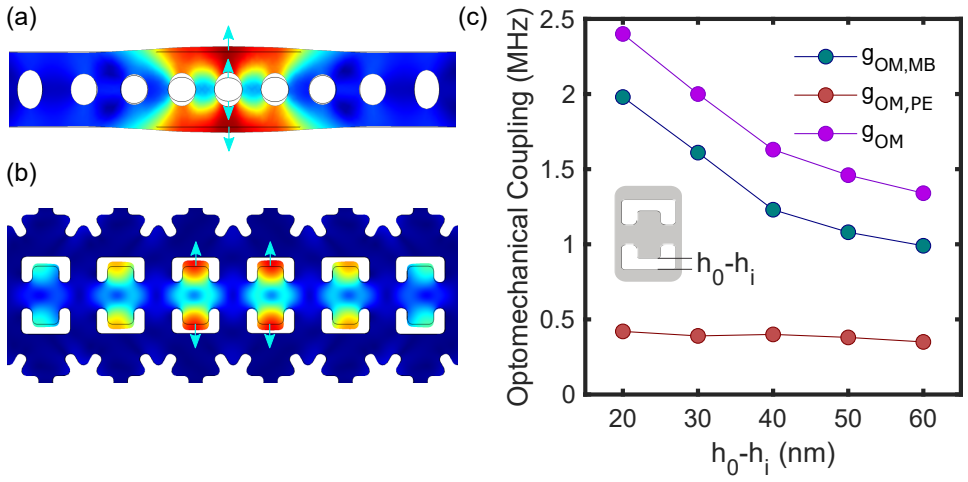

Figure 3.5: **Numerical optimization of optomechanical crystals a**, 1D OMC breathing mode. The inner moving boundaries of the ellipses have opposite phase compared to the outer boundaries at the edge of the nanobeam. Moving boundary contribution to optomechanical coupling for inner boundaries, $g_{\mathrm{OM,MB\text{-}in}}/2\pi = 341$ kHz whereas that for outer boundaries, $g_{\mathrm{OM,MB\text{-}out}}/2\pi = -388$ kHz. **b**, 2D OMC breathing mode is designed to have only outer boundaries that constructively add in phase to the photoelastic optomechanical coupling. **c,** shows the various contributions to the optomechanical coupling rate as a function of the smallest gap size $h_o - h_i$ for 2D-OMC. The red datapoints show contribution from photoelastic part $g_{\mathrm{OM,PE}}/2\pi$, the green datapoints show contribution from moving boundary $g_{\mathrm{OM,MB}}/2\pi$ and the magenta shows the total coupling rate $g_{\mathrm{OM}}/2\pi$. In comparison, the optimized value of $g_{\mathrm{OM}}/2\pi$ for 1D-OMC is in the range 900 kHz-1.1 MHz.

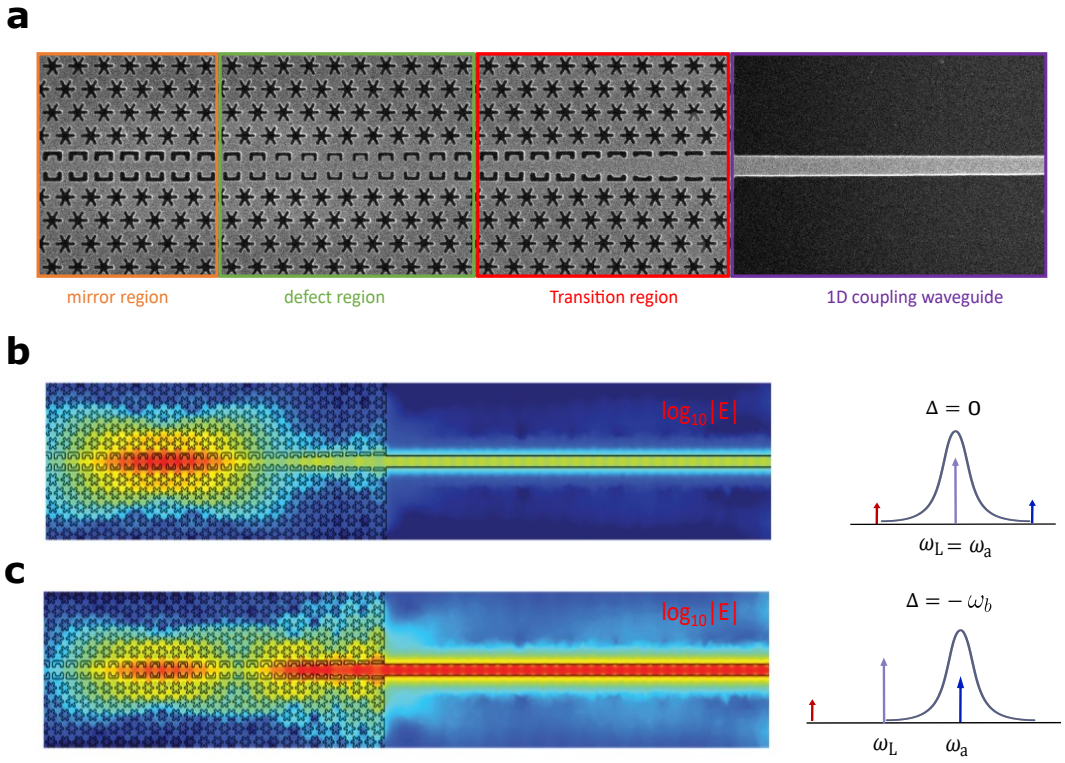

Figure 3.6: **Butt-coupling waveguide geometry. a,** 2DOMC geometry showing mirror region, defect region and the transition region. In the transition region, the fishbone unitcell is adiabatically tapered into the 1D-coupling waveguide for reduced scattering. **b,** Electric field profile in log scale when the pump laser is resonance with the optical cavity ($\Delta = 0$), where the magnitude of the field is shown with color (large field in red, zero field in blue). Majority of the input signal is coupled to the optical cavity and thus the optical intensity in the waveguide is negligible compared to the center of the cavity. **c,** Electric field profile in log scale when the pump laser is red-detuned from the optical cavity ($\Delta = -\omega_b$), where the magnitude of the field is shown with color (large field in red, zero field in blue). Majority of the input signal is reflected back due to off-resonance condition and thus the optical intensity in the waveguide is dominant compared to the center of the cavity. (b) and (c) are adopted from [28]

3.7 Optical coupling to 2D OMC cavity

Optomechanical crystal systems on a silicon substrate are not ideal. Interfacing optical photons and acoustic phonons whose frequencies differ by five orders of magnitude is complicated by parasitic effects such as optical absorption in the substrate. This absorption leads to unwanted heating and noise in the form of thermal population of the acoustic resonator. It is believed that the absorption primarily occurs at the surface, where defect states can exist. This issue is especially pronounced at cryogenic temperatures, where the thermal conductivity of silicon

drops significantly.

We will examine the mechanisms of optical absorption in more detail in the next chapter, however it is important to note here that careful design of the optical coupling waveguide is essential for minimizing these parasitic effects during device operation.

Butt-coupling waveguide design

In the preliminary design developed by our group [28], a butt-coupling geometry was employed to optically couple light into the optomechanical cavity, as illustrated in Fig. 3.6a. This structure comprises a mirror region on the left, a defect region in the center that hosts the localized optomechanical cavity, and a transition region on the right where the fishbone unit cell is gradually tapered into a one-dimensional (1D) coupling waveguide. The number of unit cells in this transition region sets the external optical coupling rate $\kappa_{e,a}$.

This type of coupling waveguide is physically connected to the optomechanical cavity and can contribute to heating due to parasitic optical absorption in the waveguide. This effect is illustrated in Fig. 3.6b and c. Assuming typical system parameters $(P_{\text{in}}, \omega_L, \kappa_{e,a}, \kappa_a, \omega_b) = (1\,\mu\text{W}, 1550\,\text{nm}, 644\,\text{MHz}, 1.28\,\text{GHz}, 10.3\,\text{GHz})$, the average intracavity photon number for different detunings can be calculated as:

$$n_a = \frac{\kappa_{e,a} P_{\text{in}}/\hbar\omega_L}{\Delta^2 + (\kappa_a/2)^2} \tag{3.12}$$

$$\approx 2000 \quad \text{for} \quad \Delta = 0 \tag{3.13}$$

$$\approx 7 \quad \text{for} \quad \Delta = -\omega_b. \tag{3.14}$$

As evident from these values, the optical energy stored in the cavity is significantly larger when the laser is on resonance ($\Delta = 0$) compared to the red-detuned case ($\Delta = -\omega_b$). In the latter scenario, much of the optical energy resides in the coupling waveguide, which can act as a source of parasitic heating.

In practical implementations, the coupling waveguide may be a long and complex structure [32, 33], which increases the likelihood of parasitic resonances due to back reflections or impedance mismatch. For such reasons, it becomes essential to physically detach the coupling waveguide from the optomechanical cavity to suppress heat transport from waveguide to the acoustic resonator, as thermal phonons can only propagate through continuous material pathways.

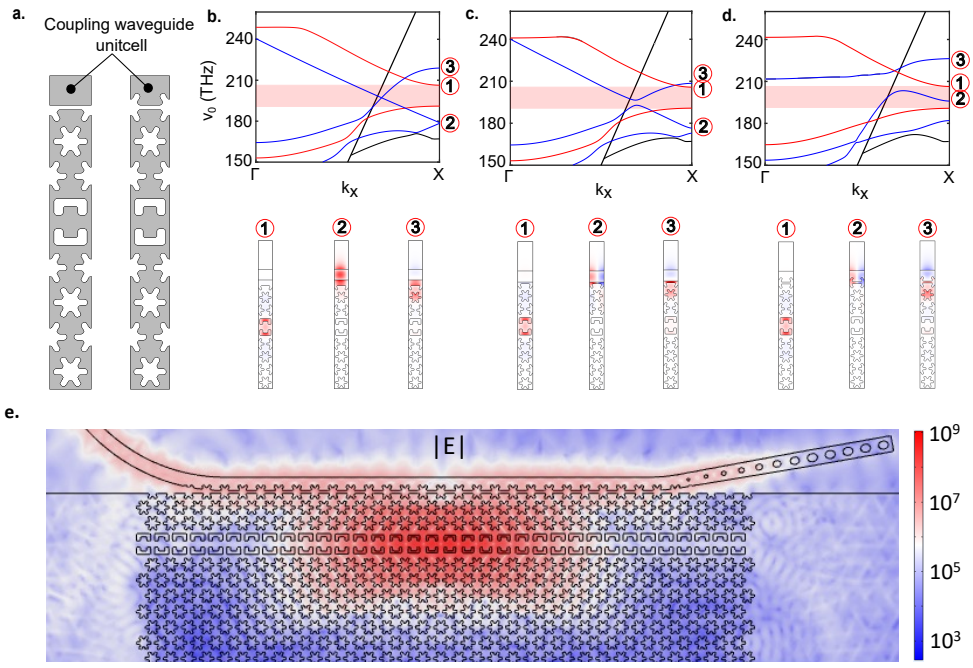

Figure 3.7: **Side-coupling optical waveguide design.** **a**, Schematic shows the supercell design for the 2D-OMC with the coupling waveguide. The left figure shows a conventional waveguide without the snowflake pattern, and the right figure shows the edge-mode coupling waveguide with half snowflakes patterned. **b, c**, show banstructures for conventional waveguide with 200 nm gap, conventional waveguide with 60 nm gap , and **d** edge-mode waveguide with 60nm gap from the 2D structure. The bottom sub figures show the mode structures at X point for the bands labeled with corresponding numbers in the top sub figures. **e**, Electric field distribution (logarithmic scale) for the combined waveguide-cavity system, incorporating the edge-mode waveguide design shown in (d).

Side-coupling waveguide design

The side-coupling waveguide needs to be designed such that there is no physical contact between the coupling waveguide and cavity while simultaneously achieving large optical coupling $\kappa_{e,a}$. Various 'mode-converter' designs have been explored in the literature [34] which convert a waveguide mode into a slot mode. However, since these slot modes have finite overlap with the bulk, they may not provide full isolation of the acoustic resonator from waveguide induced heating. Here we develop a mechanically detached side-coupled geometry where the waveguide mode of interest is localized primarily in the waveguide slab. We start by cutting the 2D-OMC cavity at the third or fourth snowflake row from the center and placing a waveguide slab nearby. Figure 3.7(a, left) shows the supercell of 2D-OMC with a slab coupling waveguide. The combined bandstructure when the waveguide-cavity

gap is 200 nm is shown in Figure 3.7(b). The shaded region shows the relevant optical bandgap of the cavity. The guided modes of the cavity are shown in red whereas the waveguide modes are shown in blue. We identify three relevant modes for the study. Mode 1, 2 and 3 with the corresponding X-point electric field profile are shown underneath the bandstructure. Mode 1 represents the cavity mode of interest, mode 2 represents the waveguide mode of interest, and mode 3 represents the parasitic edge mode localized at the edge of the cut. In this configuration, mode 3 acts as a parasitic mode that reduces the internal quality factor as it crosses the bandgap. Due to large waveguide-cavity separation, waveguide-coupling $\kappa_{e,a}$ for mode 2 is very small.

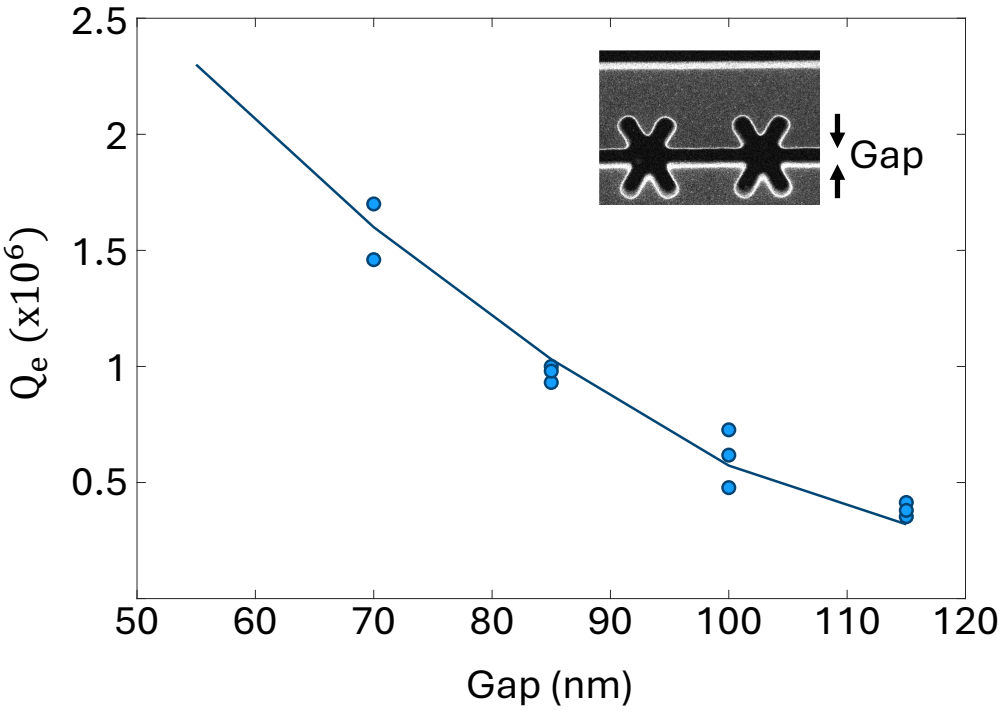

Figure 3.8: **Optical external quality factor Q_e vs gap.** The blue dots for a given gap represent Q_e measured for identically fabricated devices. The solid line represents numerical result obtained using COMSOL Multiphysics.

Figure 3.7(c) shows the bandstructure of the OMC cavity and the conventional waveguide for a waveguide-cavity gap of 60 nm. In this configuration, mode 2 weakly hybridizes with mode 3 due to close proximity, but mode 3 still acts as a parasitic mode since it crosses the cavity frequency. While this configuration provides a large external coupling rate $\kappa_{e,a}$, the internal quality factor of the cavity

is greatly reduced due to the presence of mode 3.

To mitigate this parasitic coupling, the waveguide is patterned with a half-snowflake structure, as shown in Fig. 3.7(a, right). In the corresponding bandstructure, Fig. 3.7(d), mode 3 is successfully moved out of the bandgap, while mode 2 remains confined within the bandgap. This configuration preserves large $\kappa_{e,a}$ while removing parasitic modes. The electric field distribution in log scale for the full waveguide-cavity structure, incorporating the half-snowflake waveguide design, is shown in Fig. 3.7(e). The plot highlights the efficient coupling between the waveguide mode (labeled '2' in Fig. 3.7d) and the 2D-OMC cavity mode (labeled '1' in Fig. 3.7d). For simplicity in the FEM analysis, the waveguide is not anchored to the bulk silicon.

The external quality factor, $Q_{e,a} = \omega_a/\kappa_{e,a}$, can be adjusted by changing the gap between the coupling waveguide and the OMC cavity, as shown in Fig. 3.8. The gap is varied from 70 nm to 115 nm for multiple devices, and the resulting optical $Q_{e,a}$ is measured. The solid line represents the numerically calculated $Q_{e,a}$ from COMSOL simulations. Interestingly, $Q_{e,a}$ decreases as the gap increases, which likely arises from better overlap between the cavity and waveguide modes. However, increasing the gap beyond 115 nm degrades the intrinsic quality factor $Q_{i,a}$ of the cavity, as the leaky mode 3 begins to couple to the cavity mode.

3.8 Nanofabrication and optimization

The devices in this study were fabricated on a silicon-on-insulator (SOI) platform with a silicon device layer thickness of 220 nm and the oxide layer thickness of 3 µm. The device geometry was defined using electron-beam lithography followed by Pseudo-Bosch dry-etch process to transfer the pattern through the 220 nm Si device layer. Photoresist (SPR-220) was then used to define a 100 µm deep 'trench' region into the handle silicon of the chip for coupling light to the on-chip waveguides using a lensed fiber. The devices were then undercut using a vapor-HF etch and cleaned in a piranha solution (3:1 H2SO4:H2O2) before a final vapor-HF etch to remove any native and chemically-grown oxide. This fabrication flow is shown step-by-step in Figure 3.9

The fabricated geometry is shown in Figure 3.10 along with a zoom-in of various unitcells at the bottom. The device geometry optimization is aided by image processing. Dimensions of various features are measured and fed back to the subsequent fabrication runs. Figure 3.11 provides an example of this process using the

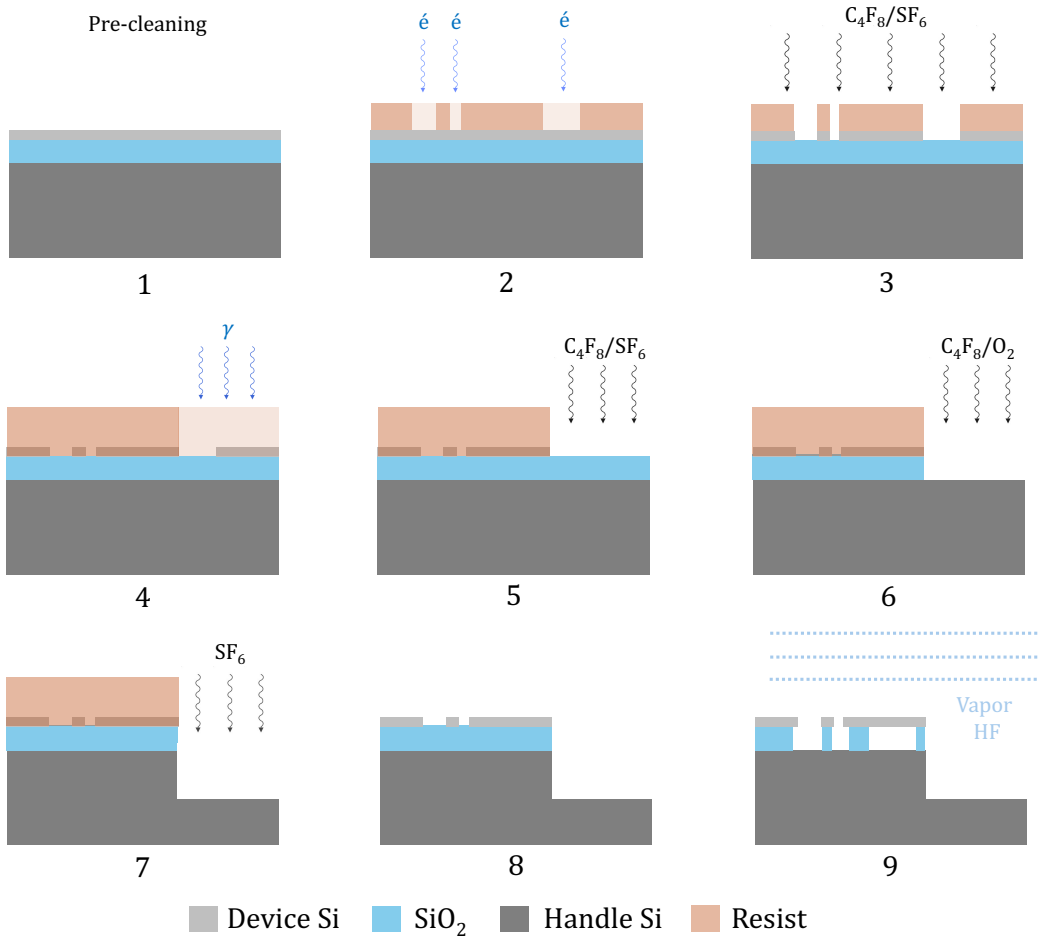

Figure 3.9: **Nanofabrication process flow for 2D-OMC**. Fabrication flow of silicon-based 2D-OMCs, including deep etching into the handle silicon layer to enable fiber-to-chip optical access.

Helium Ion Microscope (HIM) images of the fabricated geometry. Parameters h_i, w_i, h_o and w_o are fitted to the designed optomechanical defect parabola. The finite radius of curvature for all features are extracted and fed back into the Finite Element Method (FEM) simulations to optimize the optical and acoustic bandstructure.

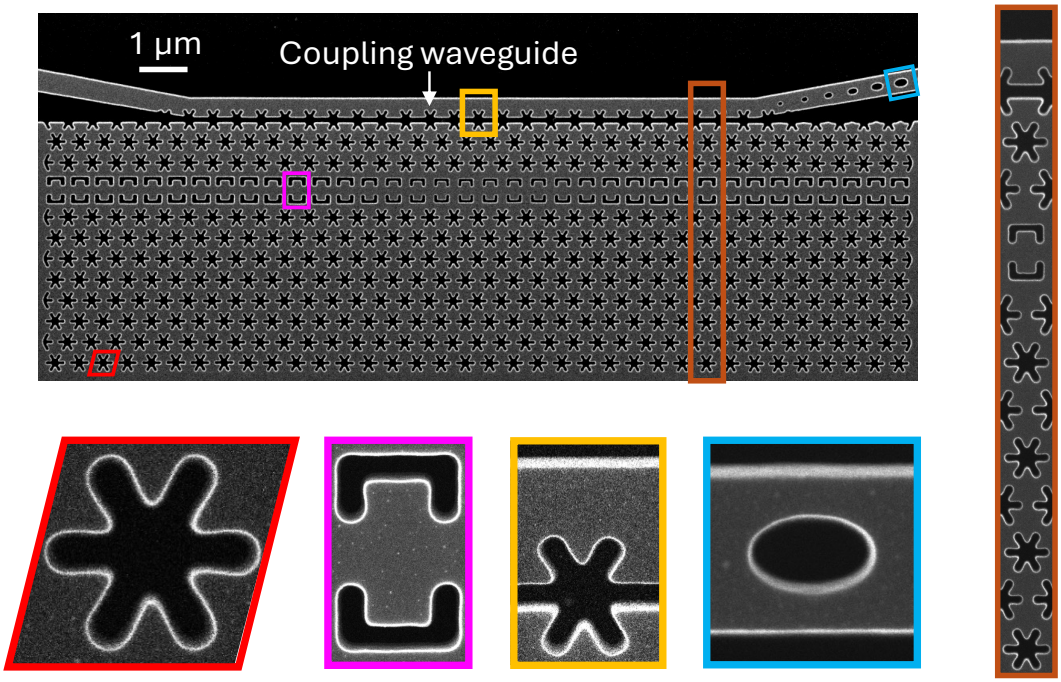

Figure 3.10: **Helium-ion microscope image of fabricated 2D-OMC cavity. a,** Helium-ion microscope image of a representative device with insets indicating (from left to right): unit cells of the 2D snowflake lattice, central fish-bone waveguide, optical coupling waveguide, and the optical waveguide mirror. The orange inset on the right shows the supercell of the geometry used to simulate optical and acoustic bandstructures.

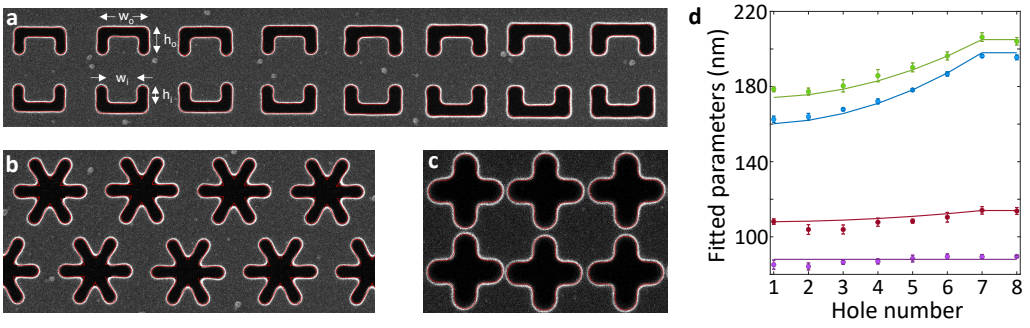

Figure 3.11: **Device optimization using image processing and feedback. a,** Helium Ion Microscope (HIM) image of the defect region of the OMC cavity. The fitted features in red are overlaid on top. **b, c** fitted HIM image of the snowflake and cross shield region. **d,** Plot showing various measured parameters (circles) from (a) and the corresponding design parameters (solid lines).

Chapter 4

HIGH-EFFICIENCY LOW-NOISE PHOTON-PHONON TRANSDUCERS

In the previous chapter, we established the basis for design of high performance optomechanical crystals and nanofabrication techniques. In this chapter, we will discuss the characterization of devices at 10mK temperature where the acoustic resonator is initialized close to the ground state due to negligible thermal occuaption $n_{\text{th}} \approx k_B T/\hbar\omega_b \ll 1$. We refer to the devices we measured as device I and II in our discussion. All measurements are performed in a dilution refrigerator, with the samples mounted to the mixing chamber plate of LD400 dilution refrigerator (Bluefors). The optical and acoustic mode parameters of both devices are tabulated in table 4.1. The primary difference between the two devices is their coupling to the external chip environment. For device I, the intrinsic acoustic damping rate, $\kappa_{i,b}/2\pi$, is measured to be 21.46 kHz, whereas device II is better isolated from the chip environment with a $\kappa_{i,b}/2\pi = 0.97$ kHz. We attribute the difference in $\kappa_{i,b}/2\pi$ between the two devices to a difference in the as-fabricated feature sizes. The effectiveness of the snowflake acoustic bandgap region in suppressing acoustic radiation from the central cavity region, depends on the frequency alignment of the localized mode and the acoustic bandgap, and is highly sensitive to the feature size and shape. A scanning electron microscope image of device I indicates that the patterned features are slightly more rounded and extended than the ideal design, whereas device II replicates the design more faithfully. Although uninentional, these as-fabricated differences in the two devices provides further information about how they thermalize with their environment.

4.1 Optical absorption-induced hot bath

Previous measurements on OMC devices operated in dilution refrigerators have shown that the acoustic mode can thermalize to temperatures well below 100 mK [36]. In our model, this coupling to the cold substrate is represented as an interaction with a cold bath of thermal occupancy $n_{\text{f}} \lesssim 10^{-3}$, coupled at the intrinsic acoustic damping rate $\kappa_{i,b}$, as illustrated in Fig. 4.1.

However, the presence of an optical field within the cavity introduces additional

[0]This chapter is based on work published in ref [35]

Parameter	Device I	Device II
λ_a (nm)	1553.4	1568.3
$\kappa_{i,a}/2\pi$ (MHz)	706	595
$\kappa_{e,a}/2\pi$ (MHz)	444	295
$\omega_b/2\pi$ (GHz)	10.44	10.29
$\kappa_{i,b}/2\pi$ (kHz)	21.46	0.97
$g_{OM}/2\pi$ (kHz)	919	742

Table 4.1: **Summary of measured device parameters:** λ_a is the optical mode wavelength, $\kappa_{i,a}$ is the intrinsic linewidth of the optical cavity, $\kappa_{e,a}$ is the coupling rate between the optical cavity and the optical coupling waveguide, ω_b is the acoustic frequency, $\kappa_{i,b}$ is the intrinsic linewidth of acoustic resonator measured using ringdown technique at 10mK temperature [36], g_{OM} is the vacuum optomechanical coupling rate.

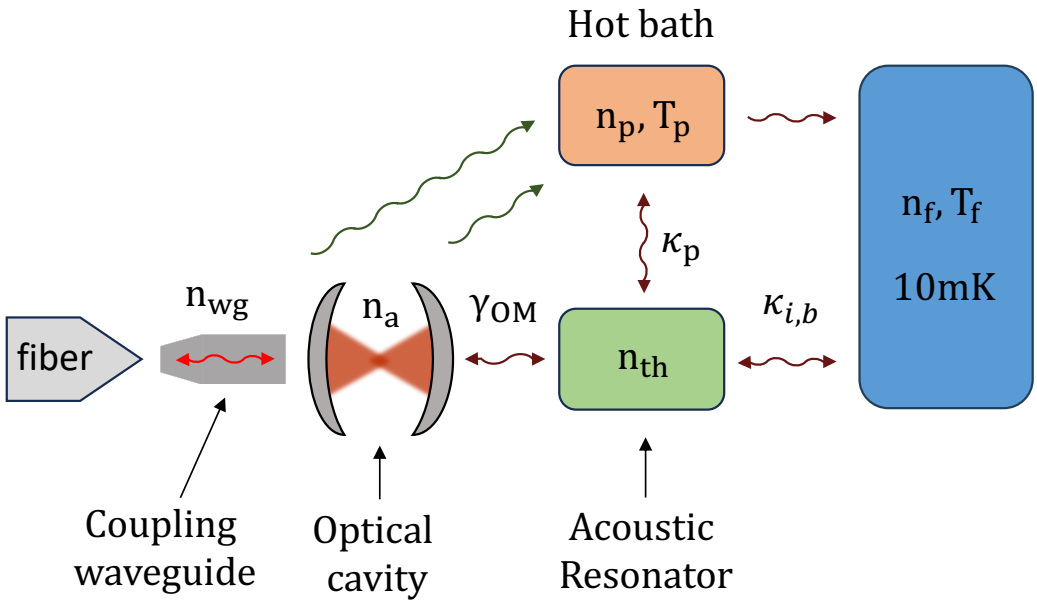

Figure 4.1: **Model for optical absorption induced hot bath:** A lensed fiber is used to coupled light into an optical cavity through a coupling waveguide giving cavity occupation of n_a and waveguide occupation of n_{wg}. The coherent interaction between an optical cavity and the acoustic resonator is given by γ_{OM}. A hot bath with effective occupation n_p and temperature T_p is generated by optical absorption from n_a and n_{wg}. The hot bath couples to the acoustic resonator at a rate κ_p. The cold bath which is characterized by the base temperature of the dilution refrigerator T_f = 10 mK and an effective bath occupancy of n_f couples to the acoustic resonator at a rate $\kappa_{i,b}$.

heating through nonlinear absorption mechanisms in the material. This absorption effectively creates a thermal phonon bath that couples to the acoustic resonator,

thereby increasing its thermal occupancy. We model this effect by introducing a hot bath with thermal occupation n_p, corresponding to a bath temperature T_p, coupled to the acoustic mode at a rate κ_p.

In addition to these baths, the acoustic resonator is also subject to optomechanical back-action from the optical mode at a rate γ_OM. In this study, we operate in a low-power regime where radiation pressure shot noise is negligible. When the laser is red-detuned from the optical cavity by the mechanical frequency (i.e., $\Delta = -\omega_\mathrm{b}$), a parametric beam-splitter interaction enables bi-directional, linear conversion between quantum states in the optical and acoustic domains as we discussed in Chapter 2.

As a first step towards characterizing the optical absorption-induced hot bath we operate the laser on resonance with the optical cavity ($\Delta = 0$) as shown in Figure 4.2a. Under this detuning condition the electric field amplitude in the waveguide is negligible compared to the cavity, and the optomechanical backaction rate is zero. This enables us to isolate optical absorption within the cavity alone without the effects of heating due to optical absorption in the waveguide or cooling due to optomechanical backaction. We measure the heating dynamics of the acoustic mode by detecting optical photons scattered from the laser field onto a motional sideband of the optomechanical cavity. In steady state, the occupation of the acoustic mode, n_m is expected to be an average of the thermal occupations of the hot and the cold baths, weighted by the coupling rates of the acoustic mode to the respective baths, as given by the relation,

$$n_\mathrm{m} = \frac{\kappa_\mathrm{p} n_\mathrm{p} + \kappa_{i,b} n_\mathrm{f}}{\kappa_\mathrm{p} + \kappa_{i,b}}. \tag{4.1}$$

Note that we will use the variable n_m to denote the acoustic occupation without optomechanical backaction, and n_th to refer to the acoustic occupation in the presence of optomechanical backaction. Figure 4.2(b) shows the schematic of the measurement setup for n_m. We send laser pulses with pulse duration, $\tau_\mathrm{d} = 50\,\mu\mathrm{s}$ at a repetition rate, $R = 1$ kHz, to the device in the dilution refrigerator via a circulator. The optical signal reflected from the device is directed to a Fabry-Perot filter setup which suppresses the pump pulses and transmits photons generated on the motional sideband of the optomechanical cavity to a superconducting nanowire single photon detector. Figure 4.3(a) shows the time-dependent occupation of the acoustic mode measured from heating induced by a square laser pulse with a peak power corresponding to $n_\mathrm{a} = 385$. The rate of increase in the occupation is used to infer $\kappa_\mathrm{p} + \kappa_{i,b}$, whereas the steady state occupation is used to infer n_m. Finally, the value of $\kappa_{i,b}$ is

measured independently from ringdown measurements [36], thereby allowing us to extract the parameters, κ_p and n_p of the hot bath from Equation 4.1.

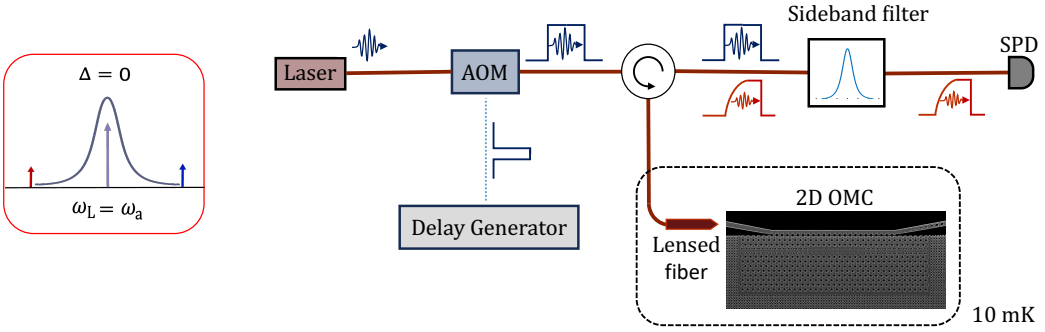

Figure 4.2: **Measurement setup for characterization of hot bath. left,** Measurement scheme for hot bath characterization. Laser with frequency ω_L is parked at the optical cavity frequency ω_a and the acoustic sideband at frequency $\omega_a - \omega_b$ is measured to extract information of the hot bath. **right,** Measurement setup for characterization of the hot bath.

Figure 4.3(b) shows n_p as a function of n_a for devices I and II along with results from similar measurements performed previously on 1D OMCs [36], and butt-coupled 2D OMCs [28]. The vertical axis on the right represents the corresponding bath temperature T_p. The solid lines around the experimental data points for devices I and II are fits to the power law, $n_p = An_a^k$. We find that the fits to the hot bath occupancies for device I and II are $2.2 \times n_a^{0.31}$ and $2.9 \times n_a^{0.21}$, respectively. For comparison, we have also shown the fits to $n_p(n_a)$ for previously measured butt-coupled 2D OMC (purple solid line) and 1D OMC (green solid line) devices, corresponding to $1.1 \times n_a^{0.3}$ and $7.94 \times n_a^{0.33}$, respectively. As expected, the thermal conductance seems to be highest for the butt-coupled 2D OMC, slightly lower for the side-coupled 2D OMC devices that are restricted to approximately the half-plane, and lowest for the 1D OMCs. Of note, the power law of the side-coupled device II of this work ($k = 0.21$), deviates from other measured 1D and 2D OMCs, and does not seem to follow from the simple phonon-bottleneck model of Ref. [36]. This suggests that the underlying mechanisms of heat conductance in these structures may be more complex than initially assumed. Previous studies on phononic crystal structures have reported varying power laws for thermal conductance [37], as well as disorder-dependent behavior [38, 39], which may provide insights into the observed n_p power laws in this work. We will explore this further in the next chapter.

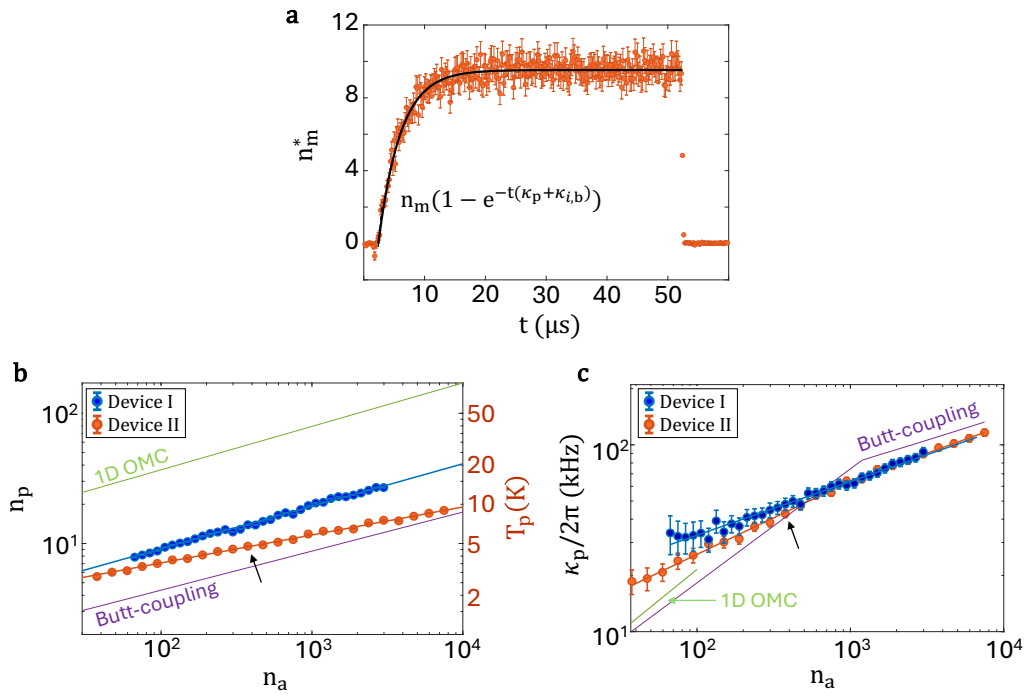

Figure 4.3: **Characterization of hot bath. a,** Measurement of the transient thermal occupation of the acoustic resonator, $n_{\mathrm{m}}^{\star}$ in response to a rectangular optical pulses on resonance with the optical cavity (pulse duration $\tau_{\mathrm{d}} = 50\mu s$, repetition rate, R = 1 kHz, and peak intracavity photon occupation, $n_{\mathrm{a}} = 385$). The black line represents an exponential fit to the observed data with the characteristic rate, $\kappa_p + \kappa_{i,b}$, and steady-state thermal occupation, n_{m}. Here $\kappa_{i,b}$ is the intrinsic damping rate of the acoustic resonator and κ_p is the coupling rate to the optical-absorption-induced hot bath. **b,** Thermal occupation of the hot bath, n_{p} estimated from measurements of n_{m} performed at varying optical power, shown on the x-axis in units of peak intra-cavity photon occupation, n_{a}. For comparison, n_p curves for 1D-OMC [36], butt-coupled 2D OMC [28] are shown. **c,** Variation of $\kappa_p/2\pi$ with n_{a}. The data point marked with an arrow in panels (b) and (c) corresponds to the data in panel (a) for $n_{\mathrm{a}} = 385$.

Figure 4.3(c) shows the variation of κ_p with n_{a}. For device II, we find the power-law, $\kappa_p/2\pi = 4.3$ (kHz)$\times n_{\mathrm{a}}^{0.39}$ when $n_{\mathrm{a}} < 1000$ and $\kappa_p/2\pi = 8.25$ (kHz)$\times n_{\mathrm{a}}^{0.29}$ when $n_{\mathrm{a}} > 1000$. The power-law exponent of 0.39 in the regime of low optical power is significantly different from 0.6 and 0.66 observed previously for butt-coupled 2D OMC and 1D-OMC devices, respectively. This reduction can be explained by the reduced n_{p} power exponent of 0.21, together with a two-dimensional phonon bath (see section 5.2) of the next chapter for details.. For device I, in the regime of high optical power with $n_{\mathrm{a}} > 1000$, $\kappa_p/2\pi = 8.7$ (kHz)$\times n_{\mathrm{a}}^{0.29}$. For $n_{\mathrm{a}} < 1000$, the measurement error on κ_p for device I is larger due to a higher intrinsic damping

rate, $\kappa_{i,b}$, thereby reducing the reliability of a fit in this regime. We observe that the power-law exponent for κ_p in the regime of high optical power is identical for devices I and II in this study, and also in close agreement with the butt-coupling geometry.

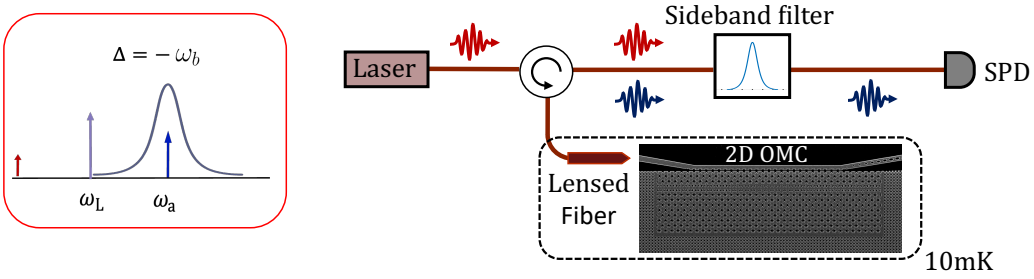

Figure 4.4: **Measurement setup for phonon-to-photon transduction under continuous-wave excitation. left,** Laser with frequency ω_L is parked at the red sideband of the optical cavity frequency ($\Delta = -\omega_b$) and the acoustic sideband at cavity frequency ω_a is measured to extract thermal occupation of the acoustic resonator **right,** Measurement setup for phonon-to-photon transduction under continuous-wave excitation.

4.2 Phonon-to-photon transduction under continuous-wave laser excitation.

After characterizing the optical-absorption-induced hot bath, we test the device with the laser tuned to the red motional sideband of the optical cavity ($\Delta = -\omega_b$), relevant for phonon-photon transduction. The thermal occupation of the acoustic mode, n_{th}, due to optical-absorption-induced heating adds finite noise to any transduced signal. Other performance metrics of interest for such a transducer are the conversion efficiency, η_{OM}, and bandwidth, κ_b. In continuous-wave operation, the conversion efficiency is given by $\eta_{\text{OM}} = \frac{\gamma_{\text{OM}}}{\gamma_{\text{OM}}+\kappa_{i,b}+\kappa_p}$. We calibrate γ_{OM} for different n_a using electromagnetically induced transparency [40] (see supplementary text, Figure B.2(a) for details). Due to the low $\kappa_{i,b}$ in our devices, we expect high conversion efficiency for modest values of n_a. Specifically, operation at $n_a \approx 13$ and 3 is expected to yield $\eta_{\text{OM}} \approx 50\%$ in devices I and II, respectively. The bandwidth of the transducer is limited by the total acoustic linewidth, which is dominated by the optomechanical backaction $\kappa_b \approx \gamma_{\text{OM}}$ in the regime of high conversion efficiency.

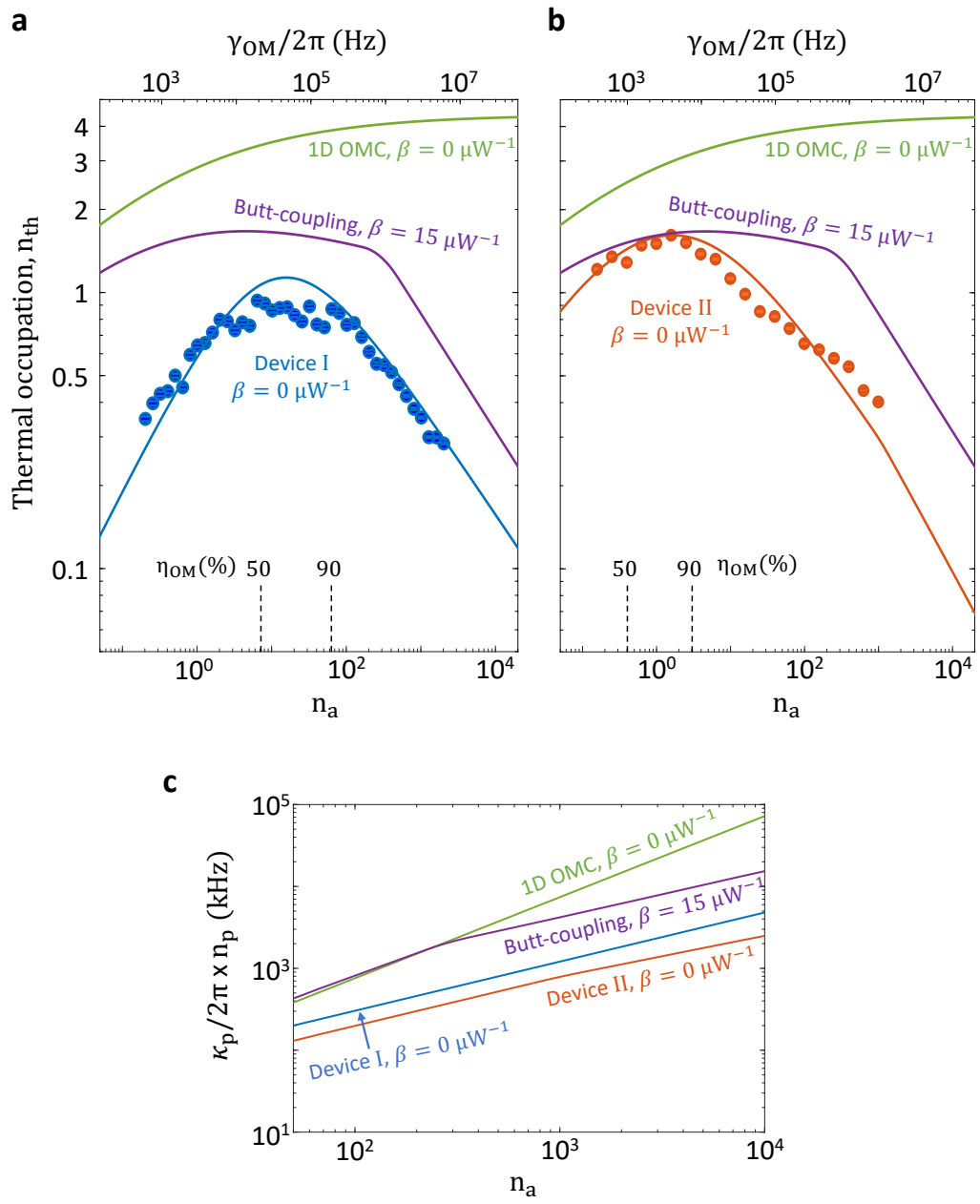

Figure 4.5: **Phonon-to-photon transduction under continuous-wave excitation.** Measured thermal phonon occupancy, n_{th} with varying optical power, shown on the bottom x-axis in units of intra-cavity photon occupation, n_{a}, and on the top-axis in units of optomechanical transduction rate, γ_{OM}. Results are shown on separate charts for **a** device I, and **b,** device II. Filled circles are data points whereas the solid line indicated with $\beta = 0\,\mu\mathrm{W}^{-1}$ is the modeled n_{th} dependence using equation 4.2. For comparison, model curves are shown for a butt-coupled 2D-OMC ($\beta = 15\,\mu\mathrm{W}^{-1}$) [28], and 1D-OMC [36]. Dashed lines indicate the n_{a} value for optomechanical transduction efficiency $\eta_{\mathrm{OM}} = 50\%$ and 90%. For $n_{\mathrm{a}} = 1$, on chip input power for device I and II are $P_{\mathrm{in}} = 0.20\,\mu\mathrm{W}$, and $0.28\,\mu\mathrm{W}$, respectively. **c,** Estimated heating rate of the acoustic resonator $\kappa_{\mathrm{p}} n_{\mathrm{p}}/2\pi$ as a function of n_{a} under $\Delta = -\omega_{\mathrm{b}}$ for different devices plotted for their measured value of β.

To characterize the transducer-added noise under continuous-wave laser excitation, we use the measurement setup shown schematically in Figure 4.4 where we perform single-photon counting at the optical cavity resonance frequency. The data in Figures 4.5 (a, b) show n_{th} measured with varying n_{a} for devices I and II, respectively. In the high power regime, specifically for $n_{\mathrm{a}} > 500$, the n_{th} data has been corrected for the limited bandwidth of the sideband filter when the acoustic bandwidth κ_{b} starts to approach the sideband filter linewidth (see supplementary text, section B.3 for details). The top x-axis displays the corresponding γ_{OM} for side-coupled devices. The green and purple curves in these panels show results from similar measurements of thermal occupancy of the acoustic mode performed previously on 1D OMCs [36] and butt-coupled 2D OMCs [28]. We observe that side-coupled 2D OMCs allow for lower thermal noise across a wide range of input optical powers. A minimum n_{th} of 0.28 ± 0.01 is achieved for device I at $n_{\mathrm{a}} = 2030$, corresponding to an optomechanical transduction efficiency of $98.6 \pm 0.2\%$, and a bandwidth of $\gamma_{\mathrm{OM}}/2\pi \approx 6$ MHz.

We model the thermal occupancy n_{th} using the heating model introduced in the previous section. However, in contrast with the measurements with $\Delta = 0$ in the previous section, the majority of the incident power is reflected under detuned operation with $\Delta = -\omega_{\mathrm{b}}$, and parasitic optical absorption in the coupling waveguide can contribute substantially to the hot bath. To include this effect in our heating model, we define an effective photon occupation associated with coupling waveguide, n_{wg}, varying linearly with the input power as $n_{\mathrm{wg}} = \beta P_{\mathrm{in}}$ for some fixed constant, β and the input power, P_{in}. We then add the contributions from both cavity and waveguide components and define the parameters of the modified hot bath as $n_{\mathrm{p}}[n_{\mathrm{a}}, \beta] \rightarrow n_{\mathrm{p}}[n_{\mathrm{a}} + \beta P_{\mathrm{in}}]$, and similarly for κ_p. The thermal occupation of the acoustic mode is then given by

$$n_{\mathrm{th}} = \frac{\kappa_{\mathrm{p}}[n_{\mathrm{a}}, \beta] n_{\mathrm{p}}[n_{\mathrm{a}}, \beta] + \kappa_{i,b} n_{\mathrm{f}}}{\kappa_{\mathrm{p}}[n_{\mathrm{a}}, \beta] + \kappa_{i,b} + \gamma_{\mathrm{OM}}[n_{\mathrm{a}}]}. \tag{4.2}$$

For small n_{a}, Equation 4.2 is dominated by heating from the hot bath $\kappa_p n_p$ and exhibits an increase in n_{th} with increasing n_a. Conversely for large n_{a}, n_{th} decreases with increasing n_a as a consequence of backaction cooling γ_{OM}. The turnaround point between these two regimes is influenced by parasitic optical absorption in the coupling waveguide. For example, the solid blue and orange curves in Figures 4.5(a) and (b) show the predicted thermal phonon occupancy if the waveguide-heating contribution, β were set to zero. We see that the experimental data from

both devices I and II is in reasonable agreement with the $\beta = 0$ curves. This indicates that waveguide-related heating is negligible in side-coupled 2D-OMC geometry. In comparison, for the butt-coupled 2D OMCs, β was measured to be $15\,\mu W^{-1}$ [28].

While n_{th} in Equation 4.2 depends on the optomechanical device parameters $\kappa_{i,b}$ and γ_{OM}, improvements purely based on geometric modifications of the device platform under detuned operation $\Delta = -\omega_b$ can be studied using the heating rate, $\kappa_p n_p/2\pi[n_a, \beta]$, and is plotted in Figure 4.5(c) for various devices. For 1D-OMC, the heating rate scales linearly ($\kappa_p n_p \propto n_a$), similar to the cooling rate ($\gamma_{OM} \propto n_a$), which results in the saturation of n_{th} to a few phonon levels as n_a increases. 2D geometries are expected to have lower magnitude of the heating rate due to larger thermal contact with the cold bath. However, due to a large $\beta = 15\,\mu W^{-1}$, the butt-coupling design exhibits almost identical heating performance ($\kappa_p n_p \propto n_a^{0.9}$) to that of 1D-OMC for $n_a < 300$, and only becomes sublinear for $n_a > 300$ ($\kappa_p n_p \propto n_a^{0.6}$). In contrast, for side-coupled geometries, the heating rate scales sub-linearly ($\kappa_p n_p \propto n_a^{0.6}$) for all n_a range measured and has a lower magnitude. Specifically, for device II, the heating rate is reduced by approximately six-fold compared to the butt-coupling design for $n_a > 300$.

4.3 Phonon-to-photon transduction under pulsed laser excitation

Pulsed transduction schemes are often preferred due to the delayed heating response of the acoustic resonator [41], which allows for the initialization of the optomechanical transduction pulse prior to the onset of heating. We characterize the performance of side coupled 2D-OMC as a transducer in pulsed mode by sending short rectangular pulses on red sideband. A pulse duration of $\tau_d = 500$ ns is selected to account for the finite rise time of the sideband filters (≈ 200 ns). The transduction efficiency in the pulsed mode is given by

$$\eta_{OM} = \frac{\gamma_{OM}}{\gamma_{OM} + \kappa_{i,b} + \kappa_p}\left(1 - e^{-(\kappa_{i,b}+\kappa_p+\gamma_{OM})\tau_d}\right). \tag{4.3}$$

Figure 4.6 shows the internal transduction noise $\bar{n}$ for device II in pulsed scheme along with similar measurements performed previously on 1D-OMC [36] and butt-coupling design [28] at $n_a = 10$. The n_a value corresponding to the optomechanical conversion efficiency $\eta_{OM} = 10\%$, 50%, and 90% for device II are indicated with dashed lines. Given the low intrinsic linewidth of the acoustic resonator for this device ($\kappa_{i,b}/2\pi = 0.97$ kHz), we used a repetition rate of 250 Hz to allow the acoustic mode to sufficiently thermalize to the cold bath between successive optical pulses. For the highest optical power we could send to the device ($n_a = 444$), we measured

$\bar{n}$ = 0.25 ± 0.01 which corresponds to a transduction efficiency of η_{OM} = 93.1 ± 0.8%. This constitutes a significant enhancement across transduction metrics over 1D-OMC with $(n_a, \bar{n}, \eta_{OM}) \simeq (10, 0.4, 4\%)$ [36].

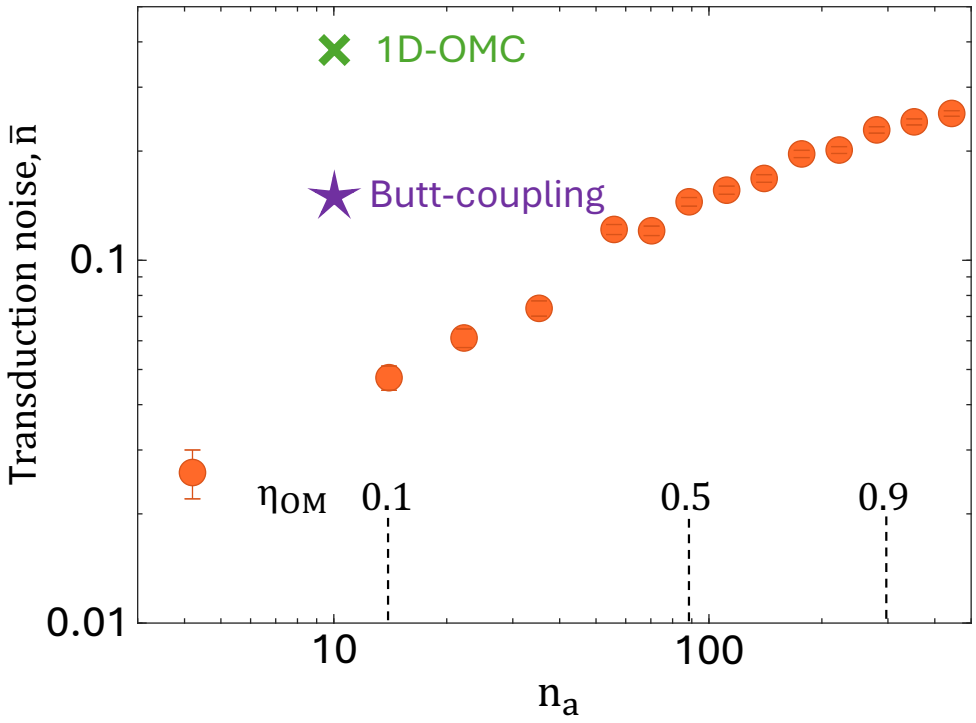

Figure 4.6: **Phonon-to-photon transduction under pulsed laser excitation**. Internal added noise, $\bar{n}$ (red data points) as a function of the peak intra-cavity pump photon number, n_a. All noise measurements are performed on device II with rectangular optical pump pulses with a pulse width of 500 ns at a repetition rate of 250 Hz. For comparison, $\bar{n}$ is shown for Butt-coupling design [28], and 1D-OMC [36]. Dashed lines indicate the n_a value for transduction efficiency η_{OM} = 10%, 50%, and 90% for device II. For n_a = 1, on chip input power is P_{in} = 0.28 μW.

4.4 Outlook

The side-coupled 2D-OMC design presented here reduces optical absorption-induced thermal noise in OMCs, a major obstacle in quantum application requiring operation at millikelvin temperatures. Table 4.2 shows a comparative analysis between 1D-OMC (device A in [36]) and 2D-OMC (device II in this work) for phonon-photon pulsed transduction. For both measurements, the repetition rate is much smaller than the intrinsic decay rate of the acoustic resonator ($R \ll \kappa_{i,b}$) which allows for thermalization with the fridge environment between subsequent optical pulses. For a fair comparison of the single photon heralding rate, we assume a common repeti-

tion rate R=10 kHz and total detection efficiency η_{ext} = 5% for both 1D-OMC and 2D-OMC. The resulting single photon heralding rate for 1D-OMC is $R \times \eta_{\text{ext}} \times \eta_{\text{OM}}$ = 20 Hz with an added noise of $\bar{n} \sim 0.4$. For 2D-OMC, the single photon heralding rate is 465 Hz with an added noise of 0.25. The photon coincidence rate for a remote entanglement experiment involves two nodes and will scale as square of the detection efficiency. For 1D-OMC, this rate is significantly smaller ($R \times \eta_{\text{ext}}^2 \times \eta_{\text{OM}}^2$=0.04 Hz); whereas the photon coincidence rate for 2D-OMC in this work is 21 Hz, which constitutes a ~500-fold improvement along with lower added noise.

Parameter	**1D-OMC**[36]	**2D-OMC (device II)**
n_{a}	10	443
η_{OM}	4%	93%
$\bar{n}$	~0.4	0.25
peak $\gamma_{\text{OM}}/2\pi$	13 kHz	1.1 MHz
Single photon heralding rate (R=10 kHz, η_{ext} = 5%)	20 Hz	465 Hz
Photon coincidence rate	0.04 Hz	21 Hz

Table 4.2: **Comparison of figures of merit for pulsed transduction:** η_{OM} is the phonon-to-photon transduction efficiency. $\bar{n}$ is the measured noise in the transduction process. Single photon heralding rate is estimated for repetition rate R=10 kHz and detection efficiency η_{ext} = 5%. The coincidence rate is the estimated for a two-node remote entanglement scheme.

Parameter	**1D-OMC** [36]	**2D-OMC (device II)**
n_{a}	569	641
η_{OM}	$\approx$ 93%	$\approx$ 97%
n_{th}	4.2	0.42
$\gamma_{\text{OM}}/2\pi$	1 MHz	1.6 MHz

Table 4.3: **Comparison of figures of merit for continuous-wave transduction**

In case of continuous wave transduction, the figures of merit for different devices are shown in table 4.3. The data for 1D-OMC is taken for device I in [36]. The transduction efficiency η_{OM} in continuous wave is given by $\gamma_{\text{OM}}/(\gamma_{\text{OM}} + \kappa_{i,b} + \kappa_p)$ which remains greater than 90% for $\gamma_{\text{OM}} \gg \kappa_{i,b}$. The thermal occupation of the acoustic resonator shows an order of magnitude improvement for device II in this work (n_{th} = 0.42), compared to 1D-OMC (n_{th} = 4.2) at similar n_{a} levels.

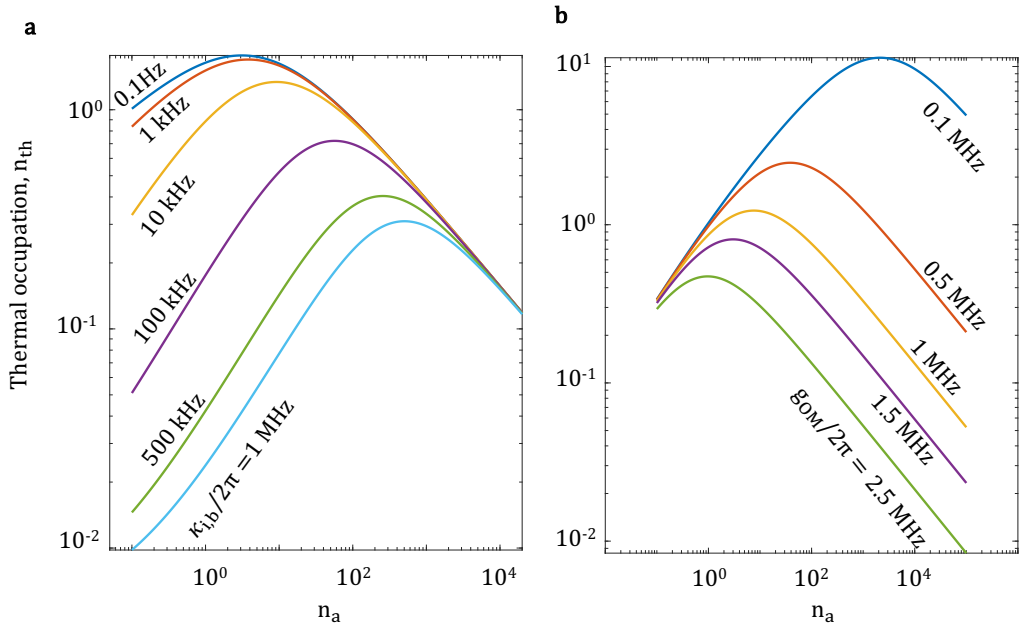

Figure 4.7: **Thermal occupation for various device parameters. a,** n_{th} as a function of n_{a} for various $\kappa_{i,b}/2\pi$. Increasing $\kappa_{i,b}/2\pi$ improves thermalization of the breathing mode to the cold bath (10 mK) dictated by equation 2 of the main text, which leads to reduction in n_{th}. **b,** n_{th} as a function of n_{a} for various $g_{\mathrm{OM}}/2\pi$. The 'turnaround' point shifts to lower n_{a} with increasing g_{OM}. For both (a) and (b), device parameters are assumed to be same as that for device I in the main text.

Effect of optomechanical parameters on thermal occupation

The steady-state thermal occupation n_{th} is governed by Equation 4.2, which depends on various device parameters. Figure 4.7(a) shows n_{th} as a function of intracavity photon number n_{a} for different intrinsic acoustic linewidths $\kappa_{i,b}/2\pi$. As the intrinsic linewidth increases, the acoustic breathing mode couples more efficiently to the cold bath at 10 mK with thermal occupancy $n_{\mathrm{f}} < 10^{-3}$, resulting in a lower n_{th} in the low-n_{a} regime. This regime has been explored in [27] using a butt-coupled design, which enables high repetition rates due to larger acoustic linewidths.

Figure 4.7(b) presents n_{th} versus n_{a} for varying single-photon optomechanical coupling rates $g_{\mathrm{OM}}/2\pi$. In the low-power regime ($n_{\mathrm{a}} < 1$), n_{th} remains largely unaffected by changes in g_{OM}. However, the "turnaround" point beyond which the optomechanical damping rate γ_{OM} dominates shifts to lower values of n_{a} as g_{OM} increases. In the high-n_{a} regime, a higher g_{OM} leads to a more pronounced reduction in n_{th}.

The parameters $(\kappa_{i,a}, \kappa_{e,a}, n_\mathrm{p}, \kappa_\mathrm{p})$ used in both panels (a) and (b) correspond to those measured for device I. In this analysis, we assume that the optical absorption-induced hot bath remains independent of the smallest optical gap $h_0 - h_i$, and hence independent of g_OM. This assumption is justified by the fact that the optical mode of interest is an air-mode, where a large fraction of the optical energy is confined within the air holes of the C-shaped structure. Reducing the gap increases field concentration in the air region but is not expected to significantly affect absorption in silicon. For example, FEM simulations show that when $h_0 - h_i = 60\,\mathrm{nm}$, the optical energy participation in silicon is approximately 13%, whereas for $h_0 - h_i = 20\,\mathrm{nm}$, it increases only slightly to 17%.

We anticipate that further reduction in thermal noise can be achieved through surface passivation techniques [42], which may help suppress optical absorption by mitigating surface defect states. In our devices, the lowest demonstrated n_th under continuous-wave (CW) operation was limited by the finite optical power that could be coupled into the device. Due to the relatively high acoustic frequency of 10.3 GHz, the achievable intracavity photon number n_a for a given input power P_in was approximately 4 times lower than that of a device operating at 5 GHz, and about 2 times lower than one operating at 7.5 GHz. Alternative 2D unit cell geometries, such as the shamrock [43] and boomerang [27] designs, have been explored to open acoustic bandgaps near 7 GHz. These geometries may enable operation at higher n_a for a given optical input power.

This result unlocks new possibilities for more quantum-coherent applications using OMCs. The compact form factor and long-lived acoustic mode of such devices are attractive for applications such as quantum memory for telecom photons [44]. While we achieved a low intrinsic decay rate of 0.97 kHz for the acoustic resonator, we anticipate that embedding the 2D-OMC in a cross phononic shield may lead to drastically lower intrinsic decay rates [36, 28]. The low thermal occupation of the acoustic resonator presents an opportunity to investigate two-level systems (TLS) in amorphous solids [36, 45, 46, 47], further expanding the potential of OMCs in quantum technologies.

The improved performance of our side-coupled 2D-OMC design in pulsed operation holds significant promise for applications in single-photon heralding and remote entanglement generation. In the context of microwave-to-optical quantum transduction, the side-coupled 2D-OMC can be integrated into a piezo-optomechanical transducer by designing a piezo-acoustic cavity that couples a microwave electrical

circuit to the optomechanical system via a phononic waveguide, as will be explored in chapter 6 and 7. Such transducers offer the potential for large bandwidth, low noise, and near-unity efficiency in converting microwave signals to optical photons and vice versa. While this study has focused on thermal handling improvements in silicon-based optomechanical devices, piezo-optomechanical transducers operate on heterogeneously integrated platforms that incorporate optically robust microwave resonators [48, 49, 50], potentially involving different heating mechanisms. Nevertheless, the results presented here establish a thermal performance benchmark for future transducers. By connecting such a transducer to an off-chip superconducting qubit module [51, 52, 53], high optical powers can be utilized without compromising qubit coherence, enabling scalable quantum networking architectures.

Chapter 5

ORIGINS OF OPTICAL-ABSORPTION INDUCED HOT BATH

In the previous chapter, we discussed an optimized geometry for the two-dimensional optomechanical crystal (2D-OMC) with a side-coupled waveguide. We observed heating of the acoustic resonator mediated by a bosonic hot bath characterized by an occupancy n_p and a scattering rate κ_p. Both n_p and κ_p exhibit specific power-law scaling. Understanding these observations which may offer insight into their mesoscopic origins and suggest potential strategies for mitigation.

5.1 Numerical Simulations for the Density of States in 2D-OMC Geometry

To gain insight into the phonon hot bath spectrum and its interaction with the acoustic breathing mode, we performed finite element method (FEM) simulations targeting all acoustic modes within the structure up to 40 GHz. Given the relevant hot bath temperature range (4–10 K), as discussed in Figure 4.3, it is important to consider all phonon modes below 1 THz. However, simulating frequencies beyond 40 GHz presents a significant computational challenge due to the large geometry and the fine mesh resolution required.

The FEM simulations were performed using a supercell geometry shown in Figure 5.1(a), along with a sample acoustic mode at 37.6755 GHz. The coupling waveguide was excluded from the simulation domain, as it is mechanically isolated from the cavity. The structure includes 2.5 and 9 rows of snowflake patterns above and below the fishbone unit cell, respectively. To accurately represent the undercut resulting from the vapor HF release process used in fabrication, an additional 3 μm silicon bulk layer is included beneath the 9-row section. Boundary conditions are set as fixed on the $-y$ edge and free on the $+y$ edge.

Figure 5.1(b) illustrates the geometry used in the FEM simulations, with mesh sizes ranging from 10 nm (minimum) to 50 nm (maximum). This mesh configuration ensures adequate spatial resolution, providing multiple sampling points per acoustic wavelength even at the highest simulated frequency.

Figure 5.1(c) shows the resulting density of states (DOS) as a function of frequency for the simulated geometry. The DOS is computed by summing over all acoustic modes across the wavevector range from Γ to X. For visualization, a frequency

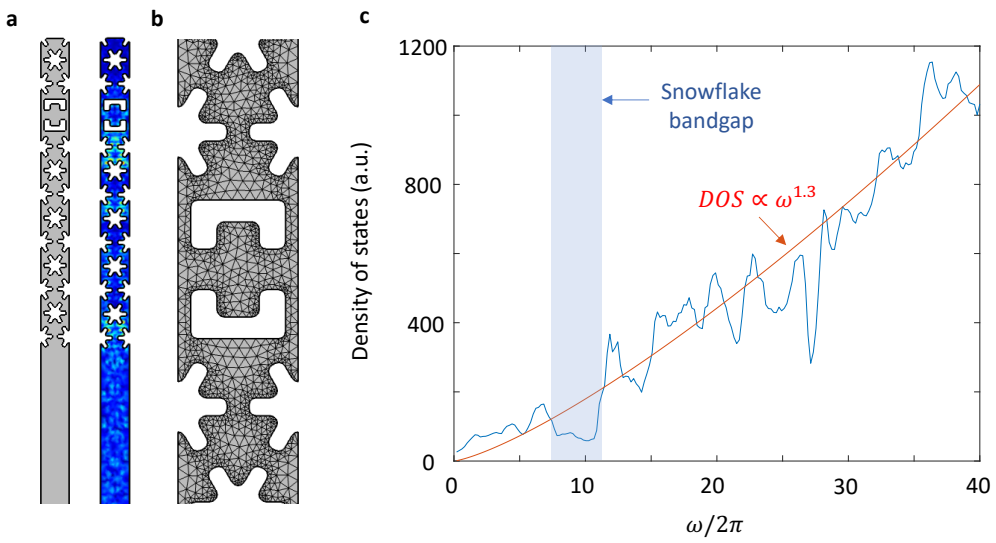

Figure 5.1: **Numerical simulations of the acoustic spectrum: a,** unitcell of the 2D-OMC mimicking the exact fabricated geometry (left) and a sample simulated acoustic mode at 37.6755 GHz (right). **b,** Meshed geometry showing a minimum and maximum element size of 10 nm and 50 nm, respectively. **c,** Density of states as a function of frequency calculated by summing all the acoustic modes from wavevector Γ to X. The red curve has a power of 1.3 which corresponds to the dimension of 2.3 for the phononic spectrum. The shaded region shows a dip in DOS due to the bandgap of the snowflakes.

bin size of 200 MHz is used. The shaded region highlights the suppression of DOS within the bandgap of the snowflake phononic structure. However, the DOS does not fully vanish in this region, due to contributions from the fishbone unit cell and the 3 μm silicon bulk layer, both of which support additional acoustic modes. The red solid line shows a power law fit of the form DOS $\propto \omega^{1.3}$, indicating that the phonon bath exhibits an effective Debye dimensionality [54] of 2.3.

5.2 Theoretical model for hot bath

The local hot bath plays a key role in determining the thermal occupation of the acoustic resonator in the presence of laser light. During the plasma etching of the device, which involves SF_6 and C_4F_8 chemistry, ion implantation creates defect states at the surface of the silicon. The hot bath is thought to be generated as these defect states, with eV energy levels, undergo phonon assisted decay to create a shower of high frequency phonons. Due to very high density of states, these phonons thermalize among themselves at a rate κ_{mix} much larger than coupling rates with the external environment and hence have a common temperature T_{p}. The acoustic

breathing mode at 10.3 GHz lies among discrete phonon modes and is protected by the phononic bandgap. Despite having spatial overlap between the hot bath and the acoustic breathing mode, the two can be considered to be independent of each other due to small coupling rate rate $\kappa_p \ll \kappa_{\mathrm{mix}}$.

To derive the expression of κ_p, we consider a simple 3-phonon scattering model where the acoustic breathing mode ω_b couples to high frequency modes ω_1 and ω_2 in the phonon bath, such that $\omega_2 - \omega_1 = \omega_b$. Using first order perturbation theory, the scattering rates in and out of the mode of interest are given by $\Gamma_+ = A(n_{\mathrm{m}} + 1)n_2(n_1 + 1)$ and $\Gamma_- = An_{\mathrm{m}}n_1(n_2 + 1)$ respectively, where n_{m}, n_1, and n_2 are the number of phonons in the corresponding modes, and A is the anharmonicity matrix of the lattice. For simplicity, we assume A to be frequency independent. The rate of change of n_{m} is then given by

$$\dot{n}_{\mathrm{m}} = \Gamma_+ - \Gamma_- = -\kappa_p^*(n_{\mathrm{m}} - n_{\mathrm{p}}^*) \tag{5.1}$$

where $n_{\mathrm{p}}^* = An_2(n_1 + 1)/\kappa_p^*$ is the effective occupancy in the steady state and $\kappa_p^* = A(n_2 - n_1)$ can be thought of as the rate at which the breathing mode reaches occupancy n_{p}^*. The total rate κ_p would be the sum of individual κ_p^* across the hot bath frequency spectrum.

$$\kappa_p = \sum_{n_1,n_2} A(n_1 - n_2). \tag{5.2}$$

In thin film patterned systems, the density of states is significantly modified in the low frequency regime such that $\omega_2 - \omega_1 = \omega_b$ is not satisfied in the continuum limit. We take the continuum limit for κ_p above a certain cutoff frequency ω_{co} where the density of states is large,

$$\kappa_p = \int_{\omega_{\mathrm{co}}}^{\infty} d\omega A\rho[\omega]\rho[\omega + \omega_b](n[\omega] - n[\omega + \omega_b]), \tag{5.3}$$

here, $\rho[\omega]$ is the phonon density of states (DOS) at frequency ω and $n[\omega]$ is the Bose Einstein occupation factor. Due to the low DOS below ω_{co}, the effective ground state frequency for the hot bath is shifted to ω_{co},

$$n[\omega] = \frac{1}{e^{\hbar(\omega-\omega_{\mathrm{co}})/k_{\mathrm{B}}T_{\mathrm{p}}} - 1}. \tag{5.4}$$

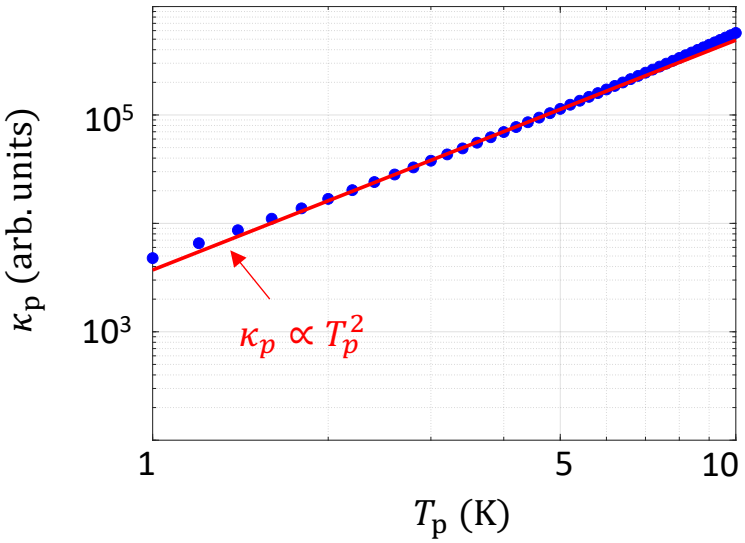

Figure 5.2: **Scaling of hot bath coupling rate κ_p as a function of bath temperature T_p.** The blue dots show theoretical value of κ_p obtained by numerically integrating equation 5.3. The solid red curve shows a theoretical power law dependency $\kappa_p \propto T_p^2$ used in previous derivation [36]. The dimensionality of phonon bath is taken as 2.3 in accordance with FEM simulations in section 5.1, and the cutoff frequency $\omega_{co}/2\pi = 20$ GHz is chosen corresponding to dimensional crossover from 2D to 3D density of states due to finite device layer thickness.

For a d-dimensional Debye phonon bath, the DOS follows the power law relation, $\rho[\omega] \propto \omega^{d-1}$. We numerically integrate equation 5.3 to find κ_p in the temperature range $T_p \in [1, 10]$ K corresponding to the experimentally observed bath temperature range. Figure 5.2 shows the numerically calculated value of κ_p in arbitrary units (blue circles). We use d=2.3 in agreement with the numerical simulations of the acoustic spectrum as discussed in section 5.1. In the next section, we will discuss how the cutoff frequency ω_{co} can influence the observed power laws of κ_p and n_p. Here, for simplicity, we define ω_{co} based on the fundamental mode determined by the thickness of the device layer ($t = 220$ nm) and the longitudinal sound velocity ($v_l = 8433$ m/s), yielding

$$\frac{\omega_{co}}{2\pi} = \frac{v_l}{2t} \approx 20\,\text{GHz}.$$

The red curve in Figure 5.2 represents the theoretical power-law dependence given by $\kappa_p \propto T_p^2$, which was the approximation used in the previous derivation in [36] and fits reasonably to the numerically calculated values of $\kappa_p[T_p]$.

In the high temperature limit $T_p \gg \hbar\omega_b/k_B$, a generalized power law for the phonon scattering rate κ_p emerges from Equation 5.3, assuming a density of states that scales

Device	n_p power law	α	κ_p power law	d
Device I	0.31	2.2	NA (low n_a)	NA (low n_a)
			0.29 (high n_a)	1.42 (high n_a)
Device II	0.21	3.77	0.39 (low n_a)	1.93 (low n_a)
			0.29 (high n_a)	1.69 (high n_a)
Device III*	0.21	3.77	0.39 (low n_a)	1.93 (low n_a)
			0.29 (high n_a)	1.69 (high n_a)
Butt-coupling	0.3	2.3	0.6 (low n_a)	1.99 (low n_a)
			0.29 (high n_a)	1.48 (high n_a)
1D-OMC	0.33	2	0.66 (low n_a)	2 (low n_a)
			NA (high n_a)	NA (high n_a)

Table 5.1: **Comparison of hot bath dimensionality parameters α and d for various devices.** Data for the butt-coupling and one dimensional OMC devices are adapted from Refs. [28, 36]. Device III, marked with an asterisk ($*$), exhibited performance identical to device II and was therefore excluded from the discussion in the previous chapter.

as ω^{d-1} in d dimensions. As derived in Ref. [36], this leads to

$$\kappa_p \propto T_\mathrm{p}^{2d-2}. \tag{5.5}$$

The effective thermal occupancy of the acoustic resonator in the steady state can be calculated by integrating n_p^* over the phonon bath frequency spectrum

$$n_\mathrm{p} = \frac{1}{\kappa_p}\int_{\omega_\mathrm{co}}^{\infty} d\omega A\rho[\omega]\rho[\omega+\omega_b]n[\omega+\omega_b](n[\omega]+1). \tag{5.6}$$

We use the identity $n_\mathrm{b}[x+x_m](n[x]+1) = (n[x]-n[x+x_m])n[x_m]$ to simplify the above equation.

$$n_\mathrm{p} \simeq \frac{n[\omega_b+\omega_\mathrm{co}]}{\kappa_p}\int_{\omega_\mathrm{co}}^{\infty} d\omega A\rho[\omega]\rho[\omega+\omega_b](n[\omega]-n[\omega_b+\omega_\mathrm{co}]) \tag{5.7}$$

$$= n[\omega+\omega_\mathrm{co}] \tag{5.8}$$

$$\approx \frac{k_\mathrm{B}T_\mathrm{p}}{\hbar\omega_b} \text{ for } T_\mathrm{p} \gg \hbar\omega_b/k_\mathrm{B}. \tag{5.9}$$

To relate $n_\mathrm{p}(T_\mathrm{p})$ and $\kappa_p(T_\mathrm{p})$ relations above with the n_a powers laws in Figure 4.3 of the previous chapter, we utilize Planck's law. In thermal equilibrium, the hot bath

acts as a black body with radiated power P_{out} that scales as $P_{\text{out}} \sim T_{\text{p}}^{\alpha+1}$, where α is thought to be the effective number of spatial dimensions of the material/structure under consideration. For a linear optical absorption process, we can write the absorbed optical power as a fraction η of the optical pump power: $P_{\text{abs}} = \eta P_{\text{in}} = \eta' n_a$. In thermal equilibrium, the power output from the phonon bath is equal to its input, $P_{\text{out}} = P_{\text{abs}} \sim n_a$ leading to the relation:

$$T_{\text{p}} \propto n_a^{\frac{1}{\alpha+1}}. \tag{5.10}$$

We then have the following relations for $n_{\text{p}}(n_a)$ and $\kappa_p(n_a)$:

$$n_{\text{p}} \propto T_{\text{p}} \propto n_a^{\frac{1}{\alpha+1}} \tag{5.11}$$

and

$$\kappa_p \propto T_{\text{p}}^{2d-2} \propto n_a^{\frac{2d-2}{\alpha+1}}. \tag{5.12}$$

Table 5.1 shows comparison of power laws for different devices. For device I, butt-coupling, and 1D-OMC, the n_{p} power law is in the range [0.3,0.33] corresponding to α in the range [2, 2.3]. However, device II and III show significantly different power law of 0.21 corresponding to $\alpha = 3.77$. We attribute this variation in α to different level of disorder in the geometry. The relation linking α and disorder in the geometry is derived in the next section. Such varying power laws have been observed in [37] which suggests that α is not necessarily equal to the dimension of the phonon bath, d, in a thin film phononic structures, and can be larger than 3 dimensions.

The κ_p power laws in the low n_a regime for Butt-coupling and 1D-OMC have been found to be in the range [0.6, 0.66], which correspond to phonon bath dimensionality of ≈ 2. For device II and III, despite having κ_p power law of 0.39 in the low n_a regime, the phonon bath dimensionality turns out to be ≈ 2 using equation 5.12. In the high power regime, the κ_p power law for all measured devices is 0.29 which could be due to a combination of 3-phonon-scattering to Akhiezer damping model [55]. Further studies are needed to understand κ_p power laws in the high power regime and will be the subject of future work.

5.3 Relation between disorder and hot bath power laws

Recent theoretical studies on two-dimensional phononic crystals have shown that phonon interference, arising either from the periodicity of holes [37, 56] or from lo-

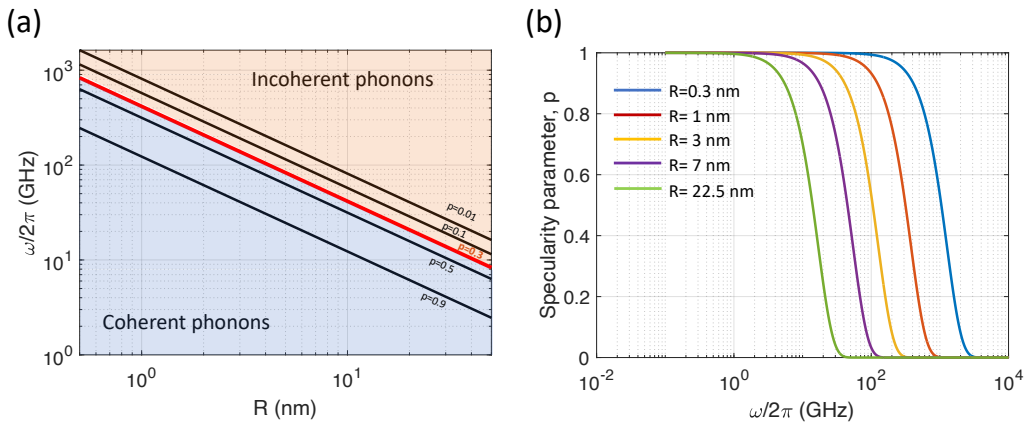

Figure 5.3: **Coherent and incoherent phonon regimes. a,** Phonon frequency as a function of characteristic imperfection R (including surface roughness, hole wall roughness, and lattice site disorder) for selected values of the specularity parameter p, ranging from 0.01 to 0.90. The blue shaded region indicates the coherent phonon regime, assuming a sharp threshold at $p = 0.3$ (shown as a red solid line). The red shaded region corresponds to the incoherent phonon regime. **b,** Specularity parameter p as a function of phonon frequency for selected values of surface roughness. The transition from fully diffusive scattering ($p = 0$) to fully specular scattering ($p = 1$) occurs over a broad range of phonon frequencies.

cal resonances in pillars [57, 58, 59], can affect the entire phonon spectrum, leading to a reduction in both the phonon group velocity and the density of states. Experimental studies at sub-kelvin temperatures further demonstrate that when phonon wavelengths are sufficiently long compared to the characteristic disorder in the geometry, thermal conductance can be controlled by phonon interference to a large extent [37, 60, 38].

To understand how phonon transport affects the observed power-law dependence of n_p on n_a, we begin with Planck's law, $T_p \propto n_a^{1/(\alpha+1)}$, where α corresponds to the effective number of spatial dimensions of the material or structure under consideration, as discussed in the previous section. In periodically patterned thin-film structures such as phononic crystals, phonon transport can be categorized into two distinct regimes: coherent and incoherent (ballistic). Coherent phonon transport occurs when the phonon phase is preserved throughout propagation. In contrast, at higher phonon frequencies, imperfections in the crystal, such as surface roughness or lattice site disorder-induced scattering, causing incoherent transport to dominate.

We define a specularity parameter p, which provides a quantitative measure of the fraction of specular (non-diffusive) phonon scattering at a surface with a given

roughness. A value of $p = 1$ corresponds to purely specular scattering, while $p = 0$ corresponds to purely diffusive scattering. The relation between the phonon frequency ω, the characteristic imperfection scale R, and the specularity parameter p is studied in Ref. [39, 61] as:

$$p(\omega)\big|_R = \exp\left[-16\pi^3\left(\frac{R}{2\pi v_l/\omega}\right)^2\right], \tag{5.13}$$

here the velocity of sound in silicon is $v_l = 8433$ m/s, and R represents the imperfections from both surface roughness σ_{eff} and lattice site disorder δ [38]:

$$R = \sqrt{\sigma_{\text{eff}}^2 + \delta^2} \tag{5.14}$$

Figure 5.3a shows the phonon frequency ω as a function of R for different values of the specularity parameter p. Cross sections of p versus ω for selected values of R are shown in Fig. 5.3b, illustrating a gradual transition from coherent to incoherent phonon transport, with p decreasing from 1 to 0 across a broad range of phonon frequencies. For simplicity, however, we adopt a sharp threshold at $p = 0.3$, following the approach in Refs. [39, 38]:

$$\frac{\omega_{\text{co}}}{2\pi}(p = 0.3, R) = 0.0493 \times \frac{v_l}{R}, \tag{5.15}$$

Note that this cutoff frequency is not the same as the dimensional crossover frequency (~ 20 GHz) associated with the transition from 2D to 3D density of states due to the finite device layer thickness ($t = 220$ nm).

Equation 5.15 can also be interpreted in terms of the phonon wavelength, using $\lambda = 2\pi v_l/\omega_{\text{co}}$. Phonons with wavelengths $\lambda \gtrsim 20R$ contribute to coherent transport, while phonons with $\lambda \lesssim 20R$ are more likely to undergo scattering and contribute to incoherent transport.

In one-dimensional optomechanical crystal (1D-OMC) geometries, the optomechanical defect is engineered by modulating both the unit cell length and the dimensions of the elliptical holes. This modulation introduces *intentional* disorder in the structure ($R \gtrsim 20$ nm) from the perspective of phonon transport, thereby reducing the cutoff frequency to approximately $\omega_{\text{co}} \sim 20$ GHz. This results in predominantly incoherent phonon transport across much of the phonon spectrum.

In contrast, in two-dimensional optomechanical crystals (2D-OMCs), the unit cell length remains fixed, and only the fishbone dimensions are modulated to define

the defect. As a result, the structural disorder is confined to a narrow linear defect region, while the lattice remains periodic in the direction perpendicular to the defect. This geometry can support a much higher cutoff frequency, provided the surface roughness remains low, thereby preserving coherent phonon transport over a broader range of the phonon spectrum.

Next we study the power emitted by coherent and incoherent phonons. We assume that a 'heater' is placed at the center of a phononic crystal which mimics the function of the optical-absorption induced hot bath in the optical mode volume. The expression for power emitted in the coherent regime is given by [62]

$$P(T_p) = \frac{1}{2\pi^2} \sum_j \int_{\gamma'} d\gamma \int_K dk\, \hbar\omega_j(\mathbf{k}) n(\omega_j, T_p) \left(\frac{\partial \omega_j(\mathbf{k})}{\partial \mathbf{k}} \cdot \hat{\mathbf{n}}_\gamma \right) \Theta \left(\frac{\partial \omega_j}{\partial \mathbf{k}} \cdot \hat{\mathbf{n}}_\gamma \right), \tag{5.16}$$

where $\omega_j(\mathbf{k})$ is the calculated PnC band structure in the first 2D BZ K, $n(\omega_j, T)$ is Bose–Einstein distribution, and only positive group velocities $\frac{\partial \omega_j}{\partial \mathbf{k}}$ with respect to the heater boundary surface normal $\hat{\mathbf{n}}_\gamma$, contribute to the emitted power, taken into account by the step function Θ.

On the other hand, the power emitted by phonons per unit cross-sectional area in the incoherent regime is given by [62]

$$\frac{P}{A} = \frac{f}{4} \langle \tau \rangle \sum_i \int d\omega\, c_i\, \rho_i[\omega]\, \hbar\omega\, (n_1[\omega] - n_2[\omega]), \tag{5.17}$$

where f is the fraction of incoherent phonons, the sum runs over the two transverse and one longitudinal bulk-phonon modes with speed of sound c_i, $\rho_i[\omega]$ is the density of states (DOS) for mode i, and $n_{1,2}[\omega]$ are the Bose-Einstein distributions corresponding to the hot bath (at temperature T_p) and the cold bath (at 10 mK), respectively. The term $\langle \tau \rangle$ denotes the average phonon transmission probability through the lattice, which can be evaluated using Monte Carlo simulations of phonon diffusion.

For the purpose of determining the power-law dependence on T_p, we neglect the proportionality constants. In the case of 2D-OMC structures, the phonon density of states scales as $\rho[\omega] \propto \omega^{d-1} = \omega^{1.3}$, corresponding to an effective phonon bath dimensionality of $d = 2.3$. Furthermore, since $n_2[\omega] \ll n_1[\omega]$ for the relevant temperature range, we can neglect the contribution from the cold bath. The emitted power per unit area then simplifies to

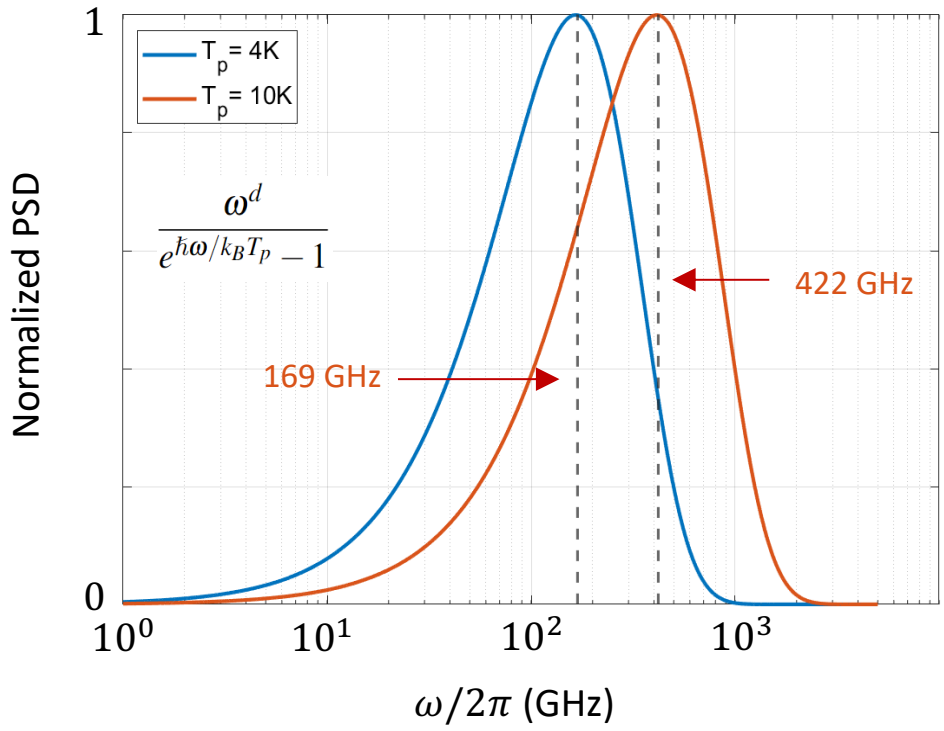

Figure 5.4: **Power spectral density for incoherent phonon transport.** Normalized power spectral density for $T_p = 4$ K (blue), and $T_p = 10$ K (red). The distribution peaks at 169 GHz and 422 GHz for the two cases, respectively.

$$P(T_p) \propto \int_{\omega_{co}}^{\infty} d\omega \, \frac{\omega^d}{e^{\hbar\omega/k_B T_p} - 1}. \tag{5.18}$$

Figure 5.4 shows the incoherent phonon spectral density, corresponding to the integrand in equation 5.18, for $T_p = 4$ K (blue) and $T_p = 10$ K (red). The dominant phonon frequencies for these temperatures are approximately 169 GHz and 422 GHz, respectively.

The total power emitted is the sum of contributions from both coherent and incoherent phonons, as described by equations 5.16 and 5.18. However, it has been shown that phononic crystal structures significantly modify the phonon bandstructure, reducing the group velocities by a factor of 3 to 5. Moreover, the thermal conductance due to coherent phonons in phononic crystals is reduced by up to two orders of magnitude compared to a pure silicon slab without phononic patterning [37, 38].

For these reasons, in this work we consider only the contribution of incoherent phonons, specifically those with frequencies above the cutoff frequency $\omega_{co}/2\pi$, to

the thermal conductance.

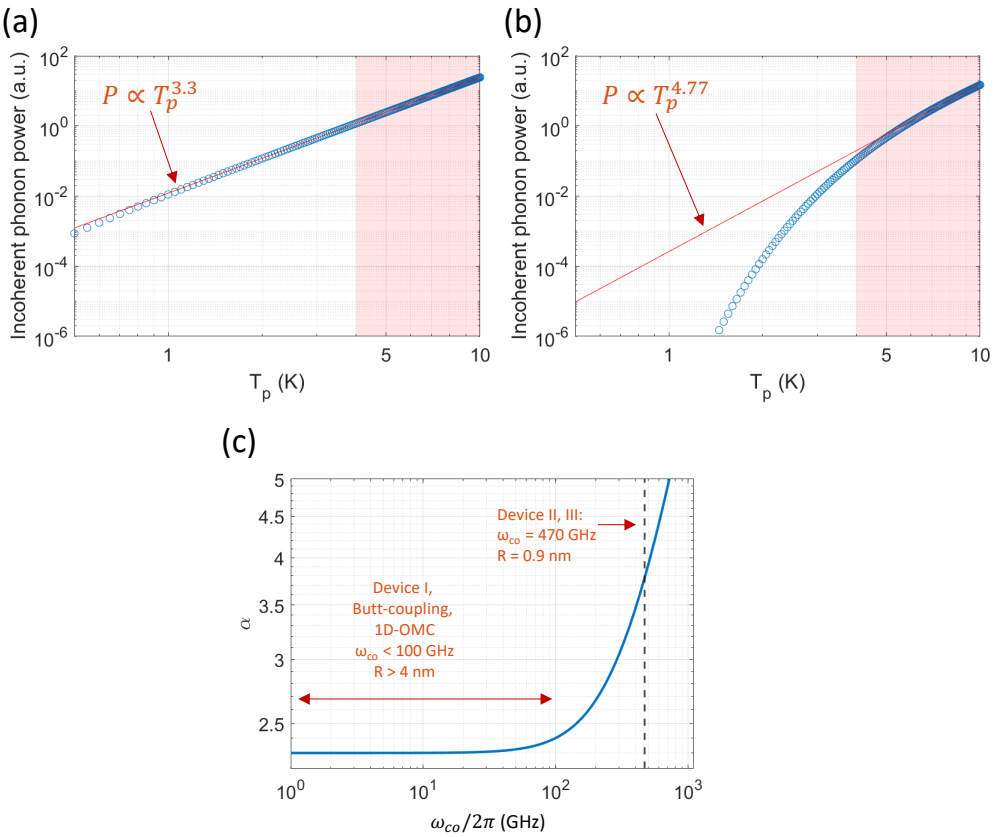

Figure 5.5: **Dimensionality for incoherent phonon transport.** Power emitted by incoherent phonons as a function of T_p for cutoff frequencies ω_{co} = **a,** 20 GHz and **b,** 466 GHz. The blue dots represent the results of numerical integration of Equation 5.18, while the red curves show power law fits over the temperature range highlighted in red. The red shaded regions indicate the relevant T_p range where experimental data for n_p is available. **c,** Extracted exponent α as a function of cutoff frequency ω_{co}. For Device I, the butt-coupling device, and the 1D-OMC, the measured value of $\alpha \approx 2.3$ suggests a cutoff frequency below 100 GHz, corresponding to $R > 4$ nm. For Devices II and III, the measured value $\alpha = 3.77$ implies a cutoff frequency of approximately 470 GHz, corresponding to $R = 0.9$ nm.

To evaluate the dependence of emitted power on T_p, we numerically integrate equation 5.18. Figures 5.5a and 5.5b display the resulting power versus temperature curves (blue dots), alongside power law fits (red curves) in the temperature range of 4 to 10 K, where experimental data for n_p is available (Fig. 4.3). From these fits, we extract exponents $\alpha + 1 = 3.3$ and 4.77, which correspond to cutoff frequencies of $\omega_{\mathrm{co}}/2\pi = 20$ GHz and 470 GHz, respectively.

The exponent $\alpha = 2.3$ in panel (a) aligns with the experimentally observed value for device I, while $\alpha = 3.77$ in panel (b) matches the value measured for device II and III. Figure 5.5c summarizes this relationship by showing the extracted exponent α as a function of cutoff frequency. Notably, for cutoff frequencies below 100 GHz, α remains approximately constant at 2.3, corresponding to characteristic roughness values $R > 4$ nm.

Previous measurements on one dimensional optomechanical crystals (1D-OMCs) reported in Ref. [36] consistently showed a power law scaling of $\alpha \sim 2$ across several devices. This behavior can be attributed to the presence of intentional disorder with $R \gtrsim 20$ nm, which significantly reduces the cutoff frequency below 100 GHz. In this regime, as indicated by Figure 5.5c, the exponent α becomes largely insensitive to variations in roughness.

For device I and the butt-coupling device, we estimate that the effective disorder $R > 4$ nm likely arises from non-optimal electron beam path (aka fracturing) during the lithography process. In contrast, device II and III exhibit a significantly higher cutoff frequency of 470 GHz, corresponding to an estimated roughness value of $R = 0.9$ nm. We note that the sidewall roughness in our devices is typically below 1 nm, which we attribute to the use of Piranha surface treatment. This may explain the extremely low disorder inferred for devices II and III.

Table 5.2 summarizes the measured values of α, as well as the estimated roughness R and cutoff frequency ω_{co}, for each device.

Device	n_p power law	α	Estimated R (nm)	$\omega_{co}/2\pi$ (GHz)
Device I	0.31	2.2	> 4	< 100
Device II	0.21	3.77	~ 0.9	470
Device III*	0.21	3.77	~ 0.9	470
Butt-coupling	0.30	2.3	> 4	< 100
1D-OMC	0.33	2.0	20**	$\lesssim 20$

Table 5.2: **Comparison of n_p power law exponents, extracted hot bath dimensionality parameters α, estimated roughness values R, and corresponding cutoff frequencies $\omega_{co}/2\pi$ for various devices.** Data for the butt-coupling and one dimensional OMC devices are adapted from Refs. [28, 36].
Device III, marked with an asterisk (*), exhibited performance identical to device II and was therefore excluded from the discussion in the previous chapter.
(**) Large estimated R for 1D-OMC is *intentional* disorder due to non-periodic lattice spacing in the optomechanical defect region.

While we have provided a phenomenological explanation for the origin of the power laws governing n_p and κ_p, an open question remains regarding the magnitude of the power law curves, specifically, the variation in the product $\kappa_p \times n_p$ across different devices, as shown in Figure 4.5c.

One possible explanation for the reduced value observed in device II is that the higher cutoff frequency $\omega_{\mathrm{co}} = 470\,\mathrm{GHz}$ leads to poorer thermalization between the hot bath and the acoustic mode of interest. While the hot bath modes rapidly thermalize among themselves at a rate $\kappa_{\mathrm{mix}} \gg \kappa_p$, increasing ω_{co} reduces the coupling between the hot bath and the acoustic mode, thereby suppressing the overall heating rate quantified by $\kappa_p \times n_p$.

This observation highlights a broader goal of the present mesoscopic study: identifying strategies to mitigate heating of the acoustic resonator induced by optical absorption. One promising approach involves increasing the cutoff frequency ω_{co}, which may reduce the coupling between the hot phonon bath and the acoustic breathing mode at 10.3 GHz. However, achieving a high ω_{co} requires extremely low levels of geometric disorder. This introduces a fundamental tradeoff, as optomechanical crystals inherently rely on intentional geometric modulation to localize both optical and acoustic modes. An alternative strategy may involve reducing the thickness of the silicon geometry below 220 nm, which could increase the discreteness of phonon modes below ω_{co}, thereby further suppressing coupling to the hot bath above the cutoff. A systematic experimental and theoretical investigation of these hypotheses represents a natural next step in the development of low-noise optomechanical systems.

5.4 Summary

In this chapter, we investigated the origins of the hot bath from a mesoscopic perspective. By analyzing the power-law dependence of hot bath occupancy n_p on intracavity photon number n_a, we extracted the effective dimensionality parameter α for various device geometries. Numerical integration of the incoherent phonon power spectrum revealed how α depends on the cutoff frequency ω_{co}, which is determined by the characteristic disorder scale R. We found that for cutoff frequencies below 100 GHz, corresponding to $R \gtrsim 4\,\mathrm{nm}$, α saturates near a value of 2.3. These results are consistent with previous observations in one-dimensional optomechanical crystals, where intentional disorder of $R \gtrsim 20\,\mathrm{nm}$ leads to a consistent power-law behavior with $\alpha \approx 2$ across multiple devices. In contrast, two-dimensional devices

exhibit reduced intentional disorder, making α more sensitive to variations in R, and leading to a wider range of observed α values. Together, these findings provide a quantitative framework for understanding phonon-mediated heat transport in engineered nanostructures and suggest potential strategies for mitigating acoustic resonator heating in next-generation optomechanical devices.

Chapter 6

DESIGN OF PIEZO-OPTOMECHANICAL TRANSDUCER WITH 2D OPTOMECHANICAL CRYSTALS

6.1 Introduction

The field of microwave-to-optical transduction has made significant progress over the past decade. Several research groups around the globe are working towards a common goal of generating entanglement between superconducting qubits mediated by optical photons. Practical architectures for such tasks involve heralded schemes [63], where only successful transduction events are used, yet these protocols still demand high efficiency and low added noise to be practical for scalable quantum computing. Steady progress toward these goals has been made using a range of physical platforms, including electro-optic transducers [64, 65, 66, 67, 68, 69, 70, 71], electro-optomechanics [72, 73, 51, 74, 33], rare-earth ion systems [75, 76, 77], magnons [78], and piezo-optomechanics [79, 32, 80, 49, 50].

Among these, piezo-optomechanical platforms have emerged as especially promising due to their compact footprint and ability to realize large coherent coupling rates. Recent demonstrations include non-classical correlations between microwave and optical photon pairs [48] and even Bell state generation [80]. However, all implementations to date have relied on one-dimensional (1D) OMC geometries, which, as discussed in the previous chapters, are susceptible to significant optical absorption-induced heating. This motivates the exploration of piezo-optomechanical transducers based on two-dimensional OMCs, which may offer improved thermal performance and design flexibility.

In this chapter, we present the detailed numerical design of a 2D-OMC-based piezo-optomechanical transducer. We will address the critical considerations for achieving efficient, low-noise microwave-to-optical conversion, focusing on the choices of geometry, materials, and mode hybridization.

The design of each cavity region must satisfy distinct and often competing requirements. The optomechanical cavity must maximize the optomechanical coupling rate g_{OM}, preserve high optical and acoustic quality factors, and ensure strong spatial overlap between the confined modes. In contrast, the piezo-acoustic cavity must provide efficient coupling between the microwave and acoustic domains by

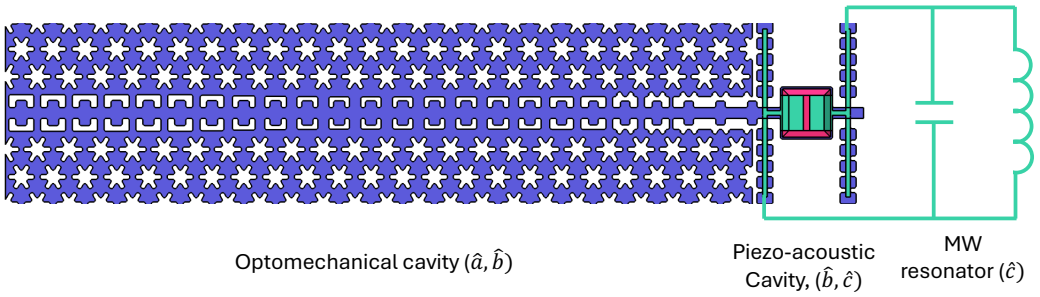

Figure 6.1: **Geometry of piezo-optomechanical transducer with 2D OMC.** Schematic of the transducer device used in this work. The device comprises two primary regions: the *piezo-acoustic cavity*, which enables coupling between the acoustic mode ($\hat{b}$) and the microwave electric field ($\hat{c}$), and the *optomechanical cavity*, which mediates coupling between the acoustic mode ($\hat{b}$) and the optical field ($\hat{a}$). These two regions are connected by a phonon waveguide, forming a hybridized acoustic "supermode."

optimizing the piezoelectric coupling rate g_{pe}, while also minimizing microwave loss and suppressing spurious crosstalk. The phonon waveguide connecting the two cavities plays a central role in enabling coherent energy exchange by hybridizing the acoustic mode $\hat{b}$ across both regions. It must be carefully engineered to support this hybridization without introducing additional loss channels or unwanted mechanical modes. Figure 6.1 illustrates the optimized transducer geometry. In the following sections, we will examine the design and function of each component individually, followed by the global optimization of the complete transducer system.

6.2 Optomechanical cavity design

Unlike the purely optomechanical design discussed in Chapter 3, where both optical and acoustic modes are confined by mirror regions exhibiting simultaneous bandgaps, the transducer geometry requires the acoustic mode to couple to a piezoelectric microwave mode. This coupling is engineered via a single-mode phonon waveguide.

Figure 6.2(a) illustrates the optomechanical cavity layout, which comprises four distinct regions: the mirror region, the localized defect, the phonon waveguide, and the phonon mode filter. Figures 6.2(b), (c), and (d) show the corresponding unit cell designs and their dimensions for the snowflake and fishbone structures. The snowflake unit cells are fixed with parameters $(a, r, w) = (500, 205, 75)$ nm, while the fishbone unit cell parameters (h_i, w_i, h_0, w_0) are gradually varied across the cavity to localize and enhance the optical and acoustic modes.

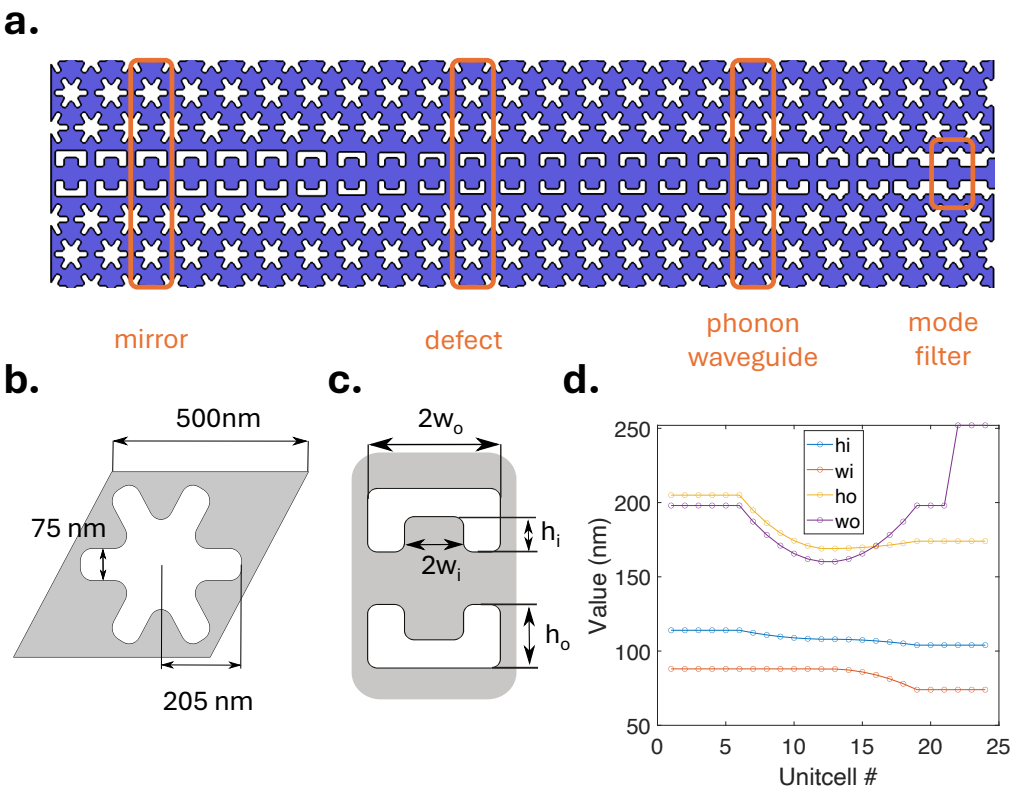

Figure 6.2: **Optomechanical cavity design of the transducer. a.** Optomechanical cavity structure showing unit cells for the mirror, localized defect, phonon waveguide, and acoustic mode filter. **b.** Unit cell of the snowflake. **c.** Fishbone unit cell engineered to maximize the optomechanical interaction rate. **d.** Spatial variation of the fishbone unit cell dimensions across the optomechanical cavity.

Figures 6.3(a) and (b) show the optical and acoustic band structures for the mirror and phonon waveguide unit cells, respectively. The mirror cell is designed to exhibit simultaneous acoustic and optical bandgaps for modes with specific symmetries, consistent with the purely optomechanical architecture. The target optical and acoustic modes are highlighted by solid red lines, which define one edge of the bandgap, while dashed red lines mark the opposite edge. Solid black lines denote other symmetry modes, which typically do not couple to the mode of interest unless symmetry breaking occurs due to fabrication-induced disorder.

The phonon waveguide retains the optical bandgap similar to the mirror cell while being transparent to the acoustic breathing mode at the frequency of interest, indicated by the dash-dotted green line. To suppress unwanted acoustic leakage between the fishbone and snowflake regions and the piezoelectric interface, an additional

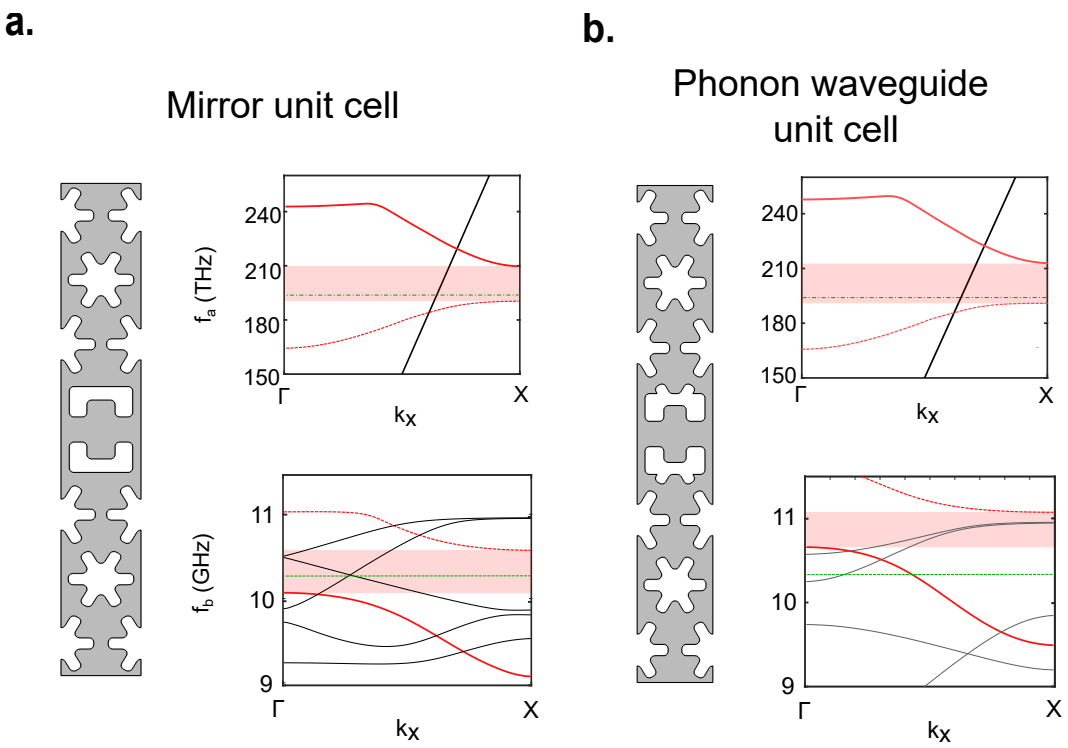

Figure 6.3: **Optomechanical bandstructure. a,** Unit cell schematic (left) for the mirror region, along with the corresponding optical (top right) and acoustic (bottom right) band structures. The solid red curves represent the bands of interest, while the dashed red lines indicate other guided modes that define the band edges. The shaded regions denote the optical and acoustic bandgaps. The dash-dotted green line represents the localized cavity mode frequency of the full optomechanical cavity. In the acoustic band structure, the bands shown in black correspond to guided modes with a different symmetry compared to the bands of interest. **b,** Unit cell schematic (left) for the phonon waveguide region, along with the corresponding optical (top right) and acoustic (bottom right) band structures. The optical bandgap remains aligned with the optical cavity mode, whereas the acoustic mode of interest (solid red) crosses the localized acoustic cavity frequency (dash-dotted green).

"bunny ear" structure is placed outside the fishbone unit cells. These structures are intentionally omitted in the defect region to enhance the optomechanical coupling rate.

Figure 6.4(a) and (b) show the optical and acoustic modes of interest in the full optomechanical geometry. The optical mode remains well-localized in the defect region, similar to the purely optomechanical crystal geometry studied in Chapter 3, whereas the acoustic mode extends into the phonon waveguide, enabling coupling to the piezoelectric cavity. The optical mode exhibits a radiation-limited quality factor of $Q \sim 10^7$ when more than six rows of snowflake mirror cells are included.

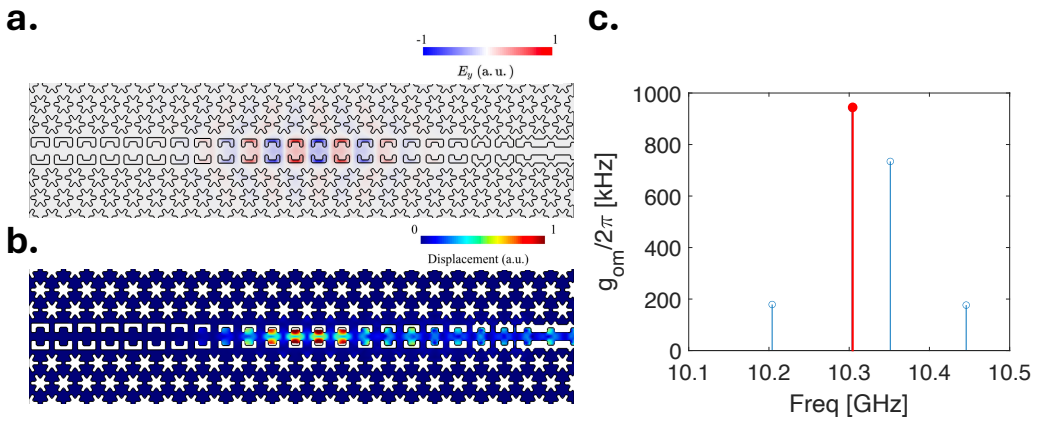

Figure 6.4: **Optomechanical mode structure.** **a,** shows the y-component of the electric field of the localized acoustic mode around 1530 nm. **b,** shows the acoustic mode of interest coupled to the phonon waveguide on the right. **c,** shows the optomechanical coupling rate $g_{\mathrm{OM}}/2\pi$ for various modes of the optomechanical structure. The mode in red corresponds to the localized mode shown in (b).

However, to reduce computational overhead, we simulate only three unit cells in the presented geometry.

Figure 6.4(c) shows the simulated acoustic mode spectrum of the geometry. The mode highlighted in red corresponds to the acoustic mode shown in panel (b) and exhibits the highest optomechanical coupling rate, with $g_{\mathrm{OM}}/2\pi = 950\,\mathrm{kHz}$. This value is lower than that observed in the purely optomechanical geometry, as the acoustic mode extends into the phonon waveguide, thereby reducing its spatial overlap with the optical mode.

6.3 Piezo-acoustic cavity design

The piezo-acoustic cavity facilitates conversion between microwave photons and acoustic phonons using piezo-electric effect as introduced in chapter 2. Various piezoelectric materials have been explored for this purpose such as Lithium Niobate, Aluminum Nitride, Gallium Phosphide, Gallium Arsenide etc. Here, we utilize Aluminum Nitride (AlN) which provides high enough piezo-electric coupling rates and is easier to fabricate. Figure 6.5a shows the piezo-acoustic cavity part of the transducer. It consists of the base 220 nm Silicon device layer, 200 nm thick AlN and 20 nm Niobium Nitride (NbN) electrodes. The AlN is etched at 57^{o} angle wrt the horizontal which is the natural etch direction for C-cut AlN [81]. Optimized dimensions of the geometry are $(\mathrm{w_x}, \mathrm{w_y}, \mathrm{w_0})$ = (760, 760, 169) nm.

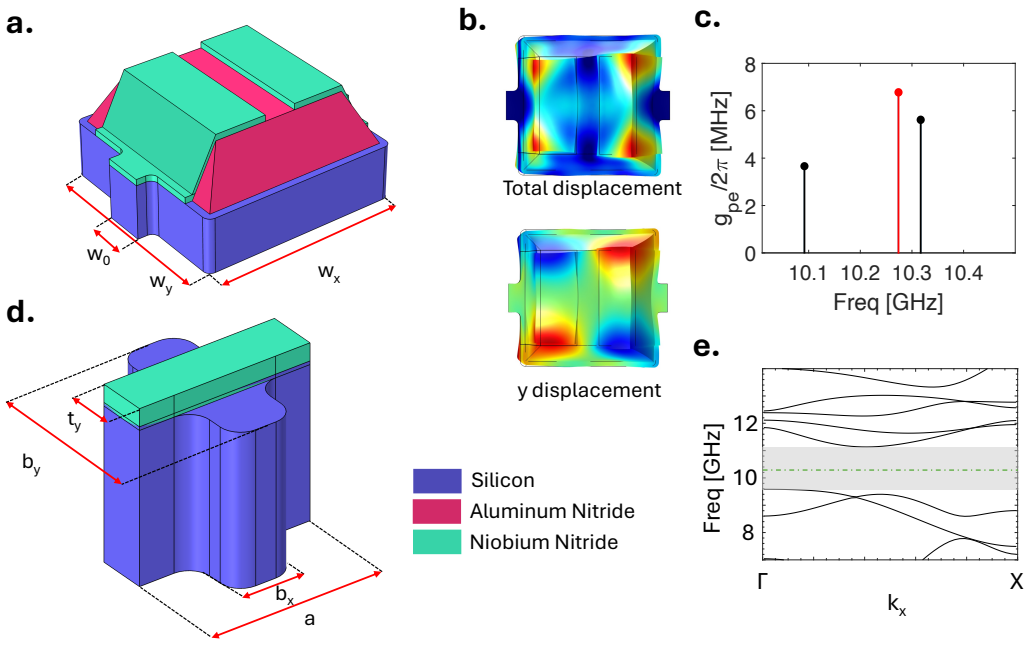

Figure 6.5: **Piezo-acoustic cavity. a,** Piezo-acoustic cavity design showing silicon-piezo-electrode stack. Piezo is made of Aluminum nitride (AlN) and has a thickness of 200nm, and $w_x = w_y = 760$ nm. The electrodes are made of 25 nm thick Niobium nitride (NbN). **b,** displacement profile for the acoustic mode of interest that hybridizes with the OMC mode of interest. the top panel shows the total displacement profile where as the bottom panel shows the y-displacement profile. **c,** Piezoelectric coupling rate, $g_{\text{pe}}/2\pi$, for different acoustic modes of the piezo-acoustic cavity. The mode of interest shown in (b) is highlighted in red and has a $g_{\text{pe}}/2\pi \approx 7$ MHz assuming it is coupled to a high impedance resonator with $C_{\text{res}} = 4.3$ fF from Fig.6.7. **d,** phononic shield used for running NbN wires with suppressed acoustic radiation loss. The geometry is optimized to have a bandgap around 10.3 GHz. The optimized values of $(a, b_x, b_y, t_y) = (252, 90, 232, 70)$ nm. **e,** Bandstructure for the phononic shield with NbN wire on top. The bandgap is centered at 10.36 GHz and has a size of 1.55 GHz

Figure 6.5(b) shows the total displacement profile (top) and the y-displacement component (bottom) of the acoustic mode of interest in the piezoacoustic cavity. The y-component exhibits a second-order breathing mode pattern, enabling strong hybridization with the breathing mode of the optomechanical cavity.

As introduced in Chapter 2, the microwave photon–phonon piezoelectric coupling can be expressed as:

$$g_{\mathrm{pe}} = \frac{\omega_b}{4\sqrt{2U_bU_{\mathrm{c}}}} \int_{\mathrm{piezo}} \mathbf{D}_b \cdot \mathbf{E}_{\mathrm{c}}\, dV,$$

where ω_b is the acoustic mode frequency, $\mathbf{D}_b$ is the electric displacement field associated with the acoustic mode, and $\mathbf{E}_{\mathrm{c}}$ is the electric field of the microwave resonator. The integral is taken over the piezoelectric region, and the fields are normalized to their respective zero-point energies, $\hbar\omega_b/2$, giving rise to the prefactor preceding the integral.

The electrodes are placed on the left and right sides of the piezoelectric region, generating an electric field primarily along the x-direction. Due to the symmetric nature of the y-displacement component, its overlap with the applied electric field, and hence the piezoelectric coupling along y, vanishes. Nonetheless, the y-component is essential for mechanical hybridization with the OMC breathing mode. The dominant piezoelectric coupling arises from the x- and z-components of the total displacement profile.

The term U_b denotes the total acoustic energy stored in the piezo-acoustic cavity, while the total electrostatic energy of the microwave mode is given by:

$$U_{\mathrm{c}} = \frac{1}{2}(C_{\mathrm{res}} + C_{\mathrm{pa}})V_0^2,$$

where V_0 is the zero-point voltage across the loaded microwave resonator. For these calculations, we assume a resonator capacitance of $C_{\mathrm{res}} = 4.3$ fF and a piezo-acoustic electrode capacitance of $C_{\mathrm{pa}} = 0.09$ fF, as discussed in Section 6.7.

Figure 6.5(c) shows the acoustic mode spectrum and the corresponding piezoelectric coupling strengths $g_{\mathrm{pe}}/2\pi$. The mode highlighted in red corresponds to the mode shown in panel (b), and achieves a coupling rate of approximately $g_{\mathrm{pe}}/2\pi \approx 7$ MHz. Figure 6.5(d) shows the phononic shield design used to route electrical wires away from the piezo-acoustic cavity. This structure enables electrical interfacing while minimizing acoustic leakage. The phononic shield consists of alternating silicon blocks and tethers, with NbN routed over the tether elements.The optimized dimensions of the unit cell are given by $(a, b_x, b_y, t_y) = (252, 90, 232, 70)$ nm, which

result in the phononic bandgap shown in Figure 6.5(e). The bandgap is centered at 10.36 GHz and spans a width of 1.55 GHz.

6.4 Full mode structure

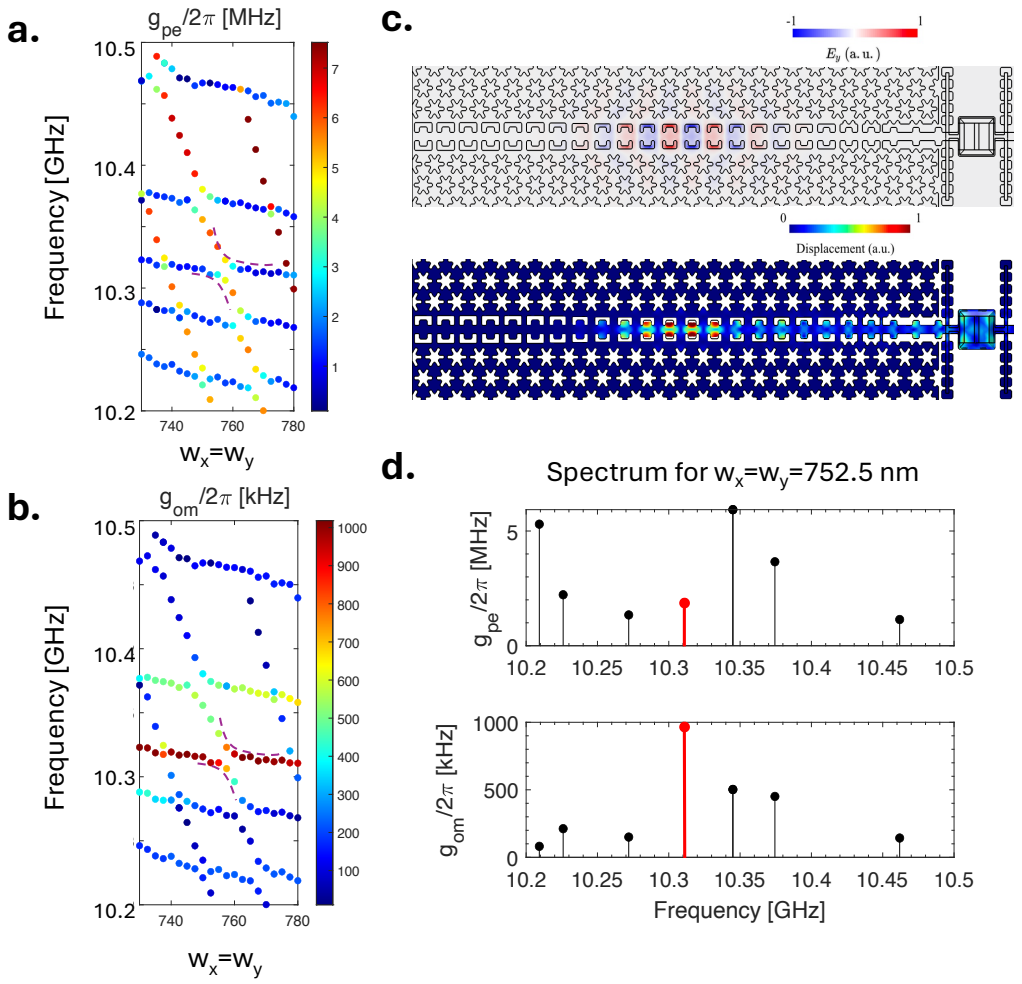

Figure 6.6: **Full transducer geometry a,** Transducer piezoelectric coupling and mode structure as a function of piezo dimension ($w_x = w_y$. Data points are colored according to $g_{pe}/2\pi$ value. Dashed lines follow the anti-crossing of the maximum $g_{OM}/2\pi$ mode **b,** Transducer optomechanical coupling and mode structure as a function of piezo dimension $w_x = w_y$. Data points are colored according to $g_{OM}/2\pi$ value. Dashed lines follow the anti-crossing of the maximum $g_{OM}/2\pi$ mode. **c,** Optical and acoustic mode of interest for the full geometry. The piezo dimensions are $w_x = w_y = 752.5$ nm. **d,** Full mode structure for $w_x = w_y = 752.5$ nm. The mode of interest is represented in red with $g_{OM}/2\pi \approx 950$ kHz and $g_{OM} \approx 1.9$ MHz.

After having designed the optomechanical and piezo-acoustic cavities, we analyze the full geometry where the acoustic modes in the two regions hybridize. To assess

the extent of this hybridization, we sweep the lateral dimensions of the piezo box such that the frequencies of the piezo-acoustic cavity cross the acoustic spectrum of the optomechanical cavity shown in Figure 6.4c. The results are presented in Figure 6.6a and b, where the box dimensions ($w_x = w_y$) are swept from 725 nm to 780 nm. We plot the coupling rates $g_{\mathrm{OM}}/2\pi$ and $g_{\mathrm{pe}}/2\pi$ as a function of box size. These plots reveal clear avoided crossings between the piezo modes and optomechanical modes, with one such crossing highlighted by dashed lines. The avoided crossing provides a measure of the phonon-mediated coupling strength between the optomechanical and piezo-acoustic modes of interest, estimated to be $g_{\mathrm{wg}} \approx 10\,\mathrm{MHz}$.

Figure 6.6(c) shows the optical and acoustic modes of interest in the full transducer geometry for a box size of $\mathrm{w_x} = \mathrm{w_y} = 752.5$ nm. The optical mode remains localized within the optomechanical region, whereas the acoustic mode forms a hybridized "supermode" that spans both the optomechanical and piezoacoustic regions. The corresponding multimode acoustic spectrum for $\mathrm{w_x} = \mathrm{w_y} = 752.5$ nm is shown in panel (d), where the mode of interest appears at 10.31 GHz, indicated in red. The optomechanical coupling rate remains slightly below the 1 MHz mark, while a piezoelectric coupling rate of approximately 2 MHz is achieved.

The choice of box size $\mathrm{w_x} = \mathrm{w_y} = 752.5$ nm is based on an optimization strategy following the criteria described in [82]:

1. Maximize the optomechanical coupling rate $g_{\mathrm{OM}}/2\pi$ while maintaining the piezoelectric coupling above 1 MHz. This ensures reduced acoustic energy participation within the piezoelectric region, which, along with the metal electrodes, contributes significantly to material loss due to high acoustic loss tangents.

2. Maximize mode isolation for the mode of interest, defined as the spectral detuning from the nearest neighboring acoustic mode. For $\mathrm{w_x} = \mathrm{w_y} = 752.5$ nm, we obtain a mode isolation of approximately 35 MHz.

6.5 Kinetic Inductance tuning

As we saw before, optomechanical interaction is a 3-wave mixing process between pump ω_L, optical mode ω_a, and acoustic mode ω_b to account for frequency mismatch. In contrast, the interaction between microwave resonator and acoustic resonator is a resonant interaction requiring $\omega_c = \omega_b$ for maximal energy transfer between the two. Due to inevitable nanofabrication disorder, static frequency

mismatches can arise between these two subsystems. Therefore, it is essential to design the microwave resonator to be *tunable* in frequency to compensate for such mismatches.

In normal conductors, inductance (L) generally arises from the energy stored in the magnetic field created by current flow—this is known as the *geometric inductance* (L_{geom}), which depends solely on the physical dimensions of the conductor. However, in superconductors, current is carried by *Cooper pairs*, which are pairs of electrons moving in a correlated manner without scattering. Despite the absence of electrical resistance, Cooper pairs still have mass, so they exhibit inertia when accelerated by an electric field. This inertial response leads to an additional inductance, known as *kinetic inductance* (L_{k}), which arises from the energy stored in the motion of Cooper pairs.

In superconducting microwave resonators, frequency tunability can be achieved by exploiting this kinetic inductance, which can be dynamically tuned by applying an external magnetic field that induces a screening current I_s. The dependence of kinetic inductance on this current is captured by the relation [83]:

$$L_k(I_s) \approx L_k(0)\left(1 + \frac{I_s^2}{I^{*2}}\right), \tag{6.1}$$

where I^* is a characteristic current scale determined by the superconducting material properties and geometry, and $L_k(0)$ is the kinetic inductance in the absence of an external magnetic field. This dependence of kinetic inductance on the screening current forms the basis of tunable superconducting circuits explored in this work.

6.6 Choice of superconducting nano-wire width

At any point in a superconductor, the momentum of a Cooper pair is given by:

$$\mathbf{p} = \hbar\nabla\Theta = e^*\Lambda\mathbf{J_s} + e^*\mathbf{A}, \tag{6.2}$$

where Θ is the phase of the macroscopic wavefunction, $\mathbf{J_s}$ is the superconducting current density, $\mathbf{A}$ is the magnetic vector potential, and $\Lambda = \frac{m^*}{n^*e^{*2}}$ is a material-dependent parameter, with e^*, m^*, n^* representing the effective charge, mass, and density of Cooper pairs.

London Penetration Depth and Current Distribution: The *London penetration depth* (λ_L) characterizes how magnetic fields penetrate into a superconductor. For thin films of NbN, typical values are $\lambda_L >\approx 300\,\text{nm}$ [84]. The ratio of the wire

width w to λ_L determines how screening currents distribute in the superconducting loop:

- **For $w \gg \lambda_L$:** The current flows mainly on the *surface* (Meissner effect), and the kinetic inductance contribution is small.
- **For $w \ll \lambda_L$:** The magnetic field penetrates the entire cross-section of the wire, and the kinetic inductance dominates.

Flux Quantization and Induced Current: Integrating around a closed superconducting loop, we obtain:

$$e^* \oint_C (\Lambda \mathbf{J_s} + \mathbf{A}) \cdot d\mathbf{l} = \hbar 2\pi n = n\Phi_0, \tag{6.3}$$

where $\Phi_0 = h/e^*$ is the flux quantum.

The integral of $\mathbf{A}$ around the closed loop gives the total magnetic flux which includes the externally applied flux Φ_{ext} and the induced flux Φ_{ind} from the screening current:

$$\Phi_B = \Phi_{\text{ind}} + \Phi_{\text{ext}}. \tag{6.4}$$

Current Response and Inductance: In the limit $w \ll \lambda_L$, the current density is approximately uniform across the wire's cross-section ($\mathbf{J_s} \approx I_s/(wt)$). We then have

$$\oint_C \Lambda \mathbf{J_s}.d\mathbf{l} = \Lambda \frac{I_s}{wt} \pi D = L_k I_s, \tag{6.5}$$

where the kinetic inductance per unit length is defined as:

$$L_k = \frac{\pi \Lambda D}{wt} = L_s \frac{\pi D}{w}, \tag{6.6}$$

where $L_s = 23\,\text{pH/sq}$ is the typical sheet inductance we get for 25 nm NbN films.

For a circular loop of diameter $D = 1\,\mu\text{m}$ and width $w = 130\,\text{nm}$, the geometric inductance is $L_{\text{geom}} = \mu_0 D \left[ln\frac{16D}{w} - 2 \right] \approx 2.66\,\text{pH}$, while the kinetic inductance $L_k \approx 0.56\,\text{nH}$, showing that the kinetic inductance dominates in the thin-wire limit.

6.7 Tunable NbN resonator design

Based on the principles of tunable kinetic inductance derived in the previous section, we design $\lambda/2$ LC resonator at 10.3 GHz to enable piezoelectric coupling to the acoustic resonator. Figure 6.7 shows a schematic of this resonator, which features a

meandering ladder geometry composed of 2 μm $\times$ 1 μm rectangular loops formed from traces of width 130 nm.

The resonator is designed to achieve a fundamental mode frequency of 10.3 GHz with a self-capacitance of

$$C_{\text{res}} = 4.3 \text{ fF}$$

leading to a characteristic impedance of

$$Z_0 = \frac{1}{\omega_0 C_{\text{res}}} = 3.6\,\text{k}\Omega.$$

Nearly the entire inductance of the resonator arises from the kinetic inductance of the superconducting film. The "arms" of the resonator extend to the piezo-optomechanical device depicted in Figure 6.1. The capacitance at the piezo-acoustic resonator is $C_p = 0.09$ fF, which is negligible compared to C_{res}. The resonator is capacitively coupled to an on-chip 50 Ω coplanar waveguide (CPW) patterned in NbN and runs across to the edge of the chip. The capacitance of the CPW is increased by adding claw structures to ensure an impedance of 50 Ω.

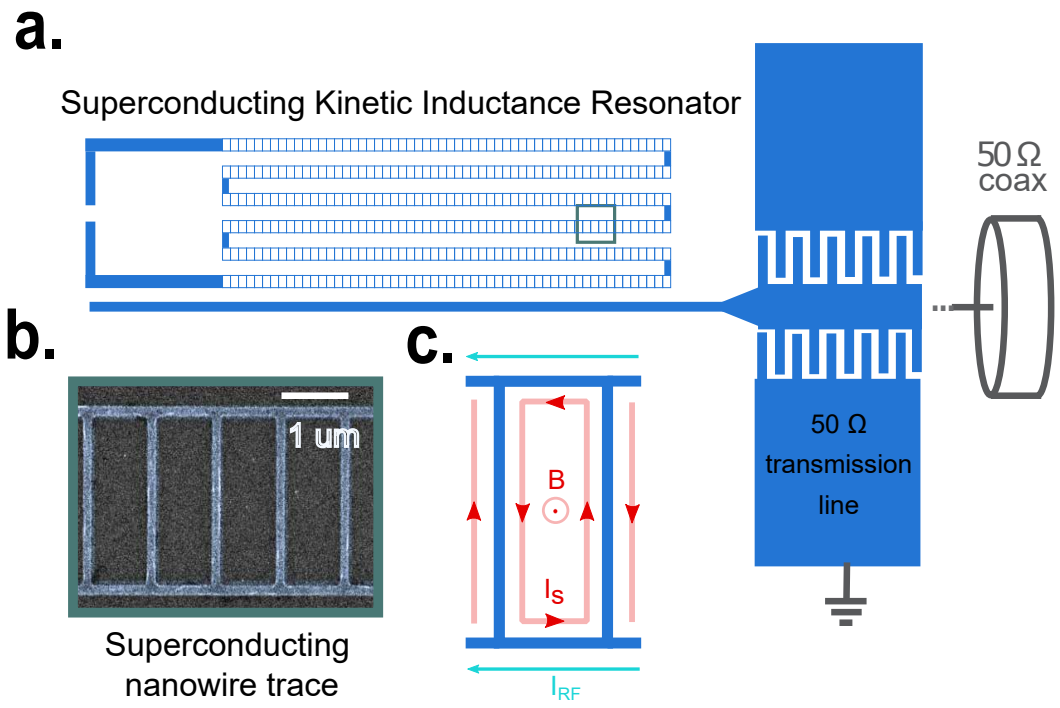

Figure 6.7: **Tunable microwave resonator. a,** Schematic of a tunable superconducting kinetic inductance resonator composed of a meandering ladder trace. The terminals of the resonator are galvanically connected to a piezo-optomechanical transducer (not shown). The resonator is capacitively coupled to a waveguide, which transitions into a transmission line. The impedance of the transmission line is matched to 50 Ω by adding claw structures to increase the capacitance. **b,** Scanning electron micrograph of the superconducting loops forming the meandering ladder trace of the kinetic inductance resonator. **c,** Unit cell of the nanowire trace, illustrating the various currents flowing through it. The cyan lines indicate the RF path, representing the microwave-frequency mode. An applied magnetic field induces a circulating DC current (red). The DC currents in the vertical traces of adjacent loops cancel due to opposing current flow in neighboring loops.

Chapter 7

FABRICATION AND MEASUREMENTS OF PIEZO-OPTOMECHANICAL TRANSDUCERS

Following the optimized design for a microwave-to-optical transducer, this chapter presents the nanofabrication process and preliminary spectroscopy results of the piezo-optomechanical transducer devices.

7.1 Fabrication of piezo-optomechanical transducers

Preparing chips for fabrication

We begin fabrication using a silicon-on-insulator (SOI) platform consisting of a 220 nm device layer, a 3 μm buried oxide (BOX) layer, and a 725 μm silicon handle wafer. In earlier generations of transducers [48, 80], a 300 nm thick AlN BOX layer was used. However, for the 2D OMC-based transducers discussed in this work, a 200 nm AlN layer was found to yield improved mode profiles and overall optical performance.

The process starts with blanket sputtering of 300 nm AlN on the SOI wafer, which is then thinned to the desired thickness via a dry etch using Ar/Cl_2 chemistry. After thinning, electron beam lithography is used to define alignment marker patterns. These are followed by deposition of a metal stack (10 nm Cr / 75 nm Au) and subsequent liftoff to leave the alignment markers in place. These preparatory steps are summarized in Figure 7.1.

AlN box fabrication

The next steps involve shaping the AlN box to the desired dimensions. From this point onward, the markers are used to align multiple electron beam lithography steps. We begin by performing electron beam lithography to define a mask. A 100 nm thick SiO_2 mask is then deposited using electron beam evaporation. This mask also protects the markers, which are prone to delamination during the subsequent BOE etch step. Next, the boxes are partially dry-etched using an Argon/Chlorine recipe, leaving approximately 25–30 nm of AlN. The remaining AlN is then wet-etched using a 25% concentrated Tetramethylammonium Hydroxide (TMAH) solution at room temperature. Finally, the SiO_2 mask is removed using a BOE solution. These steps are illustrated in Figure 7.2.

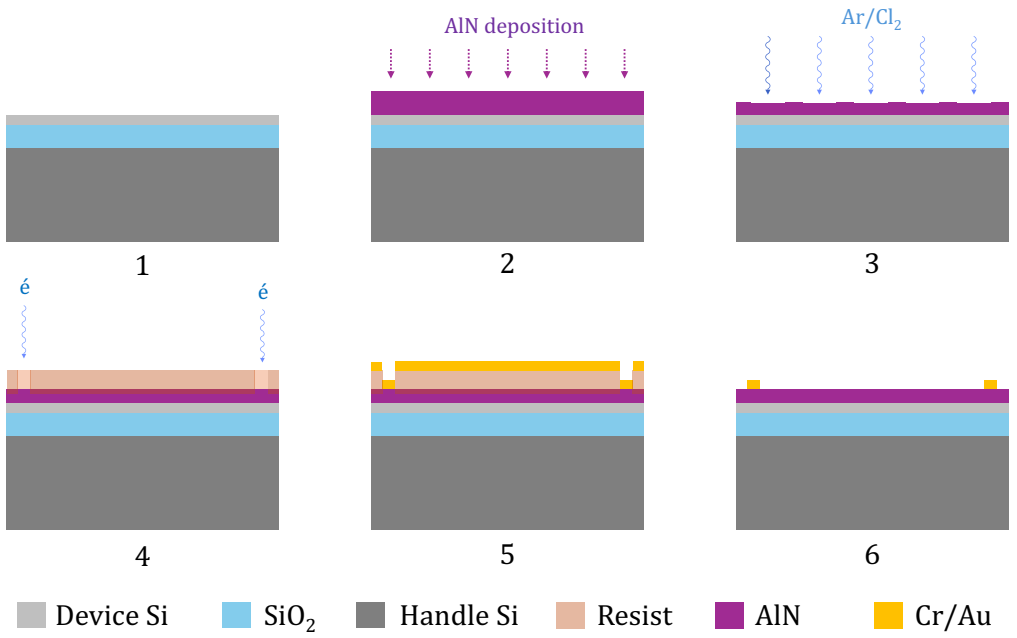

Figure 7.1: **Nanofabrication process flow for chip preparation prior to transducer fabrication.** The process includes aluminum nitride (AlN) deposition via an external vendor, subsequent thinning to the target thickness, and marker layer deposition for alignment in downstream lithography steps.

The boxes fabricated using this hybrid etch recipe (dry etch combined with wet etch) offer certain advantages compared to purely wet etch or purely dry etch processes. Figure 7.3 shows the box.

Boxes made with a purely wet etch process result in scalloped sidewall features due to the crystal-plane-dependent etch rate. These cone-like features are characteristic of anisotropic wet etching, where the etch rate varies significantly with the crystallographic orientation of the material.

In contrast, boxes fabricated using a purely dry etch process have sharper sidewall angles at the top, resulting in a more vertical profile. This dry etch process was originally developed for the first generation of transducers in our group [79] and was later adapted for the second generation [48, 80]. However, this geometry presents two main challenges:

- **Steep sidewall angle:** The sidewall profile becomes very steep near the top of the piezo box, making it difficult to achieve a galvanically continuous metal layer from the silicon surface to the top of the piezo box. To overcome this,

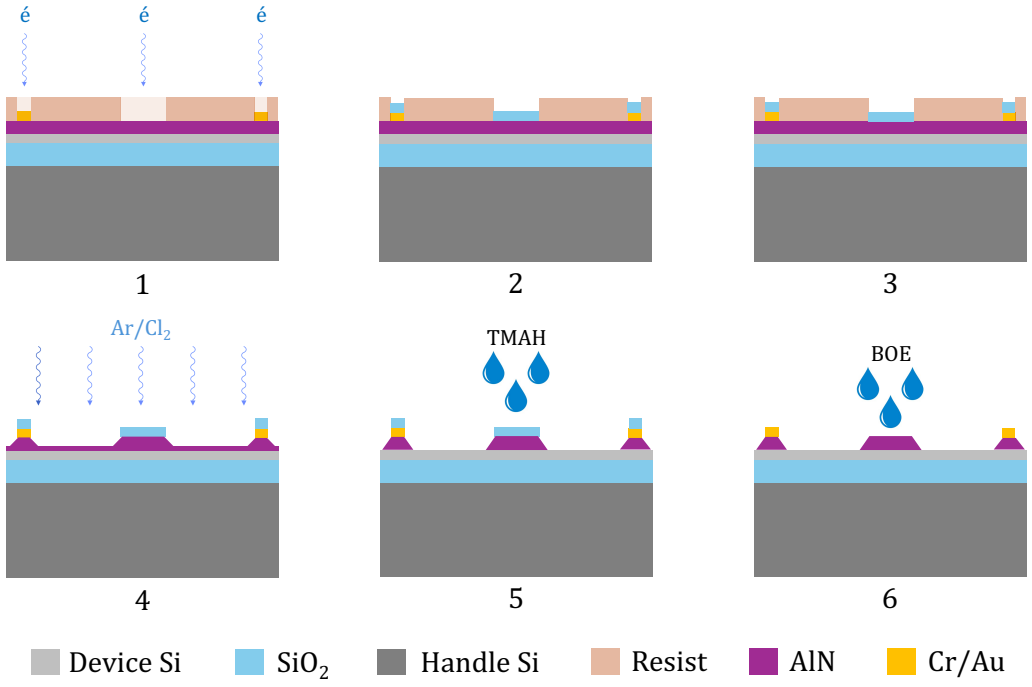

Figure 7.2: **Nanofabrication process flow for AlN box fabrication.** The process includes mask deposition and liftoff, dry and wet etch of AlN followed by mask removal.

a metal thickness of 100 nm was used in [48, 80] to ensure reliable coverage despite the challenging sidewall geometry.

- **Trench formation:** During the dry etch process, a thin trench is often etched into the silicon device layer around the piezo box, creating an additional barrier to galvanic connection from the phononic shield region to the piezo box.

The hybrid etch process addresses both of these challenges:

- **Improved sidewall profile:** The TMAH wet etch has a finite lateral etch rate, which reduces the steep sidewall angle by trimming the top of the box. This results in a more uniform sidewall angle, typically around 57 degrees, which eases metal deposition.
- **Trench-free process:** Unlike the pure dry etch, the hybrid process does not etch a trench into the silicon device layer, preserving the silicon geometry.

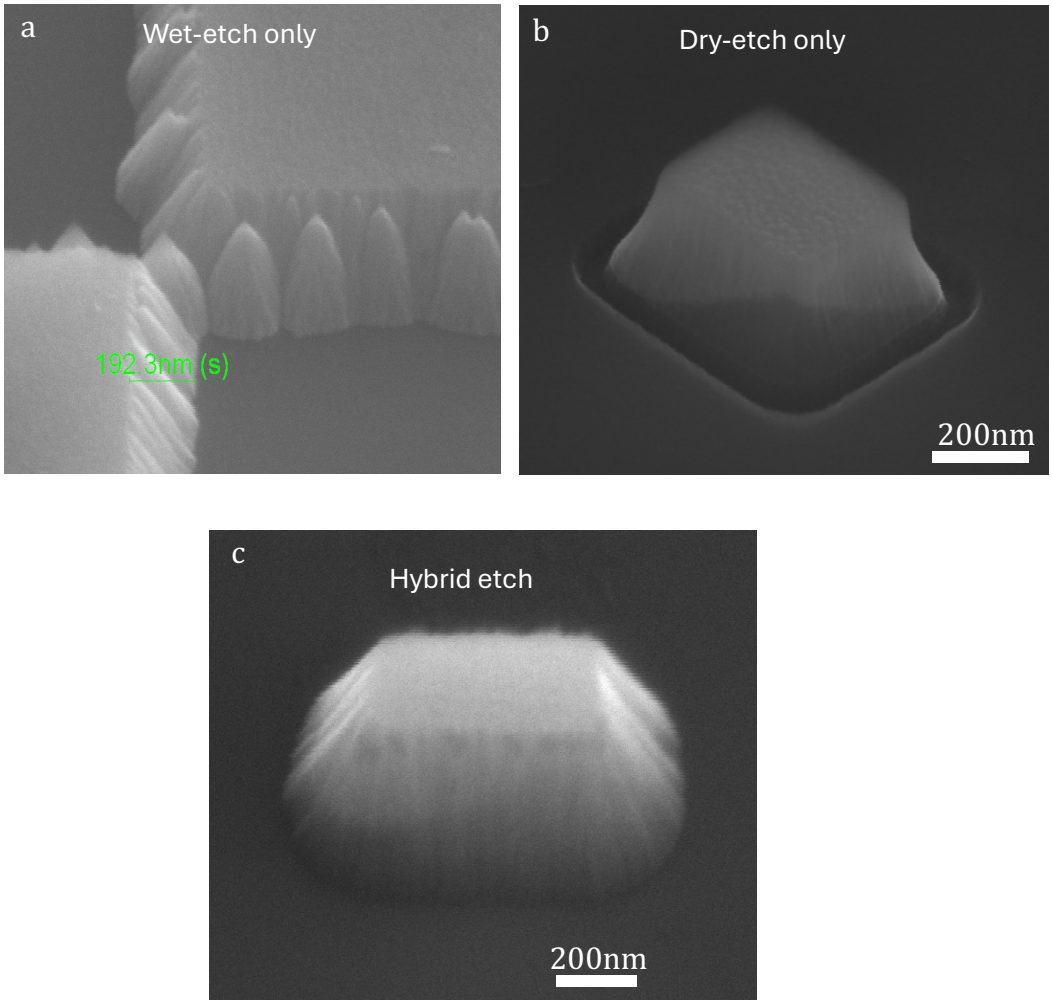

Figure 7.3: **SEM images of AlN box fabricated with different techniques. a,** Boxes made with pure wet etch using TMAH have scalloped sidewalls. **b,** Boxes made with pure dry etch results in steep sidewall angle at the top as well as trench formation. **c,** Boxes made with hybrid etch with uniform sidewall angle and trench-free silicon.

NbN deposition and resonator patterning

The NbN resonators have very small dimensions and therefore need to be defined using dry etching techniques for better repeatability. For this purpose, we use an Ar/SF_6 chemistry. The optomechanical crystal region, where sensitive optical elements reside, needs to be protected. We deposit a 100 nm thick Al_2O_3 (alumina) layer using electron beam evaporation. This step is followed by sputter deposition of a 25 nm thick NbN film. Next, electron beam lithography is used to define the resonators and electrodes, and the pattern is transferred using an Ar/SF_6 dry etching process. These steps are illustrated in Figure 7.4.

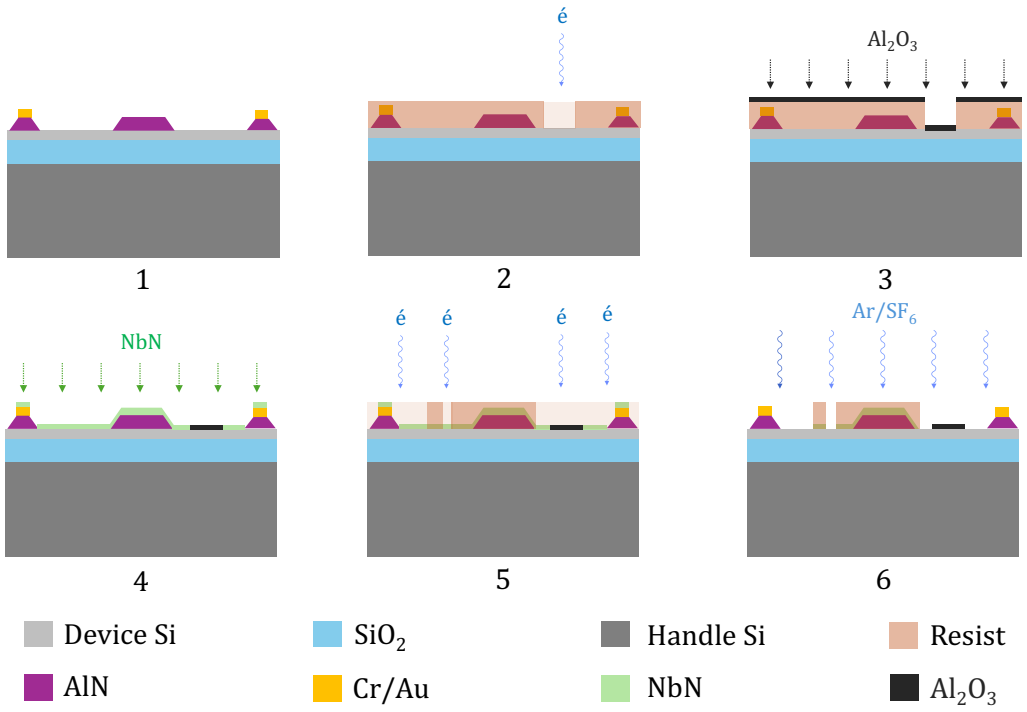

Figure 7.4: **Nanofabrication process flow for NbN resonators.** The process includes protection layer deposition for OMCs, NbN deposition followed by dry etch to define the resonators and electrodes.

Silicon patterning and DRIE

In the final step, we perform another electron beam lithography and silicon etching to define the silicon optomechanical crystals, following the recipe described in Chapter 3.

If we are fabricating devices for testing at room temperature, this step is followed by a vapor HF release to remove the underlying buried oxide layer. However, for cryogenic testing, we use a lensed fiber to couple light to the optical waveguide at the edge of the chip. This requires deep etching into the handle layer to accommodate the large diameter of the lensed fiber. To protect the rest of the chip during this deep etching, we use a photoresist (SPR-220-7) and expose only the edge of the chip using photolithography. This is then followed by sequential etching steps: SF_6/C_4F_8, O_2/C_4F_8, and SF_6 to clear the device layer, the BOX layer, and approximately 120 μm of the handle layer, respectively. These steps are illustrated in Figure 7.5.

The SEM images of the fabricated devices are shown in Figure 7.6. Panel (a) presents an optical microscope overview of a device cluster, where 16 AlN boxes are patterned with lateral dimensions swept around a nominal value of 752.5 nm. Based

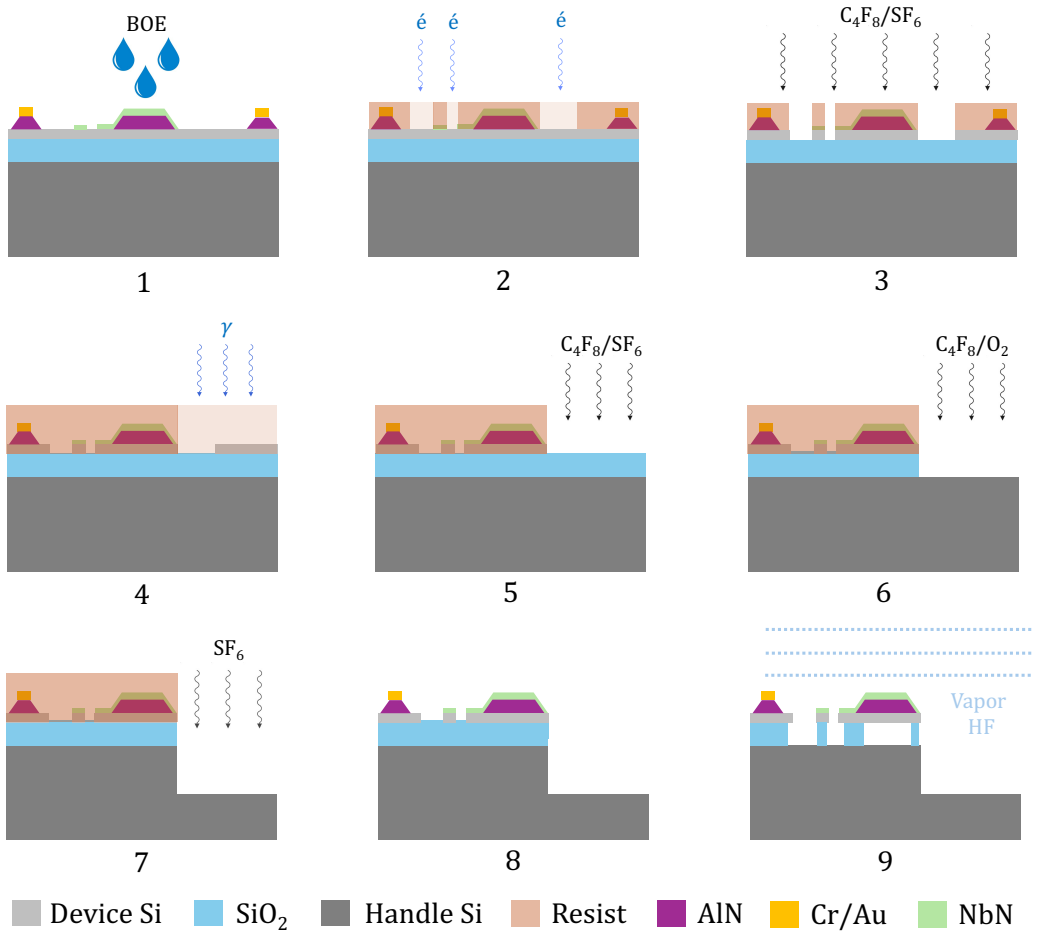

Figure 7.5: **Nanofabrication process flow for OMC and endfire coupling** The process includes silicon patterning as well as photolithography and deep etching for defining a cliff at the edge of the coupling waveguide.

on SEM imaging, four boxes are post-selected for full transducer fabrication. Only four are fabricated per cluster to minimize cross-talk between adjacent microwave resonators and to reduce mode crowding. The optical coupling port is placed approximately 1 mm laterally offset from the microwave resonator to mitigate stray light illumination.

Panel (b) shows an SEM image of a completed transducer, highlighting the connection between the microwave resonator and the piezo-acoustic cavity. The resonators are placed approximately 150 µm from the transducer. While increasing this distance could further suppress optical scattering into the resonator, it would also extend the non-loop (magnetically non-tunable) segment of the resonator arms, thereby reducing the overall frequency tunability. To mitigate stray optical guiding through

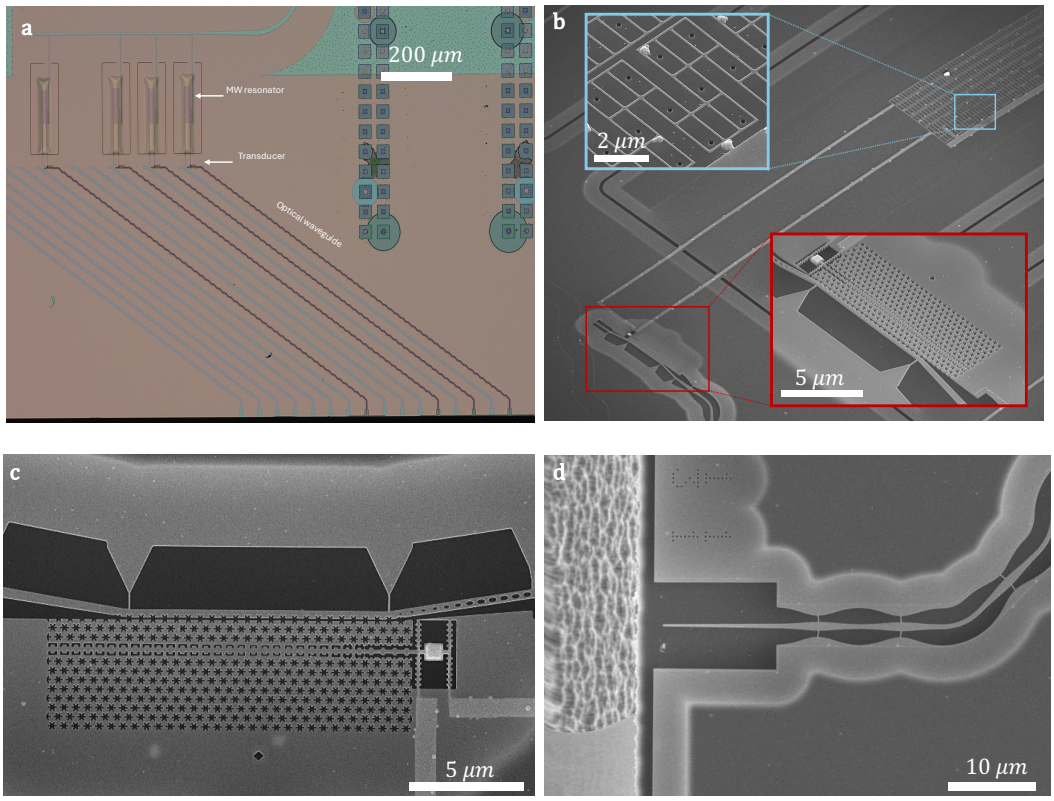

Figure 7.6: **SEM images of a 2D-OMC based microwave-optical transducer. a,** Optical microscope image showing an overview of a cluster of devices. In each cluster, 16 AlN boxes are fabricated by sweeping the lateral dimensions around a target value (752.5 nm × 752.5 nm). From this set, four boxes are selected to fabricate full transducers. The optical coupling port is laterally offset by ∼1 mm from the corresponding microwave resonator to avoid stray light illumination. **b,** SEM image of a transducer highlighting the connection between the microwave resonator and the piezo-acoustic cavity. The trenches ("canals") etched around the microwave resonator are designed to suppress stray light propagation through the device layer and mitigate its impact on microwave performance. Insets in red and cyan show zoomed-in views of the piezo-optomechanical device and microwave resonator loops, respectively. **c,** Top view of the piezo-optomechanical device, showing the side-coupled optical waveguide clamped at two points (with ∼30 nm wide tethers) to enhance mechanical stability. **d,** Tapered edge of the optical waveguide for coupling to a lensed fiber. Corrugated clamping structures improve waveguide robustness and help minimize optical insertion loss.

the silicon device layer, surrounding trenches, referred to as "canals," are etched around the resonator region. The red and cyan insets show magnified views of the piezo-optomechanical cavity and microwave resonator loops, respectively.

Panel (c) provides a top-down SEM image of the side-coupled optomechanical cavity, where the waveguide is clamped at two narrow (~30 nm wide) tethers to improve mechanical stability. Due to the modified stress profile introduced by AlN deposition and etching, these clamping structures were found to improve both the mechanical robustness and the reproducibility of the external optical coupling rate, $\kappa_{e,a}$. Panel (d) shows the tapered waveguide edge at the chip facet, which is designed for efficient coupling to a lensed optical fiber. Here, corrugated clamping is employed to enhance structural stability and minimize optical insertion loss.

7.2 Room temperature characterization

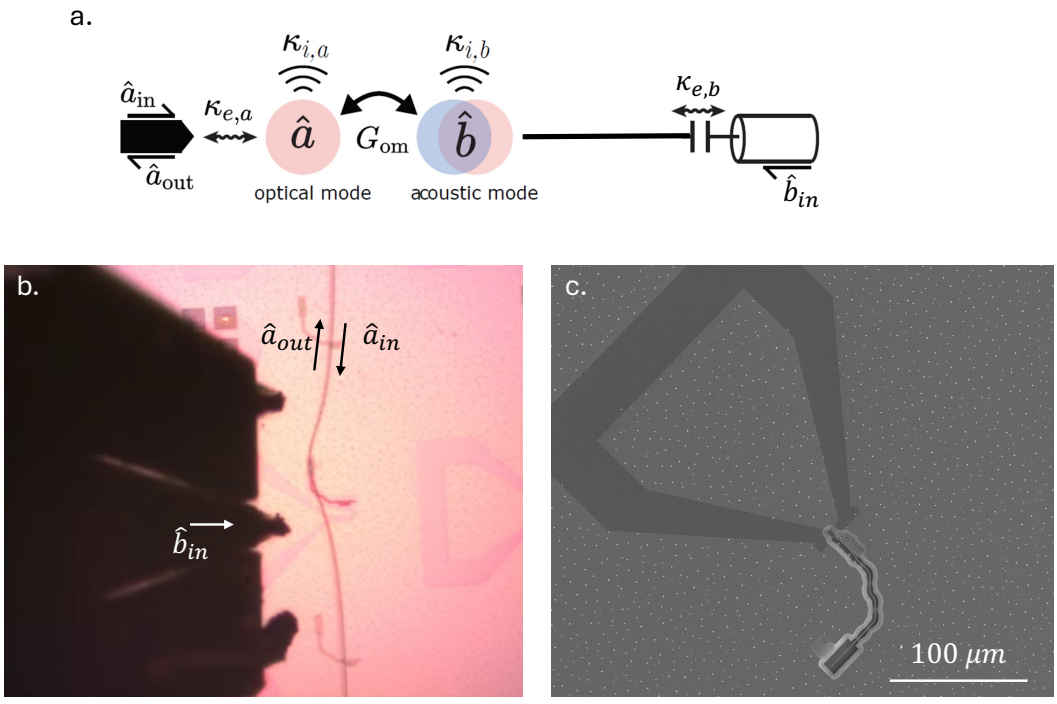

Figure 7.7: **Direct-coupled transducer measurement scheme. a,** Modal diagram of the direct-coupled transducer. The acoustic mode $\hat{b}$ is directly coupled to a microwave excitation port with an external decay rate $\kappa_{e,b}$. The remainder of the diagram is identical to Figure 2.3a. **b,** Optical microscope image of the measurement setup. A microwave signal $\hat{b}_{\mathrm{in}}$ is applied through the central microwave probe (middle arm), while the outer arms are grounded. The device is optically probed using a dimpled fiber, with $\hat{a}_{\mathrm{in}}$ and $\hat{a}_{\mathrm{out}}$ representing the input and output optical fields, respectively. **c,** SEM image of the fabricated direct-coupled transducer, showing a short optical waveguide for fiber coupling.

Before fabricating a full transducer for measurements at cryogenic temperatures, we iterate the process at room temperature. The modal diagram for room-temperature

characterization is shown in Figure 7.7a. The piezo-acoustic cavity can be directly excited using a coherent microwave signal. We use a dimpled fiber [85] for optical probing ($\hat{a}_{\text{in}}$ and $\hat{a}_{\text{out}}$) and a microwave probe for microwave excitation ($\hat{b}_{\text{in}}$) as shown in Figure 7.7b. Instead of connecting to a microwave resonator, which is not superconducting at room temperature, the piezo-optomechanical crystals are terminated with a microwave launcher, as shown in Figure 7.7c. We refer to these as *direct-coupled transducers*. Direct-coupled transducers are inherently very inefficient due to the impedance mismatch between the microwave drive and the electrodes. Additionally, NbN is not superconducting at room temperature, which leads to drastically higher losses. However, such geometries provide a quick way to iterate on the design and measure critical parameters such as optical and acoustic frequencies, optomechanical coupling rates, and initial evidence of microwave-to-optical transduction.

Figure 7.8 presents the measured optical spectrum (left) and acoustic spectrum (right) of a test device. The extracted parameters of the system are $(\lambda_a, Q_{i,a}, Q_{e,a}, g_{\text{OM}}/2\pi) = (1557\,\text{nm}, 270 \times 10^3, 332 \times 10^3, 860\,\text{kHz})$. The acoustic spectrum is obtained by weakly driving the acoustic resonator using a blue-detuned pump laser ($\Delta = \omega_b$). A coherent microwave tone is subsequently applied at the acoustic frequency, appearing as a sharp peak superimposed on the room-temperature thermo-mechanical noise background.

We estimate the microwave-to-acoustic transduction efficiency and extract a lower bound on the piezoelectric coupling rate g_{pe}. To begin, we evaluate the number of coherent phonons excited in the acoustic resonator due to the applied microwave drive, as shown in Figure 7.8(right). This is done by integrating the area under the spectrum.

Since the acoustic mode is probed with a weak blue-detuned optical drive, we assume that the background area, excluding the coherent peak, corresponds to the room-temperature thermal occupation of the acoustic resonator:

$$n_{\text{thermal,RT}} = \frac{k_B T}{\hbar \omega_b} \approx 606. \tag{7.1}$$

The number of coherently excited phonons, n_{coh}, is estimated by comparing the area under the coherent peak, A_{coh}, to that of the thermal background, A_{thermal} [86]:

$$n_{\text{coh}} = \frac{A_{\text{coh}}}{A_{\text{thermal}}} \cdot n_{\text{thermal,RT}} \approx 28. \tag{7.2}$$

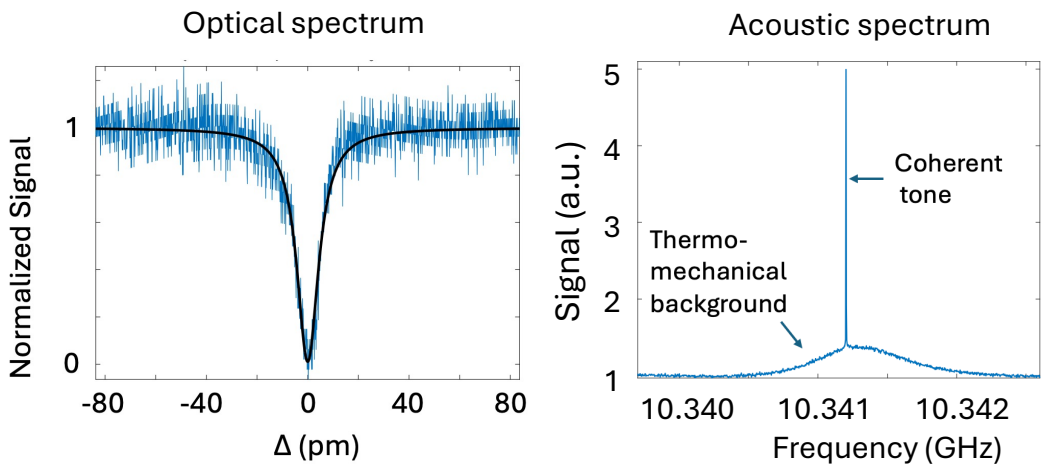

Figure 7.8: **Direct coupled transducer spectrum. left,** Optical spectrum along with a lorentzian fit. The extracted parameters are $(\lambda_a, Q_{i,a}, Q_{e,a}) = (1557\text{ nm}, 270 \times 10^3, 332 \times 10^3)$. **Right,** Acoustic spectrum measured on a fast photodetector showing coherent microwave drive on top of thermomechanical background signal. The measurements are performed with a blue detuned laser $\Delta = \omega_b$ and microwave drive on resonance $\omega_\mu = \omega_b$

Drawing an analogy to Equation 2.22, we express the relationship between n_{coh} and the input microwave photon flux $b_{\text{in}} = P_{\text{in},\mu}/\hbar\omega_\mu$ as [87]:

$$n_{\text{coh}} = \frac{\kappa_{e,b} P_{\text{in},\mu}/\hbar\omega_\mu}{\Delta_{\mu b}^2 + (\kappa_b/2)^2}, \tag{7.3}$$

where $\Delta_{\mu b} = \omega_b - \omega_\mu$ is the detuning between the acoustic mode and the microwave drive.

For the on-resonance case ($\Delta_{\mu b} = 0$), using the observed data, we estimate $\kappa_{e,b} \approx 0.1\,\text{mHz}$. This value accounts for the total losses in the delivery path, including impedance mismatch and dissipation in the room-temperature NbN feedline.

The microwave-to-acoustic transduction efficiency is then given by:

$$\eta_{\mu\to b} = \frac{\kappa_{e,b}}{\kappa_{e,b} + \gamma_{\text{OM}} + \kappa_{i,b}} \approx 10^{-10}. \tag{7.4}$$

We can utilize the estimated value of $\kappa_{e,b}$ to obtain a lower bound on the piezoelectric coupling rate g_{pe}. Following the methodology outlined in [88], we first estimate the capacitance C_b of the acoustic resonator using the Butterworth–Van Dyke (BVD) model:

$$\kappa_{e,b} = \omega_b^2 C_b Z_0, \tag{7.5}$$

where Z_0 is the characteristic impedance of the transmission line (typically 50 Ω).

Assuming the piezo-acoustic cavity is coupled to a microwave resonator with capacitance $C_{\text{res}} = 4.3$ fF, we can estimate the piezoelectric coupling strength using [88]:

$$\frac{g_{pe}}{2\pi} = \frac{\omega_b}{4\pi}\sqrt{\frac{C_b}{C_b + C_p + C_{\text{res}}}} \approx 4 \times 10^3 \text{ Hz}, \tag{7.6}$$

where C_p is the capacitance of the electrodes in the piezo-acoustic cavity. This estimate provides a lower bound on g_{pe}, limited primarily by the lossy NbN film and impedance mismatch.

7.3 Cryogenic measurement setup

Following the room-temperature characterization, we carried out low-temperature measurements of the complete transducer, including the integrated microwave resonator, at a base temperature of 10 mK. To facilitate these measurements, we developed a custom cryogenic setup compatible with dilution refrigerator environments. Figure 7.9(a–d) illustrates the packaging and integration process for cryogenic testing.

Panel (a) displays the front side of the transducer package, where deep reactive ion etching (DRIE) has been performed through the silicon handle layer to allow access for a lensed optical fiber. Panel (b) shows the backside of the package, which features MMPX microwave connectors for interfacing with the on-chip microwave resonators. The full assembly, shown in panel (c), includes a tuning coil positioned above the chip to magnetically tune the resonance frequency of the NbN microwave resonator, as well as a three-axis nanopositioner (Attocube) for aligning the fiber with the on-chip waveguide. Finally, panel (d) shows the complete setup mounted on the mixing plate of a Bluefors LD-400 dilution refrigerator, enabling simultaneous optical and microwave measurements at millikelvin temperatures.

7.4 Preliminary characterization of transducers at 10 mK temperature

Figure 7.10 presents reflection measurements of the microwave resonator. Panel (a) shows the internal quality factor $Q_{i,c}$ as a function of the average microwave intracavity photon number n_c. The inset depicts the measurement configuration, where

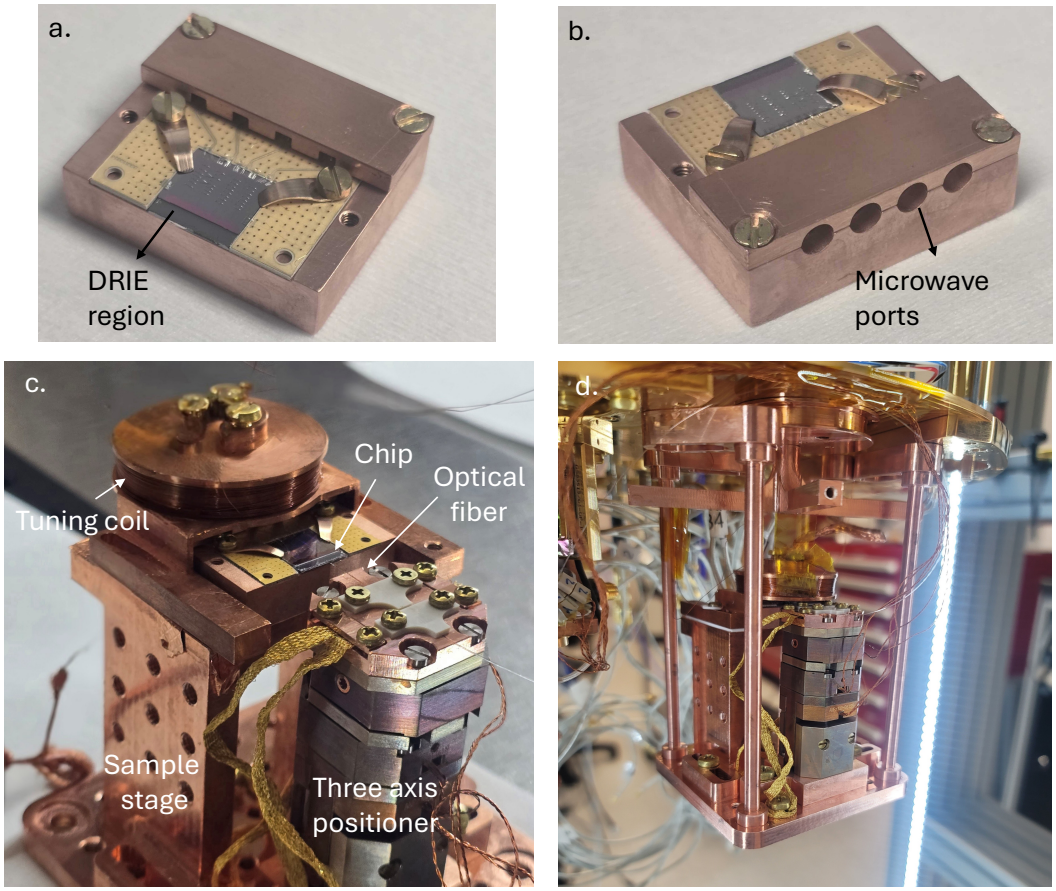

Figure 7.9: **Cryogenic measurement setup for transducers.** **a,** Front view of the transducer package, showing the deep reactive ion etched (DRIE) region in the handle layer, providing access for the lensed optical fiber. **b,** Back view of the package, highlighting the MMPX microwave ports for microwave probing. **c,** Custom cryogenic measurement setup with a tuning coil on top for tuning the resonance frequency of NbN microwave resonators. The setup includes a lensed optical fiber for coupling light to the transducers and a three-axis nanopositioner for precise alignment of the optical fiber with the on-chip waveguide. **d,** The entire assembly is mounted onto the mixing plate of a dilution refrigerator (Bluefors LD-400) for measurements at 10 millikelvin temperatures.

the resonator is probed in reflection using a circulator and a cryogenic amplifier. At the single-photon level, we measure an internal quality factor of approximately 10,000. As the drive power increases, $Q_{i,c}$ improves to around 16,000, which is attributed to the saturation of two-level systems (TLS) that couple to the resonator and contribute to its dissipation.

Panel (b) displays the tuning behavior of the microwave resonator frequency as a function of the applied current to the tuning coil. The tuning response follows

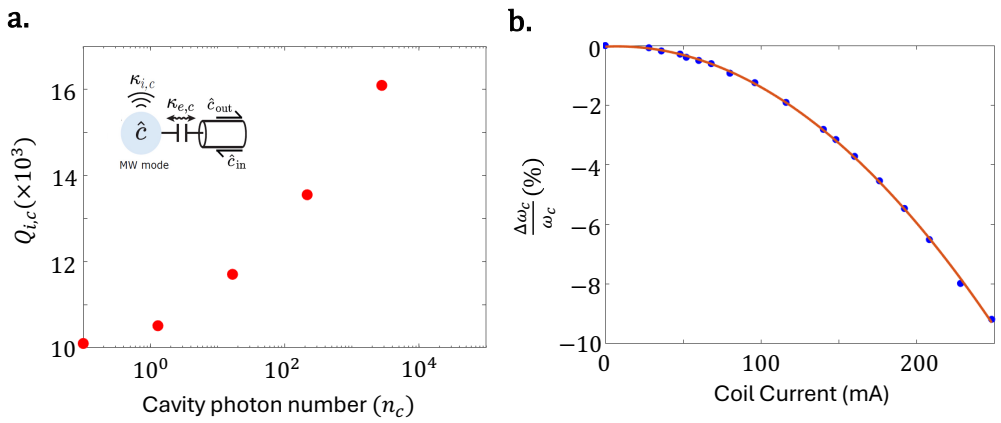

Figure 7.10: **Measurement of tunable microwave resonators. a,** The internal quality factor of the microwave resonator $Q_{i,c}$ as a function of number of photons in the microwave cavity n_c. The inset shows the measurement scheme where the resonators are probed in reflection. **b,** Tuning curve of the microwave resonator as a function of applied current to the coil placed directly above the chip. The tuning range is approximately 9% limited by flux trapping phenomena.

an approximately quadratic trend, consistent with the leading-order dependence of kinetic inductance on the screening current, as described by Equation 6.1. A total frequency tuning range of about 9% is achieved, beyond which the tuning is limited by flux trapping. This occurs when the screening current approaches the critical current of the superconducting film, leading to the entry and pinning of magnetic vortices. When flux is unintentionally trapped during tuning, we warm the dilution refrigerator above the critical temperature of the superconducting film (to ~15 K for certainty) to remove the trapped flux and restore the device to its initial state.

Figure 7.11 presents the spectroscopy measurements of the acoustic multimode spectrum. The top panel illustrates the measurement scheme, where the laser is parked on the blue sideband ($\Delta = \omega_b$), and the resulting spectrum is recorded using a fast photodetector. The middle panel displays the measured spectrum, revealing three distinct acoustic modes that couple to the optical cavity. These observed modes show strong agreement with the simulated acoustic spectrum shown in the bottom panel, which corresponds to a piezo-acoustic cavity box size of 770 nm × 770 nm.

Figure 7.12 shows the preliminary data for microwave to optical transduction for the full device including microwave resonator. In this measurement the microwave resonator is tuned in resonance with the highest g_{OM} mode ($\omega_c = \omega_b$) from Figure 7.11 and resonantly driven with a microwave tone ($\omega_\mu = \omega_c$). The measurement scheme

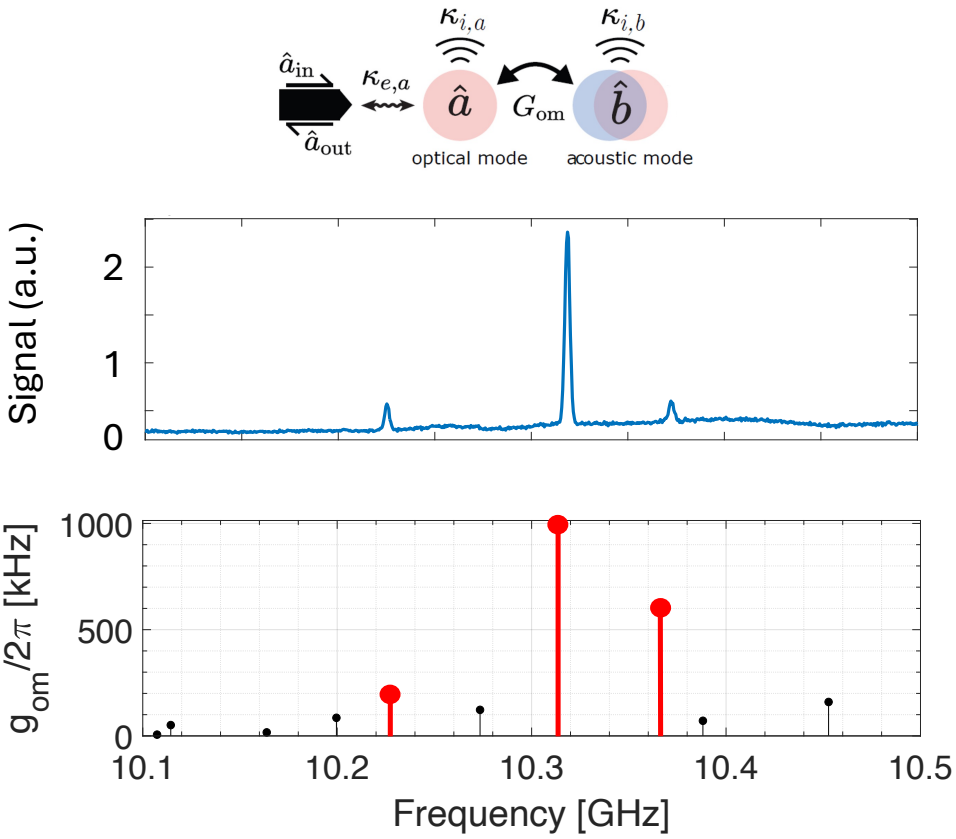

Figure 7.11: **Acoustic mode spectrum of the full transducer. Top:** Measurement scheme, where a laser is parked on the blue sideband ($\Delta = \omega_b$) and acoustic spectrum is measured in reflection. **Middle:** Measured acoustic spectrum on a fast photodetector, revealing three distinct acoustic modes. **Bottom:** Simulated acoustic spectrum of the full transducer with a piezo-acoustic box size of 770 nm × 770 nm. The peaks marked in red show good agreement in frequency with the measured data in the middle panel.

is shown in the top panel where the pump laser is parked on the blue sideband $\Delta = \omega_b$ and the spectrum is taken on a fast photodetector. Similar to the room temperature measurements, we see evidence of transduction where we see a coherent microwave tone on top of thermomechanical background.

We can estimate the piezoelectric coupling using the framework developed in section 2.5. For that purpose, we first estimate the number of coherent photons excited by the microwave tone. From equations 2.38, 2.39 and 2.40, we eliminate $\hat{a}$ and write $\hat{b}$ in terms of the microwave input $\hat{c}$:

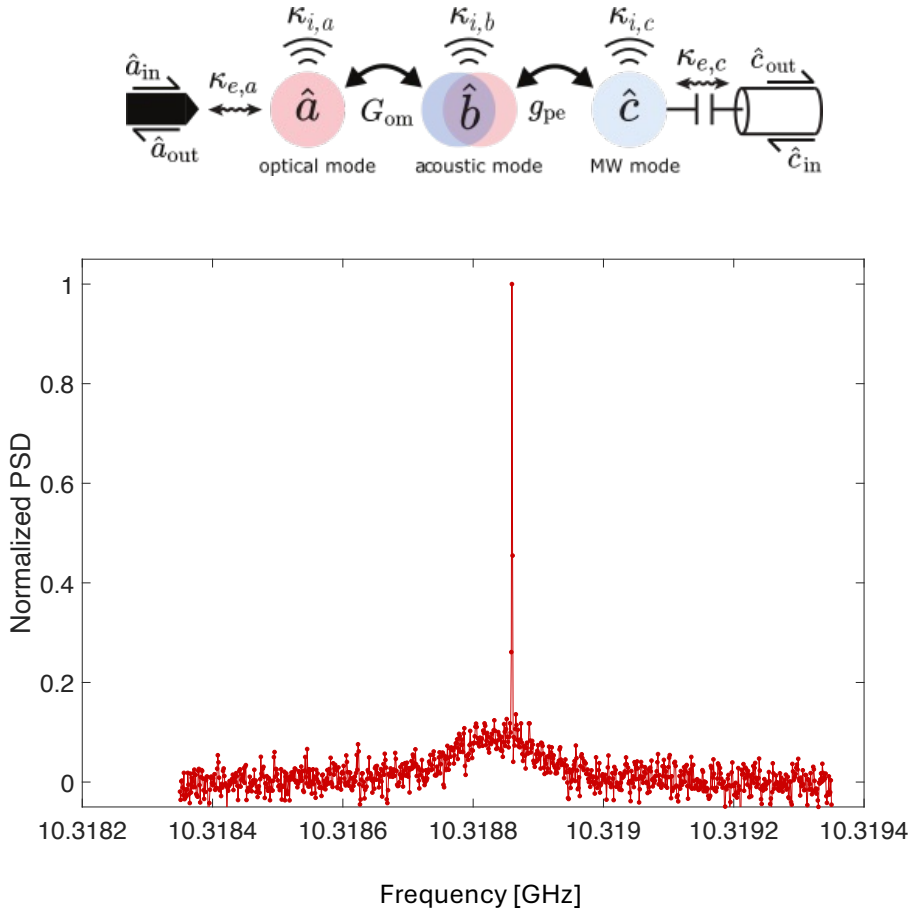

Figure 7.12: **Microwave-optical transduction at 10 mK temperature. Top:** Measurement scheme, where a laser is parked on the blue sideband ($\Delta = \omega_b$). Microwave resonator is tuned to the acoustic frequency and is driven on resonance, The acoustic spectrum is measured on a fast photodetector. **Bottom:** Measured acoustic spectrum around the mode of interest showing coherent microwave drive on top of thermomechanical background signal. Optical power corresponds to $n_a = 5$.

$$\hat{b}\left(-\frac{4G_{\rm OM}^2}{\kappa_a}+\frac{4g_{\rm pe}^2}{\kappa_c}+\kappa_{i,b}\right)=-2\frac{2ig_{\rm pe}}{\sqrt{\kappa_c}}\sqrt{\frac{\kappa_{i,c}}{\kappa_c}}\hat{c}_{\rm in} \tag{7.7}$$

where, the negative sign in front of $\frac{4G_{\rm OM}^2}{\kappa_a}$ comes from the blue detuned laser $\Delta = \omega_b$ instead of red detuned ($\Delta = -\omega_b$). The number of coherent phonons $n_{\rm coh}$ excited by the microwave drive can then be written as

$$n_{\rm coh} = \langle \hat{b}^\dagger \hat{b} \rangle = \eta_\mu \frac{P_{in,\mu}}{\hbar\omega_\mu} \frac{4\gamma_{pe}}{(\kappa_{i,b} - \gamma_{\rm OM} + \gamma_{pe})^2}. \tag{7.8}$$

The area under the thermomechanical background in Figure 7.12 was calibrated using sideband asymmetry which gave us an absolute calibration for n_{coh} by taking the area under the curve similar to room temperature transduction case. For this measurement we used $n_a \approx 5$ which leads to negligible γ_{OM} compared to the intrinsic linewidth $\kappa_{i,b}/2\pi \approx 150$ kHz For a given input power $P_{in,\mu}$, known attenuation in the input line in the dilution refrigerator (≈ -87 dB), we estimated $g_{pe}/2\pi \approx 400$ Hz.

7.5 Conclusion and future work

In summary, we have demonstrated a novel microwave-optical transduction platform based on side-coupled 2D-OMCs. Although the work presented here is still in progress, it lays the groundwork for future device iterations and improvements. We initially anticipated piezoelectric coupling rates on the order of $g_{pe}/2\pi \approx 1$ MHz, but observed values approximately three orders of magnitude lower. This discrepancy requires systematic investigation and is the focus of current and future efforts. A possible cause could be a break in the galvanic connection in the NbN layer over the phononic shield or on the slope of the AlN box, potentially arising from lithography misalignment or insufficient sputtered coating thickness.

In section 4.4 of chapter 4, we discussed the improvements in noise–efficiency performance of silicon-based, side-coupled 2D-OMCs compared to 1D-OMCs. However, the transducer geometry explored in this work is heterogeneous, comprising silicon, piezoelectric materials, and superconducting electrodes. Optical absorption induced heating in such a multi-material platform likely involves several interacting mechanisms, including the interplay of optical photons, substrate phonons, two level systems (TLS), and quasiparticles. While isolating the contribution of each mechanism to the total added noise is challenging, a previous study from our group [79] reported an approximate tenfold increase in noise at $n_a \sim 45$ compared to pure silicon 1D-OMC structures [41], for optical pulse widths on the order of 40 ns. We use this result to define an upper bound on the performance of integrated two dimensional OMC transducers relative to their pure silicon counterparts.

Reference [33] proposed the *throughput–noise* metric to enable cross-platform comparison of microwave to optical transducers operating in different regimes. The *throughput* is defined as the product of the transducer bandwidth, on-chip efficiency (including both optical and microwave coupling efficiencies η_a and η_c), and the duty cycle. In our 2D-OMC platform, the bandwidth is set by the total acoustic

linewidth $\kappa_b = \gamma_{\mathrm{OM}} + \gamma_{\mathrm{pe}} + \kappa_{i,b}$, which includes contributions from optomechanical backaction, piezoelectric backaction, and intrinsic mechanical loss. We conservatively assume the acoustic bandwidth to be $\kappa_b/2\pi \sim 5\,\mathrm{MHz}$. For continuous wave operation, the duty cycle is unity. In pulsed mode operation, we assume a repetition rate of 10 kHz and a pulse width of 500 ns, which reflects typical parameters in our transducers are operated in our lab and limited by the thermalization time of the acoustic resonator. Additionally, we assume typical external coupling efficiencies, $\eta_a \sim 0.5$ and $\eta_c \sim 0.9$.

Figure 7.13 shows a comparison of various microwave to optical transducer platforms, including the projected performance of the 2D-OMC based transducers developed in this work. The x-axis shows the input referred added noise n_{add} from microwave port, which is typically dominated by thermal noise, while the y-axis shows the throughput in kilohertz. The blue shaded region represents the quantum enabled transduction regime where $n_{\mathrm{add}} < 1$.

The projected continuous wave performance of the 2D-OMC transducer at $n_a = 2030$ is shown as a red band, spanning $0.28 < n_{\mathrm{add}} < 2.8$. The lower bound corresponds to the noise level of a pure silicon platform, while the upper bound reflects the degradation observed in the integrated transducer platform of Ref. [79], relative to the pure OMC case [41]. While reaching such high optical powers may be challenging due to potential degradation of the superconducting microwave resonator, improvements in fabrication techniques such as scatter reduction strategies recently demonstrated in [10] may make such power levels accessible, as discussed in chapter 10.

The projected pulsed mode performance of 2D-OMC transducers at $n_a = 443$ and $n_a = 4$ is shown in green. Overall, these results suggest that 2D-OMC based transducers may enable access to either the ultra low noise regime or the ultra high throughput regime, depending on the optical power and the mode of operation.

Looking ahead, the transducers developed in this work could be integrated with an off-chip qubit module via a low-loss superconducting microwave interconnect [89]. In such an architecture, a photon emitted by the transducer can be absorbed by a superconducting qubit through a cavity-assisted Raman process [90]. Furthermore, a pair of transducer-qubit modules, housed in separate dilution refrigerators, could be employed to generate optically mediated entanglement between superconducting qubits. A heralding scheme for this application is discussed in chapter 10 and will be the subject of future work.

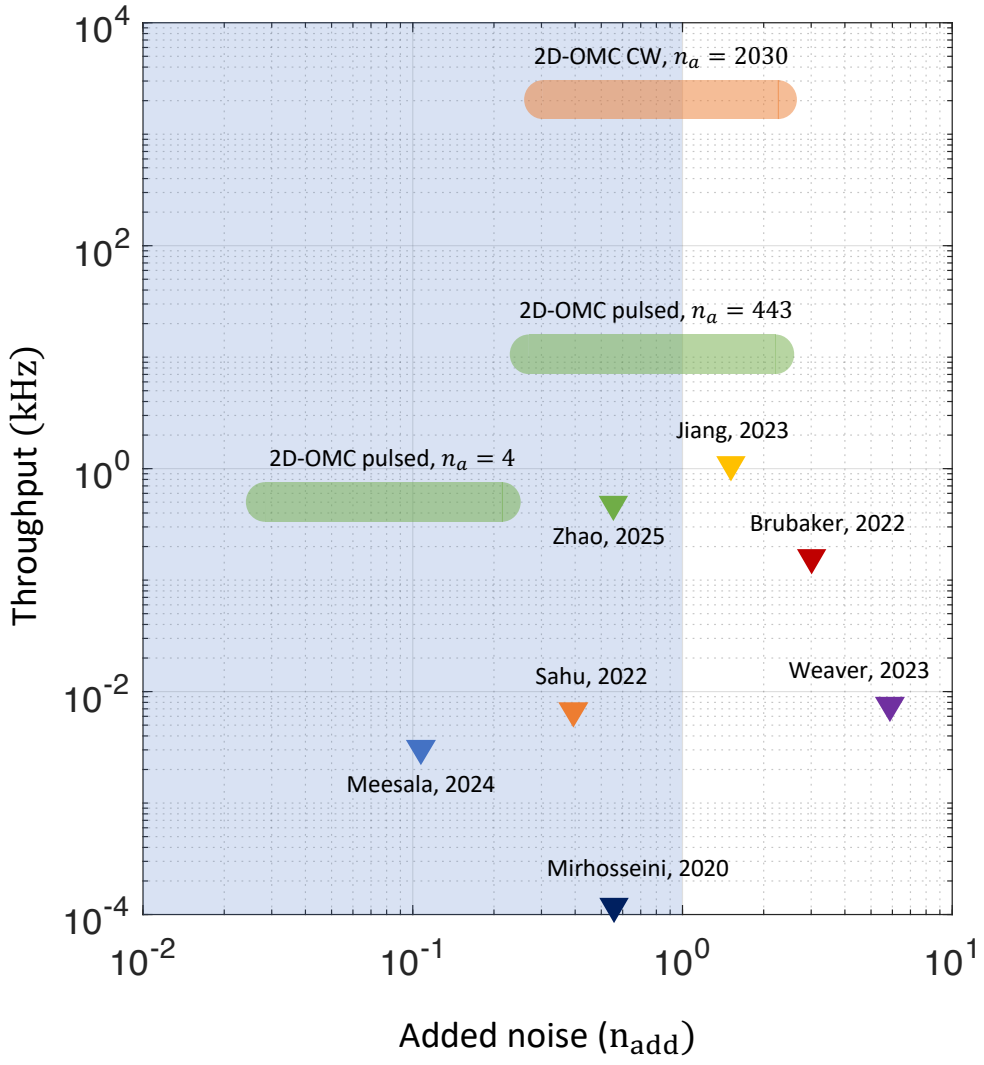

Figure 7.13: **Estimated throughput and noise performance of the 2D-OMC based microwave to optical transducer compared to prior work in the literature.** The blue shaded region represents the quantum-enabled transduction regime where $n_{\text{add}} < 1$. The red strip indicates the projected performance of the 2D-OMC transducer in continuous wave mode at $n_a = 2030$. The green strips correspond to projected performance in pulsed mode at $n_a = 4$ and $n_a = 443$, assuming a pulse width of 500 ns and a repetition rate of 10 kHz. References: Jiang, 2023 [49], Zhao, 2025 [33], Brubaker, 2022 [73], Sahu, 2022 [64], Meesala, 2024 [48], Weaver, 2023 [50], Mirhosseini, 2020 [79]

Part II

Spectral Tuning of Optomechanical Crystals for Remote Entanglement

Chapter 8

IN-SITU TUNING OF OPTOMECHANICAL CRYSTALS AT ROOM TEMPERATURE

8.1 Limitations of the state-of-the-art fabrication techniques

In the previous part, we discussed optomechanical crystals (OMCs) and their role in enabling coherent coupling between optical photons and acoustic phonons for applications in microwave-to-optical quantum transduction. As these systems scale toward larger networks and more complex functionalities, precise control over both optical and acoustic resonance frequencies becomes essential. However, state-of-the-art nanofabrication techniques—such as electron beam lithography and reactive ion etching are limited in precision, often leading to significant device-to-device variation. These fabrication-induced disorders result in resonance frequency spreads that can exceed 100 times the intrinsic linewidths, severely hindering efforts to scale these systems.

In Figure 8.1a, a scanning electron microscope (SEM) image of a representative 1D-OMC device highlights geometric imperfections introduced during fabrication. To assess the impact of such imperfections on the measured optical and acoustic resonance frequencies, we fabricated an array of 20 devices with nominally identical geometries, positioned adjacent to each other on a single chip. The cavity design features critical dimensions below 100 nm, making it particularly sensitive to nanoscale fabrication variations. In our process, electron beam lithography combined with reactive ion etching provides a feature size precision of approximately 5 nm [36]. However, due to the sequential nature of electron beam writing—where the pattern is written line-by-line; this technique is also prone to stitching errors, which can introduce additional variability across the array.

Figures 8.1b and c show the measured optical wavelengths with a standard deviation of 2.58 nm and acoustic resonance frequencies with a standard deviation of 19.8 MHz, respectively. These values are much larger than the FWHM of the optical and acoustic resonances, which are typically 10 pm and 2–5 MHz at room temperature, respectively, as shown in Figures 8.1d and e. This level of variation highlights the need for post-fabrication frequency tuning in such devices to compensate for

[0]This chapter is based on work published in ref [91]

fabrication-induced disorder. In superconducting circuits, for example, qubit and resonator frequencies can be tuned in situ via magnetic flux biasing. However, such electrical tuning mechanisms are not directly applicable to passive dielectric devices like OMCs.

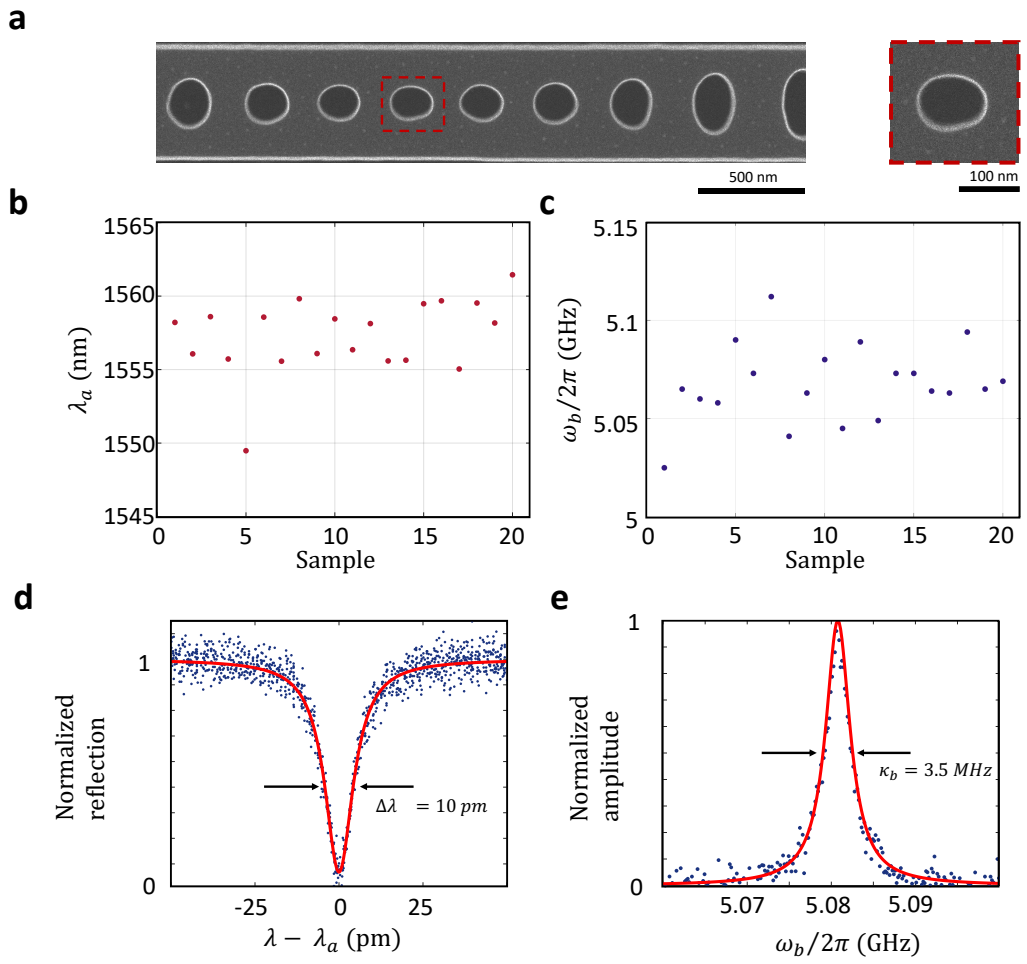

Figure 8.1: **Resonance frequency distribution of 20 OMCs fabricated with nominally identical device geometry.** **a**, SEM image of the defect unit cells of a randomly chosen OMC cavity. Inset on the right shows the magnified view of an ellipse with irregular boundaries. **b**, Optical resonance wavelengths and **c**, acoustic resonance frequencies of 20 OMC cavities. **d,** Typical optical and **e** acoustic spectrum showing linewidths of $\Delta\lambda$=10 pm and κ_b = 3.5 MHz at room temperature, respectively.

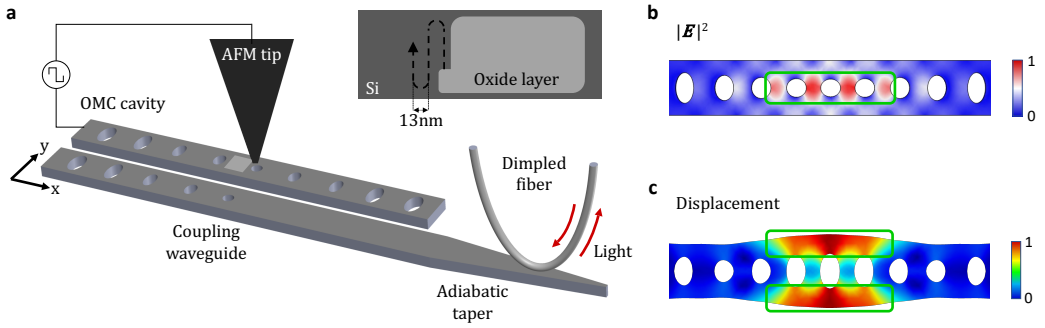

Figure 8.2: **Nano-oxidation setup schematic and OMC cavity mode profiles.** **a**, Simplified schematic of the AFM nano-oxidation setup. The AFM tip is used to perform nano-oxidation while measuring the optical and acoustic resonances of the device in real-time with a dimpled optical fiber. The AFM tip is operated in tapping mode over a grounded silicon sample and biased with a square wave voltage, allowing for electrochemical formation of an oxide layer on the silicon surface. Inset illustrates the raster scan used to generate the oxide layer. **b**, Electric field intensity profile of the optical mode. The optics-focused oxidation region is outlined in green. **c**, Displacement magnitude profile of the acoustic breathing mode. The acoustics-focused oxidation regions are outlined in green.

8.2 AFM nano-oxidation for post-fabrication tuning

Post-fabrication tuning of optical resonance frequencies in chip-scale microcavities has been achieved using a variety of techniques including laser-assisted thermal oxidation [92], strain tuning [93, 94], thermo-optic tuning [95, 96], and gas condensation [97, 98]. Atomic force microscope (AFM) nano-oxidation technique has been used to realize polarization degenerate microcavities [99], and to create low-loss microcavities from line defects in a photonic crystal [100]. However, since OMCs co-localize optical and acoustic resonances in a wavelength-scale volume, selective tuning of both optical and acoustic resonances without adding significant scattering losses is a complex endeavor and an outstanding technical challenge. Here we use AFM nano-oxidation tuning to demonstrate such control over the resonance frequencies of OMCs. In our approach, field-induced oxidation of the silicon device surface with high spatial resolution allows us to tune the acoustic resonance by modifying the local mass distribution and elasticity, and the optical resonance by modifying the local refractive index.

A simplified schematic of the experimental setup is shown in Fig. 8.2a. We perform nano-oxidation using a conductive chromium/platinum coated silicon AFM tip with a radius <25 nm [101], and track the optical and acoustic resonances in real-time by

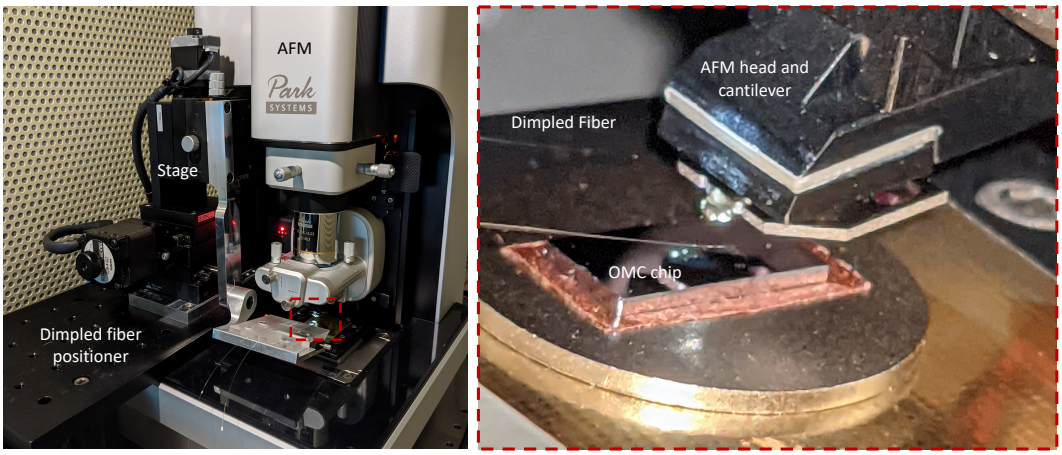

Figure 8.3: **AFM integrated with an optical test setup.** A dimpled fiber positioning stage is integrated into an AFM, allowing for real-time oxidation and optical testing. Image on the right shows a close-up view of the AFM cantilever, the dimpled fiber and the OMC chip.

performing optomechanical spectroscopy via a dimpled optical fiber coupled to the device [85]. The AFM is operated in tapping mode while a voltage bias is applied to the conductive tip, and the silicon-on-insulator (SOI) chip with a silicon device layer resistivity of 5 kΩ-cm is grounded. When the voltage-biased AFM tip is brought close to the silicon surface, a strong electric field triggers an electrochemical reaction between ions in the native water meniscus and the silicon surface, resulting in local oxidation of silicon. Importantly, this reaction can proceed even when the silicon surface is covered with native oxide, because the strong local electric field allows oxyanions (OH^- , O^-) to diffuse through the native oxide [102]. In our experiments, we maintain the AFM setup enclosure at ambient conditions with a relative humidity of 40±5% and temperature of 23±1°C, and apply a square wave voltage oscillating between ±10 V at a frequency of 20 Hz to the AFM tip.

The actual experimental system is shown in Fig.8.3. The system has three sub-parts that are controlled independently: 1) the optical fiber positioning system, comprising a three-axes linear motorized positioning stage and two rotational positioning stages, 2) the sample mount of the AFM with x and y motional degrees of freedom, and 3) the AFM cantilever with z motional degree of freedom. The entire assembly sits on an optical table to minimize vibrations during the oxidation process.

The OMC cavities in this work were fabricated on an SOI chip with a 220 nm thick silicon device layer. The cavities were patterned via electron beam lithography followed by reactive ion etching, and finally suspended by removing the buried oxide

layer with an anhydrous vapor hydrofluoric acid etch. The devices were designed to support a fundamental TE-like optical resonance at a wavelength of ~1550 nm and a breathing acoustic resonance at a frequency of ~5.1 GHz (Fig. 8.2b,c) [103]. An on-chip adiabatic waveguide coupler [104] allows for optical coupling to the OMC cavity using a dimpled optical fiber. The optical spectrum of the OMC cavity was probed in reflection mode, and the resonance frequencies were recorded before and after each step of the nano-oxidation sequence. To measure the acoustic spectrum of the device, we routed the optical signal reflected from the device to a high-speed photodetector and measured the power spectral density (PSD) of the photodetector electrical output on a spectrum analyzer. The result is proportional to the PSD of thermal displacement fluctuations of the acoustic mode which are transduced onto the optical signal via the optomechanical interaction in the device. In these measurements, the laser was blue-detuned with respect to the optical resonance frequency by a detuning close to the acoustic resonance frequency, and operated at low power to minimize optomechanical back-action on the acoustic mode [16].

8.3 Nano-oxidation characterization

From the simulated mode profiles shown in Fig. 8.2b,c, we identified two strategic oxidation regions for selective tuning of the optical and acoustic modes. Nano-oxidation in the region shown with the green rectangle in Fig. 8.2b is expected to induce a relatively large change in the optical resonance due to a high concentration of electric field energy. Here the impact on the acoustic resonance is expected to be minimal due to two reasons. First, the displacement amplitude is small in this region. Second, even though the stress amplitude is large in this region, the Young's modulus of the oxide layer when weighted by its thickness is similar to that of the original silicon. In contrast, nano-oxdiation on the regions shown with the green rectangles in Fig. 8.2c leads to a large acoustic resonance shift and a small optical wavelength shift due to the high concentration of motional mass and low concentration of electric field energy. In section D.3 of the supplementary information, we show the results of finite element method (FEM) simulations where we investigated the optical and acoustic frequency shifts due to creation of an oxide pixel at an arbitrary location on the OMC surface. This allowed us to identify candidate regions for fine tuning of optical and acoustic resonance frequencies with maximal selectivity. For coarse frequency tuning, we opted to use larger, rectangular oxide patterns instead of oxide pixels to maximize the tuning range at the expense of selectivity.

Prior to experiments on OMC devices, we characterized the effect of the AFM

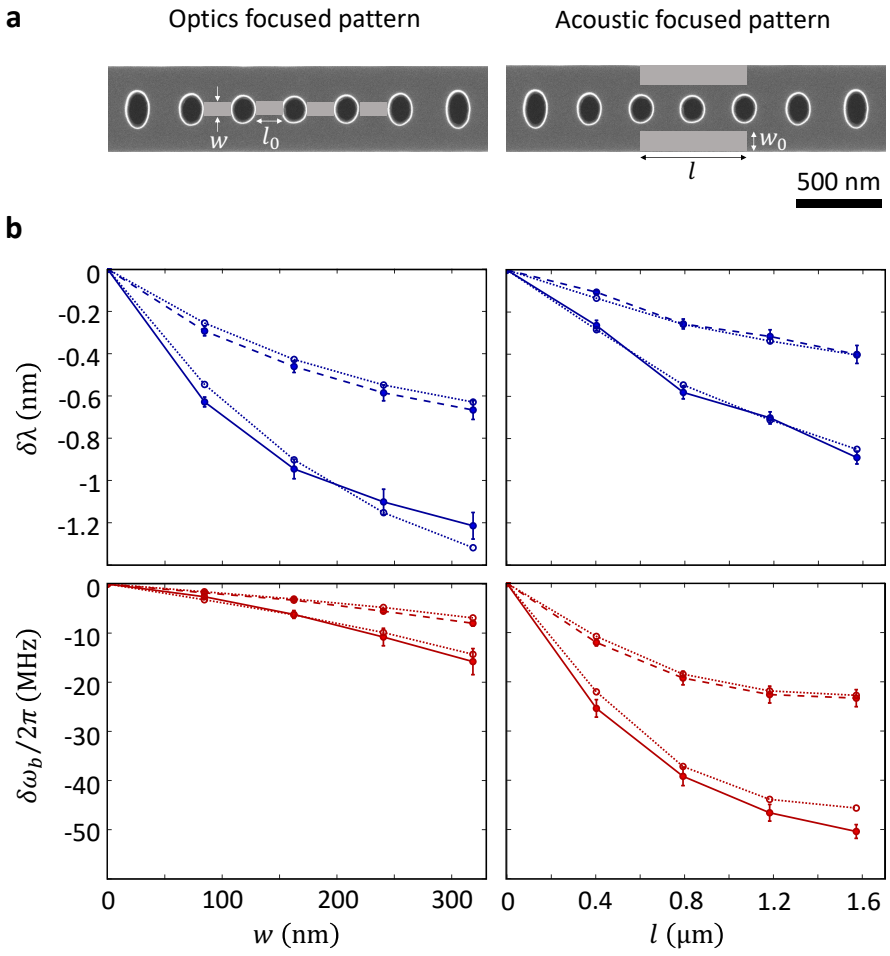

Figure 8.4: **Coarse frequency tuning of OMC cavity. a**, Oxidation patterns used for coarse tuning of optical (left) and acoustic (right) resonances. For the optics-focused pattern, the length is fixed at l_0 = 170 nm and the width, w is varied. For the acoustics-focused pattern, the width is fixed at w_0 = 120 nm and the length, l is varied. **b**, Tuning of optical and acoustic resonances as a function of the size of the oxidation pattern. Optical wavelength shift $\delta\lambda$ with respect to w (top left) and l (top right). Acoustic frequency shift $\delta\omega_b/2\pi$ with respect to w (bottom left) and l (bottom right). Solid (dashed) lines represent data taken for aggressive (mild) oxidation. Dotted lines show simulated values from finite element method simulations. Error bars represent the standard deviation across five OMC cavities measured for each dataset.

tapping amplitude and scanning velocity on nano-oxidation using a bare silicon chip. We observed that lower tapping amplitude and slower scanning velocities result in wider and thicker oxide lines. We measured the three-dimensional profiles of field-induced oxide lines and pixels using AFM measurements as described in section D.1 of the supplementary information. Based on the amount of frequency

tuning required, we operated the AFM in two distinct modes which we refer to as 'mild' and 'aggressive' tuning modes. In the mild tuning mode, the tapping amplitude and scan speed were set to 15 nm and 100 nm/s, respectively, resulting in oxide thickness of approximately 1.2 nm. In the aggressive tuning mode, the tapping amplitude and scan speed were set to 5 nm and 50 nm/s, respectively, leading to oxide thickness of approximately 2.5 nm. In the mild tuning mode, nano-oxidation was found to generate single pixels with a lateral size of approximately 25 nm. In order to obtain thicker and more uniform oxide patterns with a raster scan, we used a line spacing of 13 nm with significant overlap between neighboring lines as illustrated in the inset of Fig. 8.2a. This procedure allowed us to generate oxide layers with a thickness of 1.6 nm and 3.2 nm in the mild and aggressive tuning modes, respectively. We note that we can get oxide layers with thickness greater than 10 nm by operating AFM in the contact mode where the AFM cantilever tip is in contact with the substrate throughout the oxidation process. However, contact mode is more challenging to implement in suspended structures where large attractive forces between the surface and the AFM tip can damage the OMC and destroy the resonances.

Coarse tuning

After establishing these nano-oxidation parameters, we performed optical and acoustic resonance frequency tuning experiments on a single OMC cavity. We specifically studied the impact of two oxidation patterns: (i) an optics-focused pattern (Fig. 8.4a left) composed of four rectangles located between the five central ellipses in the beam; here the lengths of the rectangles were kept constant at l_0 = 170 nm, while their width, w was varied, and (ii) an acoustics-focused pattern (Fig. 8.4a, right) composed of two rectangles situated at the edge of the OMC cavity; here the widths of the rectangles were kept fixed at w_0 = 120 nm, while their length, l was varied. As shown in Fig. 8.4b, the experimentally measured tuning of the resonance frequencies (solid and dashed lines) agrees with simulation results (dotted lines). For the optics-focused pattern, increasing w leads to a large reduction in the optical wavelength and a smaller reduction in acoustic frequency. For the acoustics-focused pattern, increasing l leads to a decrease in acoustic frequency due to increasing motional mass ($\omega_b \propto \sqrt{1/m}$) and a decrease in the optical wavelength due to a decrease in the effective dielectric constant. Aggressive oxidation at w = 320 nm resulted in more than 1.2 nm blue shift of the optical wavelength while aggressive oxidation at l = 1.6 μm resulted in more than 50 MHz reduction in the acoustic frequency. In

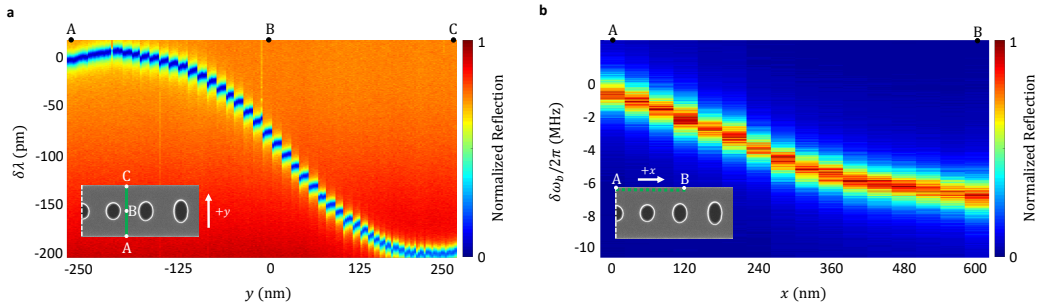

Figure 8.5: **Real-time, in-situ monitoring of the oxidation process.** **a**, Real-time spectra showing optical resonance tuning during sequential application of the oxidation pattern. As shown in the inset, the pattern is applied starting at point A, one pixel at a time, up to point C. AFM tip locations during the experiment are shown at the top of the plot with letters A, B and C which correspond to the points labeled on the inset image. Discontinuities along the horizontal axis are due to proximity effects between the AFM tip and the OMC cavity during the oxidation sequence. **b**, Real-time data showing acoustic frequency shift during pixel-wise oxidation. Oxide pixels are applied on the surface starting from point A up to point B as shown in the inset.

Fig. 8.4b, each data point represents the average value and the standard deviation obtained from five devices. For each device, the patterns were applied cumulatively, starting from the center and adding more oxide to increase either w or l at each step.

8.4 Simultaneous optical and acoustic frequency tuning

To achieve simultaneous tuning of optical and acoustic resonances, we define a joint pattern consisting of a union of the previously introduced optics-focused and acoustics-focused patterns. This is parameterized by geometric parameters w and l, and binary variables M_{O} (M_{A}) which denote mild or aggressive oxidation in the optical (acoustic) components of the joint pattern. Using the experimental data shown in Fig. 8.4, we interpolate $\delta\lambda$ and $\delta\omega_{\mathrm{b}}$ as a function of the parameters $\{w, l, M_{\mathrm{O}}, M_{\mathrm{A}}\}$. To achieve the desired frequency shifts, we developed a pattern generation algorithm to find an optimal combination of the acoustic and optics focused patterns. The algorithm takes the desired frequency and wavelength shift as the input and generates the required joint oxidation pattern by searching for the most suitable combination of l and w. The algorithm starts the search from milder oxidation modes to minimize optical scattering losses. Maximum increase in intrinsic scattering loss of $\delta\kappa_{i,a}/2\pi = 440$ MHz has been observed for $w < 350$ nm. More details on the pattern generation algorithm and the optical scattering losses are given in supplementary section D.4 and D.2, respectively.

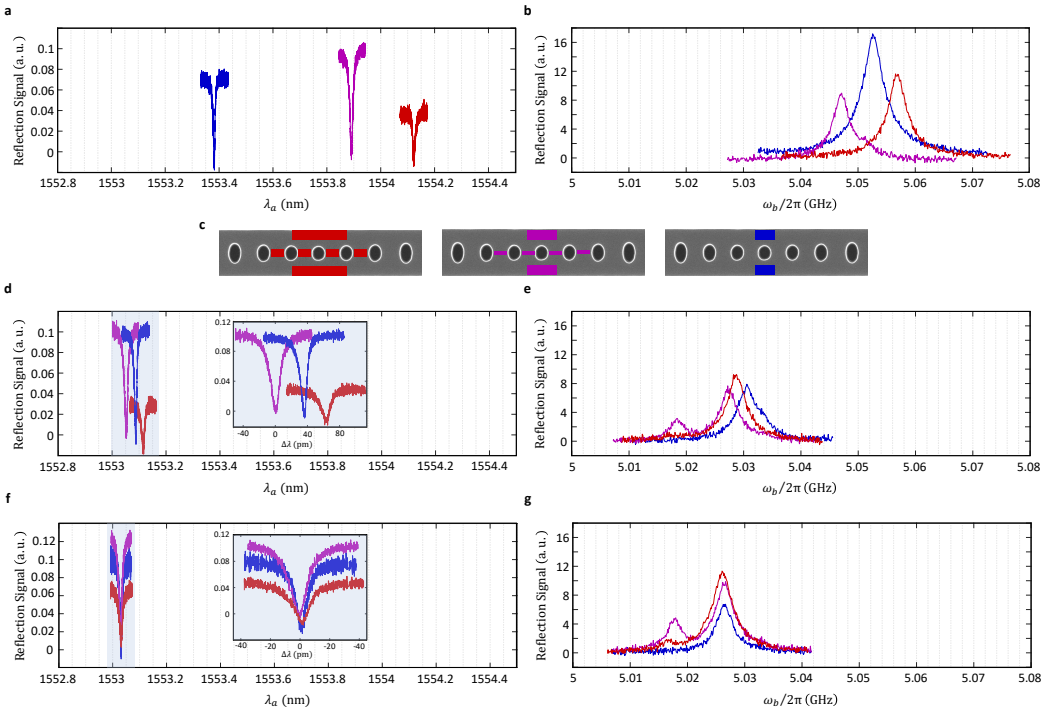

Figure 8.6: **Simultaneous optical and acoustic resonance frequency alignment of three OMC cavities.** Initial **a**, optical and **b**, acoustic resonance spectra. **c**, Joint patterns used for coarse alignment of the three OMC cavities. The patterns are shown with a color code matched to the OMC spectra, and are applied in the order shown from left to right. Resonance frequencies were recorded after every step of the nano-oxidation protocol. **d**, Optical and **e**, acoustic spectra measured after completion of the coarse alignment of sequence. **f**, Optical and **g**, acoustic spectra after completion of the real-time fine-tuning sequence. Insets in panels d and f show a zoomed-in view of the optical resonances. The satellite acoustic resonance in magenta in panels e and g is due to a neighboring OMC cavity within the evanescent field of the optical coupling waveguide.

While the pattern generation algorithm is sufficient for coarse tuning of the OMC wavelength and frequency, fine frequency alignment to within the linewidth of the optical and acoustic resonances requires pixel-by-pixel nano-oxidation with real-time feedback. This method allows for ∼1 pm precision for optical wavelength tuning and ∼150 kHz precision for acoustic resonance tuning. To quantify the sensitivity of the optical resonance wavelength to single oxide pixels, we applied a pixel-by-pixel linear oxide pattern perpendicular to the OMC long axis with a pitch of 13 nm shown in the inset of Fig 8.5a. The resonance spectra recorded in Fig. 8.5a for each incremental pixel in the oxidation sequence reveal a decrease

in the per-pixel wavelength shift towards the edges of the OMC, with an observed shift of -1.1 pm/px near the extreme points A and C. This spatial dependence is in agreement with predictions from FEM simulations, as discussed in supplementary section D.3. We perform a similar sensitivity analysis for the acoustic resonance via a pixel-by-pixel linear oxide pattern applied with a pitch of 40 nm along the edge of the OMC, shown in the inset of Fig 8.5b. The acoustic resonance spectrum is recorded after the addition of every oxide pixel, and the results are shown in Fig. 8.5b. We measure a maximum frequency shift of -1 MHz/px at point A which is in line with the center of the OMC cavity. As we move away from the center, the sensitivity eventually decreases to a value of -150 kHz/px as measured at the extreme point B.

After characterizing coarse and fine tuning of optical and acoustic resonance frequencies of a single OMC cavity, we used these techniques to perform frequency alignment of both the optical and acoustic resonances of three OMC cavities. Due to constraints on the maximum achievable tuning range, we pre-select cavities with initial optical wavelength spread <1 nm and acoustic frequency spread <20 MHz, shown on Fig. 8.6a, b. We begin with coarse tuning steps using oxidation patterns generated by the pattern generation algorithm as shown in Fig. 8.6c. This aligns the optical resonance wavelengths across all cavities to within a tolerance of <200 pm and acoustic resonance frequencies to within a tolerance of 5 MHz. The results of the coarse tuning are shown on Fig. 8.6d,e. We then proceed to real-time, pixel-by-pixel oxidation with feedback to achieve fine tuning of the resonance frequencies. After four rounds of fine-tuning, the optical and acoustic resonance frequencies were successfully tuned to within 2 pm and 500 kHz, respectively (see Fig 8.6f, g). A step-by-step description of the frequency alignment procedure is described in detail in supplementary section D.5.

8.5 Outlook

We have shown simultaneous, real-time tuning of optical and acoustic resonances in OMC cavities via AFM nano-oxidation, demonstrating optical wavelength and acoustic frequency shifts >2 nm (0.13%) and >60 MHz (1.2%), respectively. This tuning range can be improved by generating thicker oxide layers using AFM in the contact mode as we will explore in the next chapter. Such in-situ tuning methods could enable the realization of coupled optomechanical resonator arrays to study topological phases of photons and phonons [105, 106, 107, 108]. In the context of OMC-based microwave-optical quantum transducers [79, 32, 49, 50, 33], the

nano-oxidation tuning demonstrated here will enable post-fabrication frequency alignment of transducers in multiple nodes of a quantum network. Moreover, these techniques are applicable to other material systems such as silicon nitride [109], where tuning of optomechanical devices may be required [110]. Finally, AFM nano-oxidation could be a valuable technique for fundamental studies of two-level systems (TLS) in amorphous materials [111] by enabling spatially targeted creation of TLS in acoustic [36, 47] and superconducting [45] devices.

Chapter 9

WAVELENGTH ALIGNMENT OF OPTOMECHANICAL CRYSTALS FOR OPERATION AT CRYOGENIC TEMPERATURE

In the previous chapter, we introduced the AFM nano-oxidation technique for tuning optical and acoustic resonance frequencies of optomechanical crystals at room temperature. The quantum applications of optomechanical crystals require operation at cryogenic temperatures where the acoustic resonator can be close the ground state.

However, going from room temperature to cryogenic temperature leads to change the optical wavelength and acoustic frequency due to change in material properties and thermal stress which requires careful studies to achieve a desired wavelength at cryogenic temperature. This chapter presents a comprehensive tuning protocol for aligning the optical resonances of OMCs at millikelvin temperatures, addressing these critical factors.

9.1 AFM nano-oxidation in contact mode

Unlike in the previous chapter, our focus here will be exclusively on optical tuning. This approach is particularly suited for the experimental protocols involved in optically mediated remote entanglement of superconducting qubits (see next chapter), where precise wavelength alignment of optical photons is critical, while the acoustic resonator frequency can tolerate more variation. This flexibility allows us to employ contact-mode AFM oxidation, a more aggressive but less spatially precise method than tapping mode, facilitating the formation of thicker oxide layers needed for larger optical tuning ranges.

Figure 9.1 shows the optical wavelength shift $\delta\lambda_{\mathrm{AFM}}$ as a function of AFM tip voltage in contact mode. The oxidation pattern, optimized for optical tuning, is illustrated in the inset. Wavelength shifts are observed starting around 5V, reaching approximately 5-6 nm at 9V, while the corresponding acoustic mode shifts remain below 50 MHz.

The red data point at 10V represents a case where excessive oxidation resulted in an optical tuning of approximately 11 nm, but this also caused significant perturbation of the acoustic mode, rendering it undetectable through optical probing. This is

likely due to a drastic reduction in the optomechanical coupling strength, which can occur when the mechanical properties of the resonator are significantly altered by the thick oxide layer.

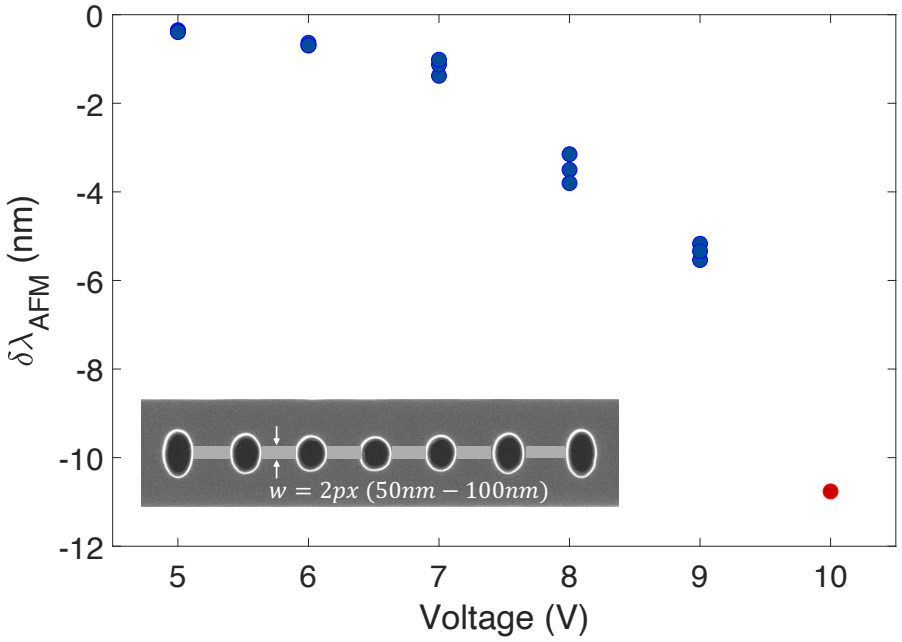

Figure 9.1: **Optical wavelength shift as a function of AFM tip voltage in contact mode**. Optical resonance shifts were measured for three OMCs over a voltage range from 5V to 9V. The red data point at 10V represents a single OMC where a significant wavelength shift was observed; however, the corresponding acoustic mode became undetectable due to excessive oxidation. The inset illustrates the dimensions of the oxidation pattern used for these measurements.

Figure 9.2 shows the change in internal quality factor as a function of different tip bias voltage. The average Q_i after fabrication we measured is $\sim 300 \times 10^3$ The red data points represent the change in internal quality factor before and after AFM nanooxidation $\delta Q_{\mathrm{i,AFM}}$. The blue data points represent change in internal quality factor before and after cooling down to 10mK temperature $\delta Q_{\mathrm{i,10mK}}$. and the green squares represent the net change in the quality factor before oxidation and after cooling down to 10mK. For up to 9V, we see a reduction of up to $\sim 100 \times 10^3$, which is up to $\sim 33\%$ of the initial value.

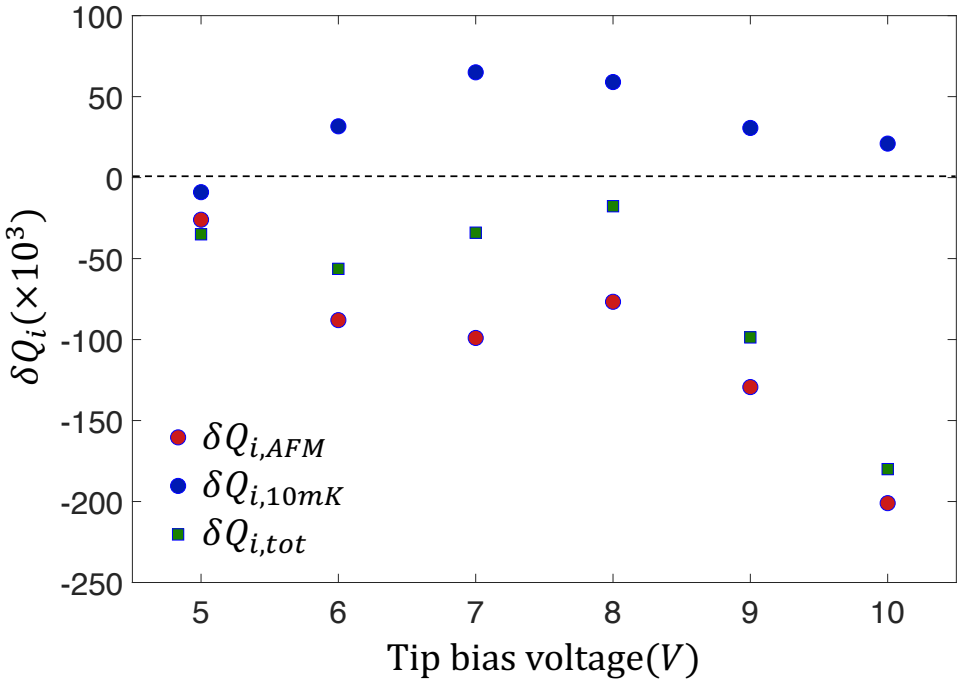

Figure 9.2: **Change in optical quality factor due to nano-oxidation and 10mK cooldown.** Red points indicate the change in Q_i immediately following AFM nano-oxidation, blue points represent the change in Q_i during the interval between AFM tuning and final cooldown to 10 mK, and green squares show the overall change from the initial Q_i to the final Q_i measured at 10 mK. The average internal quality factor after fabrication is $Q_i \sim 300 \times 10^3$.

9.2 Mechanisms influencing wavelength shifts

Native oxidation at room temperature

The final step in nanofabrication involves vapor HF release, which undercuts the silicon device layer on the SOI substrate by etching away the buried oxide. During this process, the native oxide on the silicon surface is also removed. Upon removal from the vapor HF chamber, the sample begins to reoxidize due to ambient humidity, leading to a progressive blue shift of the optical resonance. It is important to monitor this shift, as it can be on the order of 1 nm over several hours which is two orders of magnitude larger than the typical optical linewidth (~10 pm).

Figure 9.3 shows the measured change in the optical resonance wavelength as a function of time in air, recorded over a 10-hour window. In practice, the standard time required to prepare and load a sample into the dilution refrigerator is approximately 3–5 hours. This includes chip packaging, wirebonding for on-chip microwave

circuitry, and lensed fiber alignment. During this time, the optical wavelength shifts approximately linearly at a rate of 2.5 pm/min. This characterization is used to estimate the optical wavelength at the moment of dilution refrigerator pump-down, enabling more precise targeting of optical alignment for cryogenic measurements.

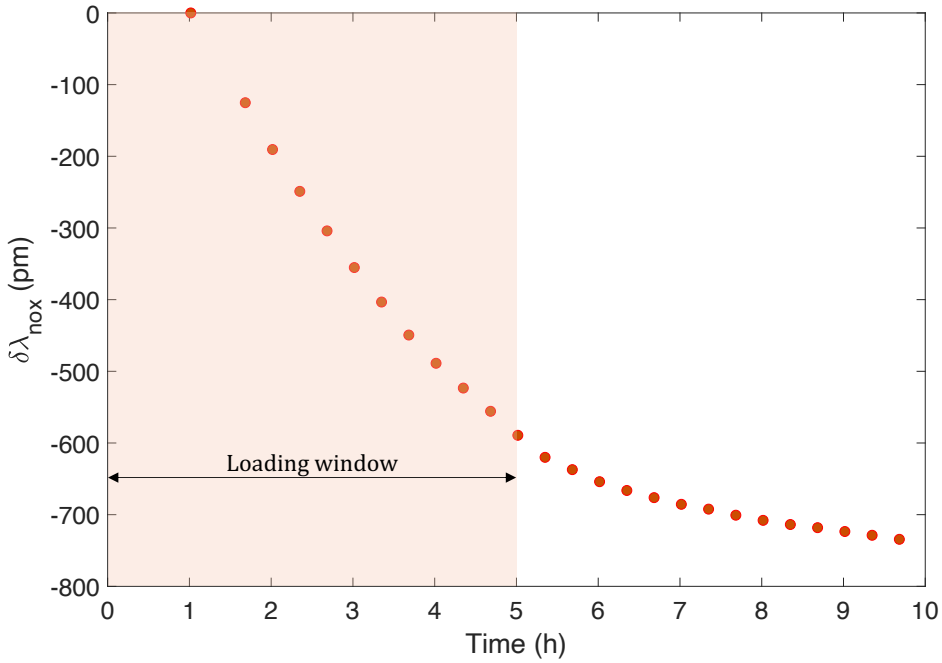

Figure 9.3: **Optical wavelength shift as a function of time due to native oxidation**. OMCs are probed continuously during a 10-hour window after fabrication to extract the rate of change in wavelength due to native oxidation at ambient conditions. The shaded region shows the typical time needed to load the sample into dilution refrigerator after fabrication.

Thermal contraction and stress

Silicon undergoes thermal expansion and contraction in response to temperature changes, characterized by its coefficient of thermal expansion, which was extensively studied in the 1970s [112]. Upon cooling from room temperature to 10 mK, the dimensional changes in the optomechanical crystal (OMC) patterns are typically negligible ($\ll$ 1 nm) and do not significantly contribute to the observed optical wavelength shifts. However, the acoustic resonator frequencies shift upward by approximately 50 MHz due to thermal contraction. This shift is accounted for during device design and is not a major concern for the experiments in this study.

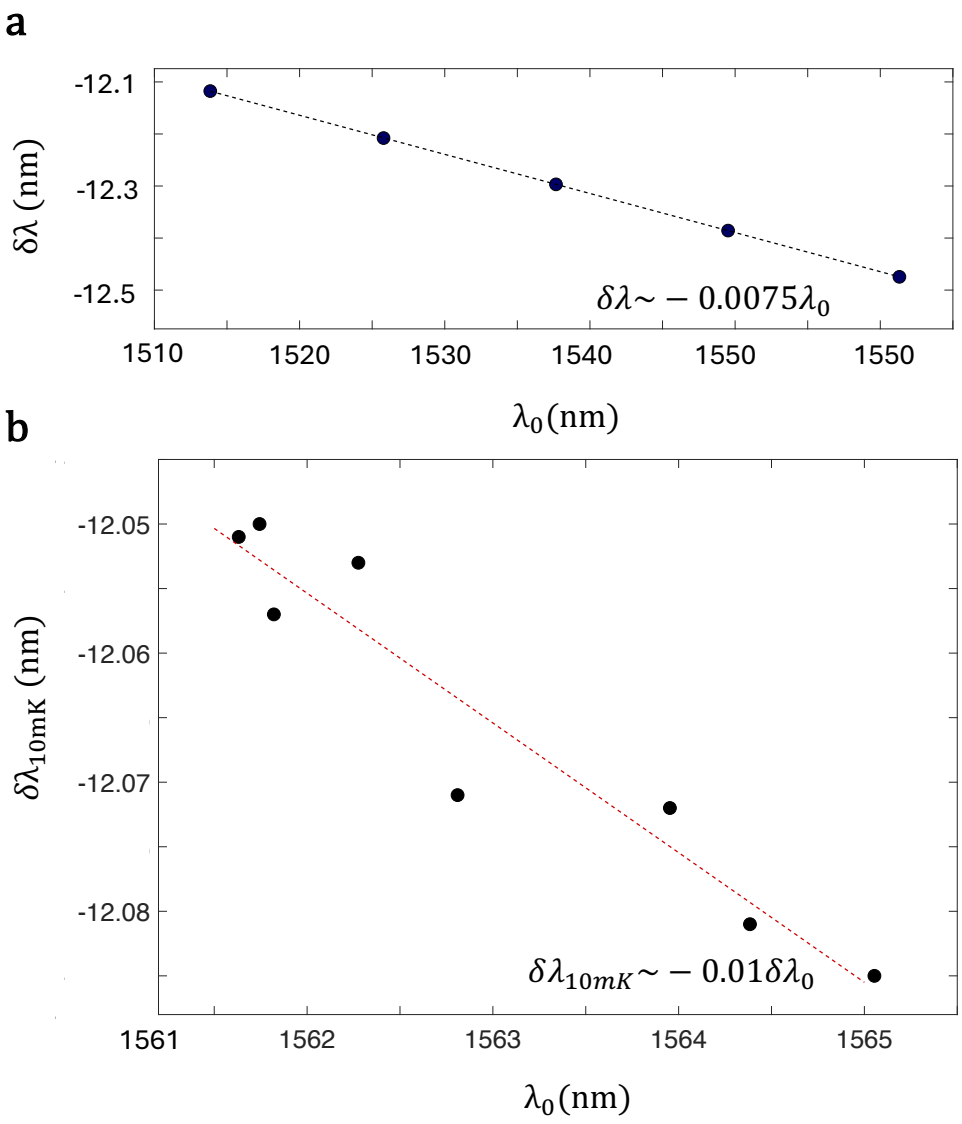

Figure 9.4: **Optical wavelength shift due to change in relative permittivity.a,** Numerical simulations of the optical wavelength shift. The optical resonance wavelength (x-axis) is swept by scaling the overall dimensions of the OMC, while the y-axis shows the corresponding wavelength shift resulting from a change in relative permittivity from $\epsilon_r = 11.7$ to $\epsilon_r = 11.5$. **b,** Experimentally observed dependence of the optical wavelength shift $\delta\lambda_{10\mathrm{mK}}$ on initial room temperature wavelength after fabrication.

Change in relative permittivity

The relative permittivity of most materials decreases as temperature drops, a phenomenon described by the thermo-optic effect. Figure 9.4a shows the numerical simulations for change in wavelength assuming a relative permittivity drop from

11.7 to 11.5 from room temperature to 10mK. In the simulations, the optical resonance wavelength (x-axis) is swept by scaling the overall dimensions of the OMC geometry. The linear relationship observed between the optical wavelength shift ($\delta\lambda$) and the initial resonance wavelength (λ_0) arises from the scaling effect of the mode volume. As the dimensions of the OMC are varied to shift the resonance wavelength, the effective refractive index of the optical mode also changes, leading to a predictable, approximately linear shift. This occurs because longer wavelength modes typically have larger mode volumes, resulting in a greater overlap with the dielectric material. This relationship is approximated as $\delta\lambda \sim -0.0075\lambda_0$ for small changes in ϵ_r, as indicated by the slope in the numerical data.

We observed similar trend in the experimental data as shown in Figure 9.4b. We fabricated and cooled down eight identical OMCs. However nanofabrication disorder led to a spread in the initial wavelength (x-axis). The observed shift in the wavelength (y-axis) is dependent on the initial wavelength. A linear fit gives a slope of ~ 0.01, close to what was observed in simulations. The discrpency between the two values could be due to the limited initial wavelength range in the experimental data.

AFM nanooxidation dependent thermal shift

Another important observation is the dependence of thermal wavelength shift on the amount of AFM-induced nano-oxide, which is controlled by the applied oxidation voltage. This effect arises due to the differing thermo-optic coefficients of silicon and silicon dioxide at cryogenic temperatures [113]. Below approximately 30 K, the thermo-optic coefficient of silicon becomes smaller than that of silicon dioxide. As a result, the amount of oxide present on the OMC becomes a significant factor in determining the final optical wavelength at 10mK temperature.

Figure 9.5 illustrates this behavior, showing that devices with greater AFM oxidation (larger $\delta\lambda_{\mathrm{AFM}}$) exhibit larger shifts in optical wavelength upon cooling. Two sets of OMCs were studied, centered around average room-temperature wavelengths of 1554.5 nm and 1564.5 nm, respectively. While both data sets display an approximately linear trend, the slope of the wavelength shift versus $\delta\lambda_{\mathrm{AFM}}$ differs between the two sets, indicating a dependence on the initial resonance wavelength.

Native oxidation dependent thermal shift

The final important contribution to the thermal wavelength shift comes from native oxide on the device. This effect has the same origin as the AFM nano-oxide

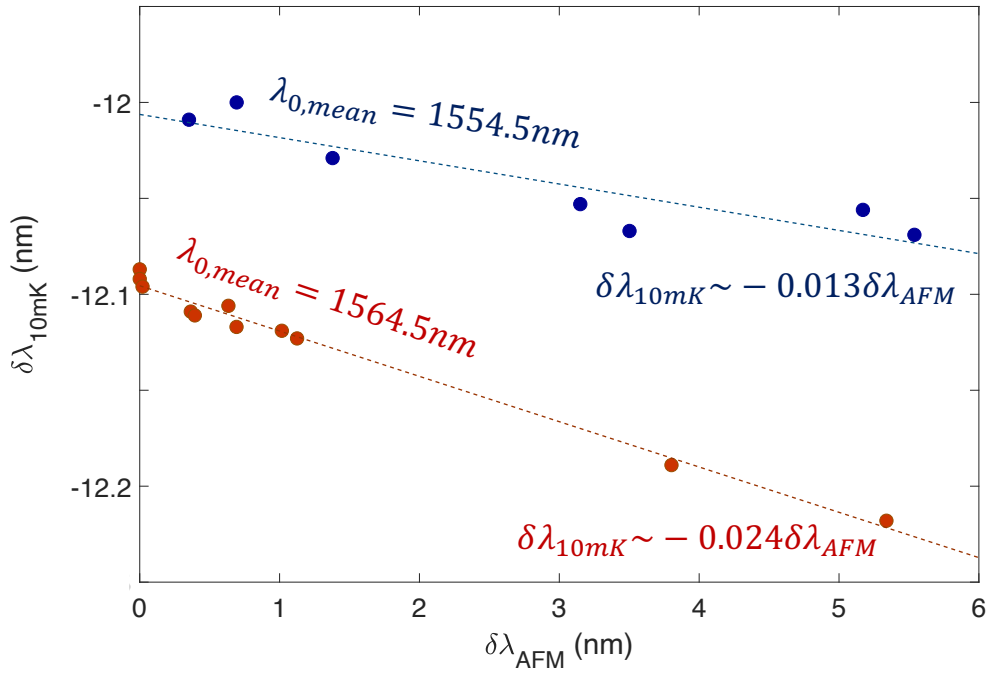

Figure 9.5: **AFM nano-oxidation dependent thermal shift.** Two separate sets of OMCs with initial average room-temperature wavelengths of 1554.5 nm (blue dots) and 1564.5 nm (red dots) are oxidized using different voltages, resulting in varying wavelength shifts $\delta\lambda_{\mathrm{AFM}}$ (x-axis). The y-axis shows the measured thermal wavelength shift $\delta\lambda_{10\mathrm{mK}}$ after cooling to 10 mK. Dashed lines represent linear fits to each dataset.

shift, namely, the different thermo-optic coefficients of silicon and silicon dioxide. However, it is more difficult to study experimentally, as it would require cooling multiple chips with different amounts of native oxide. Moreover, if we follow a consistent loading time for each cooldown, the amount of native oxide is expected to be similar across chips, leading to a predictable and repeatable shift due to this effect. In our initial analysis, we neglect this effect to keep the study simple.

9.3 AFM nanooxidation tuning for optical alignment at cryogenic temperatures

So far, we established various sources of wavelength shifts from the end of fabrication to reaching 10mK temperatures. Here we discuss the protocol to reach a desired wavelength at cryogenic temperature. The final wavelength at 10mK temperature can be written as a function of various parameters as follows

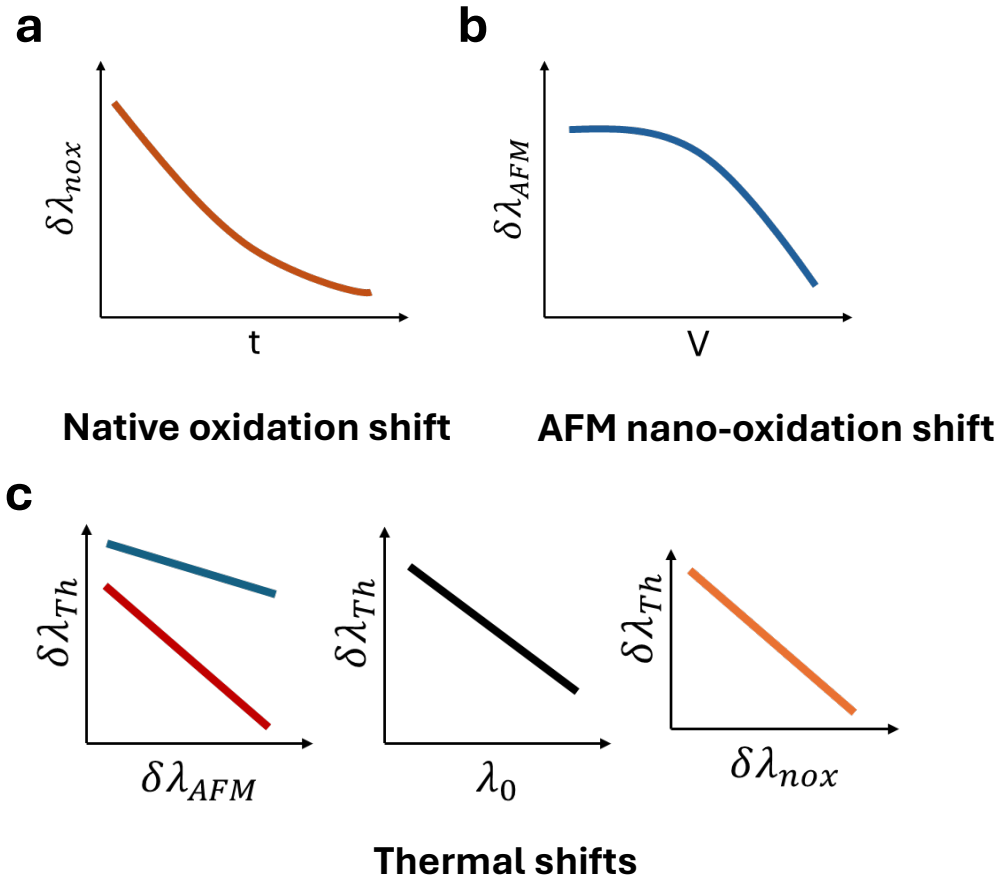

Figure 9.6: **Illustration of various sources of wavelength shifts.** **a,** Native oxidation-induced wavelength shift $\delta\lambda_{\mathrm{nox}}(t)$ as a function of time. **b,** Wavelength shift due to AFM nano-oxidation $\delta\lambda_{\mathrm{AFM}}(V)$ as a function of oxidation voltage. **c,** Thermal wavelength shifts as a function of (left) $\delta\lambda_{\mathrm{AFM}}$, (middle) initial room-temperature wavelength λ_0, and (right) $\delta\lambda_{\mathrm{nox}}$.

$$\lambda_{10\mathrm{mK}} = \lambda_0 + \delta\lambda_{\mathrm{nox}}(t) + \delta\lambda_{\mathrm{AFM}}(V) + \delta\lambda_{\mathrm{th}}(\delta\lambda_{\mathrm{AFM}}, \lambda_0, \delta\lambda_{\mathrm{nox}}). \tag{9.1}$$

A summary of these shifts we explored in previous section is shown in Figure 9.6 showing trend for a) native oxidation, b) AFM nano-oxidation and c) thermal shifts. The 'tuning knob' among these is the AFM nano-oxidation. An inverse algorithm then tells us the amount of oxidation needed and the wait time before starting the dilution refrigerator pumpdown to achieve a given wavelength $\lambda_{10\mathrm{mK}}$ at 10mK temperature.

We demonstrate this algorithm by tuning five OMCs on the same chip. Table 9.1 lists the initial room-temperature wavelengths λ_0 for each device, showing a standard

Table 9.1: Initial and final resonance wavelengths

Label	λ_0 **(nm)**	$\lambda_{\mathbf{10mK}}$ **(nm)**
λ_B	1561.451	1546.572
λ_M	1561.858	1546.488
λ_G	1562.132	1546.546
λ_Y	1562.322	1546.516
λ_R	1563.310	1546.550
Std Dev	0.694	0.032

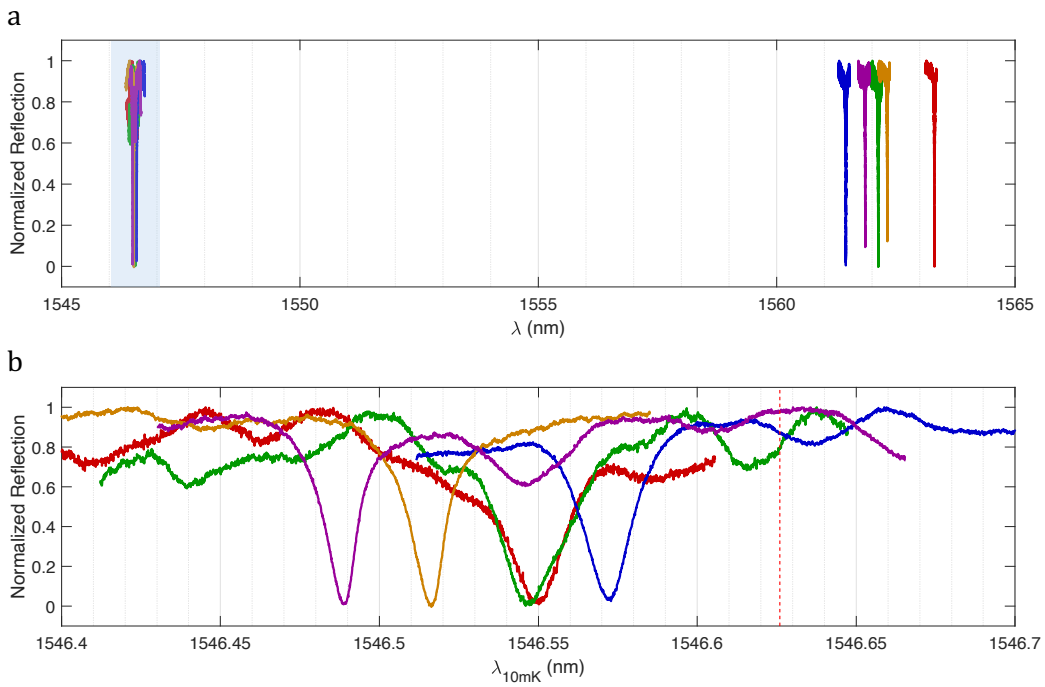

Figure 9.7: **Optical alignment of 5 OMCs at cryogenic temperatures. a,** Initial room temperature wavelengths after fabrication (right) and the final wavelengths measured at 10mK temperauture. **b,** Zoom-in of the shaded region from (a). Red dashed line indicates the target wavelength.

deviation of 692 pm due to nanofabrication disorder. The target wavelength at 10 mK is set to 1546.626 nm. Following the tuning algorithm, we applied AFM nano-oxidation to the five devices and cooled them to 10 mK. The resulting wavelengths, listed in the second column of Table 9.1, exhibit a significantly reduced standard deviation of just 32 pm.

Figure 9.7 shows the measured optical spectra before and after tuning. A global wavelength shift of 92 pm from the target wavelength (indicated by the red dashed

line in Figure 9.7b) was observed. This shift is attributed to the previously unaccounted dependence of $\delta\lambda_{\text{th}}$ on $\delta\lambda_{\text{nox}}$ in Equation 9.1. With this global offset known, future cooldowns can use the same sample loading time to compensate for this effect.

We also observed up to a 15% reduction in the intrinsic optical quality factor (Q_i) of the OMCs immediately after AFM nano-oxidation. However, this degradation was reduced to below 5% after cooling to cryogenic temperatures, consistent with the trend shown in Figure 9.2.

9.4 Discussion

In this work, we demonstrated a practical and scalable method to frequency-match optomechanical crystal (OMC) cavities using AFM-based nano-oxidation, enabling precise post-fabrication wavelength tuning at cryogenic temperatures. By applying this technique, we successfully aligned the optical resonance frequencies of five OMCs on the same chip to within approximately three optical linewidths (with one linewidth $\sim$10 pm). This level of precision represents a significant improvement over the typical disorder-induced spread observed in as-fabricated devices.

The tuning accuracy can be further improved by implementing tighter control over environmental factors such as temperature and humidity during the oxidation and cooldown process. Additionally, future studies could incorporate a refined calibration of the thermal wavelength shift due to native oxidation effects, enabling more accurate global corrections across cooldowns.

Importantly, this tuning technique is minimally invasive; while it introduces slight modifications to the device surface, it preserves the functionality and high optical quality of the optomechanical devices. Moreover, it is spatially selective and fully compatible with existing nanofabrication and packaging workflows. These features make it well-suited for scaling up to large arrays of frequency-aligned optomechanical devices, a key requirement for constructing scalable quantum networks. In particular, this approach enables the realization of multiple identical optomechanical nodes that can function as transducers or quantum memories for superconducting circuits.

Chapter 10

FUTURE DIRECTIONS

The side-coupled 2D optomechanical crystal (OMC) presented in this work represents a significant technical advancement in the field of optomechanics and transduction. By enabling a drastic improvement in phonon–photon conversion efficiency and mitigating optically induced heating, this architecture addresses two major bottlenecks in scaling optomechanical systems. The detailed analysis of optical absorption-induced heating, including its power-law dependence on optical energy and it's relation to disorder, not only improves our empirical understanding but also offers clues toward the physical origin of absorption and future mitigation strategies.

This work also establishes a foundation for integrating 2D-OMC platforms into next-generation microwave-to-optical quantum transducers. While the demonstrated systems show promise, further progress will require device iteration, tighter fabrication tolerances, and improved piezoelectric coupling g_{pe}. Looking forward, several promising directions can help realize higher efficiency, lower noise, and scalable integration:

1. **Niobium Based Superconducting Qubits:** Employing on chip niobium qubits with higher critical temperatures ($T_c > 9$ K) may lead to more robust and reproducible microwave circuits compared to NbN resonators. This approach requires process development for fabricating qubits on silicon on insulator (SOI) substrates with appropriate stress profiles. It may also help overcome limitations associated with thin film NbN, which is particularly sensitive to native oxidation, where even a few nanometers of oxide can cause significant frequency drift.

2. **Gap Engineered Qubits:** Recent studies have shown that gap engineered aluminum qubits exhibit reduced sensitivity to infrared induced quasiparticle generation [114]. A similar strategy could be extended to niobium based qubits, potentially improving optical isolation while maintaining high superconducting performance.

3. **Shielded Microwave Architecture:** Incorporating a physical "dome" or

shield around the microwave circuitry could suppress stray optical scattering that contributes to resonator degradation [10].

4. **Exploring Stronger Piezoelectric Materials:** Materials such as strontium titanate (STO) [115, 116] and barium titanate (BTO) offer higher piezoelectric coefficients than lithium niobate. Their use in transducers could enhance electromechanical coupling while allowing smaller volumes to be used, thereby retaining silicon-like mode profiles.

These strategies, in combination with scalable AFM nanooxidation frequency-tuning techniques, point toward the feasibility of building frequency-aligned arrays of optomechanical transducers, which are essential for quantum networking. A natural next milestone in this research would be to demonstrate entanglement between distant superconducting qubits mediated by optical photons.

Optically heralded entanglement between distant superconducting qubits

We consider the scheme shown in Figure 10.1, involving two nodes housed in separate dilution refrigerators. Each node contains a transducer module and a qubit module, connected via a low-loss microwave interconnect [89] and a circulator. The circulator enables unidirectional communication from the transducer to the qubit module and prevents the formation of standing waves in the interconnect. The optical outputs of the transducers are directed onto a 50:50 beamsplitter and subsequently onto superconducting nanowire single-photon detectors (SNSPDs).

The scheme employs a pulsed blue-detuned optical pump with detuning $\Delta = \omega_b$, activating the two-mode squeezing Hamiltonian. The protocol proceeds in the following steps:

1. In the absence of thermal noise, the blue-detuned pump generates a photon-phonon pair with probability p in each node:

$$|\psi\rangle_{a_1 b_1}, |\psi\rangle_{a_2 b_2} = \sqrt{1-p}\,|00\rangle + \sqrt{p}\,|11\rangle\,.$$

   The excitation probability p depends on the energy of the optical pump pulse, or more precisely, the integral of the scattering rate over the pulse duration: $p = \int \gamma_{\mathrm{OM}}\, dt$.

2. A microwave-acoustic beamsplitter Hamiltonian then swaps the acoustic excitation with a microwave excitation, resulting in a microwave-optical photon

pair:

$$|\psi\rangle_{a_1c_1}, |\psi\rangle_{a_2c_2} = \sqrt{1-p}\,|00\rangle + \sqrt{p}\,|11\rangle\,.$$

3. The microwave photon is absorbed by a superconducting qubit, leading to the joint state:

$$|\psi\rangle_{a_1q_1}, |\psi\rangle_{a_2q_2} = \sqrt{1-p}\,|0g\rangle + \sqrt{p}\,|1e\rangle\,,$$

where q_1 and q_2 denote the qubit states at nodes 1 and 2, respectively.

4. The optical signals from both nodes are combined on a beamsplitter:

   A. If no photon is detected, the protocol is restarted from step 1.

   B. If a single photon (herald) is detected on either of the detectors, the communication qubits are projected onto the entangled state:

$$|\psi\rangle_{q_1q_2} = \frac{1}{\sqrt{2}}\left(|ge\rangle + e^{i\phi}\,|eg\rangle\right) + \sqrt{p}\,|ee\rangle\,,$$

   where the phase ϕ is determined by which detector registers the photon.

This protocol forms a foundational building block for establishing long-distance entanglement between superconducting qubits using optical heralding. While significant challenges remain in scaling and stabilizing such architectures, the principles outlined here offer a promising pathway for uniting quantum information platforms operating at vastly different energy scales.

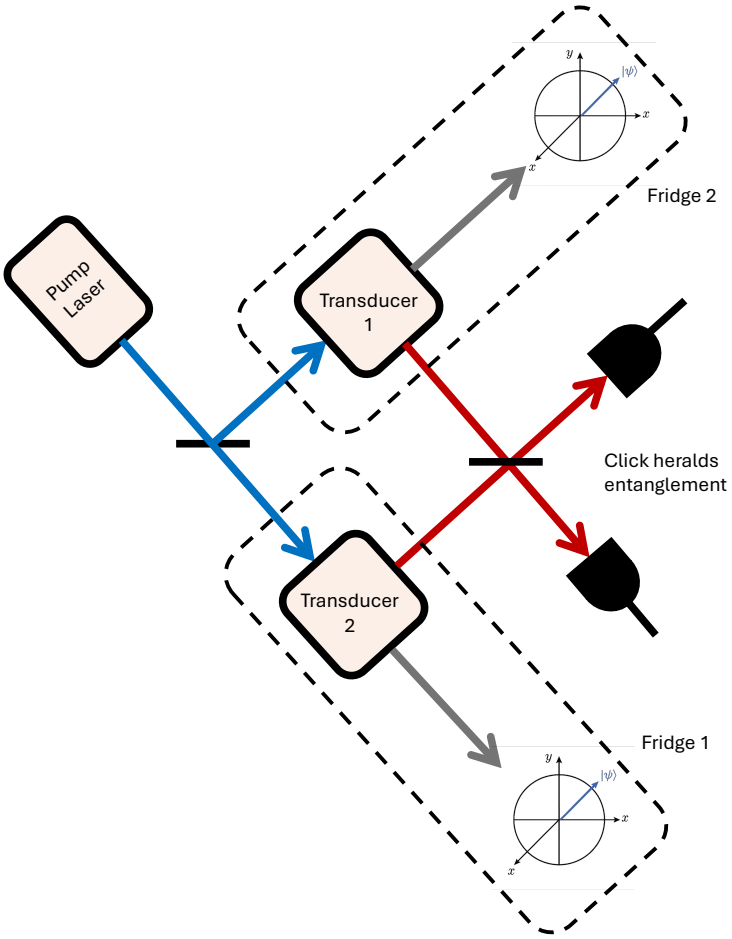

Figure 10.1: **Scheme for remote entanglement.** Pump laser photons (blue arrows) are split into two paths, each directed to a transducer housed in a separate dilution refrigerator. Each transducer functions as a microwave-optical photon pair source, generating a correlated microwave photon (brown arrow) and an optical photon (red arrow). The microwave photon is routed to a local superconducting qubit, while the optical photons are interfered on a beamsplitter and detected. A detection heralds successful entanglement between the remote qubits.

Appendix A

SUPPLEMENTARY INFORMATION FOR CHAPTER 3

A.1 Coupling waveguide spectrum optimization using FDTD simulations

Due to the nontrivial geometry of the coupling waveguide, careful optimization is required to achieve a clean optical reflection spectrum and suppress parasitic resonances that may interfere with the optical cavity. The finite difference time domain (FDTD) simulation setup, implemented in the ANSYS Lumerical software suite, is shown in Figure A.1a. The simulation begins with a Gaussian optical pulse coupled into a tapered optical waveguide. The reflected signal is measured using a monitor placed at the input, and the overlap between the input and reflected signals is used to extract the coupling efficiency between the lensed fiber and the on-chip waveguide.

Figure A.1b shows the simulated coupling efficiency as a function of wavelength. A clean reflection spectrum is obtained in the range of 1500–1600 nm. Outside this range, specifically below 1500 nm and above 1600 nm, broadband parasitic resonances appear due to reflections at various interfaces in the coupling waveguide. The central wavelength of the clean reflection window is optimized by adjusting the waveguide width and the dimensions of the half-snowflake structures patterned along its edge.

A.2 Alternative side-coupled 2D-OMC geometries

As discussed in Chapter 3, the primary goal while designing the side-coupled geometry is to mechanically decouple the optical coupling waveguide from the rest of the 2D-OMC structure. In the design process, we explored several strategies to achieve this. Figure A.2 illustrates various waveguide geometries investigated during this effort.

Panel a shows the butt-coupling geometry, where the coupling waveguide is physically detached from the sides. A key challenge in this design is engineering the physical cut: placing it too close to the optical cavity may degrade the quality factor due to fabrication-induced disorder, while placing it too far may result in the formation of a weak parasitic cavity between the cut end and the photonic crystal mirror of the optical cavity.

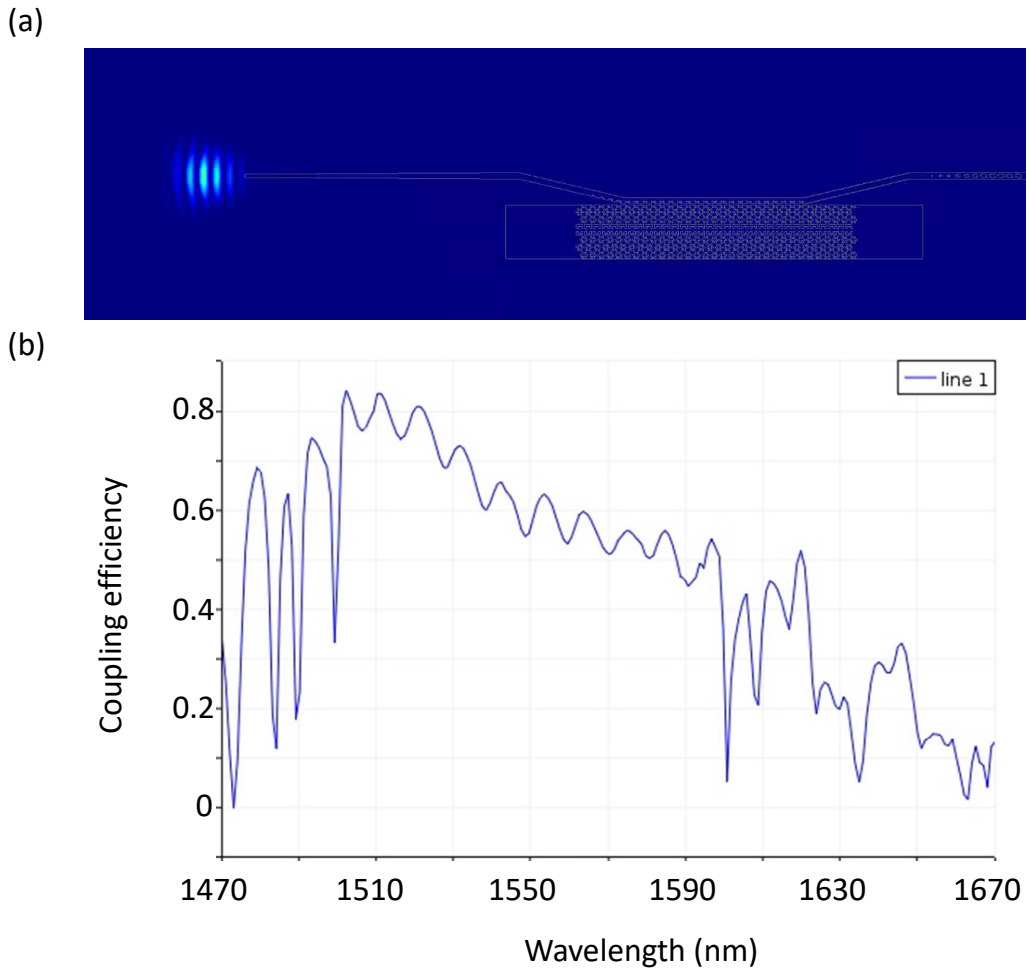

Figure A.1: **Coupling waveguide optimization using FDTD simulations. a,** FDTD simulation setup showing a Gaussian optical beam coupled into a tapered waveguide. **b,** Simulated fiber-to-chip coupling efficiency as a function of optical wavelength, illustrating a clean reflection spectrum in the range of 1500–1600 nm.

Panels b and c present the one-dimensional snowflake mirror geometry, where a row of 1D snowflakes, along with half-snowflakes at the edge of the coupler, serves as a broadband mirror to reflect the incoming signal. Although this approach offers mechanical separation, we observed a significantly reduced mirror bandwidth compared to the 100 nm bandwidth achieved in the design of Figure A.1.

Panels d and e show the hybrid 1D–2D geometry, designed to localize the optical mode across both 1D and 2D regions while confining the acoustic mode to the 2D region. The concept relies on using a tapered hole-size profile to guide the optical mode through the 1D section. However, simulations revealed a substantial reduction

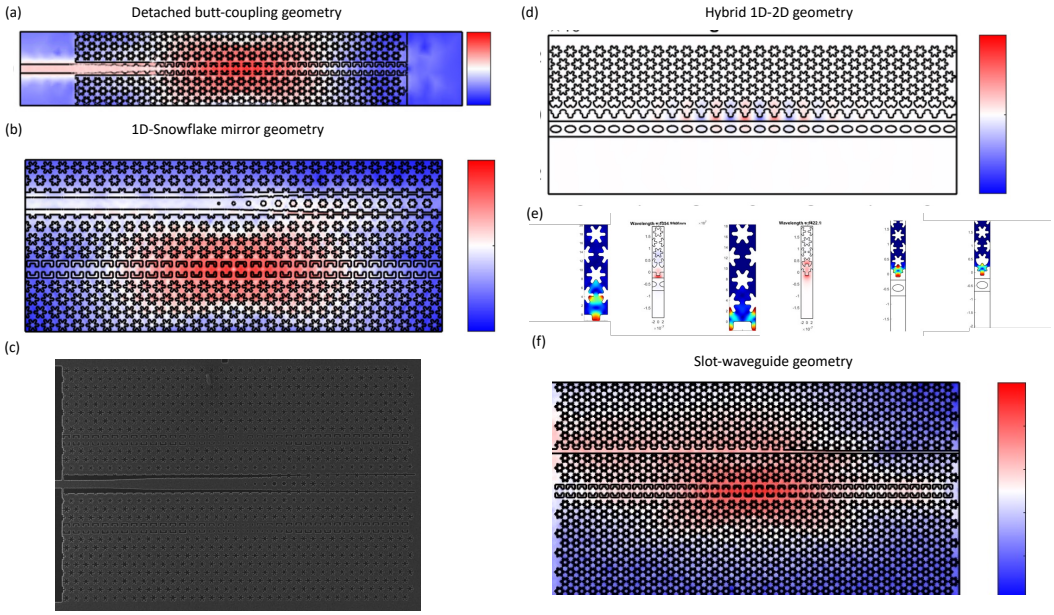

Figure A.2: **Various design geometries for side-coupled 2D-OMC. a,** Butt-coupling geometry with a detached optical waveguide. **b,** Side-coupling geometry using snowflake structures as mirrors for a one dimensional waveguide. **c,** Fabricated device corresponding to the simulation in panel b, showing 2D-OMC geometries on either side of the coupling waveguide. **d,** Hybrid 1D–2D geometry where the optical mode is distributed across both the 1D and 2D regions, while the acoustic mode is localized at the edge of the 2D geometry. **e,** Various trial designs for simulating unit cells of the hybrid 1D–2D geometry. **f,** Slot waveguide geometry in which the optical mode resides within the slot region.

in the optical quality factor, likely due to the broken vertical mirror-symmetry of the cavity (along the y-axis), which results in increased radiation loss.

Panel f displays the slot-waveguide geometry, where the optical mode propagates through a narrow slot. This mode can later be transformed into a dielectric waveguide mode using appropriate mode converters [34]. While this geometry offers promise in terms of mechanical stability, further design optimization is needed to make it viable for practical implementation.

Appendix B

SUPPLEMENTARY INFORMATION FOR CHAPTER 4

B.1 Mode occupancy calibration

To calibrate the acoustic mode phonon occupancy to the measured photon count rate on the single photon detector, we perform sideband asymmetry measurements [41]. The measured count rate for red and blue detuned pump laser are given by

$$\Gamma(\Delta = \pm\omega_\mathrm{b}) = \Gamma_\mathrm{dark} + \Gamma_\mathrm{pump} + \Gamma_\mathrm{SB,0}\left(n_\mathrm{th} + \frac{1}{2}(1 \pm 1)\right), \tag{B.1}$$

where n_th is the occupation of the acoustic resonator. Γ_dark is the dark count rate of the SPD, Γ_pump is the pump bleedthrough, and $\Gamma_\mathrm{SB,0}$ is the detected photon scattering rate per phonon. $\Gamma_\mathrm{SB,0}$ relates to the optomechanical scattering rate $\gamma_\mathrm{OM} = 4g_\mathrm{OM}^2 n_a/\kappa_a$ through the external detection efficiency, $\Gamma_\mathrm{SB,0} = \eta_\mathrm{ext}\gamma_\mathrm{OM}$. We use pulsed laser with repetition rate much smaller than the intrinsic decay rate ($R \ll \kappa_{i,b}$) such that the $n_\mathrm{th} \ll 1$ at the beginning of each pulse. $\Gamma_\mathrm{SB,0}$ can then be extracted by taking the difference between the count rate at the beginning of the pulse. For pulsed transduction measurements with short optical pulses shown in Figure 4.6 of the main text, the count rates for the red- and blue-detuned pump laser are averaged over the duration of the optical pulse. This averaging accounts for any finite rise time in the sideband scattering rates.

The hot bath measurements in the main text are performed with laser on cavity resonance $\Delta = 0$. The count rate $\Gamma(\Delta = 0)$ relates to $\Gamma_\mathrm{SB,0}$ through the sideband resolution factor $(2\omega_b/\kappa_a)^2$

$$\Gamma(\Delta = 0) = \Gamma_\mathrm{dark} + \Gamma_\mathrm{pump} + \left(\frac{\kappa_a}{2\omega_\mathrm{b}}\right)^2 \Gamma_\mathrm{SB,0} n_\mathrm{m}, \tag{B.2}$$

where n_m is the measured thermal occupation in the absence of the optomechanical backaction as defined by equation 4.1 of the main text.

B.2 Full measurement setup

The measurement setup used for the cryogenic measurements is shown in Figure B.1. A fiber-coupled, wavelength-tunable external cavity diode laser is used as the pump for all measurements. A small percentage of the laser output is sent to a wavemeter

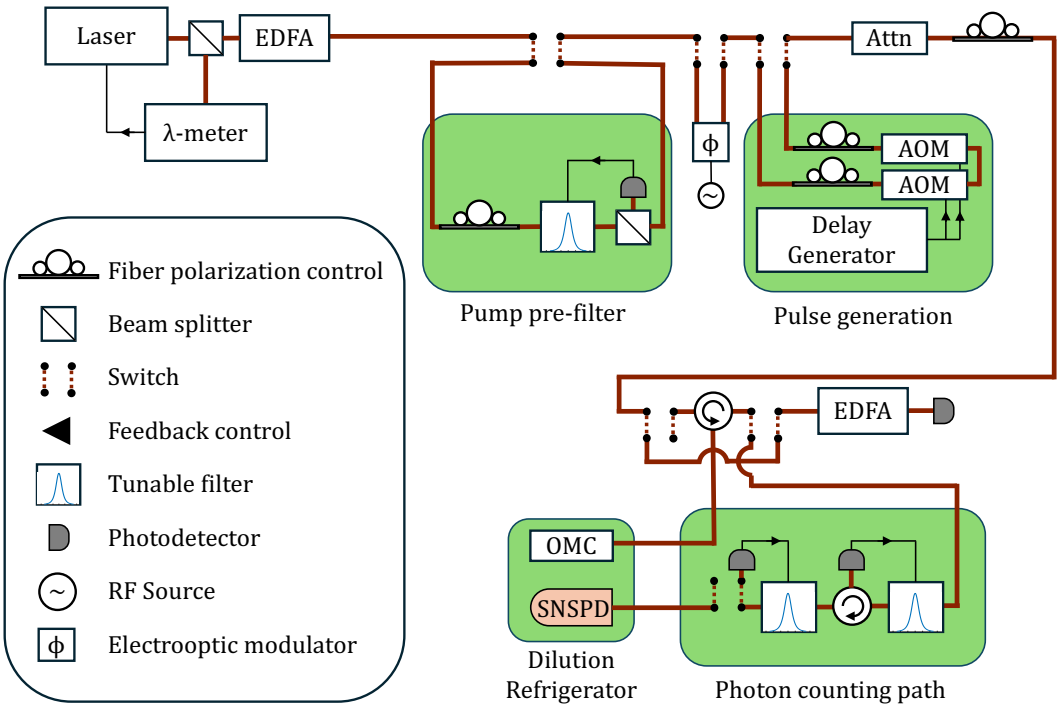

Figure B.1: **Experimental setup.** An external cavity diode laser is used to generate the optical pump signal. A small percentage of laser power is used for wavelength locking using a wavemeter (λ-meter). The laser is then passed through an Erbium Doped Fiber Amplifier (EDFA) to amplify the power, followed by a 50 MHz-bandwidth filter. It then can be switched through an Electro-optic phase modulator (ϕ) which is used during the locking sequence of the filter-bank in the photon counting path. The laser can then be switched between two different paths: (i) Continuous wave measurements (ii) a pulsed measurements. In the pulsed measurements path, two acousto-optic modulators (AOM) in series are used for generating high-extinction optical pulses which are triggered by a delay generator. Before sending to the device in the dilution refrigerator (DF), the laser is passed through a variable optical attenuator (Attn) to adjust the optical power. Upon reflection, a circulator routes the reflected laser light to either: (i) spectroscopy photo-detectors which are used for measurements of optical and acoustic spectrum, or (ii) a photon counting path consisting of two cascaded Fabry-Perot filters and a SPD operated at 800 mK.

(λ-meter) for wavelength stabilization. The laser is then amplified with an EDFA and then passed through a 50 MHz-bandwidth tunable fiber Fabry-Perot filter (Micron Optics FFP-TF2) to suppress broadband spontaneous emission noise. An electro-optic phase modulator (ϕ) in the bypass path is used to generate a sideband on the laser during the locking sequence for the sideband filters on the detection path. The

pre-filtered pump laser could be switched between (i) a continuous-wave measurement path, and (ii) a pulsed measurement path. On the latter path, we used two acousto-optic modulators (AOMs, G&H Photonics) in series to create optical pulses with extinction >120 dB on the pump laser. A digital delay generator (Stanford Research Systems DG645) is used to synchronize AOM drive pulses and trigger signals for the time-correlated single photon counting module (TCSPC, Swabian Time Tagger X).

Pump laser light is then routed via a variable optical attenuator (Attn) and a circulator into the dilution refrigerator where the sample test assembly is mounted to the mixing chamber plate cooled down to a base temperature of 10mK. A lensed optical fiber is used to couple light into the device under test. The fiber is mounted to a three-axis nanopositioner stack (Attocube Systems) which allows for in situ alignment with respect to the optical coupler on the device. The reflected pump and signal from the device can be directed via the circulator to (i) a room-temperature photodetection path with a slow detector and a fast detector (New Focus 1554B) for optical and mechanical spectroscopy, or (ii) the single-photon counting path. On the single-photon counting path, the light is passed through two tunable, fiber-coupled Fabry-Perot cavities (Stable Laser Systems) to suppress pump light reflected from the device. The filters have a bandwidth of 3.6 MHz, a free-spectral range of 15 GHz, and are connected in series with a fiber-optic circulator in between them. This setup provides approximately 100 dB of extinction for the pump light detuned by ~10 GHz from the resonance frequency.

During measurements, a locking routine is periodically used to verify that the filters are on resonance with the signal frequency. During the locking routine, we bypass the device path and generate sidebands on the pump laser by driving the EOM (ϕ) with a microwave tone at the mechanical resonance frequency of the device under test. To re-lock the filters, a sinusoidal voltage was used to dither each filter while monitoring its transmission on a slow detector. The DC offsets of the dithering signal are then changed while reducing the voltage amplitude to align the filters to the expected signal frequency from the device. After re-locking, a new round of measurements can be performed.

For single-photon counting, we used a NbN superconducting nanowire single-photon detector developed by the Jet Propulsion Laboratory (JPL). The SPD is mounted on the still plate of the dilution refrigerator at ~ 800 mK. The electrical output of the SPD is amplified by a room temperature amplifier circuit [117] and

read out by a triggered single photon counting module (Swabian Time Tagger X). To minimize the dark counts on the SPD, we filter out long wavelength infrared spectrum noise by creating fiber loops before SPD with a diameter of 1.5 inches. We observed dark count rates as low as ~ 4 (c.p.s.) and a SPD quantum efficiency $\eta_{\mathrm{SPD}} \simeq 75\%$ in our setup.

B.3 Sideband filter chain transmission factor

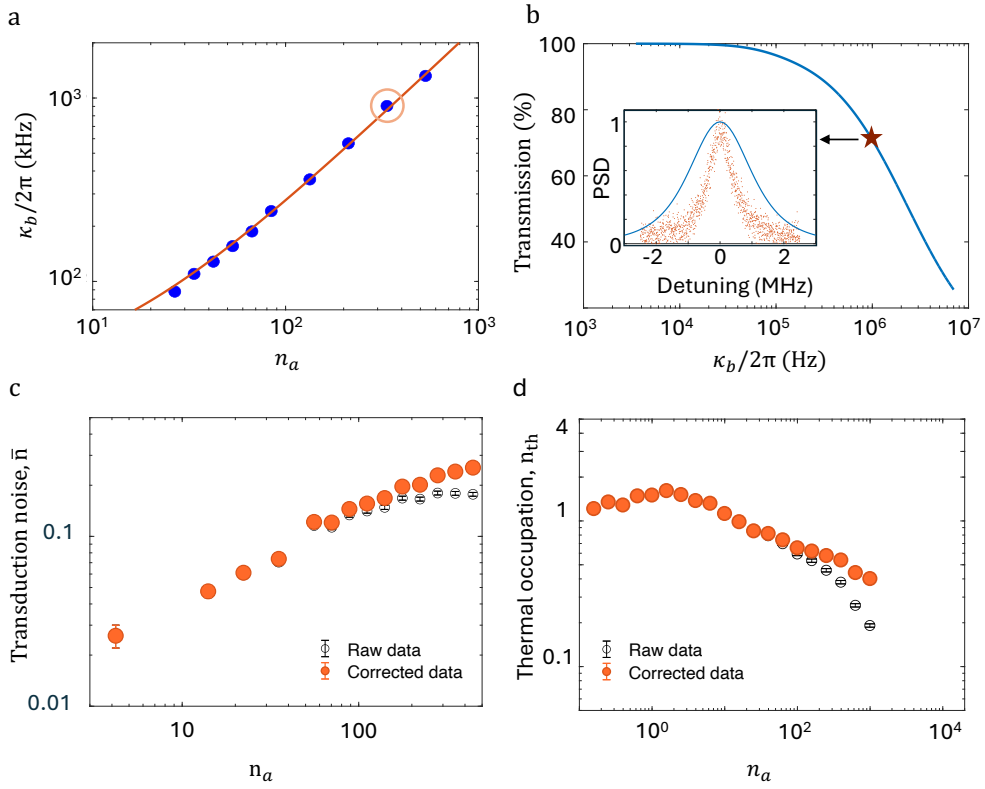

Figure B.2: **Sideband filter chain transmission: a,** total acoustic linewidth as a function of n_a measured using Electromagnetically induced transparency method (EIT) [40]. **b,** transmission through the filter chain as a function of the acoustic linewidth. The inset shows the normalized power spectral density of the filter chain (blue) and that for acoustic sideband (red) for data point marked with circle in panel a ($n_a = 335$). **c,** phonon occupancy in pulsed mode for device II. The raw data is shown in magenta whereas the corrected data is shown in blue. **d,** phonon occupancy in continuous wave mode for device II. The black circles show the raw measured data whereas the orange circles show the corrected data.

The sideband filter chain is parked at the acoustic sideband of the pump to detect the optomechanically scattered photons, while filtering out the pump. However, at large pump powers, the bandwidth of the optomechanical sideband κ_b approaches

that of the filter (=3.6 MHz). This overlap leads to a reduced measured count rate, resulting in an inaccurate estimation of phonon occupancy. Figure B.2(a) shows the acoustic linewidth κ_b as a function of n_a. Measurements are performed using Electromagnetically Induced Transparency (EIT) technique where a pump laser is placed on red sideband and a weak probe scans across a few Megahertz bandwidth across the acoustic sideband at the cavity resonance. κ_b is the sum of the optomechanical backaction γ_{OM}, intrinsic linewidth $\kappa_{i,b}$, coupling rate to the hot bath κ_p, and the pure dephasing rate κ_ϕ. For two bandpass filters in series, the transmission T of an acoustic sideband with lorentzian profile is given by

$$T = \int_{-\infty}^{\infty} H_1(f) H_2(f) \frac{\kappa_b(f)}{2\pi} df \tag{B.3}$$

where $H_{1,2} = (1 + (\frac{f}{\mathrm{FWHM}_{1,2}/2})^2)^{-1}$ is the normalized spectral response of each filter with $\mathrm{FWHM}_{1,2}$ = 3.6 MHz. The corrected phonon occupancy n_{th} can then be calculated using measured phonon occupancy $n^{\star}_{\mathrm{th}}$ using the relation

$$n_{\mathrm{th}} = n^{\star}_{\mathrm{th}} \times \frac{1}{T} \int_{-\infty}^{\infty} \frac{\kappa_b}{2\pi} df. \tag{B.4}$$

Figure B.2(b) shows the transmission factor T as a function of $\kappa_b/2\pi$. The inset shows the normalized power spectral density of the combined filter chain response (blue), and the acoustic response for $n_a = 335$. Figure B.2(c) shows the phonon occupancy before (black) and after (orange) correction in pulsed laser mode for device II. Figure B.2(d) shows the same in continuous wave mode for device II. In the case of κ_p and n_{p} measurements where the pump is placed at the optical cavity resonance, the linewidth of acoustic sideband is much smaller than the filter linewidth ($\kappa_p + \kappa_{i,b} \ll 2\pi * 3.6$ MHz) for n_a range measured in this study, so a correction factor is not required.

Appendix C

SUPPLEMENTARY INFORMATION FOR CHAPTER 7

In this chapter, we discuss additional aspects of the nanofabrication process for the full transducer that were not covered in the main text.

C.1 Dry etching recipe parameters

Table C.1: ICP-RIE deep etch recipe parameters at university cleanroom

Parameter	**Substrate SOI layer**		
	Device-layer Si	**SiO_2**	**Handle Si**
C_4F_8 flow (sccm)	50	70	0
SF_6 flow (sccm)	21	0	160
O_2 flow (sccm)	0	5	0
RF power (W)	15.5	150	0
ICP power (W)	600	2200	2500
D.C. bias (V)	60	205	20
Chamber pressure (mTorr)	10	8	90
Helium pressure (Torr)	10	5	10
Helium flow (sccm)	5.0	5.0	5.0
Table temperature (°C)	15	15	15
Etch rate (nm/min)	48	300	2900

Table C.2: ICP-RIE recipe parameters for silicon etch at Painter lab cleanroom

Parameter	**Device-layer Si**
C_4F_8 flow (sccm)	72
SF_6 flow (sccm)	30
RF power (W)	18
ICP power (W)	600
D.C. bias (V)	16
Chamber pressure (mTorr)	15
Helium pressure (Torr)	5
Helium flow (sccm)	5.0
Table temperature (°C)	15
Etch rate (nm/min)	55

C.2 Vapor HF vs aqueous HF for release

In an effort to improve the cleanliness of our devices, we explored wet HF release, which is known to leave less residue than vapor HF due to reduced contamination.

Table C.3: ICP-RIE recipe parameters for NbN etch at university cleanroom

Parameter	**NbN**
SF_6 flow (sccm)	10
Ar flow (sccm)	20
RF power (W)	20
ICP power (W)	300
D.C. bias (V)	50
Chamber pressure (mTorr)	10
Helium pressure (Torr)	4
Helium flow (sccm)	20
Table temperature (°C)	10
Etch rate (nm/min)	10

Table C.4: ICP-RIE recipe parameters for AlN etch at university cleanroom

Parameter	**AlN**
Cl_2 flow (sccm)	30
Ar flow (sccm)	73
RF power (W)	120
ICP power (W)	600
D.C. bias (V)	130
Chamber pressure (mTorr)	10
Helium pressure (Torr)	4
Helium flow (sccm)	16
Table temperature (°C)	25
Etch rate (nm/min)	125

Figure C.1 presents a comparison between the two release methods. The wet HF process (49% concentration) indeed results in cleaner devices overall; however, we consistently observed peeling of the NbN films, a phenomenon not seen with vapor HF.

In contrast, vapor HF release avoids film delamination but produces a visible byproduct resulting from a chemical reaction between NbN, vapor HF, and silicon oxide. This residue tends to deposit on or near the NbN resonators. While it does not appear to significantly degrade the mechanical quality factor of the resonators, such contamination may land on sensitive regions of the structure, including the optical mode volume, potentially reducing the optical quality factor.

Figure C.1: **Comparison of vapor HF and wet HF release.** NbN films exhibit peeling when devices are released using wet HF (49% concentration), followed by critical point drying. In contrast, devices released using vapor HF do not show peeling. However, a chemical reaction involving NbN, vapor HF, and silicon oxide appears to produce a byproduct that deposits on or near the NbN resonators.

C.3 Coupling waveguide stability in an integrated piezo-optomechanical transducer

The optical coupling waveguide in our 2D-OMC transducer geometry is approximately 1 mm long, making it susceptible to bending and tilting. Moreover, the inherent stress profile in the device layer favors out-of-plane deformation, which further destabilizes the waveguide due to its extended length. The fabrication process for full transducers begins with an AlN-on-SOI stack, which introduces a different stress profile compared to pure SOI substrates. This additional stress contributes to structural instability and results in reduced internal quality factors of the optical resonators.

To address this issue, we implemented anchors, as shown in Figure C.2. These

anchors are designed with a width of less than 50 nm, minimizing optical scattering while providing sufficient mechanical support. With this modification, we observed a highly stable and reproducible waveguide structure at both room temperature and cryogenic temperatures down to 10 mK.

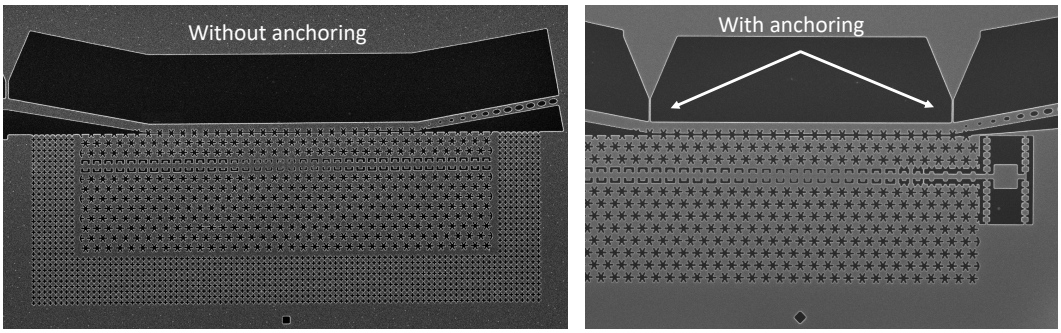

Figure C.2: **Comparison of coupling waveguides with and without anchoring.** Shown are OMC devices fabricated on SOI substrates stripped of aluminum nitride: (left) without anchoring and (right) with anchoring. The anchored design improves mechanical stability of the coupling waveguide.

Appendix D

SUPPLEMENTARY INFORMATION FOR CHAPTER 8

D.1 Characterization of nano-oxidation

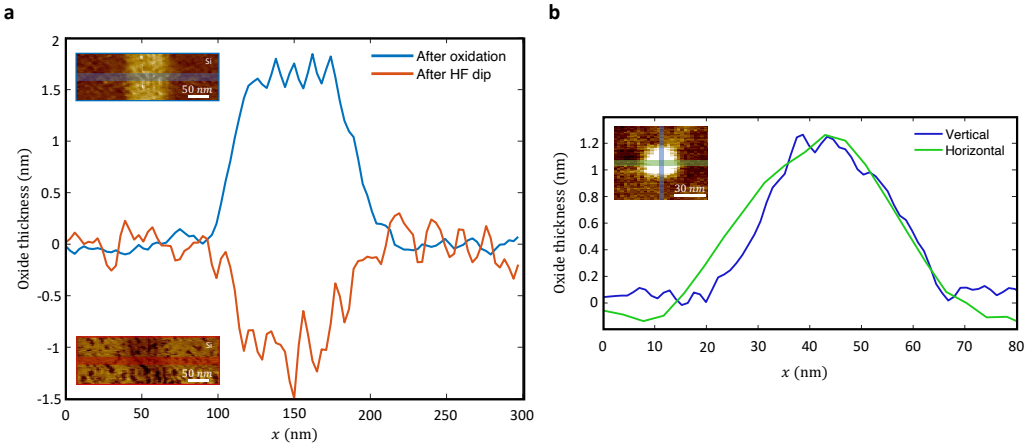

Figure D.1: **Characterization of nano-oxidation on a silicon chip. a,** Height profile of the oxide slab created by nano-oxidation (blue trace), and the depth profile obtained after removal of the oxide slab using a hydrofluoric acid etch (red trace). Insets show the AFM scan of the oxide slab (top) and the etched trench (bottom) along with horizontal line cuts used to sample the traces on the main plot. **b,** Height profile of an oxide pixel along x and y axes indicating a lateral size of ~25 nm. Inset shows the AFM scan of the oxide pixel along with x and y line cuts used to sample the traces on the main plot.

The nano-oxidation process generates oxide beneath and above the surface of silicon. Here we describe the procedure used to assess the ratio of oxide height and depth above and below the silicon surface, respectively. We first measure the post-oxidation height by performing AFM scans in the tapping mode. Subsequently, we etch the oxide in an anhydrous hydrofluoric acid vapor etching tool (SPTS PRImaxx uEtch), and perform AFM scans of the resulting trenches in silicon. The data obtained, as depicted in Figure D.1a, indicates that the oxide thickness beneath the surface is approximately 70% of the total measured thickness above the surface. Figure D.1b shows the characterization of a single oxide pixel generated in the mild oxidation mode. The size of the pixel is approximately 25nm along both x and y axes. We utilize such oxide pixels for fine-tuning of both optical and acoustic resonances in real-time as discussed in the main text.

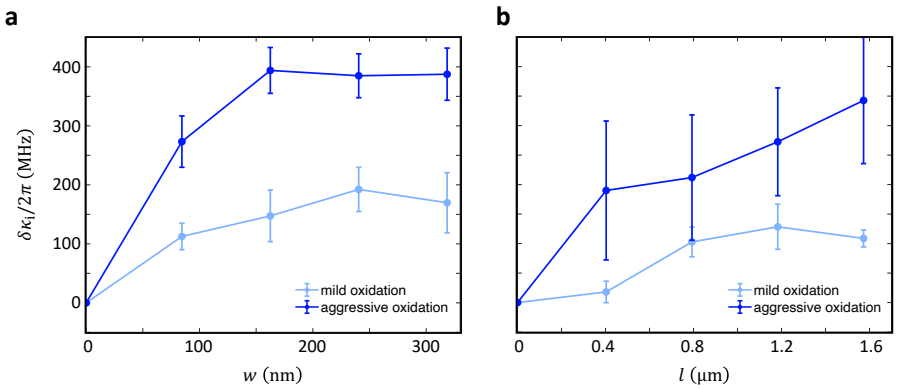

Figure D.2: **Effect of nano-oxidation on the intrinsic optical scattering rate during coarse tuning.** Change in intrinsic optical scattering rate $\delta\kappa_i$ with respect to the **a**, width w of the optics-focused oxidation pattern, and **b**, length l of the acoustics-focused pattern. Data is obtained in both mild and aggressive oxidation modes. Error bars represent the standard deviation measured across five OMCs.

D.2 Optical scattering due to nano-oxidation

In addition to altering the mechanical and optical characteristics of the local silicon surface, the nano-oxidation process can introduce roughness and additional scattering sites. Consequently, we observe an increase in the intrinsic optical scattering rate ($\kappa_i/2\pi$) during our coarse tuning experiments. As shown in Figure D.2, the change in $\kappa_i/2\pi$ is more pronounced upon increasing the size of the oxidation patterns and the thickness of the oxide layer. For optics-focused patterns generated in regions with high electric field intensity, we observe a substantial increase in $\kappa_i/2\pi$. A maximum change in $\kappa_i/2\pi$ of approximately 440 MHz is noted for the aggressive oxidation case when $w < 350$ nm. For the mild oxidation case, the change in $\kappa_i/2\pi$ is less than 200 MHz. In the case of the acoustics-focused pattern, the change in $\kappa_i/2\pi$ is less than 400 MHz for aggressive oxidation case, and less than 150 MHz for mild oxidation case when $l < 1.6$ μm.

D.3 FEM simulations for pixel-by-pixel oxidation and selectivity analysis

Figure D.3a and b show the results of FEM simulations where we mapped out how the location of a single oxidation pixel affects the optical wavelength and acoustic frequency, respectively. These profiles closely match the optical intensity and acoustic displacement profiles shown in Fig.8.2 of the main text. This is expected because oxidation at points with larger optical field concentration leads to larger change in optical energy, and thereby in the optical resonance wavelength. Similarly, oxidation at the points of maximum displacement leads to a larger fractional

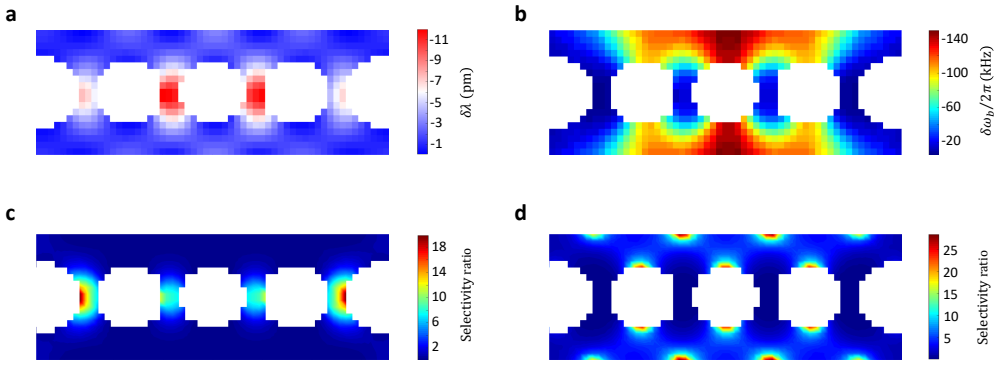

Figure D.3: **FEM simulations for pixel-by-pixel oxidation.** **a**, Optical resonance wavelength shift, $\delta\lambda$ and **b**, mechanical resonance frequency shift, $\delta\omega_b/2\pi$ simulated as a function of the location of the oxide pixel. Each oxide pixel is 25x25 nm in size with a thickness of 3.2 nm. **c**, Interpolated normalized optical selectivity, $\delta\lambda/\delta\omega_b$ and **d**, interpolated normalized acoustic selectivity, $\delta\omega_b/\delta\lambda$. The normalization is performed with respect to the maximum shifts obtained in the pixel-by-pixel oxidation profiles in panels a and b.

change in effective mass of the acoustic mode, and thereby in the acoustic resonance frequency. The exact material properties of the thin film oxide such as the density, Young's modulus and relative permittivity are specific to the oxidation process. In our approach, we use these material properties as variables and then we find what scaling allows us to match the coarse tuning experiment (Fig. 8.4 of the main text) and simulations. This way, we found that the density, Young's modulus and relative permittivity of oxide are 3500 kg/m^3, 70 GPa and 2, respectively. In the acoustic simulations, we use the anisotropic elasticity tensor of silicon with (C_{11}, C_{12}, C_{44}) = (166, 64, 80) GPa and assume a [110] crystallographic orientation for the x-axis.

In Figure D.3c and d, we plot the normalized optical selectivity, $\delta\lambda/\delta\omega_b$ and normalized acoustic selectivity, $\delta\omega_b/\delta\lambda$. Here, $\delta\lambda$ and $\delta\omega_b$ are normalized with respect to the maximum value calculated in the pixel-by-pixel oxidation profiles in Figure D.3a, b. In the case of fine tuning experiments where we seek small frequency shifts, we concentrate on the high selectivity regions. However, the locations with maximum optical selectivity, $\delta\lambda/\delta\omega_b$ do not coincide with those that produce maximum optical tuning $\delta\lambda$. Likewise, the regions with maximum acoustic selectivity are relatively small and localized at the edge of the silicon-air boundary. As a result, for coarse tuning experiments, it is more practical to use large oxide patches as opposed to individual pixels to achieve large tuning at the expense of selectivity. Details of the pattern generation algorithm used to generate the large oxide patches

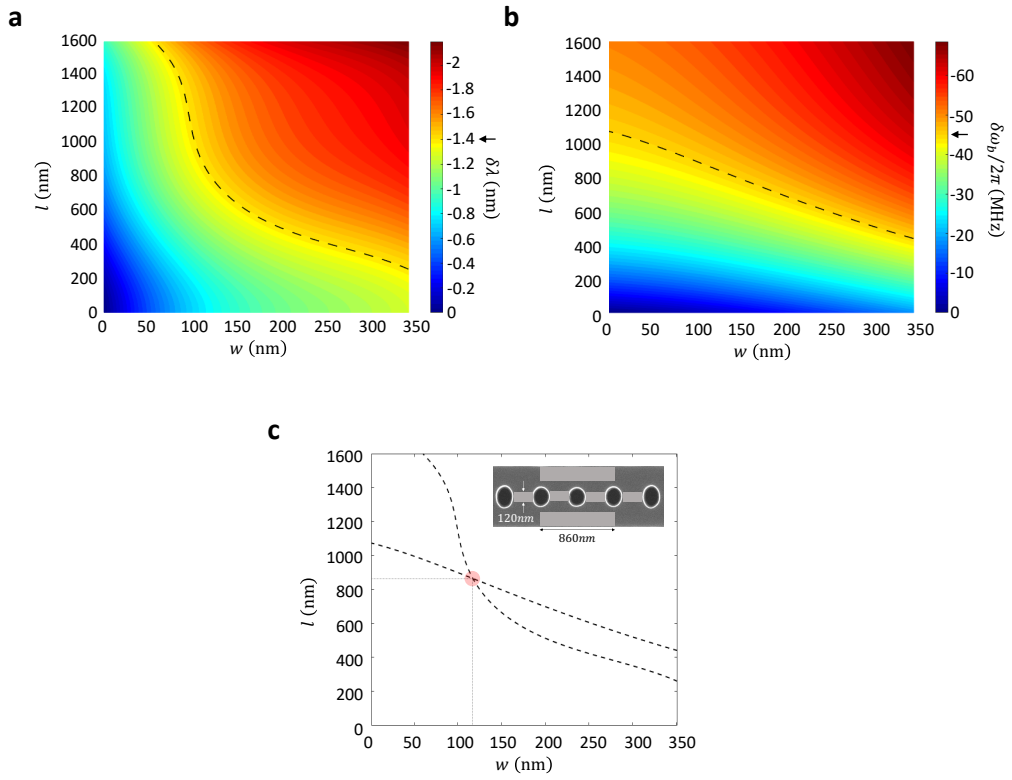

Figure D.4: **Pattern generation matrices for coarse tuning.** An example pair of experimentally determined pattern generation matrices used for aggressive optical - aggressive acoustic oxidation. **a**, Optical wavelength shift, $\delta\lambda$ and **b**, mechanical frequency shift, $\delta\omega_b/2\pi$ as a function of the width of the optics-focused component, w, and length of the acoustics-focused component, l of a joint pattern. All other dimensions and parameters are kept constant. The matrices are generated by spline interpolation of experimentally measured frequency shift data. **c**, Pattern dimension contours corresponding to $\delta\lambda = -1.4$ nm and $\delta\omega_b/2\pi = -45$ MHz. The intersection of both curves is used to determine l and w for the joint pattern used for coarse tuning. Inset shows the joint pattern corresponding to the calculated dimensions.

are given in Appendix D.4.

D.4 Nano-oxidation pattern generation algorithm

The results from coarse tuning experiments in Fig.8.4 of the main text show frequency shifts generated by either the optics-focused or the acoustic-focused pattern type. In practice, we require a union of both types of patterns to tune both optical and acoustic resonances. To enable the generation of such joint patterns, we first interpolate results from coarse oxidation experiments to create an oxidation map with frequency shifts measured with just the optics-focused and acoustic-focused

patterns. Our pattern generation algorithm uses this map to find a suitable joint pattern to target the desired simultaneous shift in optical and acoustic resonances. The pattern search begins with mild oxidation patterns and progresses to aggressive oxidation patterns if larger frequency shifts are desired. A pattern is deemed suitable if the calculated resonance shifts can target the desired optical wavelength to within 200 pm and the desired acoustic resonance to within 5 MHz. The pattern generation maps presented in Fig. D.4a,b correspond to the aggressive optical - aggressive acoustic oxidation scenario. There are three other pairs of pattern generation maps corresponding using mild optical - mild acoustic, mild optical - aggressive acoustic, and mild optical - aggressive acoustic oxidation scenarios. To illustrate the pattern search process, Figs. D.4a, b show contours corresponding to an example scenario where shifts, $\delta\lambda = -1.4$ nm and $\delta\omega_b/2\pi = -45$ MHz, are desired. As shown in Fig. D.4c, the intersection of these two contours allows us to estimate the required joint pattern with a width, $w \sim 120$ nm for the optics-focused component and length, $l \sim 860$ nm for the acoustics-focused component.

D.5 Simultaneous tuning of three OMCs: step-by-step process

In this section, we describe in detail the step-by-step tuning protocol used for frequency alignment of three OMC cavities. This involves a series of coarse tuning steps followed by real-time fine tuning steps. The experimental results for each step are shown in Fig. D.5.

1. **Step 0**: We started with three OMC cavities (red, magenta, blue) whose optical wavelengths and acoustic frequencies are λ = (1553.891, 1553.381, 1553.123) pm and $\omega_b/2\pi$ = (5.057, 5.047, 5.053) MHz, respectively.

2. **Step 1-3**: We feed λ and $\omega_b/2\pi$ to the pattern generation algorithm which generates patterns to tune each OMC to the target frequencies.

3. **Step 4-7**: At the end of step 3, all 3 OMC cavities are within a suitable range for fine tuning (typically 200 pm and 5 MHz for optics and acoustic resonances). We then employ pixel-by-pixel oxidation to fine tune the resonances while monitoring their values in real-time. The corresponding real-time wavelengths and frequencies are shown in the right most column of Fig. D.5.

At the end of three coarse and four fine tuning steps, we achieve optical wavelengths of 1553.031 nm, 1553.029 nm and 1553.031 nm and acoustic frequencies of 5.0261

GHz, 5.0264 GHz and 5.0266 GHz for the three OMCs. This indicates simultaneous optical wavelength and acoustic frequency matching within 2 pm and 500 kHz, respectively.

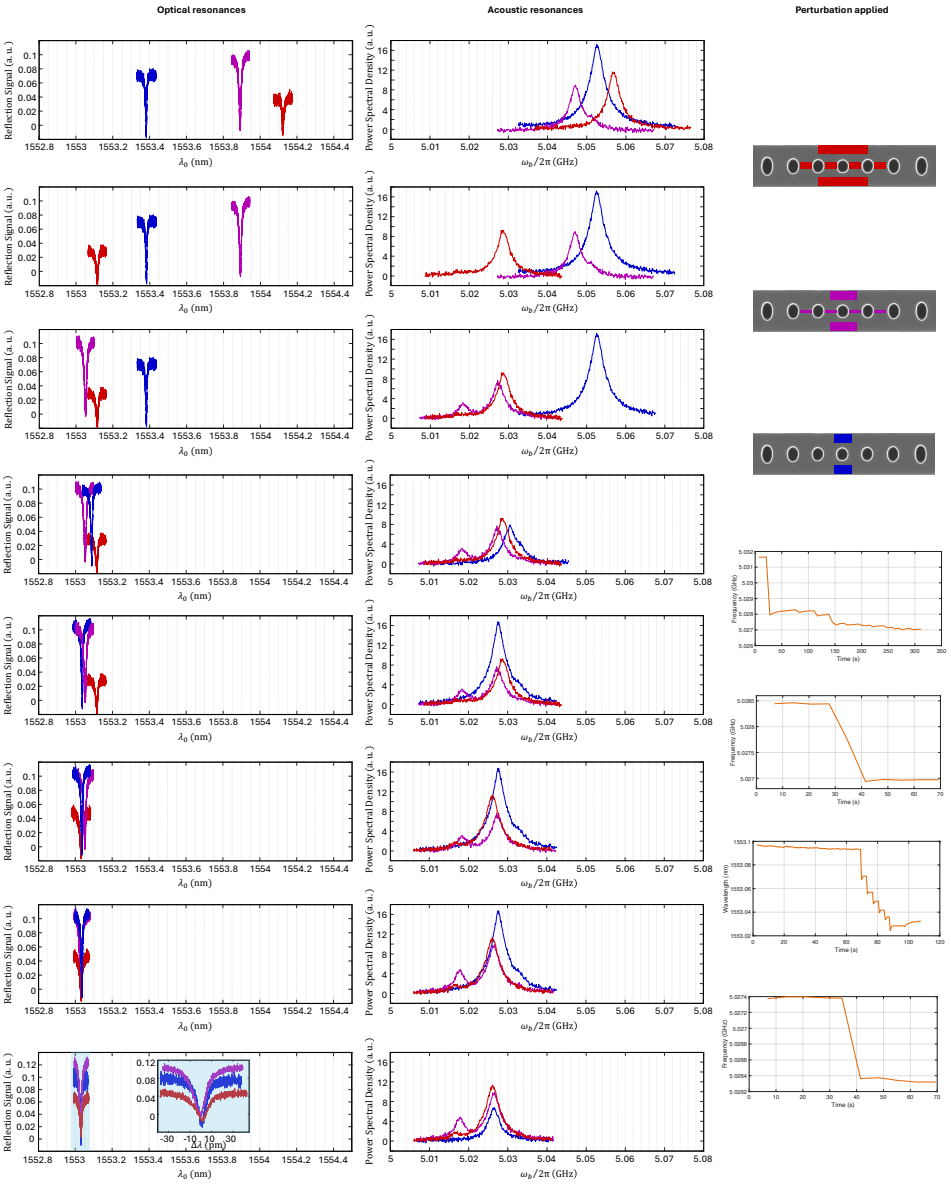

Figure D.5: **Simultaneous optical and acoustic frequency alignment of three OMCs.** Step 0 shows the initial condition of three OMCs. In steps 1-3, we generate coarse tuning patterns via the pattern generation algorithm and apply them to the corresponding OMCs. These patterns are color coded for each OMC and shown in the right column of the figure. In steps 4-7, we perform real-time fine tuning of both optical and acoustic resonances. Optical and acoustic spectra monitored during the nano-oxidation sequence in real-time are shown in the right column of the figure for each step. In step 7, the final states of e optical and acoustic resonances on the three devices are shown. The inset shows a zoomed-in plot of the three optical resonances. This seven step process allows for optical and acoustic resonance matching to within 2 pm and 500 kHz, respectively.

BIBLIOGRAPHY

[1] R. P. Feynman. “Simulating physics with computers, International journal of theoretical physics”. In: (1982).

[2] P. W. Shor. “Algorithms for quantum computation: discrete logarithms and factoring”. In: *Proceedings 35th annual symposium on foundations of computer science*. Ieee. 1994, pp. 124–134.

[3] P. W. Shor et al. *Polynomial-time algorithms for prime factorization and discrete logarithms on a quantum computer. Los Alamos Physics Preprint Archive*. 1995.

[4] L. K. Grover. “A fast quantum mechanical algorithm for database search”. In: *Proceedings of the twenty-eighth annual ACM symposium on Theory of computing*. 1996, pp. 212–219.

[5] G. Q. AI et al. “Quantum error correction below the surface code threshold”. In: *Nature* 638.8052 (2024), p. 920.

[6] IBM Quantum. *IBM Quantum Roadmap*. Accessed: 2024-03-15. 2024. URL: https://www.ibm.com/roadmaps/quantum/.

[7] H. Putterman, K. Noh, C. T. Hann, G. S. MacCabe, S. Aghaeimeibodi, R. N. Patel, M. Lee, W. M. Jones, H. Moradinejad, R. Rodriguez, et al. “Hardware-efficient quantum error correction via concatenated bosonic qubits”. In: *Nature* 638.8052 (2025), pp. 927–934.

[8] L. S. Madsen, F. Laudenbach, M. F. Askarani, F. Rortais, T. Vincent, J. F. Bulmer, F. M. Miatto, L. Neuhaus, L. G. Helt, M. J. Collins, et al. “Quantum computational advantage with a programmable photonic processor”. In: *Nature* 606.7912 (2022), pp. 75–81.

[9] H. Aghaee Rad, T. Ainsworth, R. Alexander, B. Altieri, M. Askarani, R. Baby, L. Banchi, B. Baragiola, J. Bourassa, R. Chadwick, et al. “Scaling and networking a modular photonic quantum computer”. In: *Nature* (2025), pp. 1–8.

[10] P. team. “A manufacturable platform for photonic quantum computing.” In: *Nature* (2025), pp. 1–3.

[11] H.-S. Zhong, H. Wang, Y.-H. Deng, M.-C. Chen, L.-C. Peng, Y.-H. Luo, J. Qin, D. Wu, X. Ding, Y. Hu, et al. “Quantum computational advantage using photons”. In: *Science* 370.6523 (2020), pp. 1460–1463.

[12] D. Gao, D. Fan, C. Zha, J. Bei, G. Cai, J. Cai, S. Cao, F. Chen, J. Chen, K. Chen, et al. “Establishing a new benchmark in quantum computational advantage with 105-qubit zuchongzhi 3.0 processor”. In: *Physical Review Letters* 134.9 (2025), p. 090601.

[13] W. K. Wootters and W. H. Zurek. “A single quantum cannot be cloned”. In: *Nature* 299.5886 (1982), pp. 802–803.

[14] H. J. Kimble. “The quantum internet”. In: *Nature* 453.7198 (2008), pp. 1023–1030.

[15] P. Lebedew. “Untersuchungen über die Druckkräfte des Lichtes”. In: *Annalen der Physik* 311.11 (1901), pp. 433–458.

[16] M. Aspelmeyer, T. J. Kippenberg, and F. Marquardt. “Cavity optomechanics”. In: *Reviews of Modern Physics* 86.4 (2014), p. 1391.

[17] J. Curie and P. Curie. “Développement par compression de l’électricité polaire dans les cristaux hémièdres à faces inclinées”. In: *Bulletin de minéralogie* 3.4 (1880), pp. 90–93.

[18] L.-M. Duan, M. D. Lukin, J. I. Cirac, and P. Zoller. “Long-distance quantum communication with atomic ensembles and linear optics”. In: *Nature* 414.6862 (2001), pp. 413–418.

[19] M. Eichenfield, J. Chan, R. M. Camacho, K. J. Vahala, and O. Painter. “Optomechanical crystals”. In: *Nature* 462.7269 (2009), pp. 78–82.

[20] J. Chan, A. H. Safavi-Naeini, J. T. Hill, S. Meenehan, and O. Painter. “Optimized optomechanical crystal cavity with acoustic radiation shield”. In: *Applied Physics Letters* 101.8 (2012).

[21] A. H. Safavi-Naeini. *Quantum optomechanics with silicon nanostructures*. 2013.

[22] J. Chan. *Laser cooling of an optomechanical crystal resonator to its quantum ground state of motion*. California Institute of Technology, 2012.

[23] T. Asano, Y. Ochi, Y. Takahashi, K. Kishimoto, and S. Noda. “Photonic crystal nanocavity with a Q factor exceeding eleven million”. In: *Optics express* 25.3 (2017), pp. 1769–1777.

[24] A. H. Safavi-Naeini and O. Painter. “Design of optomechanical cavities and waveguides on a simultaneous bandgap phononic-photonic crystal slab”. In: *Opt. Express* 18.14 (July 2010), pp. 14926–14943.

[25] J. D. Joannopoulos, S. G. Johnson, J. N. Winn, and R. D. Meade. “Molding the flow of light”. In: *Princet. Univ. Press. Princeton, NJ [ua]* 12 (2008).

[26] A. H. Safavi-Naeini, J. T. Hill, S. Meenehan, J. Chan, S. Gröblacher, and O. Painter. “Two-dimensional phononic-photonic band gap optomechanical crystal cavity”. In: *Physical Review Letters* 112.15 (2014), p. 153603.

[27] F. M. Mayor, S. Malik, A. G. Primo, S. Gyger, W. Jiang, T. P. Alegre, and A. H. Safavi-Naeini. “High photon-phonon pair generation rate in a two-dimensional optomechanical crystal”. In: *Nature Communications* 16.1 (2025), p. 2576.

[28] H. Ren, M. H. Matheny, G. S. MacCabe, J. Luo, H. Pfeifer, M. Mirhosseini, and O. Painter. "Two-dimensional optomechanical crystal cavity with high quantum cooperativity". In: *Nature communications* 11.1 (2020), pp. 1–10.

[29] S. Liu, H. Tong, and K. Fang. "Optomechanical crystal with bound states in the continuum". In: *Nature communications* 13.1 (2022), p. 3187.

[30] A. N. Babar, T. A. S. Weis, K. Tsoukalas, S. Kadkhodazadeh, G. Arregui, B. Vosoughi Lahijani, and S. Stobbe. "Self-assembled photonic cavities with atomic-scale confinement". In: *Nature* 624.7990 (2023), pp. 57–63.

[31] A. Bozkurt, C. Joshi, and M. Mirhosseini. "Deep sub-wavelength localization of light and sound in dielectric resonators". In: *Optics Express* 30.8 (2022), pp. 12378–12386.

[32] S. Meesala, S. Wood, D. Lake, P. Chiappina, C. Zhong, A. D. Beyer, M. D. Shaw, L. Jiang, and O. Painter. "Non-classical microwave-optical photon pair generation with a chip-scale transducer". In: *arXiv preprint arXiv:2303.17684* (2023).

[33] H. Zhao, W. D. Chen, A. Kejriwal, and M. Mirhosseini. "Quantum-enabled microwave-to-optical transduction via silicon nanomechanics". In: *Nature Nanotechnology* (2025), pp. 1–7.

[34] H. S. Dutta, A. K. Goyal, V. Srivastava, and S. Pal. "Coupling light in photonic crystal waveguides: A review". In: *Photonics and Nanostructures-Fundamentals and Applications* 20 (2016), pp. 41–58.

[35] S. Sonar*, U. Hatipoglu*, S. Meesala, D. P. Lake, H. Ren, and O. Painter. "High-efficiency low-noise optomechanical crystal photon-phonon transducers." In: *Optica* 12.1 (2025), pp. 99–104.

[36] G. S. MacCabe, H. Ren, J. Luo, J. D. Cohen, H. Zhou, A. Sipahigil, M. Mirhosseini, and O. Painter. "Nano-acoustic resonator with ultralong phonon lifetime". In: *Science* 370.6518 (2020), pp. 840–843.

[37] N. Zen, T. A. Puurtinen, T. J. Isotalo, S. Chaudhuri, and I. J. Maasilta. "Engineering thermal conductance using a two-dimensional phononic crystal". In: *Nature communications* 5.1 (2014), p. 3435.

[38] J. Maire, R. Anufriev, R. Yanagisawa, A. Ramiere, S. Volz, and M. Nomura. "Heat conduction tuning by wave nature of phonons". In: *Science advances* 3.8 (2017), e1700027.

[39] M. R. Wagner, B. Graczykowski, J. S. Reparaz, A. El Sachat, M. Sledzinska, F. Alzina, and C. M. Sotomayor Torres. "Two-dimensional phononic crystals: Disorder matters". In: *Nano letters* 16.9 (2016), pp. 5661–5668.

[40] A. H. Safavi-Naeini, T. M. Alegre, J. Chan, M. Eichenfield, M. Winger, Q. Lin, J. T. Hill, D. E. Chang, and O. Painter. "Electromagnetically induced transparency and slow light with optomechanics". In: *Nature* 472.7341 (2011), pp. 69–73.

[41] S. M. Meenehan, J. D. Cohen, G. S. MacCabe, F. Marsili, M. D. Shaw, and O. Painter. “Pulsed excitation dynamics of an optomechanical crystal resonator near its quantum ground state of motion”. In: *Physical Review X* 5.4 (2015), p. 041002.

[42] M. Borselli, T. J. Johnson, and O. Painter. “Measuring the role of surface chemistry in silicon microphotonics”. In: *Applied Physics Letters* 88.13 (2006).

[43] O. Florez, G. Arregui, M. Albrechtsen, R. C. Ng, J. Gomis-Bresco, S. Stobbe, C. M. Sotomayor-Torres, and P. D. Garcıa. “Engineering nanoscale hypersonic phonon transport”. In: *Nature Nanotechnology* 17.9 (2022), pp. 947–951.

[44] A. Wallucks, I. Marinković, B. Hensen, R. Stockill, and S. Gröblacher. “A quantum memory at telecom wavelengths”. In: *Nature Physics* 16.7 (2020), pp. 772–777.

[45] M. Chen, J. C. Owens, H. Putterman, M. Schäfer, and O. Painter. “Phonon engineering of atomic-scale defects in superconducting quantum circuits”. In: *arXiv preprint arXiv:2310.03929* (2023).

[46] A. Y. Cleland, E. A. Wollack, and A. H. Safavi-Naeini. “Studying phonon coherence with a quantum sensor”. In: *arXiv preprint arXiv:2302.00221* (2023).

[47] M. Yuksel, M. Maksymowych, O. Hitchcock, F. Mayor, N. Lee, M. Dykman, A. Safavi-Naeini, and M. Roukes. “Strong Coupling of Nanomechanical Vibrations to Individual Two-Level Systems”. In: *arXiv preprint arXiv:2502.18587* (2025).

[48] S. Meesala, S. Wood, D. Lake, P. Chiappina, C. Zhong, A. D. Beyer, M. D. Shaw, L. Jiang, and O. Painter. “Non-classical microwave–optical photon pair generation with a chip-scale transducer”. In: *Nature Physics* (2024), pp. 1–7.

[49] W. Jiang, F. M. Mayor, S. Malik, R. Van Laer, T. P. McKenna, R. N. Patel, J. D. Witmer, and A. H. Safavi-Naeini. “Optically heralded microwave photon addition”. In: *Nature Physics* 19.10 (2023), pp. 1423–1428.

[50] M. J. Weaver, P. Duivestein, A. C. Bernasconi, S. Scharmer, M. Lemang, T. C. v. Thiel, F. Hijazi, B. Hensen, S. Gröblacher, and R. Stockill. “An integrated microwave-to-optics interface for scalable quantum computing”. In: *Nature Nanotechnology* (2023), pp. 1–7.

[51] R. Delaney, M. Urmey, S. Mittal, B. Brubaker, J. Kindem, P. Burns, C. Regal, and K. Lehnert. “Superconducting-qubit readout via low-backaction electro-optic transduction”. In: *Nature* 606.7914 (2022), pp. 489–493.

[52] T. van Thiel, M. Weaver, F. Berto, P. Duivestein, M. Lemang, K. Schuurman, M. Žemlička, F. Hijazi, A. Bernasconi, E. Lachman, et al. "High-fidelity optical readout of a superconducting qubit using a scalable piezo-optomechanical transducer". In: *arXiv preprint arXiv:2310.06026* (2023).

[53] G. Arnold, T. Werner, R. Sahu, L. N. Kapoor, L. Qiu, and J. M. Fink. "All-optical single-shot readout of a superconducting qubit". In: *arXiv preprint arXiv:2310.16817* (2023).

[54] C. Kittel and P. McEuen. *Introduction to solid state physics*. John Wiley & Sons, 2018.

[55] Y. Liao, T. Shiga, M. Kashiwagi, and J. Shiomi. "Akhiezer mechanism limits coherent heat conduction in phononic crystals". In: *Physical Review B* 98.13 (2018), p. 134307.

[56] R. Anufriev and M. Nomura. "Reduction of thermal conductance by coherent phonon scattering in two-dimensional phononic crystals of different lattice types". In: *Physical Review B* 93.4 (2016), p. 045410.

[57] B. L. Davis and M. I. Hussein. "Nanophononic metamaterial: Thermal conductivity reduction by local resonance". In: *Physical review letters* 112.5 (2014), p. 055505.

[58] H. Honarvar and M. I. Hussein. "Spectral energy analysis of locally resonant nanophononic metamaterials by molecular simulations". In: *Physical Review B* 93.8 (2016), p. 081412.

[59] R. Anufriev and M. Nomura. "Heat conduction engineering in pillar-based phononic crystals". In: *Physical Review B* 95.15 (2017), p. 155432.

[60] I. Maasilta, T. Puurtinen, Y. Tian, and Z. Geng. "Phononic thermal conduction engineering for bolometers: From phononic crystals to radial casimir limit". In: *Journal of Low Temperature Physics* 184 (2016), pp. 211–216.

[61] J. M. Ziman. *Electrons and phonons: the theory of transport phenomena in solids*. Oxford university press, 2001.

[62] Y. Tian, T. A. Puurtinen, Z. Geng, and I. J. Maasilta. "Minimizing coherent thermal conductance by controlling the periodicity of two-dimensional phononic crystals". In: *Physical Review Applied* 12.1 (2019), p. 014008.

[63] M. Weaver, G. Arnold, H. Weaver, S. Gröblacher, and R. Stockill. "Scalable Quantum Computing with Optical Links". In: *arXiv preprint arXiv:2505.00542* (2025).

[64] R. Sahu, W. Hease, A. Rueda, G. Arnold, L. Qiu, and J. M. Fink. "Quantum-enabled operation of a microwave-optical interface". In: *Nature communications* 13.1 (2022), p. 1276.

[65] R. Sahu, L. Qiu, W. Hease, G. Arnold, Y. Minoguchi, P. Rabl, and J. M. Fink. "Entangling microwaves with light". In: *Science* 380.6646 (2023), pp. 718–721.

[66] L. Fan, C.-L. Zou, R. Cheng, X. Guo, X. Han, Z. Gong, S. Wang, and H. X. Tang. "Superconducting cavity electro-optics: a platform for coherent photon conversion between superconducting and photonic circuits". In: *Science advances* 4.8 (2018), eaar4994.

[67] T. P. McKenna, J. D. Witmer, R. N. Patel, W. Jiang, R. Van Laer, P. Arrangoiz-Arriola, E. A. Wollack, J. F. Herrmann, and A. H. Safavi-Naeini. "Cryogenic microwave-to-optical conversion using a triply resonant lithium-niobate-on-sapphire transducer". In: *Optica* 7.12 (2020), pp. 1737–1745.

[68] J. Holzgrafe, N. Sinclair, D. Zhu, A. Shams-Ansari, M. Colangelo, Y. Hu, M. Zhang, K. K. Berggren, and M. Lončar. "Cavity electro-optics in thin-film lithium niobate for efficient microwave-to-optical transduction". In: *Optica* 7.12 (2020), pp. 1714–1720.

[69] M. Zanner, T. Orell, C. M. Schneider, R. Albert, S. Oleschko, M. L. Juan, M. Silveri, and G. Kirchmair. "Coherent control of a multi-qubit dark state in waveguide quantum electrodynamics". In: *Nature Physics* 18.5 (2022), pp. 538–543.

[70] W. Fu, M. Xu, X. Liu, C.-L. Zou, C. Zhong, X. Han, M. Shen, Y. Xu, R. Cheng, S. Wang, et al. "Cavity electro-optic circuit for microwave-to-optical conversion in the quantum ground state". In: *Physical Review A* 103.5 (2021), p. 053504.

[71] Y. Xu, A. A. Sayem, L. Fan, C.-L. Zou, S. Wang, R. Cheng, W. Fu, L. Yang, M. Xu, and H. X. Tang. "Bidirectional interconversion of microwave and light with thin-film lithium niobate". In: *Nature communications* 12.1 (2021), p. 4453.

[72] R. W. Andrews, R. W. Peterson, T. P. Purdy, K. Cicak, R. W. Simmonds, C. A. Regal, and K. W. Lehnert. "Bidirectional and efficient conversion between microwave and optical light". In: *Nature physics* 10.4 (2014), pp. 321–326.

[73] B. M. Brubaker, J. M. Kindem, M. D. Urmey, S. Mittal, R. D. Delaney, P. S. Burns, M. R. Vissers, K. W. Lehnert, and C. A. Regal. "Optomechanical ground-state cooling in a continuous and efficient electro-optic transducer". In: *Physical Review X* 12.2 (2022), p. 021062.

[74] H. Zhao, A. Bozkurt, and M. Mirhosseini. "Electro-optic transduction in silicon via gigahertz-frequency nanomechanics". In: *Optica* 10.6 (2023), pp. 790–796.

[75] J. G. Bartholomew, J. Rochman, T. Xie, J. M. Kindem, A. Ruskuc, I. Craiciu, M. Lei, and A. Faraon. "On-chip coherent microwave-to-optical transduction mediated by ytterbium in YVO4". In: *Nature communications* 11.1 (2020), p. 3266.

[76] J. Rochman, T. Xie, J. G. Bartholomew, K. Schwab, and A. Faraon. "Microwave-to-optical transduction with erbium ions coupled to planar photonic and superconducting resonators". In: *Nature Communications* 14.1 (2023), p. 1153.

[77] T. Xie, R. Fukumori, J. Li, and A. Faraon. "Scalable microwave-to-optical transducers at the single-photon level with spins". In: *Nature Physics* (2025), pp. 1–7.

[78] N. Zhu, X. Zhang, X. Han, C.-L. Zou, C. Zhong, C.-H. Wang, L. Jiang, and H. X. Tang. "Waveguide cavity optomagnonics for microwave-to-optics conversion". In: *Optica* 7.10 (2020), pp. 1291–1297.

[79] M. Mirhosseini, A. Sipahigil, M. Kalaee, and O. Painter. "Superconducting qubit to optical photon transduction". In: *Nature* 588.7839 (2020), pp. 599–603.

[80] S. Meesala, D. Lake, S. Wood, P. Chiappina, C. Zhong, A. D. Beyer, M. D. Shaw, L. Jiang, and O. Painter. "Quantum entanglement between optical and microwave photonic qubits". In: *Physical Review X* 14.3 (2024), p. 031055.

[81] K. Airola, S. Mertin, J. Likonen, E. Hartikainen, K. Mizohata, J. Dekker, A. T. Sebastian, and T. Pensala. "High-fidelity patterning of AlN and ScAlN thin films with wet chemical etching". In: *Materialia* 22 (2022), p. 101403.

[82] P. Chiappina, J. Banker, S. Meesala, D. Lake, S. Wood, and O. Painter. "Design of an ultra-low mode volume piezo-optomechanical quantum transducer". In: *Optics Express* 31.14 (2023), pp. 22914–22927.

[83] A. S. Kher. *Superconducting nonlinear kinetic inductance devices*. California Institute of Technology, 2017.

[84] S. Kubo, M. Asahi, M. Hikita, and M. Igarashi. "Magnetic penetration depths in superconducting NbN films prepared by reactive dc magnetron sputtering". In: *Applied physics letters* 44.2 (1984), pp. 258–260.

[85] P. E. Barclay, K. Srinivasan, M. Borselli, and O. Painter. "Efficient input and output fiber coupling to a photonic crystal waveguide". In: *Optics Letters* 29.7 (2004), pp. 697–699.

[86] K. C. Balram, M. I. Davanço, J. D. Song, and K. Srinivasan. "Coherent coupling between radiofrequency, optical and acoustic waves in piezo-optomechanical circuits". In: *Nature photonics* 10.5 (2016), p. 346.

[87] W. Jiang, C. J. Sarabalis, Y. D. Dahmani, R. N. Patel, F. M. Mayor, T. P. McKenna, R. Van Laer, and A. H. Safavi-Naeini. "Efficient bidirectional piezo-optomechanical transduction between microwave and optical frequency". In: *Nature communications* 11.1 (2020), p. 1166.

[88] E. A. Wollack, A. Y. Cleland, P. Arrangoiz-Arriola, T. P. McKenna, R. G. Gruenke, R. N. Patel, W. Jiang, C. J. Sarabalis, and A. H. Safavi-Naeini. "Loss channels affecting lithium niobate phononic crystal resonators at cryogenic temperature". In: *Applied Physics Letters* 118.12 (2021).

[89] J. Niu, L. Zhang, Y. Liu, J. Qiu, W. Huang, J. Huang, H. Jia, J. Liu, Z. Tao, W. Wei, et al. "Low-loss interconnects for modular superconducting quantum processors". In: *Nature Electronics* 6.3 (2023), pp. 235–241.

[90] P. Kurpiers, P. Magnard, T. Walter, B. Royer, M. Pechal, J. Heinsoo, Y. Salathé, A. Akin, S. Storz, J.-C. Besse, et al. "Deterministic quantum state transfer and remote entanglement using microwave photons". In: *Nature* 558.7709 (2018), pp. 264–267.

[91] U. Hatipoglu*, S. Sonar*, D. P. Lake, S. Meesala, and O. Painter. "In situ tuning of optomechanical crystals with nano-oxidation." In: *Optica* 11.3 (2024), pp. 371–375.

[92] C. L. Panuski, I. Christen, M. Minkov, C. J. Brabec, S. Trajtenberg-Mills, A. D. Griffiths, J. J. McKendry, G. L. Leake, D. J. Coleman, C. Tran, et al. "A full degree-of-freedom spatiotemporal light modulator". In: *Nature Photonics* 16.12 (2022), pp. 834–842.

[93] C. W. Wong, P. T. Rakich, S. G. Johnson, M. Qi, H. I. Smith, E. P. Ippen, L. C. Kimerling, Y. Jeon, G. Barbastathis, and S.-G. Kim. "Strain-tunable silicon photonic band gap microcavities in optical waveguides". In: *Applied physics letters* 84.8 (2004), pp. 1242–1244.

[94] I. Luxmoore, E. D. Ahmadi, B. Luxmoore, N. Wasley, A. Tartakovskii, M. Hugues, M. Skolnick, and A. Fox. "Restoring mode degeneracy in H1 photonic crystal cavities by uniaxial strain tuning". In: *Applied Physics Letters* 100.12 (2012), p. 121116.

[95] M. S. Nawrocka, T. Liu, X. Wang, and R. R. Panepucci. "Tunable silicon microring resonator with wide free spectral range". In: *Applied physics letters* 89.7 (2006), p. 071110.

[96] A. Faraon, D. Englund, I. Fushman, J. Vučković, N. Stoltz, and P. Petroff. "Local quantum dot tuning on photonic crystal chips". In: *Applied Physics Letters* 90.21 (2007), p. 213110.

[97] S. Mosor, J. Hendrickson, B. Richards, J. Sweet, G. Khitrova, H. Gibbs, T. Yoshie, A. Scherer, O. Shchekin, and D. Deppe. "Scanning a photonic crystal slab nanocavity by condensation of xenon". In: *Applied Physics Letters* 87.14 (2005), p. 141105.

[98] S. Strauf, M. T. Rakher, I. Carmeli, K. Hennessy, C. Meier, A. Badolato, M. J. DeDood, P. M. Petroff, E. L. Hu, E. Gwinn, et al. "Frequency control of photonic crystal membrane resonators by monolayer deposition". In: *Applied Physics Letters* 88.4 (2006), p. 043116.

[99] K. Hennessy, C. Högerle, E. Hu, A. Badolato, and A. Imamoğlu. "Tuning photonic nanocavities by atomic force microscope nano-oxidation". In: *Applied physics letters* 89.4 (2006), p. 041118.

[100] A. Yokoo, T. Tanabe, E. Kuramochi, and M. Notomi. "Ultrahigh-Q nanocavities written with a nanoprobe". In: *Nano letters* 11.9 (2011), pp. 3634–3642.

[101] *Atomic force Microscopy: Park systems*. URL: https://www.parksystems.com/.

[102] R. Garcia, R. V. Martinez, and J. Martinez. "Nano-chemistry and scanning probe nanolithographies". In: *Chemical Society Reviews* 35.1 (2006), pp. 29–38.

[103] J. Chan, A. H. Safavi-Naeini, J. T. Hill, S. Meenehan, and O. Painter. "Optimized optomechanical crystal cavity with acoustic radiation shield". In: *Applied Physics Letters* 101.8 (2012), p. 081115. DOI: 10.1063/1.4747726. URL: https://doi.org/10.1063/1.4747726.

[104] S. Gröblacher, J. T. Hill, A. H. Safavi-Naeini, J. Chan, and O. Painter. "Highly efficient coupling from an optical fiber to a nanoscale silicon optomechanical cavity". In: *Applied Physics Letters* 103.18 (2013), p. 181104.

[105] V. Peano, C. Brendel, M. Schmidt, and F. Marquardt. "Topological phases of sound and light". In: *Physical Review X* 5.3 (2015), p. 031011.

[106] V. Peano, M. Houde, C. Brendel, F. Marquardt, and A. A. Clerk. "Topological phase transitions and chiral inelastic transport induced by the squeezing of light". In: *Nature communications* 7.1 (2016), pp. 1–8.

[107] C. Brendel, V. Peano, O. J. Painter, and F. Marquardt. "Pseudomagnetic fields for sound at the nanoscale". In: *Proceedings of the National Academy of Sciences* 114.17 (2017), E3390–E3395.

[108] H. Ren, T. Shah, H. Pfeifer, C. Brendel, V. Peano, F. Marquardt, and O. Painter. "Topological phonon transport in an optomechanical system". In: *Nature Communications* 13.1 (2022), p. 3476.

[109] F.-S. Chien, Y. Chou, T. Chen, W.-F. Hsieh, T.-S. Chao, and S. Gwo. "Nanooxidation of silicon nitride films with an atomic force microscope: Chemical mapping, kinetics, and applications". In: *Journal of Applied Physics* 89.4 (2001), pp. 2465–2472.

[110] R. D. Delaney, M. D. Urmey, S. Mittal, B. M. Brubaker, J. M. Kindem, P. S. Burns, C. A. Regal, and K. W. Lehnert. "Superconducting-qubit readout via low-backaction electro-optic transduction". In: *Nature* 606.7914 (June 2022), pp. 489–493. ISSN: 1476-4687. DOI: 10.1038/s41586-022-04720-2. URL: https://doi.org/10.1038/s41586-022-04720-2.

[111] J. Lisenfeld, A. Bilmes, S. Matityahu, S. Zanker, M. Marthaler, M. Schechter, G. Schön, A. Shnirman, G. Weiss, and A. V. Ustinov. "Decoherence spectroscopy with individual two-level tunneling defects". In: *Scientific Reports* 6.1 (2016), p. 23786. ISSN: 2045-2322. DOI: 10.1038/srep23786. URL: https://doi.org/10.1038/srep23786.

[112] G. White. “Thermal expansion of reference materials: copper, silica and silicon”. In: *Journal of Physics D: Applied Physics* 6.17 (1973), p. 2070.

[113] J. Komma, C. Schwarz, G. Hofmann, D. Heinert, and R. Nawrodt. “Thermo-optic coefficient of silicon at 1550 nm and cryogenic temperatures”. In: *Applied physics letters* 101.4 (2012).

[114] M. McEwen, K. C. Miao, J. Atalaya, A. Bilmes, A. Crook, J. Bovaird, J. M. Kreikebaum, N. Zobrist, E. Jeffrey, B. Ying, et al. “Resisting high-energy impact events through gap engineering in superconducting qubit arrays”. In: *Physical Review Letters* 133.24 (2024), p. 240601.

[115] C. P. Anderson, G. Scuri, A. Chan, S. Eun, A. D. White, G. H. Ahn, C. Jilly, A. Safavi-Naeini, K. Van Gasse, L. Li, et al. “Quantum critical electro-optic and piezo-electric nonlinearities”. In: *arXiv preprint arXiv:2502.15164* (2025).

[116] A. Ulrich, K. Brahim, A. Boelen, M. Debaets, C. Sun, Y. Huang, S. S. Saseendran, M. Baryshnikova, P. Favia, T. Nuytten, et al. “Engineering high Pockels coefficients in thin-film strontium titanate for cryogenic quantum electro-optic applications”. In: *arXiv preprint arXiv:2502.14349* (2025).

[117] D. Zhu, M. Colangelo, C. Chen, B. A. Korzh, F. N. Wong, M. D. Shaw, and K. K. Berggren. “Resolving photon numbers using a superconducting nanowire with impedance-matching taper”. In: *Nano Letters* 20.5 (2020), pp. 3858–3863.